Guiding Deep Brain Stimulation Neurosurgery with Optical Spectroscopy

Thèse

Damon Depaoli

Doctorat en biophotonique
Philosophiæ doctor (Ph. D.)

Québec, Canada

Guiding Deep Brain Stimulation Neurosurgery with Optical Spectroscopy

Thèse

Damon Thomas DePaoli

Sous la direction de:

Daniel Côté, Co-directeur principal de recherche
Martin Parent, Co-directeur de recherche

Résumé

Savoir différiencier les différentes types de tissus représente un aspect important lors d'interventions médicales, que ce soit pour aider au diagnostic d'une maladie ou pour le guidage chirurgical. Il est généralement très difficile de distinguer les tissus sains des tissus pathologiques à l'oeil nu et la navigation chirurgicale peut parfois être difficile dans les grands organes où la structure ciblé se trouve enfouie profondément. De nouvelles méthodes susceptibles d'accroître la réussite de telles interventions médicales suscitent actuellement de l'intérêt chez les professionnels de la santé. La spectroscopie optique, en analysant les interactions lumière-tissu dans une plage spectrale définie, est un outil permettant de différencier les tissus avec une résolution et une sensibilité bien supérieures à celles de l'œil humain.

Tout au long de cette thèse, je détaillerai comment la spectroscopie optique a été utilisée pour créer et améliorer un système de guidage optique utilisé pour la stimulation cérébrale profonde en neurochirurgie, en particulier pour le traitement de la maladie de Parkinson. Pour commencer, je montrerai comment les informations spectroscopiques peuvent fournir une rétroaction peropératoire en temps réel à un neurochirurgien, au cours de la phase d'implantation de la procédure, avec une sonde qui n'induit aucune invasion supplémentaire. Je présenterai l'investigation de deux modalités spectroscopiques différentes pour la discrimination tissulaire pour le guidage, soit la spectroscopie à réflectance diffuse et la spectroscopie de diffusion Raman anti-Stokes cohérente. Les avantages et les inconvénients des deux techniques, ainsi que leurs aptitude à la traduction prometteuse pour cette application seront abordés.

Par la suite, je présenterai une nouvelle technique d'analyse de données pour extraire l'oxygénation des tissus à partir de spectres de réflectance diffus dans le but d'améliorer la précision de mesure en spectroscopie rétinienne et ultimement de porter un diagnostique. Bien que conçu pour la rétine, l'algorithme peut également être utilisé pour analyser les spectres acquis lors d'une neurochirurgie afin de fournir des informations à la fois discriminantes et diagnostiques. Finalement, je montrerai des preuves de diffusion anisotrope de la lumière dans les axones myélinisés de la moelle épinière et discuterai des conséquences que cela pourrait avoir sur les simulations actuelles de la propagation des photons dans le cerveau, qui feront partie intégrante d'un guidage optique efficace.

Abstract

Differentiating tissue types is an important aspect of guiding medical interventions whether it be for disease diagnosis or for surgical guidance. However, diseased and healthy tissues are often hard to discriminate by human vision alone and surgical navigation can be difficult to accomplish in large organs where the target structure lies deep within the body. New methods that can increase certainty in such medical interventions are therefore of great interest to healthcare professionals. Optical spectroscopy is a tool which can be exploited to probe discriminatory information in tissue by analyzing light-tissue interactions with a spectral range, resolution and sensitivity much greater than the human eye.

Throughout this thesis, I will explain how I have leveraged optical spectroscopy to create, and improve, an optical guidance system for deep brain stimulation neurosurgery, specifically for the treatment of Parkinson's disease. I will begin by describing how spectroscopic information can provide real-time feedback to a surgeon during the procedure, in the hopes of ultimately improving treatment outcome. To this end, I will present the investigation of two different spectroscopic modalities for optical guidance: diffuse reflectance spectroscopy, and coherent anti-Stokes Raman scattering spectroscopy. The advantages and disadvantages of both techniques will be discussed along with their promising translatability for this application.

Following this, I will present a novel data analysis technique for extracting the tissue oxygenation from diffuse reflectance spectra with the aim of improved diagnostic information in retinal spectroscopy. While designed for the retina, the algorithm can also be used to analyze spectra acquired during a neurosurgery to provide both discriminatory and diagnostic information. Lastly, I will show evidence of anisotropic light scattering in the myelinated axons of the spinal cord and discuss the implications this may have on current photon propagation simulations in the brain, which will be integral for effective optical guidance.

Contents

List of Tables

List of Figures

Dedicated to Grandma & Nona

You gotta be lucky to be good

Steve Hackett

Remerciements

Tout d'abord, je voudrais remercier mon superviseur, le Dr Daniel Côté, qui, sur un coup de tête, m'a amené à Québec en 2014 pour commencer ma maîtrise. Bien qu'il y ait beaucoup à dire, je vais rester bref. Merci de me donner assez de liberté pour explorer ma propre curiosité et de m'avoir donné la confiance nécessaire pour devenir un penseur indépendant. Ma décision de rester dans la recherche est vraiment le résultat de votre présence dans votre laboratoire.

Ensuite, mon co-directeur, le Dr Martin Parent, dont la présence est devenue de plus en plus importante pour moi au fil de mes études. Merci de m'avoir appris votre approche méthodique de la science et d'être toujours un mentor fiable. Si j'ai le plaisir de diriger mon propre groupe de chercheurs, j'espère le faire avec une compassion similaire.

Un grand merci également à mes mentors proches: Dr Frederic Leblond et Dr Laurent Goetz. Vos deux contributions tout au long de mon parcours ont été précieuses pour guider mes objectifs scientifiques et mon cheminement de carrière. Merci au groupe de direction de biophotonique: Dr Paul De Koninck et le conseiller du programme, Dr Mario Methot. Ce programme offre la flexibilité nécessaire pour développer sans limitation

Je tiens également à remercier tous mes anciens collègues des laboratoires Côté et Parent pour avoir rendu mon séjour au Centre de recherche CERVO aussi agréable. Un merci spécial à mon premier collègue, mentor et ami au Québec, Nicolas Lapointe, de m'avoir intégré à la culture québécoise depuis mon arrivée à l'hôpital Robert Giffard.

Enfin, aucune de mes réalisations n'aurait été possible sans le soutien de mes incroyables parents, Colleen et Tom. Merci à vous deux pour votre soutien durant ce long voyage académique.

Appreciations

First and foremost, I would like to thank my supervisor Dr. Daniel Côté, who on a whim, brought me to Quebec City in 2014 to start my MSc. While there's lots to say, I will try to keep it short. Thank you for providing me enough freedom to explore my own curiosity and for instilling in me the confidence to become an independent thinker. My decision to stay in research is truly a result of being in your lab.

Next, my co-supervisor Dr. Martin Parent, whose presence became more and more important to me over the course of my degree. Thank you for teaching me your methodical approach to science and for always being a dependable mentor. If I ever have the pleasure to lead my own group of researchers, I hope to do so with a similar compassion.

Also a considerable thanks to my mentors at-arms-length: Dr. Frederic Leblond and Dr. Laurent Goetz. Both of your inputs throughout my journey have been invaluable in guiding my scientific objectives and my overall career path. Thanks to the biophotonics leadership group: Dr. Paul De Koninck and Dr. Mario Methot. This program has just the right flexibility to grow without limitations.

I would also like to thank all my past labmates in the Côté and Parent labs for making my time at CERVO so enjoyable. A special thanks to my first colleague, mentor and friend in Quebec, Nicolas Lapointe, for ingraining me into Quebec culture ever since my arrival at Robert Giffard Hospital.

Lastly, none of my accomplishments would have been possible without the support of my amazing parents, Colleen and Tom. Thank you both for all the support during this long academic journey.

Avant-propos

This thesis consists of 5 scientific articles, with 3 published, 1 in review and 1 in the final stages of preparation before submission. The journals associated with these articles are world-renowned with relatively high impact factors for engineering endeavours, such as: Scientific Reports (IF: 4.525), Journal of Neurosurgery (IF: 4.059) and Neurophotonics (IF: 4.129). The central project of this thesis was the development and integration of a fiber-based optical guidance system for deep brain stimulation (DBS) neurosurgery using optical spectroscopy. Along the way, new spectroscopic discoveries and applications were realized through this work in other parts of the central nervous system such as the retina and the spinal cord. All of the work is included as the extensions emphasize the translatability of the skills acquired throughout this degree. The work presented herein was performed during my doctoral degree at the CERVO Brain Research Center under the supervision of Prof. Daniel Côté and Prof. Martin Parent. Prof. Côté is a renowned biophotonics expert with a specialization in microscopy and Prof. Parent a renowned neuroanatomist well known for his contributions in Parkinson's disease. Together, their expertise helped to guide each of my projects, even if not explicitly mentioned. Here, I describe each of the works that will be presented in this thesis.

The list of articles and their corresponding chapters are described here:

1. DePaoli, D. T.*, Lemoine, E.*, Parent, M., Leblond, F., & Côté, D. C. (2019). Raman Spectroscopy for Neurosurgery. (*in preparation*) *Co-First Authors
2. DePaoli, D. T., Lapointe, N., Messaddeq, Y., Parent, M., & Côté, D. C. (2018). Intact primate brain tissue identification using a completely fibered coherent Raman spectroscopy system. Neurophotonics, 5(03), 1. https://doi.org/10.1117/1.NPh.5.3.035005 [1]
3. DePaoli, D. T., Goetz, L., Gagnon, D., Maranon, G., Prud'homme, M., Cantin, L., & Côté, D. C. (2019). Intraoperative fiber optic guidance during chronic electrode implantation in deep brain stimulation neurosurgery: proof of concept in primates. Journal of Neurosurgery, 1–10. https://doi.org/10.3171/2019.1.JNS182600 [2]
4. DePaoli, D. T., Tossou, P., Parent, M., Sauvageau, D., & Côté, D. C. (2019). Convolutional Neural Networks for Spectroscopic Analysis in Retinal Oximetry. Scientific

Reports, 9(1), 11387. https://doi.org/10.1038/s41598-019-47621-7 [3]

5. DePaoli D. T.*, Gasecka, A.*, Bahdine, M., Deschenes, J.M., Goetz, L., Perez-Sanchez, J., Bonin, R., De Koninck, Y., Parent, M., & Côté, D. C. (2019). Anisotropic light scattering from myelinated axons in the spinal cord. Neurophotonics (*In review*) *Co-First Authors

.

Chapter 1 is a Review, in the final stages of preparation, on Raman spectroscopy for neurosurgery. This reviem is planned to be submitted for peer review and summarizes the current leading edge technology and data science that is being deployed in the operating room using Raman modalities for neurosurgery. Furthermore, it goes into depth on spontaneous and coherent Raman counterparts to allow the readers to make better-informed devices before embarking down the application-specific development road. Lastly, it provides a perspective from our team, the designated experts, on the future of this modality in the operating room. I was a co-first author on this publication, contributing to the writing and editing of the Introduction, Hardware Review and the closing section. The data analysis section was written by my colleague (and other co-first author) Émile Lemoine. We edited the entire document together along with help from Dr. Parent, Dr. Leblond and Dr. Côté.

Chapter 2 is an accepted research article in the journal, *Neurophotonics (SPIE publishing)*. This article was the first fruition of the central neurosurgery-driven research project which aimed to develop a fiber-optic sensing device for tissue identification during DBS neurosurgery. The fiber optic device herein used coherent anti-Stokes Raman scattering (CARS) to create an ultra small form factor Raman spectroscopy probe such as to allow it to be housed within the deep brain stimulation (DBS) electrode during its implantation. Until this work, no silica based CARS probes had been successfully implemented due to the complicated non-linear effects that occur when high peak-power pulses (required for CARS generation) propagate through dispersive media. We enabled this through careful experimentation and by using a new laser source which minimized these effects. Raman spectroscopy is a unique modality in the sense that it can provide fingerprint type information from a sample, meaning that eventually it could be used to classify specific brain structures directly. The creation of fiber-based CARS probes is sought-after due to the increased signal generation in comparison to spontaneous Raman (allowing faster sensing speeds and smaller probes), and the optically sectioned signal generation (allowing high resolution sensing and imaging). We also showed that the system is completely portable and all-fibered - therefore ready for clinical translation. This is a rare feet, as laser sources for CARS are normally large and require optical tables for free-space alignment. This work set the stage for clinical, fiber-based CARS spectroscopy and imaging. My role in this work was all-encompassing, from creating the optical probe, to performing the measurements and data analysis, to working with Halifax Biomedical Imaging (our industry collaboration) to improve and guide the development of

our specialized laser. Nicolas Lapointe worked on this project at an earlier stage, which allowed me to have the success I did. Dr. Messadeq provided insights into the optical probe. I wrote this manuscript in its entirety with aid from Dr. Parent and Dr. Côté.

Chapter 3 is a proof of concept research article, in primates, for the ability of spectroscopic information to guide DBS electrode implantation from within commercially available DBS electrodes. This work was published in the renowned journal for neurosurgeons: *Journal of Neurosurgery (Journal of Neurosurgery Publishing)*, showing its translatable merit. In this work, we used diffuse reflectance spectroscopy (DRS) to discern tissue structures due to its efficient process, also allowing small form factor probes and the added ability to sense through the semi-opaque DBS electrode tip. Since DRS information is limited to sensing the colour of the tissue, only blood vessels, white matter, grey matter, and white-grey matter tissue regions can be discriminated. However, along the trajectory of the DBS electrode to a target brain structure, many different tissues are passed through, and the order of these structures holds information. We term the ordered tissue information an optical barcode based on the pattern of the alternating tissue types. The idea of using optical barcodes based on tissue order was therefore proposed to predict on and off trajectory implantations to the target nuclei. We validated these predictions in living, intact primate brain, which while smaller, are reasonably neuro-anatomically similar to human counterparts. This work was the first time the idea intraoperative fiber-optic guidance *during the implantation* of the chronic DBS electrode was presented, and was a considerable step forward in terms of translation due to this. Personally, I was involved in every step of this work, from making the probes to performing the surgeries, to acquiring and analyzing the data, to performing histological sectioning. The surgeries were planned and executed with help from my colleagues Dr. Goetz, Dr. Gagnon and Dr. Parent. Gabriel Maranon performed the blood vessel detection under my supervision. Dr. Prud'homme and Dr. Cantin help guide the project with their neurosurgical expertise. I wrote this manuscript with aid from Dr. Goetz, Dr. Parent, and Dr. Côté.

Chapter 4 was the result of a collaborative research effort during a MITACS internship at Zilia Inc., a start-up in Quebec City performing retinal tissue oximetry. Zilia was in the need for an improved algorithm to perform retinal oximetry, which involves the analysis of DRS spectra - very similar to the ones that are acquired in the brain. Due to my experience in DRS spectroscopic analysis and the direction of my project going into the use of advanced data science techniques for tissue classification, I worked on this application in collaboration with Zilia and my colleague Prudencio Toussou. The fruition of this collaboration led to the presented article in the journal *Scientific Reports (Nature publishing)*. This work showed the considerable advantages of using machine learning to perform oxygen saturation measurements and is a central piece in Zilia's technology where accurate and precise measurements are paramount for eventual disease diagnosis and monitoring. For this work, I created a simulated database of DRS spectra which could be acquired from the retina, covering the

vast variability found from a biological structure. I then coded and compared several published and non-published algorithms based on few-wavelength and multi-wavelength analysis models for measuring the concentration of oxygenated hemoglobin from a given DRS spectra. Prudencio provided the convolutional neural network architecture which we slowly optimized together by tuning the simulated data. Prudencio and I wrote the description of the machine learning algorithm together, while I uniquely wrote the rest of this manuscript, along with revisions from Dr. Parent, Dr. Sauvageu and Dr. Côté.

Chapter 5 is a research article currently in review, also in the journal *Neurophotonics (SPIE Publishing)*. This work was done in collaboration with a post-doctoral researcher in the lab, Dr. Alicja Gasecka. For the neurosurgery project which in one instance may use DRS and barcode type information, efficient optical simulations for the expected DRS spectra acquired along a given descent would be critical for predicting where the probe (and electrode) are in the brain. To this end: creating simulated optical barcodes, patient specific by means of the pre-operative MRI, would be advantageous. However, improvements to classical Monte Carlo implementations were expected due to the observed anisotropic scattering of myelinated axons in nervous tissue. To make these observations quantitative, the ideal tissue structure to study this anisotropy was the spinal cord due to the directionally collinear axons in the white matter and the randomly oriented axons in the grey matter. We showed in this work empirical evidence of anisotropic scattering along myelinated axons and analyzed the effects that this new information may have for traditional Monte Carlo simulations. My contribution to this work was overseeing and participating in the measurements of the directionally dependant scattering coefficients, acquiring the transmission images of the various section, creating the modified three-dimensional Monte Carlo code to take into account multi-directional scattering coefficients and lastly performing the imaging alluding to optical waveguide effects in myelin,shown in the appendix. Dr. Gasecka oversaw the work carried out using the punch-through method, provided the CARS images of the different spinal cord sections and helped with the waveguide-hypothesis imaging. Jean Michael Deschenes and Mohamed Bahdine performed the measurements for the scattering and effective attenuation coefficients, respectively. Dr. Goetz and Dr. Perez-Sanchez provided tissue sections and insight into spinal cord morphology. Dr. Gasecka and I wrote the article together with the help of Dr. Côté. Dr. Bonin, Dr. De Koninck and Dr. Parent reviewed and edited the manuscript.

ection This thesis is the result of a highly multi-disciplinary project which required and exercised knowledge from fields including, but not restricted to: neuroscience, neurosurgery, tissue optics, mechanical, electrical, industrial and biomedical engineering, as well as nonlinear physics. As such, the topic and the knowledge acquired is broad. This is reflected in the Introduction which contains an expansive topic range with only essential information presented for each by means of a concise review. The goal was not to be an expert in each of these sections, but to understand each enough as to progress the application-specific objective. This multi-disciplinary profile is characteristic of a Biophotonics graduate and the Biophotonics program.

The first segment of the introduction will present the clinical need that instigated and propelled the motivation for this project. To achieve this, Parkinson's disease's (PD) neuropathological and neuroanatomical manifestations as well as the clinical features will be described. Following this, treatment options will be briefly over-viewed to orient the reader towards the treatment to be improved herein: deep brain stimulation (DBS) neurosurgery. Along with the literature summary, perspectives will be given on the improvements optical guidance can provide, drawing from literature, surgical experience in primates, and observations from human equivalents.

The second segment of the introduction will focus on engineering aspects of the devices implemented in the future chapters. To begin, we will briefly overview tissue optics, with a special interest in nervous tissue interactions. Subsequently, a review of the modalities which were used in the future chapters will be discussed in some detail. From there, I will describe optical simulations and their role for this application as well as optical probe considerations which evidently are important for the systems developed.

Finally, given the background information provided in the introduction, in the last segment, I will formally re-iterate and overview the achieved research objectives and provide the outline for this thesis project.

0.1 Parkinson's disease

PD is the second-most common neurodegenerative disease on the planet after Alzheimer's disease (AD). Globally, it affects 2-3% of the population above the age of 65[4]. Even with age-standardized statistics, the prevalence rate of PD is ever-increasing with a 21.7% increase from 1990 to 2016[5]. The most critical risk factor for developing PD is age, however, there is also considerable evidence of environmental factors playing a role in disease prevalence[6]. There exists no cure for the disease; however, there are symptomatic treatment strategies which can prolong life expectancy and increase patient's quality of life (QOL)[7]. It is therefore paramount to improve these treatments for optimal patient care until a possible cure is found.

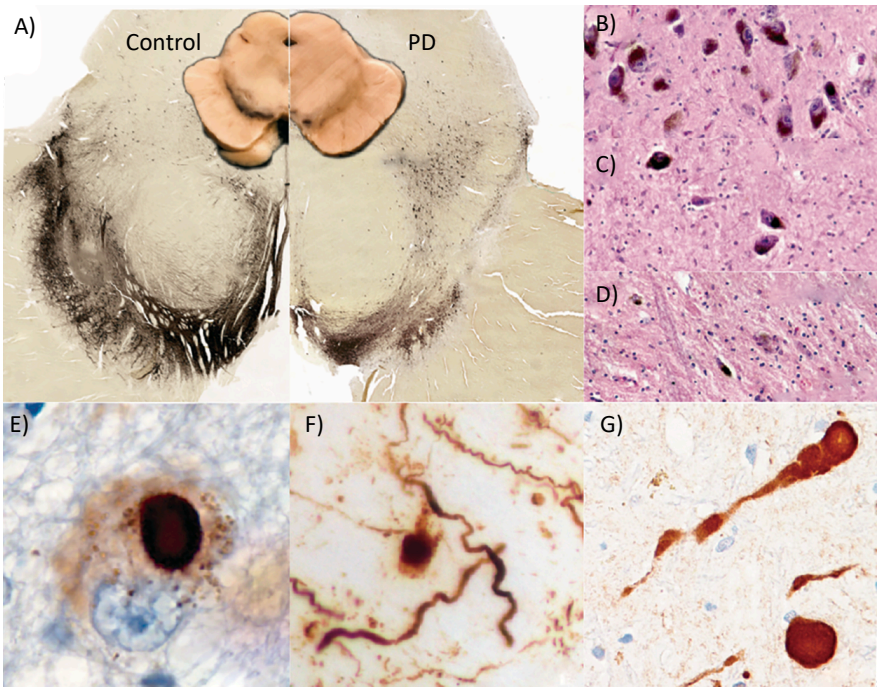

Figure 0.1 – Pathologic features of PD. A) Control and PD midbrain, showing loss of melanin pigment. Insets also show immuno-histochemical staining for tyrosine hydroxylase, the rate limiting enzyme for the synthesis of dopamine. B-D) Haematoxylin and eosin staining showing progressive pigmenation loss in the SN. From top to bottom: (B) control (C) moderate PD (C) severe PD. Immuno-histochemical staining of α-synuclein E) Intracellular Lewy bodies F) Deposits in neuronal cell processes and extracellular dot-like α-synuclein structures G) α-synuclein spheroids in axons. Image from reference [9].

0.1.1 Neuropathology of the disease

While characteristic of other neurodegenerative diseases, macroscopic brain atrophy is not a typical hallmark of PD. The main pathologic features of PD are a loss of dopaminergic neurons in the Substantia Nigra Pars Compacta (SNc) which project to the striatum, and the accumulation of an intracellular protein α-synuclein and their aggregates, termed Lewy bodies[8]. Also of note, with the loss of the dopaminergic neurons housing neuromelanin, the pigmentation of the SNc also decreases with disease progression. This change is even visible with the naked eye (shown in Figure 0.1)[4]. While it is not possible to diagnose PD based on a single one of these manifestations, due to their individual prevalences in other neurodegenerative diseases, the observation of both dopaminergic neuronal loss and α-synuclein aggregation is a conclusive diagnostic for PD[4].

Another pathological manifestation that is fairly universal among neurodegenerative dis-

eases is cerebrovascular alterations. In already diagnosed PD samples, vascular changes are prominent [10], however, it can be difficult to differentiate PD from vascular Parkinsonism (VP)[11]. More recent work has shown that in comparison to control brain samples, capillaries in PD counterparts are shorter in average length, fewer in number, and more fragmented with reduced branching [12]. While not the primary objective of this work, spectroscopic techniques such as the ones used herein could provide information on vascular changes and melanin abundance during neurosurgery which could be interesting for diagnosing and monitoring the disease-state of PD in pathologic terms.

0.1.2 Visible and non-visible symptoms of PD

PD is a debilitating condition in its later stages with both motor and non-motor symptoms which have serious implications on an individuals independence and QOL. Traditionally characterized by its motor symptoms, PD can be diagnosed by its cardinal motor features: resting tremors, rigidity, akinesia (or bradykinesia) and postural instability[13]. Interestingly, these motor symptoms are often uni-lateral or asymmetric in severity[14]. In advanced stages of PD, patients can also develop gait problems which can result in falls[15]. Some patients also experience freezing, during which they temporarily lose all ability to move. All of these motor symptoms are highly patient dependant which has prompted PD subtypes that have different aetiologies, pathogenesis and rates of progression[16].

Progress in the field is more recently emphasizing the many non-motor symptoms of PD. Many of these symptoms increase in importance for patients in the late stages of the disease, and some even precede motor manifestations[9]. In fact, even decades-old surveys put depression as one of the main QOL factors in PD[17]. In summary: the major neuropsychiatric symptoms are anxiety, apathy and depression with respective prevalence rates of 60%, 60% and 35% within the patient population[9]. In sensory disturbances, olfaction is greatly affected with a 90% prevalence rate of a reduced sense of smell. In pain and somatosensory manifesations, a 30-85% prevalence rate of abnormal sensations has been reported. Fatigue and insomnia are also key symptoms and their role in the disease progression is less understood. Finally, in the latest stages of the disease, cognitive decline and dementia are anticipated as 83% of patients are reported to be affected by cognitive dysfunction[9]. The time courses for the onset of these symptoms can be seen in Figure 0.2.

0.1.3 Basal Ganglia and its role in PD

PD treatments mostly target nuclei which are part of the brain network known as basal ganglia. This network is integral in the control of the movements and it is the changes within this network that cause the motor symptoms of PD. As such, we will briefly overview the nuclei which are considered to be a part of the basal ganglia and what happens to each of these nuclei after considerable progression of PD. There are four main levels to the motor

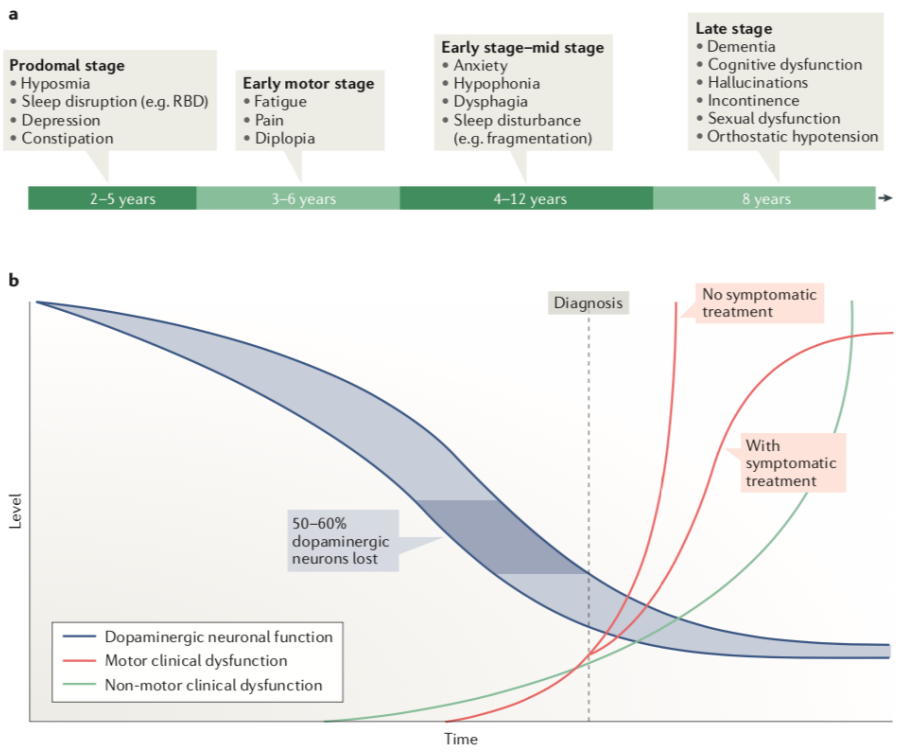

Figure 0.2 – Time courses of Parkinson disease features. A) A schematic representation of the potential timeline by which the non-motor features of PD may manifest. B) Graphic depiction of the rates of development and progression of the features. Image from Reference [9]

system hierarchy: the spinal cord, the brainstem, the motor cortex and the association cortex. The cerebellum and the basal ganglia can be considered important side loops for controlling and modulating the motor movements within this hierarchy, without directly causing motor movement. This is apparent through the damaging of specific basal ganglia structures, resulting in unique motor symptoms.

The classical model of the basal ganglia includes direct and indirect pathways, both comprising sequential excitatory glutamatergic and inhibitory GABAergic projections.The basal ganglia is composed of the following structures: caudate nucleus, putamen, nucleus accumbens (or ventral striatum), globus pallidus, subthalamic nucleus, and the substantia nigra (composed of both the SNc and the substantia nigra pars reticulata (SNr)). In the traditional indirect and direct pathways, the striatum is the main gateway to the basal ganglia from excitatory cortical projections. The primary motor cortex and the primary somatosensory cortex project mainly to the putamen, whereas the premotor cortex and supplementary motor areas project to the caudate head. These projections further converge to the internal globus pallidus (GPi) and the substantia nigra pars reticulata (SNr) either directly or indirectly through

the external globus pallidus (GPe) or both the GPe and STN[18]. The output from GPi and SNr is then directed to the thalamus, which then projects back to the cortex. This forms the complete cortico-basal ganglia-thalamo-cortical loop. The STN is the main excitatory (glutamatergic) structure within the basal ganglia, while pallidal and striatal structures are mainly inhibitory (GABAergic). Dopamine release from the SNc, modulate both the D1- and D2- receptor families in the striatum, which are at the origin of the direct (predominantly excitatory) and indirect (predominantly inhibitory) pathways, respectively, resulting in the precise balancing of excitation and inhibition in thalamo-cortical connections. This balancing act is important for the understanding the fall out of equilibrium in PD after the loss of these dopaminergic neurons in the SNc. Figure 0.3 B) shows a nice representation of this effect which results in increased inhibition from both the SNr and the GPi to the thalamus.

In more recent years, the understanding of the basal ganglia has increased and has brought to light other connections both between the basal ganglia structures themselves, as well as new pathways from the cortex directly to deeper basal ganglia nuclei. An important new pathway for PD and its treatment using DBS (discussed later) is the hyperdirect pathway, which contains projections from the cortex directly to the STN (a major target for DBS), which may help to better understand both the disease and the treatment[19].

0.1.4 Invasive and non-invasive treatments for PD

Unfortunately, at present day there is no cure for PD, and treatments have not been shown to slow disease progression[20]. However, there do exist symptomatic treatments which can be grouped into two categories: non-invasive and invasive.

Non-invasive treatments traditionally center on the replacement of dopamine through various approaches. Over 50 years ago, the breakthrough treatment of using the dopamine precursor, L-DOPA, to treat PD was clinically confirmed [21]. It continues today to be the gold standard treatment protocol for PD and nearly all PD patients will require this agent at some point of the disease[22]. Unfortunately, the prolonged usage of this agent ultimately results in motor complications, including motor response oscillations (cause by inconsistent drug delivery, due to short pharmacokinetic half-lives) and drug-induced dyskinesias (mechanisms which are still incompletely understood)[22]. Dopamine agonists are another dopamine-centered therapy which have the advantage of a longer half-life than L-DOPA, however, they have an overall decreased effect size and can induce drowsiness and impulse dyscontrol[13], [23]. There are many other, less common and symptom-specific pharmacological treatments which include adenosine receptor antagonists (istradefylline), calcium channel inhibitors (salfanamide), anticholinergics (many), and serotonin antagonists (clozapine)[4]. Regardless, over time, all pharmacologic treatments reduce in effectiveness and in the latest stages of the disease, motor symptoms render the patient completely dependant on others for every day tasks.

When this occurs, invasive procedures may be considered to give back independent living. While in the past, pallidotomy was a viable treatment plan for advanced stage PD[24], DBS quickly became the favorite in clinical practice[24]. This was due to its non-destructive nature, parameter adaptability, the ability to perform bilateral intervention in a single session and finally due to its improvements in both the off- and on-medication PD states[25], [26].

Lastly, it is important to note that clinical and animal model evidence is surmounting that the neuropathologic hallmarks, such as dopaminergic cell death, greatly precede the first visible motor symptoms of the patient[27]–[29]. In this respect, it is critical that new early on diagnostics are produced to catch the degeneration earlier.

0.2 Deep brain stimulation for Parkinson's Disease

In 1987, Professor Benabid and colleagues presented their seminal paper on using high frequency stimulation in the ventral intermediate nucleus (VIM) of the thalamus for the treatment of tremors[30]. Following this, drawing from primate research[31], the Grenoble group published their clinically validated study of subthalamic nucleus (STN) targeted DBS for the treatment of all the cardinal motor symptoms of PD[32]. This triggered the clinical resurgence of brain stimulation, hailed as one of the most important discoveries in clinical neurosciences in the past two decades[33].

While it is estimated that over 160,000 patients have received DBS therapy world-wide[34], the underlying mechanisms of its treatment efficacy still remain unclear[35]. Originally thought to cause "functional lesions," it was the belief that DBS stimulation silenced or reduced the activity of over-active basal ganglia neurons[35], [36]. However, more modern research has shown that DBS acts through more than immediate excitatory and inhibitory mechanisms. At present day, it is theorized that the mechanisms of DBS are multifactorial, including immediate neuromodulatory effects, synaptic plasticity, and long-term neuronal reorganization[35], [36].

While we still struggle to understand the underlying mechanisms, the clinical use of DBS is ever expanding. In this thesis, we focus on DBS for the treatment of PD, however, other applications for DBS are constantly being developed. These range from standard of care uses in pain relief, to a plethora of preclinical (schizophrenia positive and negative symptom) and clinical phase 1-3 (depression, obsessive compulsive disorder, tinnitus, Tourettes syndrome, AD, addiction, anorexia, epilepsy) studies for new treatment avenues[35]. Furthermore, the age at which a patient is considered eligible for PD related DBS is lowering with the recent FDA approval of early-stage DBS treatment after only 4 years of diagnosis and 4 months of motor complications[37]. With this, improvements to the DBS procedure will also grow in importance. Such improvements already under investigation to improve the treatment efficacy of DBS include: closed loop stimulation[38], directional stimulation[39], functional

targeting[40]–[42], and finally intraoperative guidance[1], [2].

0.2.1 Neuroanatomy and surgical targets

Nowadaways, the main targets for PD related DBS surgery are the STN and the GPi. These two nuclei are critical structures in the basal ganglia (motor control unit of the brain) and become hyper-(STN) and hypo-active(GPi) when dopaminergic outputs from the SNc are decreased[36]. This loss of dopaminergic output thus causes a fall out of network equilibrium and ultimately results in the motor manifestations we are familiar with in PD. And, while the mechanism is still unknown, high-frequency DBS stimulation proximal to these target nuclei can successfully return the network to equilibrium. A simplified functional representation of the basal ganglia network in healthy, PD and PD under STN-DBS can be seen in Figure 0.3. Of note, while this figure does not include the pedunculopontine nucleus (PPN), this brain region is an important basal ganglia structure and has more recently been used as a target for DBS in the treatment for freezing of gait (FOG) in PD patients[43], [44].

Between the two common targets, STN-DBS has been reported to have improved treatment efficacy compared with GPi-DBS for motor function outcomes, and a similar outcomes for risks of cognitive, mood, and behavioural complications[45], [46]. That said, the treatment is still patient specific, based primarily on the symptoms of the patient[47]. STN-DBS has the main advantage of an allowed reduction in medication while on stimulation, along with less frequent battery changes, and a more favourable economic profile[47]. GPi-DBS on the other hand provides more robust dyskinesia suppression and a greater flexibility in adjusting medication plans[47]. This project focused on creating guidance systems specifically for STN targeted DBS; however, the optical systems developed are fully translatable for any DBS target.

0.2.2 Procedural variations in DBS surgery and the need for intraoperative guidance

For the sake of clarity, I will discuss only the targeting and surgical procedure of STN-DBS. Being the smaller and deeper brain structure, the STN can be considered a more difficult brain region to accurately target for implantation. Furthermore, it is the consensus optimal target, even if treatments are patient-specific.

It is well understood that a major deciding factor in the efficacy of DBS treatment is the surgical accuracy of the stimulating contact terminals resting within or against the target nuclei. The surgical procedure of STN-DBS, therefore, understandably consists of many pre-operative steps to ensure effective implantation accuracy. The overall surgery can be broken down into 4 phases: (1) Pre-operative targeting phase (software representation shown in Figure 0.4 A)), (2) Intra-operative targeting phase, (3) Implantation phase and (4) Post-operative

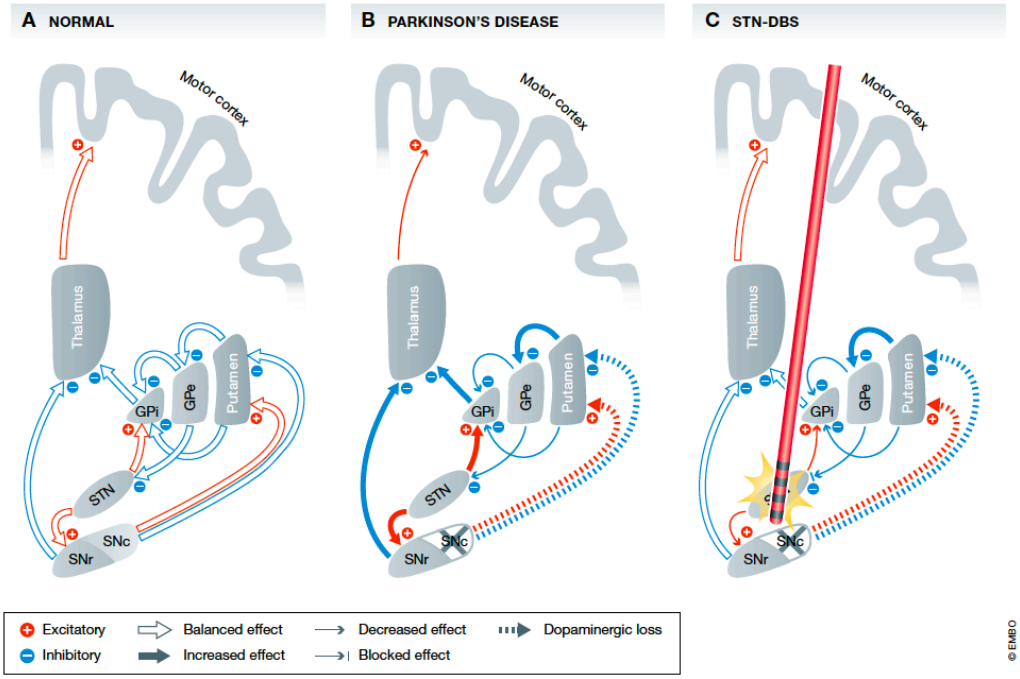

Figure 0.3 – Simplified representation of the basal ganglia network. A) Normal brain with physiologically balanced output to the motor cortex. B) PD Brain with dopaminergic neuronal loss in the SNc, leading to widespread excitatory and inhibitory changes. C) PD brain under STN-DBS, reducing excitatory output to the GPi and substanita nigra pars reticulata which balances system. Image from reference [36]

imaging phase (Example of post-operative image reconstruction using Lead-DBS software is provided in Figure 0.4 D)). Also provided is a schematic for the timing of these phases, presented in Figure 0.5.

To quantify the importance of target accuracy, Okun et al. analyzed DBS surgeries with unsuccessful treatment outcomes and found that nearly 50% of the cases were due to lead mis-placement[51]. Furthermore, in their following studies, they showed that re-positioning of the leads in these patients, some by only 1mm, rescued the treatment's efficacy[52]. These observations were also supported by electrical field simulations, showing that an electrode shift of only 1 mm greatly effects the efficacy of stimulation.[53]. In more recent work, even the atlases and softwares used by major commercial companies have been shown to produce considerable differences (>~1mm) in their targeting outputs[54], [55]. Due to this, there is a lot of debate on the optimal targeting strategy for STN-DBS and procedures vary greatly between hospitals. Some of the strategies in contention are: direct vs. indirect visualization

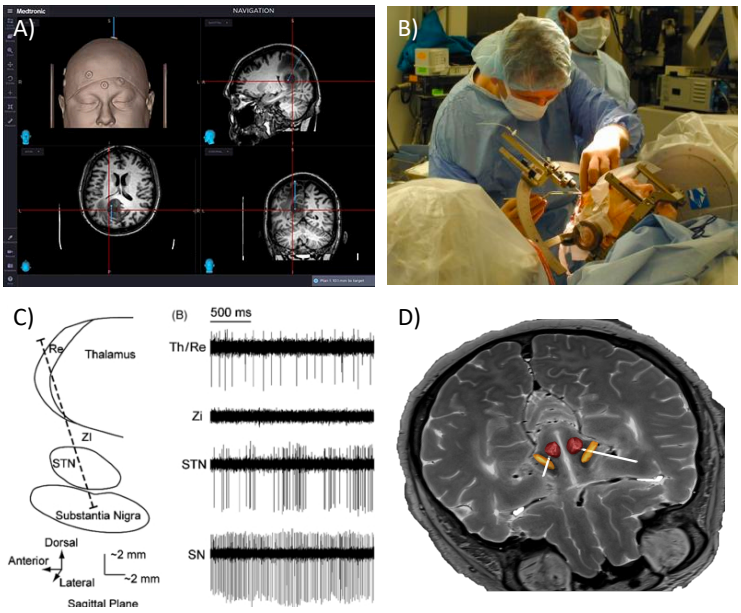

Figure 0.4 – DBS Procedural overview. A) Surgery planning software from Medtronic using stereotactic pre-operative MRI. Image from reference [48]B) Example surgery photo after transferring patient to operating room, with stereotactic frame attached. Image from [49]. C) Microelectrode recording signals, showing characteristic burst-firing patterns from STN neurons. Image from reference [50]. D) Post-operative MRI reconstruction of a bi-lateral STN implantation using LeadDBS software. Yellow structure and red structures are the segmented regions of the STN and SN, respectively.

of STN for targeting[56], awake or asleep surgery[57], direct implantation, intraoperative MRI (iMRI) guided, or microelectrode guided intraoperative targeting[33], [58], as well as even choosing the optimal target location within the STN[59]. On top of all of this, there is considerable differences between the electrodes and battery designs between commercial providers[60].

Briefly, direct visualization means that the surgeon uses an MRI capable of providing enough contrast such as to visualize the STN itself (3T or 7T systems) to plan the implantation trajectory. Indirect targeting of the STN involves an atlas-based calculation of the STN's position in reference to another brain structure, readily visible from a 1.5T MRI scan. The optimal structure for referencing is the red nucleus, due to its visibility and proximity to the STN[56]. While direct targeting seems like the optimal choice from common sense, the pitfall is that it is difficult to differentiate the STN and the SN, resulting in questionable improvements over indirect targeting[56].

Awake surgery is helpful for surgeons as it allows for test stimulation to be performed intraoperatively, such as to monitor a patients response before closing the cranium. This test stimulation requires patients to stay off their medication for a certain amount of time so that the

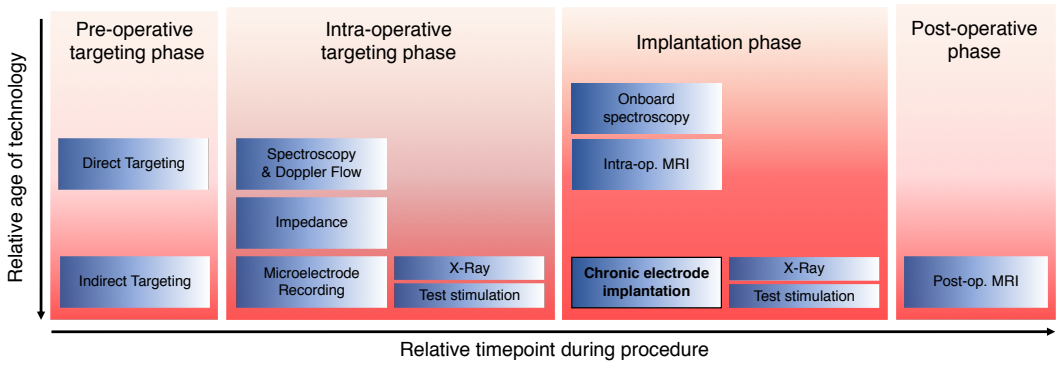

Figure 0.5 – DBS Procedural timeline. A surgeon may choose any of the techniques along the timeline to assure an on target trajectory.

surgeon can confirm that the implantation was accurate enough to provide motor-symptom improvement. Asleep surgery, on the other hand, has a multitude of obvious advantages: 1) it can be faster and require less personnel, 2) the patient can stay on their medication as no intraoperative testing is needed, and 3) it is overall more enjoyable for the patient. However, the use of general anesthesia (GA) prohibits test stimulation and historically, it was also said that GA limits micro-electrode recording (MER) usability due to a decreased firing pattern in the STN. However, this is also in debate and certainly depends on the nature and level of the anaesthetic being used [61].

MERs are traditionally performed intraoperatively, prior to the chronic DBS electrode placement and the technique is considered the gold standard for locating the dorsolateral region of the STN, for refining the subsequent lead placement, following pre-operative MRI trajectory planning (Example of information acquired using MER in Figure 0.4 C))[62]. However, some hospitals are now emphasizing the importance of reduced surgical time and costs, consequently decreasing the usage of MER for target-mapping[63]. MER is considered specifically important to minimize the risk of brain shifts, which are a major source of lead misplacement in DBS surgery[64], [65]. These shifts cause errors in the pre-operative planning, and while they can occur at any time during the surgery, they are most probable upon cranial opening. A report studying brain shift showed that on average, there is a shift of 1.8 mm between pre- and post-operative magnetic resonance images (MRI) in DBS surgery[66]. Along with brain shifts, there exits other causes for lead misplacement such as stereotactic frame misalignment and inter-individual anatomical variation with respect to brain-atlas targeting[64]. For this reason, most experienced neurosurgeons prefer the use of MER recording to ensure optimal treatment. However, while it is the gold standard and provides characteristic markers for the STN, MER is not perfectly engineered for surgical guidance. To begin,

the measurements are discretely acquired at various depths, while what is required is the detection of subtle boundaries of the stereotactic targets[67]. Furthermore, while the resolution of MER is high, the distance between discrete measurements is actually quite far rendering this attribute mute. Also, MER requires a pause before each acquisition (~1 minute) to allow for the tissue to equilibrate, considerably increasing the surgical time if multiple tracts are recorded[67].

In the case of GA surgeries which do not use MER guidance, iMRI can be deployed. iMRI, as the name suggests, allows surgeons to monitor the surgical implantation (in low-resolution), in real time during the chronic electrode descent. However, as is to be expected, special tools which are not magnetic must be used and an MRI must be available for an entire procedure. This greatly increases the complexity and costs of the procedure to the point where it is unreasonable for many hospitals. For this reason, intraoperative optical guidance represents a specifically interesting source of surrogate information in addition to, or in lieu of, MER. Furthermore, the optical information provided can be acquired rapidly and continuously, as it does not require tissue equilibration, therefore even overcoming some of the pitfalls of MER.

In research, comparing the anesthetized/direct implantations and awake/MER-guided implantations, the overall outcomes seem to be similar, putting into question the improvements provided by MERs[57], [68], [69]. That said, recent research has shown that direct implantations are only on target in 80% of trials, concluding that MER is still imperative for confirming optimal trajectories[33]. This type of contradictory information is common in the literature and makes drawing conclusions difficult.

To elaborate the importance of our proposed optical guidance, imagine the following thought experiment. Direct implantations and subsequent analysis indicate that 20% of implantations could have been improved if MER had been done prior to the implantation [33]. In this scenario, if a nominal 100 implantations are performed, 80 are considered successful. Now, if MER was performed in all of these surgeries, a minimum of two electrodes would be descended for each trajectory (one recording and one chronic stimulating electrode), resulting in a minimum of 200 electrodes sent into human brains for a theoretical 100% success rate. The word "minimum" should be emphasized, as often up to 5 recording electrodes may be descended into the brain to find the optimal implantation location using, giving an upward bound of 600 total electrodes descended. Now, if the directly implanted chronic electrodes rather had optical guidance from within its hollow core, providing similar information to that of a precedent MER, only the 20% of off-target implantations would have had to be repositioned. Even more interesting, is that the optical information could tell the surgeon exactly where to move to reach the target, using the information from the off-target trajectory. This means that only 120 electrodes would be descended with the same theoretical outcome of 100% optimal placements. Not only does this allow the faster treatment options

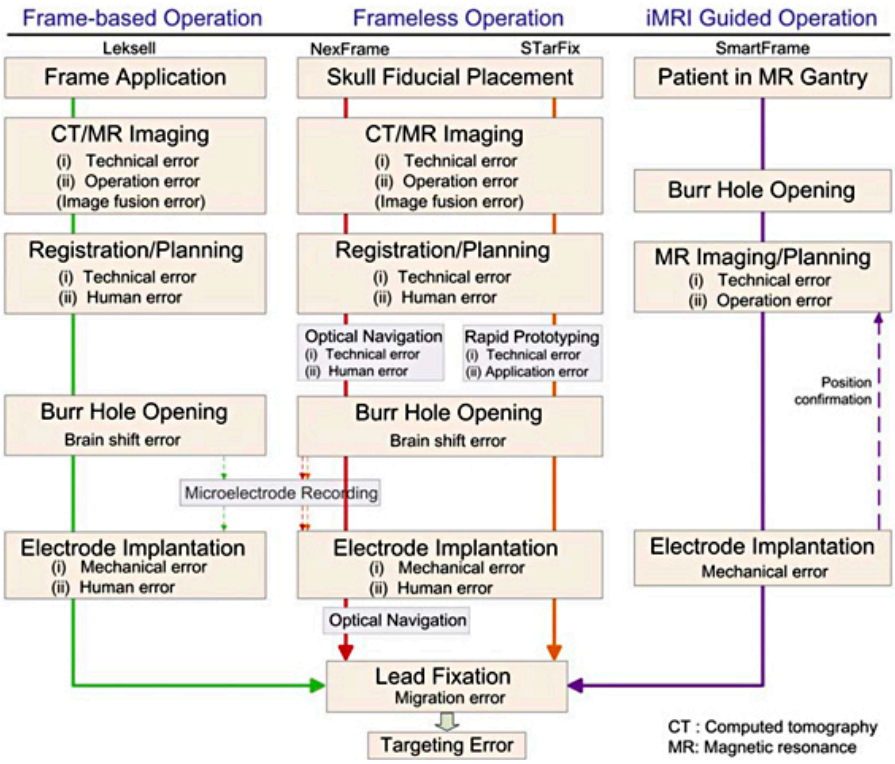

Figure 0.6 – Sources of targeting error during the DBS procedure. Several routine surgical systems are specifically mentioned for frame-based (most common), frameless and iMRI guided procedures. Optical navigation, as shown in the Frameless Operation column after electrode implantation, could either alleviate or be used to explain error from all the previous steps by providing true electrode position. Image from reference [70]

(GA, direct implantation) but it does so in a much more economical fashion than iMRI guidance. Furthermore, unlike MER, optical information could also be used to detect oncoming blood vessels and therefore minimize the hemorrhage rate in DBS surgery[71].

A robust literature review summarizing normal targeting errors along with their believed causes is provided elsewhere[70]. Shown in figure 0.6 is an overview of where, and how, error throughout the surgery accumulates for several different systems and procedures. Overall, what becomes apparent is the clinical need for intraoperative guidance during the chronic electrode's implantation. The availability of this could circumvent much of the accumulated error from the planning process, due to the information being provided onboard the final electrode.

0.2.3 Previous attempts at optical guidance for DBS

Several groups have analyzed the ability of optical information to provide guidance for PD related DBS surgery, with experimental results dating as far back as 1998 [72]. While there

are many who have performed research in animal models, two main groups stand-out for pioneering the clinical realization of these systems: the Giller group in U.S.A., and the Wårdell group in Sweden.

Following their first experiments in 1998, Giller and colleagues continued to set the foundation for the use of diffuse reflectance spectroscopy (DRS) for DBS guidance with a plethora of computations[73]–[76], phantom validations[77], [78], and experimental validations in both animals[79] and finally in humans in 2009[80], [81]. Giller's most recent study in 2009 presented several different probe designs, either being housed on the canula of chronic electrode, or as a separate probe descended before the chronic electrode's implantation[81]. While the device acquired spectra, the authors used only the near-infrared (NIR) reflectance value at a single wavelength along the probe trajectory to infer the probe's location. Using this technique, they found that NIR detection of the STN could be considered reliable evidence of its presence, but that the absence of the STN in the NIR recordings did not prove that the track missed the STN[81]. Since then, there has not been new research articles on the topic from the Giller team. Around this time, in 2008, the Wårdell team at Linköping University started presenting their findings with both laser doppler flow (LDF)[83] measurements and DRS[84]. Both of the original works displayed the ability of the techniques to differentiate white and grey matter along a probe trajectory. In 2009, they presented a DRS/impedance probe and using it, performed 21 trajectories in living humans[82]. The impedance measurements matched well with the reflectance measurements, which in this work were chosen to be at both at 573nm and 780nm. Following this, they contributed further clinical validations of their systems[85] along with new algorithms for chromophore quantification[86] and oxygen saturation[87], [88]. In 2016, Dr. Wårdell was the first to use the term "optical barcodes" to refer to the sequential optical discrimination of tissues along a DBS trajectory; it is an illustrative term which I use in this thesis[89]. In 2018, the same group provided a critical validation of the safety aspects of using their optical probe with respect to hemorrhage occurrences, concluding that the optical information decreases hemorrhage risk[90]. In their systems, the optical probes are also used for tissue interrogation prior to the chronic DBS electrode's descent.

The optical systems that we present in this thesis have two central improvements for DBS optical guidance: 1) The probe sizes are small enough to be placed within the DBS electrode, allowing for the first time on-board optical guidance during the implantation phase of the procedure. and, 2) The exploitation of spectral information to provide more discriminatory content than that provided solely from single wavelength reflectance values. Especially in the case of CARS spectroscopy, wherein the potential for high-resolution, fingerprint-type brain region classification may be possible. Depictions of the Giller and Wårdell probes are presented in Figure 0.7, along with the most recent images of our CARS and DRS probes.

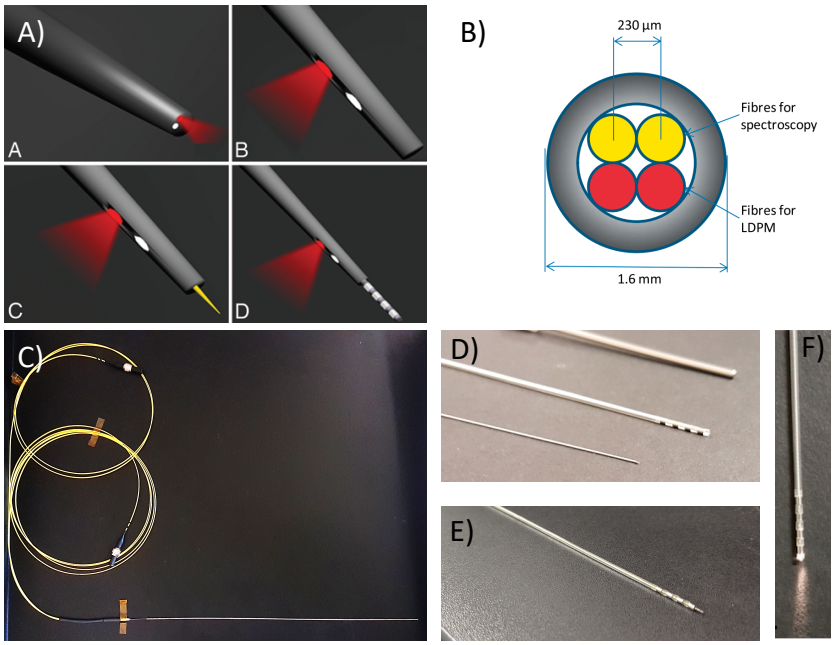

Figure 0.7 – DBS optical guidance probes. A) Probe concepts presented by the Giller team. Inset images (A-D) represent different probe concepts the group has either attempted or simply conceived. Images from reference[81]. B) Probe tip depiction from the Wårdell team. Image from reference[82]. C) Entire DRS probe within Medtronic's 3389 DBS electrode. D) Close up of DRS optical probe, electrode tip and guide cannula tip, from bottom to top. E) Close up of multi-modal CARS, DRS probe, with electrode tip removed. F) DRS probe within Medtronic's 3389 DBS electrode, with light source on. Images (C-F) are from this thesis work and are displayed for reference.

0.3 Optical properties of nervous tissues and their label-free interrogation

When photons hits nervous tissue, there is a multitude of elastic and inelastic interactions that may or may not occur simultaneously. Neurophotonics in a research setting is, more or less, the exploitation of these processes with the goal to study nervous tissue. Neurophotonics in a clinical setting, on the other hand, while still exploiting the same phenomena, is used more-so for monitoring the nervous system, guiding neurosurgical intervention and diagnosing or even treating neurologic diseases. In this thesis, we exploited two main optical phenomena for the clinical goals of neurosurgical guidance and retinal diagnostics: DRS and CARS spectroscopy. Rather than producing images, spectral information is interpreted using state-of the art spectral analysis. Using DRS and CARS spectra, we show the ability to differentiate tissue sub-types for guiding DBS neurosurgery. Furthermore, using simulated

DRS spectra, we create robust algorithms for extracting the oxygenation of the illuminated tissue for retinal (and brain) tissue. To effectively do any of these tasks, simulations of light-tissue interactions are invaluable for understanding where the detected light comes from during the procedure. Using previously known, as well as experimentally measured, optical properties we provide new simulation options to deal with the complexity of nervous tissue. This section will give a quick background on the optical phenomena which may occur when light strikes nervous tissue, the spectroscopic methods used specifically in this thesis to achieve the clinical endpoints and finally information on the importance of effective light propagation simulations in nervous tissue.

0.3.1 Light-tissue interactions

Photons which interact with tissue can go through two main processes: absorption and scattering. Absorption is where energy from a photon is transmitted into stored energy in the molecule, either through electronic or vibrational mechanisms. Sometimes, this absorbed energy is re-emitted through effects such as fluorescence, inelastic scattering (Raman) or acousto-mechanical waves. Elastic scattering on the other hand, does not alter the energy of the incident photons, rather it can change the photons propagation direction, polarization and/or phase. Together these effects can provide molecular information of tissue under interrogation both at the micro and macro scale. Light is considered a great biomedical tool as it can be used non-invasively and in a non-damaging way, using low incident energies. On the other hand, if intense enough, optical energy can also be used to cause planned harm to the tissue through photo-thermal, photochemical of even photo-biological processes. Using light in a non-damaging way, to investigate the absorption and scattering interactions, makes up the basis of optical guidance, diagnostics and monitoring. Using light in a controlled, but damaging, way is the basis of optical therapy, for instance in the case of laser eye surgery [91]. In Figure 0.8, a summary of optical phenomena and their illumination parameters are depicted[91].

In this work, we exploit light-tissue interactions to perform optical guidance during DBS neurosurgery, specifically by using efficient and label-free spectroscopy. In the first iteration, DRS is deployed to create optical barcodes based on the colour differences observed in brain tissue during the placement of the chronic electrode. In the second iteration, CARS is investigated for high-resolution spectroscopy to visualize thin white matter boundaries, like those that surround the STN. CARS has also been chosen due to its potential to provide regional fingerprinting after system optimization and adequate data analysis. In the later chapters, we also analyze and simulate light-tissue interactions in nervous tissue to improve the utility of the acquired DRS information.

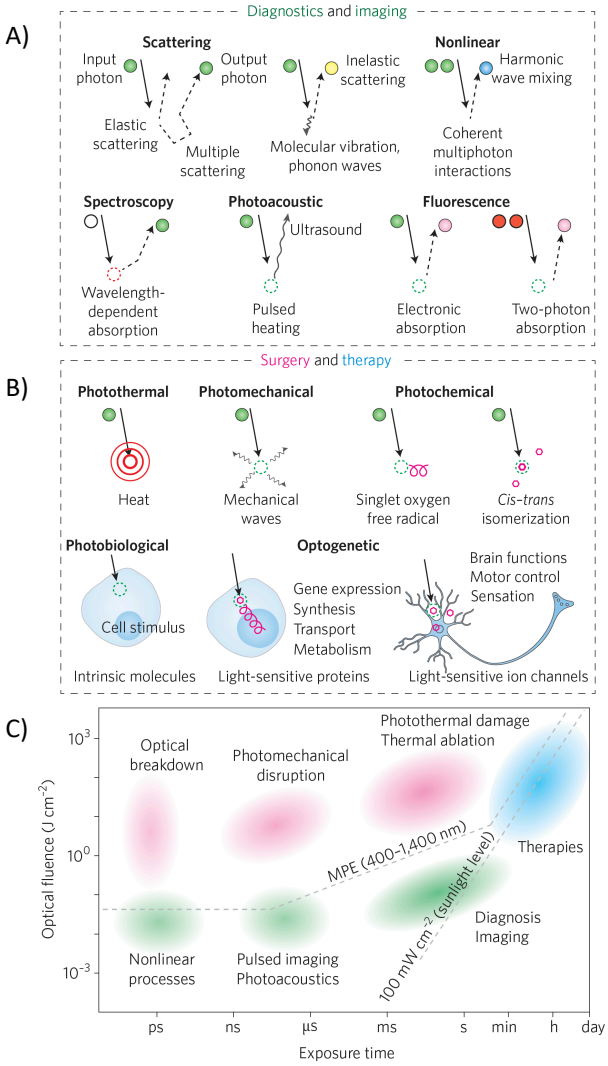

Figure 0.8 – Light-tissue Interactions. "a) Optical effects exploited in diagnostics and imaging (left), and surgery and therapy (right). Circular objects denote incoming and outgoing photons, with their trajectories indicated by solid and dotted arrows. Colours of the circles represent the spectrum of the light; dotted circles indicate the absorption of input photons. For the case of therapy, specific effects of light on tissue and cells are indicated. b) Optical techniques mapped according to their optical fluence and exposure time (either total illumination time for continuous-wave light, or pulse duration for pulses). Colours represent medical areas: green for diagnostics, pink for surgery and blue for therapy. MPE, maximum permissible exposure." Figure and caption from reference [91]

0.3.2 Diffuse reflectance spectroscopy

DRS is the analysis of the wavelength dependant absorption and elastic-scattering processes that occur when an incident photons interacts with a given medium. When applied to tissue, the spectral acquisition can provide information on both its structural and biochemical

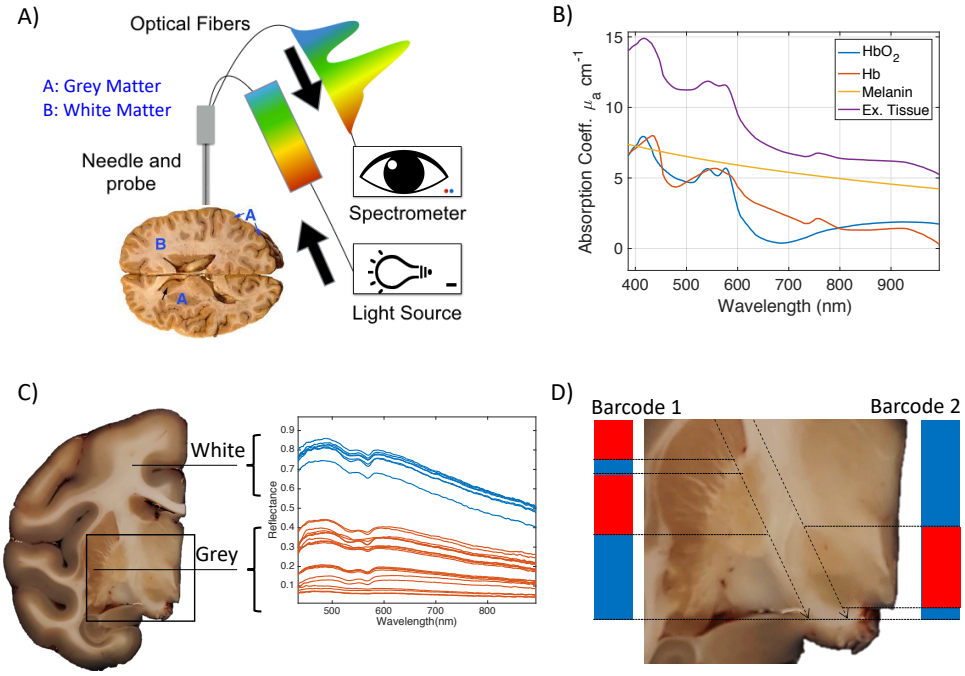

Figure 0.9 – DRS for tissue identification and optical barcodes. A) Depiction of DRS setup. B) Example absorption coefficients of common tissue chromophores and of an example tissue being an additive combination of all three. Coefficients and figure idea from Reference [92]. C) Example of optical barcodes produced by discriminating between white and grey matter along an on target and off target trajectory towards the STN in primate brain. D) Example of DRS spectra acquired using our system in white and grey matter.

properties. While scattering has more direct ties to the structure of the particles in the sample, absorption is more dependant on the biochemical nature. Elastic scattering can be split into two main types: Rayleigh scattering, which has a strong wavelength dependency and occurs when the wavelength is on the order of the molecule's size, and Mie scattering which is broadly wavelength independent and occurs more commonly with particles much larger that the wavelength. As for visible wavelength absorption, the main absorbers in human tissue are: hemoglobin, melanin, bilirubin, beta-carotene and water (further in the IR). The absorption coefficient of a of a tissue is simply the sum of the contributions from all absorbing chromophores in the optical volume.

Often, DRS is used to calculate the absorption and scattering coefficients of a tissue. These values are useful as they can be used to solve the Radiative Transport Equations (RTE) and therefore simulate the fluence of light in an tissue volume[93]. Traditionally, direct methods to measure these coefficients required thin, excised tissue, such that single scattering events dominated the interaction. Bulky systems were also required to quantify ballistic

transmission, scattering angle and total reflectance. Using the detected values, solutions to the RTE could be generated using the Diffusion approximation, the Kubelka-Munk method, or most commonly the Inverse Adding Doubling (IAD) method[93]. For thin samples with no scattering, the Beer-Lambert Law (BLL) is also is an acceptable means to extract the absorption coefficient of a sample[94]. In the backwards direction, wherein no transmittance information is available, the process is more complicated and requires more assumptions. Still, it is possible to get approximations of these coefficients using fiber probes, allowing measurements *in vivo*[95]. To achieve this, Monte Carlo (MC) simulations are deployed to relate the measured light intensities to the optical coefficients[95]. Other techniques, such as the modified-Beer-Lambert law (MBLL) have been used, which adds a term to the BLL to account for wavelength-dependant path-length differences caused by scattering[96], [97]. For certain applications, the MBLL is extremely useful in its simplicity, however, it has been put in question for its validity due to the heterogeneity of the path-length in most arrangements[98]. Overall, the measurement of the optical properties using DRS in living tissues remains a somewhat open problem as the model used in deriving the optical properties must account for irradiation profiles and geometries specific to the detection tool.

An interesting use for the calculation of the absorption coefficient is in the derivation of tissue oxygenation. An example of the MBLL's usefulness is in the simplistic retrieval of the additive absorption coefficient measured within a DRS optical volume. Once it is retrieved, it can be decomposed using the known absorption coefficients of the constituents (oxygenated and deoxygenated hemoglobin, fat, water, melanin) within the volume using a least squares regression analysis. Example absorption coefficients for a simulated tissue, as well as common tissue chromophores are plotted in Figure 0.9. Once decomposed, using the ratio of oxygenated and deoxygenated hemoglobin conformations, the tissue oxygenation can be measured. The problem persists, however, that the optical path-length varies with the heterogeneity within the optical volume in the tissue. Therefore, errors may be accrued in using the MBLL. In Chapter 4 we show another brute-force technique to perform this oxygenation measurement by training a neural network using spectra simulated with highly variable parameters, mimicking differences in path-length. In this way, the neural network can learn to ignore the path-length differences and provide more robust oxygenation measurements.

On the other hand, DRS can also be used simply for tissue differentiation and diagnosis, ignoring altogether the complicated process of extracting the optical coefficients. In the case of the neurosurgery, using DRS has been investigated for improving the classification of brain tumours for resection[99], detecting oncoming blood vessels during biopsies[100], [101], monitoring oxygen dynamics[102] and providing optical guidance for functional surgery[81]. In our neurosurgical guidance system described in Chapter 2, while we do perform statistical data analysis, it is solely for the purpose of differentiating tissue types to create our optical barcodes. A depiction of a fiber-based DRS spectroscopy system, as well

as the idea behind tissue-discriminating bar-codes and corresponding examples of white and grey spectra can be found in Figure 0.9.

0.3.3 Spontaneous and coherent Raman spectroscopy

Spontaneous Raman (SR) spectroscopy was first discovered by Sir C. V. Raman in 1928[103]. However, it wasn't until the laser was invented that its utility in the biological sciences began to be realized. Finally, around the year 2000, its *in vivo* potential was shown[104]. Since then, In the last 20 years, SR's biomedical impact dramatically increased due to the incremental improvements in sources and detectors, accumulating over time. Still, SR is a very inefficient process making it difficult to collect enough photons with small form factor probes such as the ones required for onboard DBS guidance. Coherent Raman (CR), including CARS and stimulated Raman scattering (SRS) are interesting alternatives to SR spectroscopy, due to the increased signal efficiency, intrinsic optical sectioning and the lack of parasitic autofluorescence contributions[105], [106]. The spectral and energy-level diagrams for spontaneous and coherent Raman processes can be found in Figure 0.10.

In Chapter 1, we provide a comprehensive background for SR, CARS, and SRS, as well as a thorough review of Raman technologies for the application of neurosurgical guidance. Furthermore, in this chapter, considerations with respect to background parasitic signals, noise, and even optical radiation limits are discussed for each modality. Rather than reiterate the text, please refer to this chapter for the information.

0.3.4 Fiber optics for spectroscopic probes

Fiber optics have a long history in the biomedical sciences due to their ability to transport light into areas of the body with a minimally invasive footprint, allowing us to image and sense deeper into tissue. A conventional fiber optic is composed of 3 main layers: the core, which the light travels through; the cladding, which wraps the core in a lower refractive index medium; and a jacket, which provides protection to the fragile conduit. The ability of these small optical conduits to transport light so efficiently is thanks to an optical effect called total internal reflection (TIR), permitted by the lower refractive index cladding (n_{clad}) around the higher refractive index fiber core (n_{media}). This difference in refractive index creates a critical angle wherein any light travelling from the core to the cladding with an incident angle less than the critical angle, will be reflected, rather than refracted. These regions of the fiber optic are shown in the case of a multimode fiber in Figure 0.11 A). In this respect, anything can act as a fiber optic as long as the refractive index relationship remains. That said, the most common forms of fiber optics in the visible and NIR wavelength regime are made of silica or plastic (such as PMMA) due to their low absorption in this range. Also important is the refractive index of the medium (n_{media}) at the interfaces of the optical fiber as

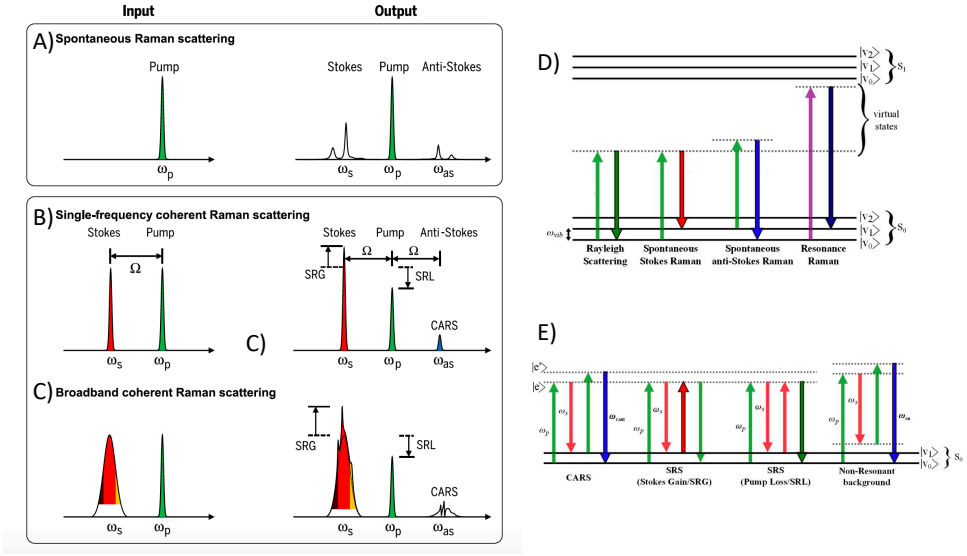

Figure 0.10 – Raman process overview. A) Explanatory spectral diagram of spontaneous Raman generation showing weak emission at many Stokes and anti-Stokes wavelengths. B) Explanatory spectral diagram of coherent Raman processes, such as CARS and SRS, in the case of single frequency generation. C) Explanatory spectral diagram of coherent Raman processes in the case of broadband frequency generation. While not shown here, broadband generation can also be achieved by wavelength-sweeping one of the input lasers in orientation B. This type of spectral CARS was used in our later work in Chapter 2. D) Energy level diagrams for spontaneous Raman processes including Rayleigh, Stokes and anti-Stokes Raman, and resonance Raman scattering. E) Energy level diagrams CARS, SRS, and the non-resonant background which is major source of background only in the case of CARS. A),B) and C) were adapted from reference [107]. E) and D) were adapted from reference [108]. Abbreviations: SRG: stimulated Raman gain; SRL: stimulated Raman loss; Ω: arbitrary vibrational shift; andω_{vib}, ω_{p}), ω_{s}, and ω_{as} was denote the frequencies of arbitrary vibrational shift, pump, Stokes, and anti-Stokes beams, respectively; e and e' refer to virtual energy states; v_{n} refer to energy levels; S_{n} refer to vibrational energy states; Note that Ω from B) is equivalent to ω_{vib} in D) and E)

this decides the half angle (α) and the numerical aperture (NA), which effectively describes the light cone a fiber can accept [109]. The formula for the NA is shown in Equation 1.

$$\text{NA} = n_{\text{media}} \sin \alpha = \sqrt{n_{\text{core}}^2 - n_{\text{clad}}^2} \tag{1}$$

Nowadays, there are many physical forms of specialty optical fibers for biomedical imaging

and spectroscopy due to an increasing demand for high performance. However, in this work, we aimed to use off-the-shelf components to maximize the potential of translation. Therefore, we deploy the 3 most traditional examples of fiber optics which fall broadly into the categories of step-index singlemode (SI-MM), step-index multimode (SI-MM) and gradient-index multimode. Step-index simply refers to the step down in refractive index between the core and cladding, whereas gradient-index refers to a gradually decreasing refractive index within the core. SI-MM are important where in light needs to be focused after the fiber optic, or where phase needs to be conserved and modal dispersion minimized. SI-MM fibers are especially important for transporting high-peak power pulses such as the ones used for CARS, to maintain the optical pulse quality. SI-MM fibers are useful for collection as they allow the collection and transmission of much more light that singlemode (SM) counterparts. GI-MM fibers are interesting in that they can conserve imaging information along the fiber, however, it must remain rigid for this application. They can also be used as "micro-lenses", allowing the focusing of light at the tip of a delivery fiber. To achieve this, the GI-MM is cleaved at a specific length calculated according to the desired focal distance from the fiber tip. The cleaved GI-MM is then spliced to the tip of a delivery fiber (after a multimode "spacer" which allows the beam radius to expand after the singlemode core for more effiecient focusing) and an effective lens is produced. This is how we focus the light in Chapter 2. An example of these three type of fibers are shown in Figure 0.11 B).

In biomedical spectroscopy, the probe design is very important. Some probes may deploy a single optical fiber, while others may deploy several. The major tradeoff in this respect is the collection of photons versus the probe size. If small probes are required, either an efficient modality or a technically-demanding probe tip may be required to collect enough discriminatory signal. In our case, the hollow core of the DBS electrode (~400μm) limits our probe OD to either single fiber or few fiber arrangements. Therefore, we require efficient spectroscopic modalities, such as, DRS and CARS. For example, comparable spontaneous Raman systems (in terms of acquisition time) would normally deploy an upwards of 8 optical fibers[110]. Another important consideration comes from the cost and scalability of the device. If specialty optical fibers which are expensive and fragile are used, the commercialization of such a device would be more difficult. However, this may be the price to pay to acquire useful information in the imaging landscape[111]. Lastly, the probe tip can be designed to maximize excitation and collection overlap; however, this can add some complexity to the manufacturing of the probe. An example of various probes with their light cones of emission and collection are shown in Figure 0.11 C).

0.3.5 Simulating light-tissue interactions

Knowing the optical properties of a tissue is extremely useful for clinical applications of biomedical optics. With accurate properties, it is possible to better plan dosage in therapy,

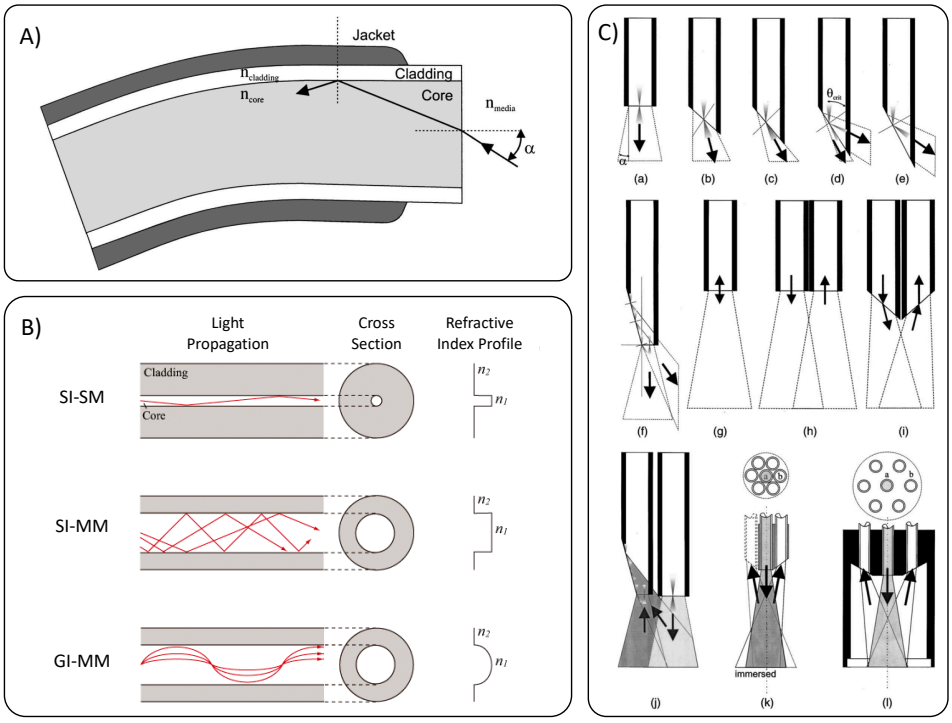

Figure 0.11 – Fiber optic overview. A) Schematic of classic multimode fiber optic showing a single TIR event. B) Schematics of step-index singlemode (SI-SM), step-index multimode (SI-MM) and gradient-index multimode (GI-MM). C) Example of fiber optic spectroscopy probes along with their emission and collection cones of acceptance. Image A) and C) from reference [109]. Image B) from reference [112].

estimate what volume of tissue is being interrogated for improved diagnostics and even to simulate expected information to help predict locations in surgical guidance. To do all these things, we commonly use software based on Monte Carlo (MC) for simulating photon propagation. The simulation itself, iteratively injects an individual photon into the defined medium and calculates its path as it randomly walks, until all of its energy is deposited[113]. In this way, MC statistically samples the probability distributions for step size and angular deflection per scattering event in a homogeneous medium to effectively solve the RTE for the experiment. The most famous software implementation of this was "Monte Carlo modelling of light transport in multi-layered tissues (MCML)", by Wang et al. in 1995, which as the name suggests, allowed for simulations with multiple layers of homogeneous tissue to be simulated[114]. To use MCML, only 4 properties of the tissue are required: the absorption coefficient, the scattering coefficient, the anisotropy factor and the refractive index (n)[92]. The absorption coefficient (μ_a) describes how much energy to deposit in a given photon-step, the scattering coefficient (μ_s) describes how far the next step may be, and the anisotropy factor (g) describes which direction the step may go. There are many resources for these

values in nervous tissue, however, there is a large standard deviation between them due to tissue state at the time of measurement, tissue heterogeneity, and anisotropy of the tissue[92], [115]. In general, white matter is observed having a higher scattering coefficient than grey matter in the brain (white matter: $\mu_s \approx$ 300-600 cm^{-1}, grey matter: $\mu_s \approx$ 100-300 cm^{-1} at 600 nm), and both have relatively low absorption coefficients in comparison to other tissue structures (white & grey matter: $\mu_a \approx$ 0.5-5 cm^{-1})[115]. Along with the anisotropy factor (white and grey matter: g$\approx$ 0.9) and refractive index (white and grey matter: n$\approx$ 1.33) these terms represent enough information to simulate most linear light-tissue interactions with high precision, making it an extremely powerful tool.

In more recent years, advanced implementations of MC for photon propagation in tissue have been developed for: improved simulation speed[116], 3-D simulations,[117], [118] and use mesh-based objects for more realistic boundaries[119]. Furthermore, while we discuss here the norm for nervous tissue measurements, it is becoming outdated, as many techniques are showing just how heterogeneous "white" and "grey" matter really are[120]. Specifically, white matter is especially complicated due to the highly-ordered axon-insulating myelin sheaths which are shown in Chapter 5 to cause directionally-dependant scattering events. It is even theorized that the myelin sheaths may act as biological optical waveguides[121]–[123]. In either case, anisotropic scattering will cause error in traditional MC packages which assume isotropic media. To account for this, In Chapter 5, we use Jacques' mcxyz code to simulate light propagation in the anisotropic spinal cord, by editing the original software package to include 3-D scattering coefficients. While this addition does not solve all the problems myelin organization creates, it may provide a more accurate approximation.

0.4 Research goal and thesis outline

The overarching goal of this thesis project was the research and design of an optical guidance system for DBS neurosurgery with the ultimate purpose of improving this form of treatment for PD patients. This endeavour was founded on the idea of using CARS for high resolution white and grey matter delineation, and following this with fingerprint-type regional differentiation, all from within the chronic DBS electrode. In this way, the optical system would be capable of providing feedback and guidance to the neurosurgeon, comparable to MER but on-board the implanted electrode, therefore adding no additional invasiveness to the procedure.

At the time of my arrival, the specialty laser which was destined for the CARS project was still in development. This allowed us time to build prototype systems using different modalities, to expedite the development of the experimental protocol. The only design criteria was that the replacement modality must also be efficient enough to have a small collection form factor, such as to be placed within the DBS electrode. DRS was an ideal modality to be-

gin the endeavour due to its precedent use for this application (albeit with large probes), its highly efficient process, and the semi-opaque nature of the commercially-available DBS electrodes which, obviously, allowed visible light to pass through. While spontaneous Raman could seem like a more plausible replacement for CARS, the low signal-generation efficiency and high background signal from the plastic electrode would have made it complicated. This work started using bare fibers in mice, then rats to show the ability of DRS to provide discriminatory information similar to what was previously published by others. After considerable mechanical design improvements, the device was prepared to perform the same measurements from within the DBS electrode. To do this, larger, more anatomically-similar brains to humans were required, as to accommodate the large DBS electrode (OD of 1.3mm). The culmination of this work was an *in vivo* proof-of-concept study in primates presenting the implications of spectroscopic optical guidance during DBS electrode implantations and is described in detail in the paper provided in Chapter 3.

In the meantime, during the fruition of the DRS system, the specialty lasers from Halifax Biomedical Imaging (HBI, formerly Genia Photonics) arrived at the research center, allowing simultaneous progression of the two modalities for the common goal. CARS spectroscopy had never been done before in an all-optical-fiber system, and therefore, this direction was much more research intensive in comparison to the DRS counterpart. While DRS required engineering to make the mechanical and data analysis system, CARS required dedication to finding something which may not exist: CARS signal at the tip of a silica optical fiber. After about 2 years of considerable efforts, we were indeed successful in creating such an all fiber system and producing CARS spectra in scattering brain tissue. Presented in Chapter 2, the portable CARS system showed the high potential for CARS-based optical guidance by performing high-resolution white and grey matter delineations in primate cortex.

Over the course of my project, I became increasingly interested in the data analysis aspect of biomedical spectroscopy. To become proficient in this space I required a deeper understanding of the light-tissue interactions, which were producing the detected information. Specifically, I became interested in deconstructing measured spectra into quantifiable subspectra (or known biological components), to not only discriminate tissue sub-types, but to research them. Furthermore, I wanted to understand why white matter was unpredictable in its reflectance values, after accumulating a large database of experimental measurements in this tissue type. These curiosities took me down two separate paths, connected in their ability to be used for improved optical guidance in neurosurgery.

The first side project, centered on spectral analysis, was the novel use of machine learning (ML) for quantifying the amount of hemoglobin and its oxygen saturation in a DRS spectra. This project was done in collaboration with a local med-tech start-up called Zilia Inc. Their interest was in retinal oximetry and I was tasked with creating a robust algorithm to quantify oxygen saturation from measurements acquired on the optic nerve head (ONH), in the

back of the eye. The algorithm that was produced, presented in Chapter 4, was shown theoretically, to be more robust and accurate than current state-of-the-art algorithms and paved the way for the company's continued ML-based spectral analysis. In terms of my projects central goal, the technique can also be used on spectra acquired in the brain, along probe trajectories in DBS, to extract valuable oximetry measurements. Furthermore, the technique is highly adaptable and can be used to measure other chromophores or scatterers more present in brain tissue, such as neuromelanin in the SN.

The second side project was an interesting discovery on the anisotropic nature of scattering in myelinated axons. Along with providing empirical measurements of this effect, we also showed the possibility that this observation may be caused by the myelinated axons acting as optical waveguides. For DBS surgery, if DRS-based optical guidance is to be used to detect the location of the electrode within the brain based on its "optical barcode", optical simulations will be required based on the patient-specific neuroanatomy - derived from pre-operative MRI. While this may already be possible using Monte Carlo software to simulate photon propagation, current implementations do not take into account the possibility of anisotropic scattering. To make more experimentally-true simulations, such an optical effect should be taken into account and therefore, this discovery has serious implications in the simulations required for optical guidance in DBS neurosurgery. In Chapter 5, we present these discoveries along with an altered 3-dimensional Monte Carlo package which can be used with anisotropic scattering coefficients.

Lastly, since the first publication on our CARS probe, this project continued to advance in the background. We made improvements to the laser-system which allowed higher signal generation, we analyzed more thoroughly the signal collection which permitted more efficient probes. These advancements resulted in the acquirement of CARS spectra in fresh human brain samples and in human cadavre heads. While more acquisitions are required for this work to be at the publication stage, the knowledge acquired over the 5 years of this thesis was valuable and ready to be shared. To this respect, we have nearly finished writing a review article which summarizes the use of Raman in clinical neurosurgery and provides our opinions for the future of the field. The current state of this Review is provided in Chapter 1. While the publication is still in preparation and subject to change, it acts as an informative introduction to fiber-delivered SR and CR technologies, specifically important for understanding the technological accomplishments presented in Chapter 2.

In summary, this thesis represents considerable works towards the goal of creating an optical guidance system for DBS neurosurgery for improved treatment of PD. My hope is that in reading the original information provided within this thesis that the clinical impact of such a final system will become obvious.

Chapter 1

Raman Spectroscopy for Neurosurgery

Damon DePaoli[a,b*], Émile Lemoine[c,d*], Martin Parent[a], Frederic Leblond[c,d], Daniel C. Côté[a,b]

* Authors contributed equally to this work
[a] Université Laval, CERVO Brain Research Center, Neuroscience, Québec, Quebec, Canada
[b] Université Laval, Center for optics, photonics and lasers (COPL), Physics Engineering, Québec, Canada
[c] Department of Engineering Physics, Polytechnique Montréal, Montréal, Canada
[d] Centre de Recherche du Centre Hospitalier de l'Université de Montréal, Montréal, Canada

1.1 Résumé

Bien que le potentiel clinique de la spectroscopie Raman soit anticipé depuis des décennies, il ne fait que commencer à être employé en neurochirurgie. Le principal intérêt clinique en Raman découle de sa capacité à fournir des informations moléculaires peropératoires sans marquage à partir de tissus. En analysant ces informations avec des modèles de science de données efficaces, la spectroscopie Raman peut être utilisée pour fournir une rétroaction discriminatoire en temps réel et des conseils aux neurochirurgiens. Bien qu'il soit évident que la discrimination tissulaire peropératoire peut améliorer les résultats du traitement dans des procédures telles que les résections tumorales, l'ampleur de l'amélioration, ainsi que l'implication de Raman dans d'autres neurochirurgies, sont encore inconnues. En raison de la faible génération de signaux dans les systèmes Raman spontanés et de la complexité de la génération de signaux dans les systèmes Raman cohérents, peu de dispositifs peuvent être considérés comme pouvant être traduits dans leur état actuel. Cela dit, avec les avancées technologiques et les nouvelles techniques d'analyse des données présentées ces dernières années, la détection vibratoire est sur le point de devenir un outil révolutionnaire pour les neurochirurgiens. Cette perspective résumera les succès de la traduction au niveau des systèmes, en fournissant des connaissances en optique et en science des données qui sont nécessaires à la mise en œuvre de tels dispositifs. Par la suite, il donnera un aperçu des considérations chirurgicales pour l'intégration du flux de travail et des perspectives futures essentielles pour l'optimisation d'un système Raman pour la neurochirurgie.

1.2 Abstract

While the clinical potential for Raman spectroscopy has been anticipated for decades, it has only just begun to be exploited in neurosurgery. The main translatable interest in Raman is derived from its capability to provide label-free molecular information from tissue, intraoperatively. By analyzing this information with effective data science models, Raman spectroscopy can be used to provide real-time disciminatory feedback and guidance for neurosurgeons. While it is obvious how intraoperative tissue discrimination can improve treatment outcome in procedures such as tumor resections, the extent of the improvement, as well as Raman's implication in other neurosurgery's is still unknown. Due to the weak signal generation in spontaneous Raman systems and the complicated signal generation in coherent Raman systems, few devices can be considered translatable in their current state. That said, with the technological advancements and novel data analysis techniques presented in recent years, vibrational sensing is poised to be a revolutionary tool for neurosurgeons. This Perspective will summarize translational successes at a systems level, providing both the optics and data science knowledge required to implement such devices. Subsequently, it will give an overview on surgical considerations for workflow integration and future outlooks critical for optimizing a Raman system for neurosurgery.

1.3 Introduction

While the clinical potential for Raman spectroscopy has only just begun to be exploited in neurosurgery. The main translatable interest in Raman is derived from its capability to provide label-free, non-invasive molecular information from tissue, intraoperatively. By analyzing this information with effective data science models, Raman spectroscopy could soon be used to provide real-time discriminatory feedback and guidance for neurosurgeons. While it is obvious how intraoperative tissue discrimination can improve treatment outcome in procedures such as tumor resections, the extent of the improvement, as well as Raman's implication in other neurosurgery's is still unknown.

Led by efforts in fluorescent imaging, optical technologies in general have seen a renaissance in neurosurgery over the last couple decades. Namely in tumor margin detection, 5-aminolevulinic acid–induced protoporphyrin IX (ALA-PpIX) fluorescence for glioblastoma multiforme (GBM) resection has made fluorescent imaging a clinical mainstay[124], [125]. Since then, a multitude of other modalities have been investigated for tumor margin detection in neurosurgery including quantitative exogenous fluoresence[126], [127], endogenous fluorescence lifetime imaging (FLIM)[128]–[130], optical coherence tomography (OCT)[131], hyperspectral imaging[132], finally Raman spectroscopy [133]. Furthermore, improvements in other neurosurgical procedures using biomedical optics have also began to be investigated. For example, in deep brain stimulation (DBS) optical guidance has been proposed using laser doppler flow measurements (LDF)[134], diffuse reflectance spectroscopy (DRS)[2], [81], [82] and even coherent Raman [1]. During epilepsy surgery, hyperspectral imaging has been investigated to help guide resection [102]. Finally, during biopsy retrieval, OCT has been used to image and size blood vessels to avoid hemmorhaging[135] and Raman has been recently shown promise in effective tumor localization [136], [137]

Due to it's fingerprint type information and safe operating conditions, Raman could be considered an ideal clinical modality, however, the Raman process is inelastic and inefficient making its implementation difficult in a clinical setting. To overcome this, there has been considerable efforts to improve both the source and detectors used for spontaneous Raman (SR) spectroscopy. These incremental advances in technology have only recently accumulated to provide clinically relevant signal to noise ratios (SNR) for the discrimination of tissues within the operating theatre. Alongside these advances, newer, coherent Raman (CR) modalities have been under development, also becoming more clinically relevant thanks to advances in fiber-laser sources and novel nonlinear techniques to perform rapid, spectral imaging. Lastly, propelled by advances in the fields of genomics, proteomics, and machine vision, data science tactics for harvesting information from 1D,2D and even 3D infor-

mation has exploded in recent years. With these novel data science methods, both SR and CR modalities are poised to revolutionize neurosurgery for intraoperative disease diagnosis and surgical guidance. The devices will be application specific, however, an entire Raman toolbox is under development in the research setting which we hope to summarize effectively here.

As is the case with any optical system, there are major trade-offs to be considered in terms of desired information (field of view (FOV), resolution) and tolerable acquisition speed (optical power, integration time). This trade-off scenario becomes even more complex for Raman methods due to the added spectral domain and the low abundance of Raman photons (especially in the case of SR). To this end, we provide a complete review of leading-edge systems' optical and mechanical properties so that future endeavours can built with clear improvement objectives in mind. We also provide a comprehensive review on optically-mediated tissue heating which is a critical consideration when developing clinical devices using optical radiation. This is even more pronounced in the case of CR modalities as will be seen. Throughout every section, following the review, we will provide insight and perspectives on both the past and future of Raman spectroscopy for the given application.

Finally, we will use our experience in optical technology deployment during neurosurgery to discuss successful integration techniques for piercing the surgical workflow. This will be comprised of clinical standards considerations, commercial partnerships and strategies, registration of optical information in current neuronavigation platforms, and where next frontiers lay in neurosurgical, and neurological, Raman.

1.3.1 Neurosurgery procedures at a glance

1.3.1.1 Oncological neurosurgery

Surgery is the mainstay of treatment for most neoplastic diseases of the brain. Diagnosis and treatment of patients affected by brain tumors rely on a combination of clinical expertise, neuro-imaging technologies, and intra-operative tools, and vary widely depending on factors such as predicted tumor malignancy and localization, genetic profile of cancer cells, and patient characteristics and preferences; as such, the precise role that Raman spectroscopy should play in this setting needs to be adapted in a patient-to-patient basis.

The approach to the treatment of brain cancer starts with a thorough review of the clinical history and medical record. Extensive neuroimaging with Magnetic Resonance Imaging with gadolinium, sometimes in addition to other modalities (MR Spectroscopy, Diffusion imaging, Perfusion imaging) is performed and interpreted by the neurosurgeon with the help of expert neuro-radiologists in order to accurately characterize the nature of the lesion and establish a baseline with which post-therapy studies can be compared. A set of images is usually also acquired to be used in conjunction with a Neuronavigation tracking device during the surgery. A panoply of imaging cues is used to establish a preliminary diagnosis of the disease, such as the presence of vasogenic edema and necrosis, contrast-enhancement of the tumor, shape and size of the lesion and variation in intensity across MRI sequences [138]. At this point, the medical team will decide whether surgical resection is the appropriate approach for the patient, how aggressive the surgeon must be in the extent of the resection, and whether the patient will benefit from adjunctive or alternative treatment (radiotherapy, chemotherapy and immunotherapy). In primary brain cancers, high-quality evidence suggests that maximal safe resection improves functional outcomes and patient survival, regardless of tumor grade [139]–[143]. This is also true for brain metastases in patients with good functional status, solitary lesion and limited systemic invasion. In all cases, the objective of the surgery is to both remove as much cancer as possible and obtain a quality tissue sample that will help orient further therapies and prognosis [144], [145].

After the decision is taken to proceed with surgical resection, the neurosurgeon plans his approach to the tumor based on the preoperative imaging. The best approach would be one that is short and avoid critical cranial or brain structures such as nerves, arteries or eloquent brain areas. During the surgery, brain retraction is mini-

mized, and a combination of bipolar electrocautery, microscopic scissors, forceps and other instruments are used to dissect structures and advance to the tumor while keeping the surgical cavity free of blood and debris. Modern neurosurgical procedures are almost always performed using a surgical microscope. During the approach, surgeons rely on anatomical landmarks and Neuronavigation tracker to locate the tumor margin. Unfortunately, once the dura mater is opened and intracranial pressure equilibrates with ambient air, the brain shifts inside the cavity and Neuronavigation based on preoperative imaging can become misleading. Moreover, invasive cancer cells can falsely appear as normal brain on the MRI images. Once the tumor is reached, it is slowly dissected from the surrounding brain and removed with forceps or suction. In the case of invasive cancers, the limit between cancer and normal brain—or tumor margin—can be extremely challenging to visualize inflammation, neo-vasculature and varying degree of invasive cancer affect the morphology of the normal tissue, even for the trained eye of a neurosurgeon. During the operation, some of the tumor sample is frozen and sent to a neuropathologist to obtain a preliminary diagnosis of the tumor. The rest of the resected tissue will be fixed in paraffin and sent to the neuropathology laboratory, where different stains and markers will help achieve a more precise diagnosis.

For some patient, surgery cannot be initially performed; this is the case in sick patient who might not survive a major surgery, in patients with lesions deep inside the brain, or in patients in which the nature of the lesion is unclear. In these cases, the medical team could opt to perform a brain biopsy in order to obtain a quality tissue sample that could help guide clinical decision-making and establish a prognosis. The ideal trajectory is planned on preoperative MRI images. For the calculation of this trajectory, surgeons use commercial softwares from companies such as Medtronic, Boston Scientific and Abbott. There exist a variety of frame- or frameless-based devices that are then used to orient the needle and guide it to the biopsy target based on the programmed trajectory. In the surgical theater, a small burr hole is drilled in the cranium, the guiding-device is attached to the patient head, and the biopsy needle is advanced inside the brain until it reaches the lesion. The biopsy needle consists in an inner and an outer cannula, both with a rectangular biopsy window (patient end) through which a tissue sample can be aspired by applying suction to the other end of the needle (surgeon end). Once tissue is sucked inside the rectangular window, the inner cannula is rotated inside the outer cannula and is retracted towards the surgeon end outside of the needle, where the sample is fixed and sent to neuropathology for analysis. Usually, at least 4 and up to 20 samples are extracted in this manner to ensure that there is at least one sample that contains enough cells to achieve a reliable diagnosis. Importantly, there is a high rate (10%) of non-diagnostic biopsies, and even if a diagnosis is achieved, it is found to be inexact in 23% of cases **reithmeierIntraindividualComparisonHistopathological2013** .

1.3.1.2 Functional neurosurgery

Functional neurosurgery aims to relieve patient suffering from chronic neurological disorders such as Parkinson's disease, dystonia, pain or epilepsy. Deep brain stimulation (DBS) consists in the surgical insertion of electrodes deep inside the brain, where they will modulate precisely targeted neurological structures to correct dysfunctional brain circuits. While many conditions can benefit from DBS surgery, its most common application is for alleviating motor symptoms of Parkinson's Disease (PD). We will use DBS for PD as our example herein.

In DBS surgery, the treatment efficacy is more or less decided by the accuracy of electrical contacts on the chronic electrode being placed precisely in a target nuclei. The most common target nucleus for PD is the subthalamic nucleus (STN), followed by the internal globus pallidus (GPi), which are both relatively small and deeply-situated brain structures. Due to the importance of target accuracy, the surgery consists of many steps after a patient has been selected for the treatment. The pre-imaging, surgical planification and electrode insertion shares many similarities with brain biopsies. Electrode trajectory and target location are identified on a preoperative MRI. A favorable trajectory would travel mostly through white matter, avoiding cell-rich brain structures such as the putamen and caudate nucleus. As for brain biopsies, frame or frameless devices are used to guide the needle

according to the preoperative planning. The surgery begins with the drilling of a small hole in the cranium to allow entry for the DBS electrodes. Depending on the hospital, a surgeon may opt to perform microelectrode recordings (MER) to optimize a planned trajectory (by searching for the characteristic neuronal activity of the STN) or she might opt to implant the chronic electrode directly using only the pre-operative planning. Importantly, to perform MER, precedent sharp microelectrodes must be descent into the brain, all the way past the target structure. This act may increase risk of tissue damage and hemorrhaging, but can result in a more effective surgery, especially if brain shift occurs during the cranial opening phase. Subsequently, the MER probes are removed and the chronic electrode is sent down the same trajectory using the still in place canulla. Once the chronic electrode has fully descended, most commonly the patient is asked to perform practiced tests while the surgeon increases the stimulation current to query whether the trajectory planning was on target, judged by the patient's intraoperative motor response improvements. Once a satisfactory improvement is confirmed, a wire is ran subcutaneously from the cranial opening to a battery pack/transceiver which is then implanted underneath the clavicle. Finally, after the surgery there are a multitude of stimulating parameters for the neurologist and aids to optimize with the patient to maximize their treatment benefit.

1.3.2 Basic understanding of Raman modalities

While it is not the objective of this Perspective to provide theory on the Raman effect, it is important to have an idea of the signal generation with respect to the sample and the optical power used. Furthermore, the wavelength of the generated signal can be an important design factor given operating room lights and background signals. Lastly, the spectral content of the signal is a critical aspect of the diagnostic ability for a clinical system and so the techniques to acquire spectra with traditionally single-frequency CR techniques are also mentioned. For complete theory, there is already an abundance of resources at the readers disposal [108], [146]–[148].

1.3.2.1 Spontaneous Raman scattering (SR)

Since its discovery by Sir C. V. Raman in 1928, inelastic scattering has been widely used as a molecular probing tool in the fields of biology and chemistry. At the heart of Raman spectroscopy is the concept of vibrational energy: molecules in a sample are not static—they vibrate, with a given mode and frequency. The vibrational mode describes the oscillating pattern between the atoms of the molecule; the frequency is a function of the strength of the molecular bonds and the mass of the connected atoms. At room temperature, most molecules are in their ground state, i.e. vibrational state with lowest energy level. When excited by electromagnetic radiation, the molecules will either absorb or scatter the exciting photons. When particles are smaller than the radiation wavelength, most of this scattering is elastic: the molecule is transiently raised to a virtual energy level and immediately recovers its ground state by emitting back a photon at the same frequency than the exciting light, a phenomenon referred to as Rayleigh scattering. In 1/1*106 of cases, however, the frequency of the emitted photon will have changed. This phenomenon is called the Raman effect, or inelastic scattering: the shift in light frequency reflects a change in the vibrational energy level of the molecule. The Raman spectrum is a mapping of the intensity of scattered light as a function of its shift in frequency, or Raman shift. It is a rich and tangled vibrational profile of the molecules present in the illuminated sample [103].

Spontaneous Raman spectroscopy systems therefore require a single wavelength light-source, collection fibers, diffracting system and photon-detector. A notch optical filter is used to get rid of the Rayleigh scattered photons and reflected light, which are orders of magnitude more intense than the Raman scattered signal. At room temperature, Stokes scattering, where inelastically scattered photons are of lower energy than the exciting light source, is much more common than Anti-Stokes scattering, where the scattered photons have gained energy. Therefore, Spontaneous Raman system only aim to detect the Stokes signal. As we will mention later, however, targeting Anti-Stokes signal can be appealing in biological tissue because of the sparsity of other signal source in this frequency range [103].

Spontaneous Raman is a linear phenomenon: the resulting spectrum is the linear combination of all the signal from the individual molecules in the illuminated sample, and the Raman intensity increases linearly as a function of exposition time and light-source power. This property facilitates the analysis and deconstruction of the spectra and balances out the contribution of Raman active molecular species. Spontaneous Raman suffers from two important limitations that are related to clinical application: low Raman signal and high contribution of other signal sources such as fluorescence in the frequency range. More recent vibrational spectroscopy techniques aim to overcome these challenges [149].

1.3.2.2 Coherent anti-Stokes Raman scattering (CARS)

In 1999, Zumbusch from the Xie group revived CARS imaging for biological tissues[150]. Subsequently, groups continued to show the promise for this label-free modality in a multitude of biological structures, creating contrast from vibrations in DNA, lipids, proteins and water [151]–[154]. In 2005, Wang et al. presented the first imaging of myelin in *ex vivo* guinea pig spinal cord [155]. Soon after, the landmark study by Evans et al. reported the first CARS imaging of *in vivo* tissue at video rate speeds[156]. Since then, many others have followed in refining and optimizing CARS for *in vivo* imaging of nervous tissue[157]–[162]. This scientific push for CARS in brain tissue was, and still is, driven by the biological structure of myelin, having an abundance of CH_2 molecules. High concentration of the probing molecule is important for the non-linear CARS signal generation, making it specifically useful for brain imaging.

Historically, CARS has been known for several advantages over SR imaging: 1) Orders of magnitude more sensitive than SR at a specific vibration, 2) intrinsically optically sectioned due to non-linear signal generation 3) signal generation is blue-shifted, removing the need for 1-photon autofluorescence removal, and 4) signal is optimally generated with picosecond pulses, therefore minimizing multiphoton damage [105].

The signal generation for CARS is proportional to the quadratic intensity of the pump field (I_{pump}) multiplied by the stoked field (I_{stokes}), as summarized in equation 1.1. CARS also scales quadratically with the number of oscillators (N) in the optical volume, making it specifically useful for interrogating high-density substances.

$$I_{CARS} \propto I_{\text{pump}}^2 * I_{\text{stokes}} * N^2 \tag{1.1}$$

While CARS signal is actually generated at the both the stokes (CSRS) and anti-stokes frequency (CARS), the anti-stokes signal is more commonly detected as it is stronger and unaffected by autofluorescence. The frequency shift of the CARS signal can be calculated given frequencies for the pumps (ω_{pump}) and stokes fields (ω_{stokes}) as is shown in 1.2.

$$\omega_{\text{as}} = 2\omega_{\text{pump}} + \omega_{\text{stokes}} \tag{1.2}$$

The main sources of background signal for CARS is known as the non-resonant background, and is independent of the Raman shift (ie. excitation wavelength independant). Due to this background, CARS is limited in sensitivity to sensing only high-concentration molecules, in contrast to SRS.

1.3.2.3 Stimulated Raman scattering (SRS)

Just under a decade after the Xie group introduced CARS to biological imaging, it was the Xie group again in 2008 with the landmark study by Freudiger et al. presenting fast SRS imaging of biological tissue, *in vivo* [106]. While it this was not the first use of SRS in microscopy, it was the first to use optical powers that were safe for live animal imaging, enabled by phase-sensitive lock-in detection. The potential for SRS was clear from this point and it was rapidly advanced by several groups, displaying its ability to image DNA mitosis**Lu2015**, protein dynamics[163], and even neurotransmitter concentrations [164]. SRS has an improved sensitivity for

low-concentration molecules over CARS, as it is not subject to the wavelength-independant, non-resonant background. Due to this increased sensitivity, SRS is ideal for imaging nuclear contrast for use in neuropathology as will be shown herein[165], [166].

Briefly, the signal generation for SRS is still non-linear, however, it is proportional only to the product of the intensity from the pump field and the stokes field, as summarized in equation 1.3. An advantage of SRS over CARS is that it has an oscillators density (N) dependence that is linear (as is also the case with SR), making the detected signal easier to correlate to molecular concentrations within the sample.

$$I_{SRS} \propto I_{\text{pump}} * I_{\text{stokes}} * N \tag{1.3}$$

The wavelength of signal generation for SRS can correspond to a stimulated Raman gain (SRG) or a stimulated Raman loss (SRL) depending on which frequency is the probe (ie. which is modulated for detection.) This is represented in equation 1.4.

$$\omega_{\text{SRL}} = \omega_{\text{pump}}, \omega_{\text{SRG}} = \omega_{\text{stokes}} \tag{1.4}$$

Laser noise, shot noise, and electronic noise are all sources of noise in SRS imaging. They are especially important to minimize due to the modulated aspect of SRS, wherein small changes in the excitation laser is measured. The main sources of background for SRS are raman-independant pump-probe effects. These effects include transient absorption, cross-phase modulation, and photothermal effects all of which are not observed in CARS as the signal is generated at a new wavelength[148]. A theoretical review of the signal to noise ratio (SNR) for CR techniques is provided by Min et al.[147].

1.3.2.4 Spectral imaging with CR modalities

CR imaging was historically used for single frequency imaging, creating contrast from the coherent vibration of a single molecular bond. However, this type of imaging is limited in spectral information and therefore also in its diagnostic capability. To this end, strategies to produce CR spectra have been developed, in hopes of creating systems with the best aspects of both SR and CR imaging (ie. fast, hyperspectral image acquisition). These techniques and their implementations are reviewed in detail by Alfonso-Garcia et al.[146]. Briefly, Such strategies include: 1) wavelength sweeping either the stokes or pump wavelength with narrow band excitation wavelengths. In this strategy, the main benefit is the random access wavelength selection and the use of a single point detector due to the temporally encoded spectra[160]. 2) Multiplex CR or broadband CR where one narrowband pulse and one broadband pulse are combined to create a simultaneous spectra. The spectral resolution is determined by the width of the narrow pulse and the signal must detected by a spectrometer. This technique has the added advantage of being non-resonant background-free in the case of CARS [167]. 3) Spectral focusing wherein spectrally chirped pump and Stokes pulses are temporally sweeped creating complete raman shift spectra. This strategy also uses a single point detector and can make whole spectra rapidly[168], [169]. 4) Temporal sweeping of two replicas of a broadband pulse, resulting in temporal interferences. A single point detector is used and the detected information is in the form of a interferogram and require a fourier transform to view the spectral information[170].

The technique deployed for hyperspectral CR imaging is not important in the topic of this Perspective, however, in designing a clinical system the economic impact and technical difficulty of its implementation should be considered. It is clear that there will be a tradeoff between spectral information and acquisition speed, and so it is important to design accordingly. For instance, if the system requires broad spectral information for diagnosis, the wavelength-swept option may not be advantageous. However, if the vibrations of interest are known, as is

the case in SRS based histology, wavelength swept systems and their random access capabilities may provide images much faster.

1.4 Hardware considerations for Raman systems in neurosurgery

In recent years both spontaneous (SR) and coherent Raman (CR) modalities have shown great potential for improving neurosurgical workflows. For SR, the surge in clinical translation is due mainly to the increase in probe efficiencies caused by more readily-available micro-optical components and incremental improvements in sensitive detectors. These incremental advancements have summed up to allow the inefficient process of SR photon generation to provide a strong enough signal for high-accuracy tissue classification at clinically relevant acquisition speeds, even with small form-factor probes. For CR, the clinical adoption can be mostly traced back to the breakthroughs in compact fiber-laser sources. The drastic decrease in laser size and increase in robustness has allowed the development of entire coherent Raman microscopy systems capable of being easily transported in and out of the operating room (OR) with a single cart[171].

The useful exploitation of the Raman effect in neurosurgery can been divided into 3 main system types: 1) Single point Raman-spectroscopy probes for the interrogation of still intact tissue (mainly SR systems), 2) Portable Raman microscopes for rapid histopathological evaluation after tissue resection (mainly CR systems), and 3) Endoscopic Raman imagers for intact tissue histopathology and surgical guidance (SR and CR prototypes).

This section provides an overview of the hardware and technical considerations required for successful clinical implementation of these systems. With single-point probes being the only system-type succeeding to be used in intact tissue, during a neurosurgery, a special focus will be given to their implementation. However, some researchers have put a real emphasis on putting vibrational imaging systems into the hands of neurosurgeons (mainly for neurophathology) in the OR, and so, we will also include a section on those breaking barriers. Lastly, we will group the promising vibrational endoscopes that are at the bleeding edge of clinical Raman sensing.

1.4.1 Neurosurgical Raman Spectroscopy of intact brain tissue using point probes

A major advantage of Raman spectroscopy comes from the nearly non-existent requirement for tissue preparation. Therefore, its most useful clinical implementations should stem from this facilitation in the form of intact tissue interrogation. To date, there have been no publications presenting *in vivo* implementations of human vibrational brain imaging. Even intraoperative spectroscopic measurements in humans have only begun being reported in the last 5 years [133]. While there are many pioneers of Raman sensing in neuroscience, few have successfully made the jump from fundamental research to clinical utility in neurosurgery. Tables 1a and 1b summarize the relevant clinical work using point-probe systems; however, they will also be briefly described here.

In 2007, Santos et al. from the Puppels group began the conversation of high wavenumber (HWNM) Raman spectroscopy for fiber optic brain tissue sensing[172]. By only measuring the Raman shift far from the excitation wavelength (the HWNM), they showed the probe needed no distal optics to remove parasitic Raman background from the silica fiber. They followed this with with two more studies both with and without the fiber optic probe in *ex vivo* porcine brain tissue, showing the ability of SR in the HWNM to classify brain regions [173], [174]. Unfortunately, no *in vivo* work in the brain followed from the group. Another system for brain tissue sensing with a SR probe was reported by Beljebbar et. al in 2010, which included an analysis of Raman spectra taken from an *in vivo* mouse model of C6 glioblastoma [175]. In this report, the probe acquired data in the fingerprint region, was compact and designed professionally (SEDI, France); however, this system also did not make it into the clinic.

The next major advancement of Raman systems in neurosurgery was presented by Jermyn et al. in 2015 [133], marking the first use of Raman spectroscopy in living human brain tissue. This was an important study that showed the ability of SR to be used in the operating room, even in the face of clinical challenges. Moreover, the system was shown to successfully discriminate normal brain tissue from all tumor grades with a 90% accuracy. Much of the system's success was enabled by a professionally designed optical probe (EmVision LLC) to maximize photon collection, a state-of-the-art deep-cooled charge coupled device (CCD) for photon detection, and high-level data analysis procedures. Also important is the effort put into the industrial design of the probe: it was small enough to be hand-held, ergonomic (encasement form, fiber flexibility, non-fragile) enough as to not be too inconvenient to the neurosurgeon, and used neuronavigation markers on the back-end to register locations of measurements in the surgical planning suite. Since then, the same group has pushed for real translation of this system by better characterizing the systems operating conditions in the OR [176], improving the data analysis to minimize parasitic ambient light contributions [177] and comparing tumor margin localization between magnetic resonance imaging (MRI) and SR [178]. This system has been commercialized (ODS Medical) and is now in clinical trials for superficial tumor delineations to quantify the clinical improvement of its use. More recently, in 2017, another multimodal instance of the same probe was presented to perform SR, auto-fluorescence (AF), and diffuse reflectance spectroscopy (DRS) for increased classification accuracy [179]. This system also used a different data analysis procedure and showed that it was translatable to other cancers, (colon, melanoma and lung); however, the sample size was small. In 2018, Desroches et al. followed up on the work by the Puppels group by using only the HWNM region to interrogate human brain tissue, intraoperativeley[136], [172]. In this study, two probes were used in both *ex vivo* porcine tissue and *in vivo* human tissue, with the clear goal of being a proof-of-principle device for HWNM tumor classification. The major advantage of such a system is the minimized Raman background from silica in the HWNM regime, meaning that filters at the probe tip would not be required and therefore smaller probes may be used.

The next milestone in intraoperative SR was the acquiring of spectra from deep in the brain by Desroches et al. in 2019 [137]. In this work, the mandrin of a biopsy needle was replaced by an optically similar probe (EmVision LLC) from Jermyn et al. in 2015, with the significant differences being its smaller size and its angle facing detection [133]. The probe had some spectral discrepancies from the original, due likely to the magnesium flouride prism used for side-reflection. While this work is preliminary, it does present the first intraoperative deep brain SR measurements and opens the door for Raman-guided biopsy sampling. While not intraoperative, other interesting probes have been implemented on *ex vivo* tissue. In 2016, Stevens et al. presented a probe design which used a collimated beam through an empty biopsy needle to measure signal from *ex vivo* porcine tissue [180]. This probe is unlikely to be brought into the clinic due to the free-space optics involved and the long integration times required. However, it did present an interesting approach to acquire the signal from the low wavenumbers below 700 cm^{-1} - routinely ignored due to the parasitic background signal from silica. In 2018, DePaoli et al. presented a CR spectroscopy probe to investigate *ex vivo* primate tissue [1]. The system was composed of compact fiber sources, a sensitive photon counting detector and simple silica-optics probes for optical transport. Rather than being measured using a spectrometer, the spectra were encoded in time using fast tuning lasers for the stokes wavelength. The major implication of this system was the short integration time (10 ms for low resolution HWNM spectra), given the size of the probe - being small enough to be placed within a DBS electrode hollow core for functional neurosurgery guidance. Furthermore, since the signal is blue-shifted from the excitation wavelengths, no autofluoresence (AF) removal is required. This system also holds potential due to its optically sectioned signal generation which allows for distal tip sensing (ie. on the other side of the DBS electrode), as well as its ability to delineate smaller brain structures (important for DBS guidance). It is important to note, however, that more work will need to be done to understand the maximum permissible exposure (MPE) in brain tissue before iterations of this system can be used in humans (see table 1a).

Table 1a – Optical characteristics of neurosurgical point-probes. Abbreviations: Avg. = Average, Res. = resolution. Notes: *Number of wavelengths = 10, corresponding to ref [1]. **Average of 3s acquisition time[137], [181]. Irradiance (I) is calculated using the formula: $I = \frac{P_{avg}}{A}$, where P_{avg} is average power, and A is the area of the beam spot on the tissue. The higher limit of the average power range is used for each case. Radiant exposure (H) is calculated using the formula: $H = I \times t$, I is irradiance and t is the acquisition time ie. the time of light exposure.

Reference	Specimen	*In vivo*	Modality	Raman Excitation Wavelength (nm)	Raman Shift (cm^{-1})	Excitation Spot Size (mm)	Avg. Optical Power (mW)	Irradiance (W/cm^2)	Acquisition Time (s)	Radiant Exposure Single acq. (J/cm^2)	Spatial Res. (mm)	Spectral Res. (cm^{-1})
2007[182]	Porcine	No	SR	719	2400-3800	0.3	80	113	10	1131	~1	8.0
2010[175]	Mouse	Yes	SR	830	900-1800	0.4	120	95	5	477	~1	4.0
2015[110]	Human	Yes	SR	785	381-1653	0.5	37-64	33	0.15	4.9	~1	1.8
2017[99]	Human	Yes	SR,(AF,DRS)	785	381-1653	0.5	27-75	38	0.15	5.7	~1	1.8
2018[1]	Macaque	No	CR	792,1030-1044	2800-3050	0.01	80	1.0×10^5	$0.001\times\lambda$	1019*	< 0.01	1.0
2018[181]	Human	Yes	SR	671	2800-3600	0.35	10	10	2.0-6.0	31**	~1	1.8
2019[137]	Human	Yes	SR	671,785	400-1800,2800-3600	0.35	20	21	1.1-6.3	62**	~1	1.8

Table 1b – System characteristics of neurosurgical point-probes. Abbreviations: OD = Outer diameter, SM = singlemode, MM = multimode, N/A = Not available.

Year	Probe Encasement	Probe OD (mm)	Autoclave Ready	Optical setup	Detector	Optical Transport	Probe Description	Purpose
2007[182]	None	0.33	Yes	Uncased probe Free space optics	−70°C Cooled CCD (Renishaw)	Silica	1×300 μm MM source Same Fiber collection No filters	Research probe for brain tissue classification in neurosurgical guidance
2010[175]	Details N/A (Sedi-ATI)	1.6	Yes	All fibered System on cart	Details N/A, CCD (Horiba)	Silica	1×400 μm MM source 9×200 μm MM collectors No filters Lower AF due to 830 excitation	Stereotactic probe for Tumor delineation in mouse cancer models
2015[110]	Stainless steel needle tube (EmVision LLC)	2	Yes	All fibered System on cart	−40°C Cooled CCD (Andor)	Silica	1×200 μm MM source 7×300 μm MM collectors Micro-optic emission filter Micro-optic collection filter Custom lens	Hand held probe for tumor delineation and guided resection
2017[99]	Stainless steel needle tube (EmVision LLC)	2	Yes	All fibered System on cart	−40°C Cooled CCD (Andor)	Silica	1×272 μm MM Raman source 7×300 μm MM collectors 1×300 μm MM AF/DRS source 1×300 μm MM AF/DRS collector Micro-optic emission filter Micro-optic collection filter Custom lens	Multimodal hand held probe for tumor delineation and guided resection for improved cancer classification
2018[1]	Stainless steel needle tube (In-house)	0.4	Yes	All fibered System on cart	Photon Counter (H8259-02, Hamamatsu)	Silica	1×125 μm SM source 1×125 μm MM collector Optional GRIN lens for distal focusing	Modified DBS stylet for electrode implantation trajectory measurements in macaque cortex
2018[181]	Modified biopsy canula (Medtronic, Inc.)	2	Yes	All fibered System on cart	−40°C Cooled CCD (Andor)	Silica	1×125 μm MM source/collector Angle polish for side viewing No micro-optical components required	Modified biopsy needle canula housing fiber-optic probe for biopsy guidance
2019[137]	Modified biopsy mandrin (EmVision LLC)	0.9	Yes	All fibered System on cart	−80°C Cooled CCD (Andor)	Silica	1×100 μm MM source 12×100 μm MM collectors Micro-optic emission filter Micro-optic collection filter Prism for side-viewing	Modified biopsy needle mandrin housing fiber-optic probe for biopsy guidance

1.4.1.1 Spontaneous Raman spectroscopy is the current tool of choice for neurosurgical point-probes

Due to the low signal generation of SR photons, highly efficient systems must be designed such that the energy required to create the Raman signal remains within the safety limits of optical radiation exposure on biological tissues. Due to this difficulty only the most efficient systems have succeeded in acquiring measurements in intact living brain. The few successes can be traced back to professionally designed optical systems which squeeze the most SR photons possible out of a specific experiment [133], [136], [137], [183].

If implemented correctly, there are major advantages of SR systems over CR systems for clinical spectroscopy use. Specifically, since SR is a linear process it allows several leniencies in the system design, such as: 1) The use of a continuous laser source rather than a pulsed laser. Using a continuous laser source allows for a smaller, considerably less expensive system. 2) The use of standard silica optical fibers for transporting the optical energy from the laser output to the patient. Pulsed laser systems (required for CR) are plagued by pulse-deteriorating non-linear effects occurring during their transport through a dispersive media (such as silica optical fiber) [184]. Due to these non-linearities pulsed laser systems are often equipped with expensive fibers designed for decreased non-linearities. This greatly increases the cost of a system, as well as the fragility. 3) the linear nature of Raman signal generation means that the light does not need to be focused to produce the SR signal. Resolution aside, this is an advantage as a larger excitation spot-size decreases the overall irradiance on the tissue. 4) SR is linearly proportional to the concentration of molecules allowing for direct molecular quantification. SRS also innately shares in this advantage over CARS; however, there are techniques to achieve linear proportionality even with CARS. [106], [185].

1.4.1.2 Coherent Raman spectroscopy is less mature but has potential for clinical utility

CR is best exploited in imaging systems due to its intrinsic optical sectioning and rapid contrasting at a single molecular vibration. However, there is niche uses for CR spectroscopy. Due to the small excitation volume ($<$10 μm diameter) CR spectroscopy can provide very-high resolution sensing with orders of magnitude higher molecular sensitivity than SR; however, this also means that the optical energy must be focused and confined to a small volume to create the signal. This small excitation spot size translates to high irradiance levels and this is the limiting factor in clinical CR systems [186], [187]. Fiber-based CR spectroscopy is a new technology that has room for improvement, unlike the somewhat ceilinged SR counterpart. For starters, CR sources can be designed with the laser repetition rates optimized to provide more CR signal without increasing the average power, and therefor heating of the tissue, while still keeping the peak power below ionization limits [188], [189]. Furthermore, fast-wavelength tuning CR systems allow for time-encoded signals which can access molecular bonds in a random-access manner. This means that spectra with only desired wavenumbers can be created, drastically decreasing the acquisition time with proper vibration selection [1], [160]. Also, the optically sectioned signal allows probe designs such that the signal can be excited far from the fiber tip on the other side of a transparent material, without sacrificing the collection efficiency (as would be the case for confocal SR). This is especially useful if the probe must be placed within a biocompatible sleeve having its own parasitic Raman signal at the interrogation wavelength [89], [190].

1.4.1.3 Spectrocsopic blood vessel detection should be investigated using Raman spectroscopy

There is a clinical risk of haemorrhaging in performing deep brain neurosurgeries (ie. DBS, biopsies) as the surgeon cannot see oncoming blood vessels. Although other optical systems have been presented to fill the clinical need, Raman technologies have not yet been fully exploited for the task. Recently, a translational success was presented using intraoperative OCT for accurate blood vessel detection and size estimation from within

a standard biopsy needle during neurosurgery [135]. Other optical technologies that have investigated blood vessel detection in neurosurgery are laser Doppler flow and diffuse reflectance; however, ability to measure blood vessel size using OCT does make it especially interesting [134], [191], [192].

It is unlikely that a surgeon will use multiple optical probes during a single procedure, and therefore, the idea of having an OCT mandrin for blood vessel detection during needle descent, followed by a Raman mandrin to guide the tumor resection in the region of the planned biopsy is somewhat redundant. Furthermore, there is not much procedural diversity in medical professions, therefore a consensus probe will likely be chosen and used across the neurosurgical community. That probe could be either Raman or OCT, or size permitting, a multimodal combination.

1.4.2 Rapid and Portable Raman Microscopes for operating room histopathology

Histology is time-consuming, requiring fixation, sectioning, and staining of freshly excised tissue. The potential of intraoperative Raman technologies originate from the lack of of tissue preparation and therefore rapid feedback *in situ*. This is specifically beneficial in the case of neurosurgeries wherein delayed classification could lead to possible repeated cranial openings. In this section we will overview the work that has been done towards, and the successful implementation of, vibrational imaging systems in the OR for same-room neuropathology.

SR microscopes are fundamental in dissecting Raman differences in neuropathology [193]–[196]; however, they are traditionally too slow to be used intraoperatively. On the other hand, CR systems, using the knowledge gained by SR research, have shown high potential for clinical translation.

The first display of rapid CARS imaging for healthy and cancerous mouse brain tissue delineation was by Evans et al. in 2007 [197]. This work was done *ex vivo* on orthotopic human astrocytoma mouse model and the tumor boundaries were defined by the lack of CH_2 signal in the tumor regions. Since then, there has been considerable interest in CARS based histology. In 2014 Uckermann et al. provided thorough evidence for lipid decreases in tumor regions infiltration in an orthotopic glioblastoma and brain metastasis mouse model using CARS [198]. By combining CARS with modalities such as two-photon excited fluorescence (TPEF) and second harmonic generation (SHG), detailed images of tissue with structures such as extracellular matrix, blood vessels, and cell bodies can be created. One of the advantages of CARS over SRS is the ease of multimodal imaging due to the non-modulated lasers which are required for SRS. Due to this, groups have shown the ability of intrinsic TPEF and SHG to aid CARS in brain cancer histology [199]. Galli et al. also perfomed multimodal imaging on excised human tissue samples after 5-aminolaevulinic acid (5-ALA) was preoperatively administered and showed that it did not interfere with the CARS signal [200]. In 2019, the group also reported that even with the small FOV that is generally created using endoscopes, this information was discriminatory and comparable to that which can be made *in situ*[201].

The problem, however, with CARS for histology is the low signal generation from proteins (represented by CH_3 contrast). This fact somewhat limits the ability of CARS images to be directly compared to the gold standard hematoxylin and eosin (H&E) where-in unspecific staining of nuclei and proteins is performed[202]. SRS on the other hand does not suffer from this shortcoming. In 2012, Freudiger et al. first demonstrated the use SRS to create images with H&E type information using the vibrational contrast from only CH2 and CH3 bonds [202], [203]. The following year, the same group found a high correlation between SRS histology (SRH) and H&E staining (κ = 0.98) for glioma detection in human brain tissue [165]. In the same report they then used an epi-detected microscope to image and guide resection of a mouse brain tumor *in vivo*[165], [204]. In 2015, the group reported continued progress in using SRH to accurately detect and classify tumor infiltrated tissue sections with high accuracy [166]. This alluded to the possibility of pathologist-free interpretation of tumor margins for rapid-feedback in the OR. In 2016, Lu et al. took the translatability a step further by analyzing fresh human samples,

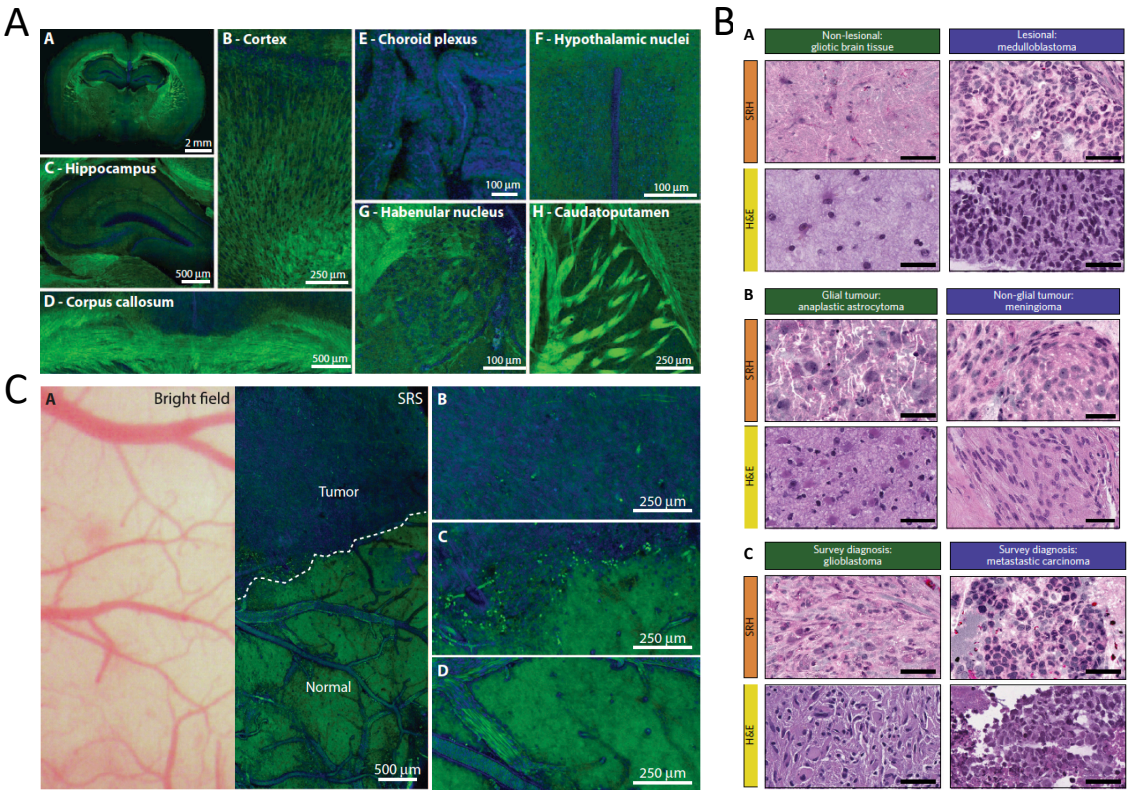

Figure 1.1 – SRS contrast in brain tissue A.) Epi-SRS images of fresh brain slices from normal mice brain in various brain regions. Lipids are shown in green and proteins in blue. Referring to the inset sub-figure labelling: 2-mm coronal slice (A), cortex (B), hippocampus (C), corpus callosum (D), choroid plexus (E), hypothalamic nuclei (F), habenular nucleus (G), and caudato-putamen (H)[165]. B.) Brightfield and SRS imaging through cranial window, 24 days after implantation of human GBM xenografts, for comparison of information. Referring to the inset sub-figure labelling: (A) Same FOV bright-field and SRS image of xenograft boundary. Brightfield appears normal, whereas SRS microscopy within the same FOV demonstrates distinctions between normal and tumor-infiltrated areas. (B to D) Higher-magnification views of tumor (B), at the tumor-brain interface (C), and within normal brain (D)[165]. C.) Comparative examples of processed SRH and H&E images of gliotic brain tissue, medulloblastoma , anaplastic astrocytoma, meningioma, glioblastoma and metastatic carcinoma. These images were used in a web-based survey to compare diagnostic outcomes using the two histological methods. [171]

showing that some additional discerning features (which can be seen using SRS with the fresh sample) are lost in the tissue preparation phase of H&E staining [205]. One of the most exciting aspects of this work is that the images are freely available to help improve diagnostic training in the future [206].

Made possible by advances in portable and robust fiber laser systems [207]; the first true fruition of CR *in situ* potential was presented by Orringer et al. in 2017, wherein the group reported a clinical SRS system for intra-operative neuropathology [171]. Using this system, freshly resected tissue sections were squished and imaged,

all from within the OR. By taking several small field of view (FOV) images they created interpretable stimulated Raman histology (SRH) mosaics on the order of 2.5 minutes. In terms of output, the Raman information was used to digitally recreate H&E type staining, and to perform automatic tissue classification using these images. The optical characteristics of the system are presented in tables 2a & 2b. Furthermore, the reports states that the system has remained in use for over a year within the operating room without problems or realignment, which speaks to the robustness of system's engineering. Long term robustness is an interesting point which is not often mentioned in optical reports, but should be imperative in clinical designs. In 2018, the group reported on the use of this system for *in situ* pediatric brain tumour classification with %100 accuracy [208]. Also, In 2018, Bae et al. presented an epi-detected hyperspectral SRS system for the subtyping of glioblastomas using HWNM spectra[209]. This system is interesting due to the spectral information and epi-detection orientation and is included in tables 2a & 2b.

Table 2a – Optical Characteristics of state-of-the-art imaging systems for neurosurgery. Notes and abbreviations: N/A = Not applicable or not available, * = Hard to distinguish from publication, estimates are used, ** = Peak irradiance and single pixel radiant exposure are calculated from the pusle peak power and the airy disk spot size, using the N.A. and wavelength of the published system (Table 2b) to derive the spot size from the Airy disk formula ($r_{airy} = \frac{1.22 \times \lambda}{2 \times NA_{obj}}$). *** = Image area irradiance and radiant exposure use the same equations as in table 1a. For the radiant exposure calculation, total image acquisition time is use from table 2b. The wavelength used for all calculations was the one with the highest average power. For SRS this is the higher wavelength and for CARS this is the lower wavelength. It is critical to note that these values are extremly variable with respect to the optical arrangement, however, they are important to consider for clinical systems which aim to image intact tissue.

Purpose	Reference	Excitation Wavelengths [Pump, Stokes] (nm)	Power Sample Surface (mW)	Rep Rate. (MHz)	Pulse Width. (ps)	Pulse Energy Single Pulse (nJ)	Peak Power Single Pulse (W)	Peak Irradiance Single Pulse (W/cm^2)**	Pixel Dwell Time (μs)	Irradiance Image Area (W/cm^2)***	Radiant Exposure Image Area (J/cm^2)***
Rapid Histology	2017[171], [207]	[790,1010-1040]	[120,140]	40	2	6.5	3250	2.62×10^{11}	2	163	327
	2018[209]	[680-1300,1041]	[20,40]	80	2	0.75	375	3.0×10^{10}	2.4	234	6900
	2019[201], [210]	[781,1005]	[50*]	80*	1.2	0.625	520	7.3×10^{10}	0.4	220	4.5
Handheld Imager	2018[211]	[680-1300,1041]	[40,40]	80	2	1	500	9.9×10^{9}	6	283	850
	2018[212]	785	500	N/A	N/A	N/A	N/A	N/A	N/A	3.5	300
Endoscope	2017[213]	[816,1064]	[40,40]	80	6	1	167	5.7×10^{7}	N/A	88.9	890
	2018[111]	[800,1040]	[20,10]	80	0.1	0.375	3750	1.0×10^{15}	N/A	29.3	23.4
	2018[214]	[817,1064]	[60,35]	76	6	1.25	208	6.9×10^{9}	6	989	376

Table 2b – Physical Characteristics of state-of-the-art imaging systems for neurosurgery. Notes and Abbreviations: *Hard to distinguish from paper, WD = Working Distance, OD = Outer Diameter, N/A = Not applicable or Not available. Total image acquistion time was calculated using single band imaging time multiplied by the number of bands imaged.

Purpose	Year	Specimen	Modality	Portability	Orientation	Reported Spatial Res. [lateral, Axial] (μm)	NA Objective	FOV (μm)	Wavenumber Acq. Time (s)	Spectral Range (cm^{-1})	Spectral Res. (cm^{-1})	Total Acq. Time (s)
Rapid Histology	2017[171], [207]	Human Fresh resection	SRS	Fibered laser On cart	Transmission	[0.36,1.8]	1	400×400	2	2845, 2930	N/A	4
	2018[209]	N/A* Snap frozen	SRS	Free space Optic table	Backward	[0.45*,N/A]	1	160×160	0.95	2800-3020	7	29.5
	2019[201], [210]	Human Fresh	CARS, TPEF, SHG	Free Space Optic table	Backward	[0.5,N/A]	1	150×150	0.02	2845	N/A	0.02
Handheld Imager	2018[211]	Canine Snap frozen	SRS	Hand held Optic table	Backward	[1.4,N/A]	0.5	168×168	0.125	2800-3000	15	3
	2018[212]	Calf Fresh	SR	Hand held (2 cm WD) On cart	Backward	[100,N/A]	N/A	4000×3500	0.7	940-1800	120	84
Endoscope	2018[213]	Skin	CARS/TPEF/SHG	8mm OD Endoscope Optic table	Backward	[10,N/A]	0.5	$\pi \times 150^2$	10	2845	N/A	10
	2018[111]	Colon	CARS/SHG	4mm OD Endoscope Optic table	Backward	[0.8,5.9]	0.45	320×320	0.8	2885	N/A	0.8
	2018[214]	Human nerve Cryosection	CARS/TPEF	2.2mm OD Endoscope Optic table	Backward	[1.4,N/A]	0.5	310×310	3.8	2841	N/A	3.8

1.4.3 Towards CR endoscopes for label-free imaging of intact during neurosurgery

SR systems have dominated clinical implementation of fiber delivered spectroscopy, while CR systems are the method of choice for biological imaging. This creates a crossroads at imaging endoscopy for the two types of modalities: On the one hand SR systems are traditionally too slow for *in vivo* imaging as the signal is intrinsically weak and dispersed spectrally, on the other, CR systems traditionally require bulky lasers and complicated optical transport methods for the high-peak power pulses. There have, however, been considerable technological advances in the past decade for both system types showing that vibrational endoscopy is close to a reality in neurosurgery.

To date, SR imaging "endoscopes" have not been deployed for neurosurgical improvement. In fact, there are few SR imaging endoscopes reported to date. There have, however, been interesting attempts at handheld systems for mesocopic Raman imaging. St-Arnaud et al. presented two iterations of a wide-field Raman imaging system using a multicore imaging fiber for image transport and a tunable filter in the detection path for temporally encoded Raman spectra[212], [215]. While the system required long intergration times and high optical power, due to the widefield illumination irradiance levels are actually quite low (see tables 2a & 2b. In the future, specific Raman bands could be selected for imaging - greatly decreasing imaging time.

CARS endoscopes have been under investigation since 2006, wherein Légaré et al. presented backwards imaging of polystyrene beads using a SM fiber for illumination and collection[216]. Since then, other groups have gone through the trouble of characterizing and improving our understanding of the inherent limitations of CARS endoscopes using traditional silica optics [217], [218]. Due to these limitations, specialty fibers optics for pulse delivery with reduced dispersion and background Raman signal have been investigated[219]–[221]. However, it was not until only recently that reasonably translatable CARS endoscopes have began to be reported. While none of the systems have been used *in vivo* or in brain tissue, these promising candidates for neurosurgical use will be included here. In 2017, Lukic et al. presented a multicore imaging fiber system which allowed for multimodal CR imaging with no moving parts at the 8mm outer diameter probe tip [213]. Using this system they imaged a skin tissue sample with 300 μm field of view and a 10s acquisition time. While the probe is quite large for neurosurgery, considerable downsizing could be possible with microoptical component. In 2018, Lombardini et al. reported a high performance CARS endoscope with <1 μm resolution, capable of producing CARS images of a $310\times310\mu$m FOV in only 0.8s[111]. The outer diameter of this probe is 4 mm and images were presented on fresh colon tissue. This system is also capable of variable FOVs and multimodal imaging. The high performance acheived is mainly due to the sophisticated design, using specialty optical fibers (Double clad, Kaggomé lattice) and a precision-spliced microlenses. While this may seem fragile for the clinic, it is part of the tradeoff for high performance imaging systems. Finally, also in 2018, Zirak et al. presented a 2.2 mm rigid CARS endoscope (187mm in length) for neurosurgery applications. The endoscope was shown to be capable of high resolution, fast CARS imaging with the smallest form factor to date [214]. The technology is enabled by recent advances in GRIN lens technology, where in long versions of the image-conserving fibers (previously used for *in vivo* CARS endoscopy in mice [161]) are now capable of being manufactured. That said, the system still uses large free-space lasers and an optic table for alignment. Therefore, while it is promising, some engineering still remains to make the system fibered and ready for the clinic. These 3 systems are included for comparison in tables 2a & 2b.

In 2010, Saar et al. presented the first report of fast epi-detected SRS with acquisition times of ~100 ms using 50 mW for both the pump and stokes wavelength [204]. However, the detection scheme in the report used a 10×10 mm photodiode (PD) with a whole drilled in the center, wherein the excitation lasers were focused through. A year later Saar et al. presented a scanning-fiber-endoscope (SFE) version of the system using ~130 mW total power for excitation and the same detection apparatus. Unfortunately, *in vivo* work has not been presented since using the device[222]. In 2018, building on earlier work in delay-line tuning, Liao et al. presented a handheld hyperspectral SRS microscope capable of HWNM spectroscopic images (15 cm^{-1} spectral resolution) on the

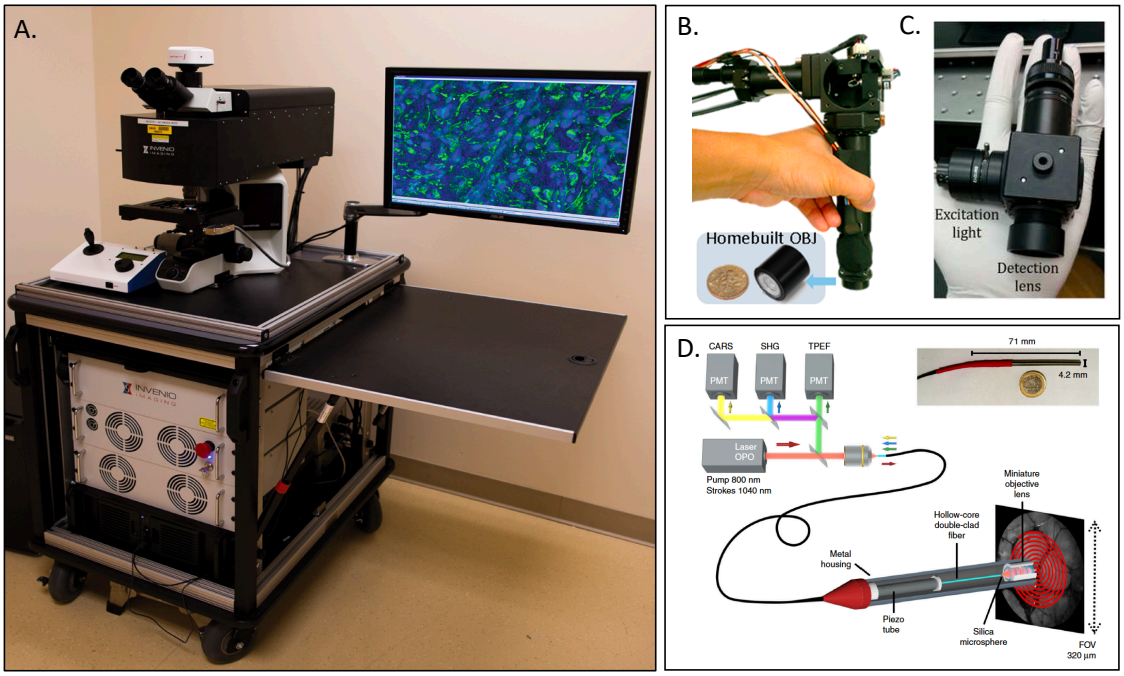

Figure 1.2 – Translational Raman Imaging systems A.) On cart SRS microscope for intra-operative imaging of freshly resected brain tissue.[171]. B.) Fiber-delivered, Handheld SRS microscope [211]. C.) Handheld widefield SR imager with large FOV [212]. D.) Multimodal CARS, TPEF, SHG endoscope [111]

order of 3s [211], [223]. Using this system, the team imaged sections of healthy and cancerous canine brain tissue, but did not go into much detail on the ability to distinguish the two samples. While the proof-of-concept system is relatively bulky for the limited FOV, the potential for downsizing is apparent. The details of this system are also available in tables 2a & 2b for comparison.

1.4.3.1 CARS or SRS endoscopy

SRS has been reported to have improved nuclear contrast in comparison to CARS due to a decreased non-resonant background, allowing faster imaging speeds of low concentration molecules [106], [107], [203]. While this is true, publications on systems imaging in the backward (epi) direction using SRS are fairly scarce. In microscopy, this trend is mainly due to the ease of which CARS is added to traditional laser scanning microsopes used for TPEF and SHG. In clinical applications, however, this is likely due to the overall increased complexity of SRS detection. Gottschall et al. provide a good resource for understanding the benefits of each CR modality in their review on advances in laser concepts for multiplex CARS [224]. Briefly, due to the small and modulated signal production in SRS, it requires a more complicated (lock-in) detection scheme. Also, in the push for fiber laser systems, laser noise becomes a major factor that is not a relevant issue for CARS, causing the requirement for even more complex detection solutions (balanced lock-in). Furthermore, the SRS signal, being at the same

wavelength as the source (pump or stokes), means that other factors such as two-photon absorption and cross phase modulation still can contribute to parasitic background, albeit them less damaging than non-resonant contributions in CARS. Lastly, detecting at the same wavelength as the source also means that traditional dichroics cannot be used, therefore only polarization modules, or non-collinear (surrounding PDs) detection can be used to split the returning signal from the excitation, which is less efficient.

CARS on the otherhand, while easier to implement, is limited to sensing high-concentration molecules due to its quadratic proportionality with concentration and its inherent non-resonant background. While this is a single point it is more limiting than the previous stated for SRS.

Another factor which can play a considerable role in clinical applications is the operability of the system under ambient lighting. SRS has an advantage here for 2 reasons: 1) the modulated signal can easily be removed from the background contributions and 2) the wavelength of detection is further into the near-infrared (NIR) regime, being at the wavelength of excitation. Interestingly, traditionally considered an advantage of CARS in microscopy, the blue-shifted signal generation is somewhat of a burden in the clinic as the detected wavelengths are normally near the visible regime where there is strong contributions from surgical lighting. This can, however, be circumvented by pushing CARS sources more into the NIR.

Overall, the optimal solution is application specific. If the desired molecule to be imaged is lipids, of which there is an abundance of in white matter, CARS may be ideal due to its easier implementation. This may be the case in neurosurgical guidance systems for functional neurosurgery. If, however, nuclear contrast for histology is the goal, SRS may be the optimal modality due to a decreased non-resonant background and direct interpretability to traditional H&E staining.

1.4.3.2 The information trade-off of Raman systems

There are three central information trade-offs in clinical Raman systems: 1) FOV vs. resolution 2) Acquisition speed vs. spectral information 3) Form factor vs. spatial information. Therefore, as devices move forward, solutions will have to be application specific. Consider the following scenarios to conceptualize this: 1) A surgeon is looking macroscopically at a cranial opening, trying to discern cancerous from healthy brain tissue. 2) A deep-seated tumor is detected on MRI and a biopsy is required for confirmation of malignancy. 3) A surgeon is performing DBS implantation for PD patient using only pre-operative MRI planning. During intraoperative stimulation, the patient does not respond favourably, signalling an off-target implantation.

1) In this scenario, the surgeon needs to know the tumor boundaries at a resolution with which he or she is capable of removing the tissue. At present day histopathologic confirmation is required and the optimal system for this would be a rapid SRS microscope since it can provide high resolution images with enough information that can be interpretable by a pathologist [171]. For tumor boundary delineation, however, a more ideal system could be a widefield, low resolution imaging system which could be overlayed into a surgical microscope. Such a Raman imager should capable of tumor boundary delineation at the resolution of the surgeons resection tools and at high speeds[212]. Unfortunately, current wide-field systems are too slow, and therefore a compromise in spectral information would be required. We could imagine, however, wide-field Raman imaging of only a few vibrational bands with enough information such as to remove the need for histopathologic confirmation. Tradeoff: Acquisition time, Spectral information

2) Here the surgeon would want a device that could be descended into the volume of investigation and analyze the tissue region without the need for tissue removal. For this, the ideal system would be a CR endoscope, capable of cellular imaging and creating H&E type images from within the brain for tissue-type classification. Presently, endoscopes are too large for deep intraoperative brain imaging, however, systems are being developped for this purpose[214]. On the other hand, spectroscopic probes can be smaller and traditionally provide

much richer spectral information for tissue classification[137]. In the future clinical trust in spectral measurements may improve to a point where a small FOV image does not add much greater classification accuracy than a volumetrically acquired spectrum. If this becomes a reality, spectroscopy could be a more economic implementation. Tradeoff: Form factor, spectral information.

3) In this scenario, the surgeon would like to know the current location of the stimulating contacts deep in the brain with respect to the target nuclei to fix the trajectory. DBS neurosurgery is slightly more complicated in the sense that the contact terminals of the chronically-implanted electrode must be located within 1 mm of the target structure to be effective[52], [225]. The most common target structure for PD treatment is the motor-area of the subthalamic nucleus, located in the midbrain (near the floor of the brain) and is only a couple of mm^3 in size. Many surgeons perform the implantation using only pre-operative MRI planning and have found immense success. However, there are cases where the surgery do not have the anticipated outcomes and the main cause for this is lead misplacement [51]. For guidance, a high-resolution spectroscopy or imaging device could be optimal as long as the information acquired could allude to the macroscopic position of the electrode. Imaging a small FOV onboard and along the descent of the chronic electrode would be an ideal solution. For instance from within the hollow part of the electrode itself. However, this would require an endoscope of an extremely small form factor ($<400\mu$m) to fit within the electrode's hollow core. Spectroscopy on the other hand could perform the sequential measurements and allude to the position based on solely on the order of the spectroscopic information acquired[2]. That said, higher resolution spectroscopy would be desirable to give a better estimate of electrode location [1]. Tradeoff: Form factor, spatial information

1.4.4 Optical exposure to brain tissue

While optical systems progress and technological advancements permit the interrogation of intact, living brain tissue, we will remain limited by the amount of optical irradiance which can be introduced into the interrogated volume without causing serious cellular damage. It is rather straight forward to calculate the maximum permissible exposure (MPE) of continuous-wave (CW) optical radiation for tissues such as the retina and the skin thanks to the availability of international standards [226], [227]. However, this should not necessarily be used as a guideline for Raman systems investigating the brain, especially in medical interventions. To begin, these standards are not designed for deliberate laser exposure during medical procedures [226], [227]. Therefore, the safety factors may not need to be so strictly enforced (3x safety factor for skin MPE). Also, skin differs considerably from brain tissue. First, it can be an orders of magnitude more absorbing due to higher melanin concentrations, and the rate of the absorption of light greatly affects tissue heating [92], [228]. Second, the thermal properties of brain tissue vary greatly from skin due to a considerable increase in blood perfusion[228]. This increased blood perfusion is required due to the high metabolic output of the brain, which itself produces thermal energy[229]. Lastly, brain sensitivity to thermal damage is somewhat unclear. Reports of minor local temperature changes of only 2° C have been shown to cause thermal damage to metabolically active brain cells [229]. However, it has also been shown that the awake animal brain naturally fluctuates in temperature within this range of 2° C [230]. In terms of photothermal damage at the cellular level it has been shown that injuries are reversible for temperature increases up to 43° C [231].

For SR systems, information on linear photothermal effects caused by absorption in the brain can be interpreted from optogenetic research. Christie et al. used fMRI changes to analyze temperature variations from 445nm light outputted from a 200 μm optical fiber, implanted in a living mouse brain[232]. For consistency with the summary to come, at 10mW input power, their linear relation between optical radiation and temperature predicted an increase in 4°C at the fiber tip. In 2015 Stujenske et al. presented an experimentally-validated theoretical model for photothermal heating of brain tissue at 532nm using Monte Carlo and a modified version of Pennes bio-heat equation[233]. In this work, they showed that with a 62 μm excitation fiber at 10 mW continuous illumination (Irradiance: $3312 mW/mm^2$) that there was a ~4° C increase in temperature in the maximum heat-

ing location (~100μm away from fiber tip). They then repeated the simulation with a 200μm excitation fiber (Irradiance: 318 mW/mm^2) and found only a ~2° C increase in temperature. Therefore, an order magnitude increase in illumination area (or reduction in irradiance) produced only 50% less heating. In 2016, Shin et al. presented a combination of theoretical and experimental analysis on living mouse brain tissue during optogenetic stimulation at 473nm[234]. The experimental results were measured using a fiber-optic encapsulated by a thermo-couple canula. They also found that the maximum temperature would be observed 100 μm away from the fiber tip and that the temperature increase could be estimated by 0.25°C/mW with respect to the time averaged power. Extrapolating this metric into irradiance with a nominal 10mW continuous input power, we get a theoretical temperature increase of 2.5°C, matching well with estimations by Stujenske [233]. In 2017 Senova et al. used a thermal imager to map temperature changes during 473 and 638nm illumination directly on living mouse brain[235]. With their optical setup, they found no histological changes in the tissue or *in vivo* local field potential changes in the tissue under 200 mW/mm^2 irradiance at a 40 Hz duty cycle. While their observed temperature increases seem low in comparison to other reports ($< 1^\circ$ C), careful analysis of the terminology shows relatively well matched results to Stujenske and Shin: continuous 600 mW/mm^2 at 30% duty cycle (60Hz, 5ms) gives an time averaged irradiance of 200 mW/^{2}, extrapolating the difference between the 200 and 62μm fibers to the 400 μm fiber used gives a theoretical temperature change of ~1.5° C [233], [235], [236]. Furthermore, Stujenske et al. presented these simulations at a 532nm illumination wavelength meaning a small reduction factor could be applied as 532nm has a higher absorption peak than both wavelengths used in Senova's study (473 and 638nm) [236]. It rests that animal preparation (window size), numerical aperture of the fiber optic as well as pulse lengths can play roles in these measurements.

Things become more complicated when we consider photo-induced effects of CR systems. CR systems are complicated as normally they: 1) are focused tightly to a small area, creating high irradiances, 2) have focal points that are scanned rapidly to image, decreasing light on time in a single position and 3) can induce non-linear damages, including photochemical ablation and optical breakdown [187], [237], [238]. Furthermore, even CR phenomena can directly increase photothermal damage[186]. To understand non-linear limitations for imaging systems, we can pull from research in multi-photon (MP) fluorescence microscopy. Because of shorts pixel dwell times due to rapid focal point scanning, instantaneous heating through linear absorption is often considered negligible in comparison to non-linear damage for multi-photon systems [187], [237]. However, continuous scanning of the same FOV can produce a volumetric heating effect that must be accounted for [192], [239]. In 2001, Hopt et al. presented a well experimented general equation for the number of image scans which could be performed with a given illumination scheme. They also described a general formula for tissue damage rate, D, which was proportional to the optical power to the nth degree (P^n), repetition rate(f_{rep}), and pulsewidth (τ_{pulse}) of the laser used (see equation 1.5). In their experiments using 120 fs pulsed lasers they showed that non-linear damages greatly dominate over linear heating and reported a power dependance of n = 2.5 [187]. In 2006, Fu et al. used 2.5 picosend lasers in a CARS microscope and by varying the repetition rate concluded the linear mechanisms of tissue heating and damage (n=1) prevail up to a peak power of 219 W, after which non-linear effects are dominant(n = 1.8)[186]. An exponential power dependancy of 1.8 using picosecond pulses does not contradict the observations with femtosecond pulses by Hopt et al., as it was also shown that tissue damage scales non-linearly with the pulse-width ($1/\tau^{1.5}$)[187]. Indeed, the differences of femtosecond and picosecond pulse regimes have been shown with respect to optical breakdown by Vogel et al. [238].

Podgorski et al. presented another experimental measurement of thermal damage during long term scanning using tightly and loosely focused MP microscope orientations. They concluded that in a 1 mm^2 scanning FOV, peak temperature increases followed the relation of 1.8°C/100mW of average power, and that up to 250mW was safe for continuous use[239]. In 2018, Picot et al. presented an experimentally validated thermal model for analyzing temperature changes in *in vivo* brain tissue during volumetric imaging for MP optogenetics[192]. However, it is difficult to draw useful conclusions for CR imaging as emphasis was put on large spot-size holographic excitation of optogenetic proteins. Galli et al. presented a technique to monitor tissue damage using

endogenous CR and fluorescent signal increases during MP image scans[210]. They saw with irradiances of 0.13×10^{12} mW/cm^2 (54mW average power with their illumination scheme) observable endogenous damage to the tissue would appear after 60-100 scans, while with an irradiance of 0.05×10^{12} mW/cm^2 (20mW average power with their illumination scheme) there was no observable photodamage even after 10,000 scans. Moreover, they concluded that this coincided with well with Vogel et al.'s theoretical limits in that the illumination was well below optical breakdown but within the range of low density plasma formation[238].

$$D \propto P^n * \tau_{\text{pulse}} * f_{\text{rep}} \tag{1.5}$$

As with linear examples, illumination schemes are difficult to summarize for non-linear systems, and therefore the understanding is too incomplete to draw general safety conclusions. Furthermore, damage thresholds are highly sample dependant and so it is hard to extrapolate conclusions from experiments made not in living brain. That said, advantageous CR systems can be created. For instance, we can reason that picosecond pulsewidths are beneficial for CR over femtosecond, not only for spectral resolution but also for the decreasing damage rate. Since CR scales with $1/\tau$, it is clear that photodamage ($\propto 1/\tau^{1.5}$) will increase faster than the signal generation when decreasing the pulsewidth[187], [240]. Furthermore, using equation 1.1 and 1.5, we can conclude that lower repetition rates will be most advantageous. To explain, CARS and SRS cause a combination of linear (n=1) and non-linear phototoxic effects (n=1.8), and we also know that they have peak power dependencies of n=3 and n=2, respectively, for signal generation; therefore, decreasing the repetition rate, at a constant average power, will increase signal faster than damage rate (clearly this is more true for CARS than SRS)[188]. This should be true until non-linear optical breakdown effects, described by Vogel et al., begin to occur [238]. We hypothesize the optimal system for clinical CR would operate in the NIR (pump & stokes = 1000 - 1500nm), have a relatively low repetition rate near 1 MHz and use pulsewidths between 1 - 10 ps, operating at about 15 mW total average power.

1.4.4.1 International standards for deliberate optical exposure to brain tissue

To standardize optical exposure limits for Raman sensing in human brain tissue, a complete analysis of tissue damage with both SR and variable CR systems will be required. Such an analysis must be done in living tissue, consider variable optical systems, and analyze short and long term damage effects (ie. neuronal-activity changes and histology manifestations).

That said, it should be noted that the current international standards, along with their exposure limits, do not apply to laser medical procedures, as quoted: "Does not apply to deliberate exposure as an integral part of medical treatment," in the ICNIRP document[227] and "does not apply to patients undergoing laser medical procedures," in the ANSI standard, both of which are referring to the enforcement of MPE limits [226]. While Raman systems are not directly used for treatment, they can be considered an integral part. We must also consider the benefit accrued by the use of the optical tool which may aid a procedure, even if tissue-heating occurs past the safe limits at the most intense location of the illumination. This point is confounded greatly when we consider that the tissue under interrogation often could be damaged to a greater degree in the absence of guidance from the optical tool (ie. tumor resection past tumor boundary, blood vessel clipping in biopsies, microelectrode lesioning in DBS surgery, incorrect lead placement and tissue lesioning in DBS surgery) At the least, safety factors may not need to be so strictly enforced for brain tissue (3x safety factor for skin MPE).

1.5 Data analysis for spectroscopic information

While most research for the clinical translation of neurosurgical Raman systems have been centered on the hardware, a focus is emerging on the analytic aspect of the technology. The Raman effect is an inherently rare phenomenon hidden amongst other optical events such as elastic scattering and fluorescence and gives rise to a complex signal, especially in living tissue [241], [242]. Signal processing and analysis methods are key to extract the Raman signal from the data acquired by the cameras, process it into a format interpretable by computers and design algorithms that can learn to recognize a tissue phenotype based on its Raman signature. Competencies at the intersection of signal processing, data mining and machine learning are now essential to design cutting-edge biomedical Raman spectroscopy systems.

Many challenges relating to the translation into portable operating systems are targeted by recent analytic innovations. The Raman signal is orders of magnitude lower than other forms of light that reach the camera's photon detector, and this drawback is accentuated by poor control on experimental conditions—bloody tissues, light polluted surgical theaters, and in-hand manipulation of the devices. Furthermore, while tissue diagnosis is almost always confirmed by certified neuropathologists, there remains diagnostic uncertainty in areas of heterogeneous and infiltrative tissue that must be accounted for when modeling the Raman signal [243]. Finally, the data-generating process is extremely complex: while the Raman signal is emitted by distinct molecular vibrations, the tissue is composed of thousands of interacting and co-dependent molecules that are heavily influenced by external, confounding factors [244].

1.5.1 Signal processing

Raw Raman acquisitions are characterized by low Raman signal, high amounts of shot noise and intense signal from background sources (mainly tissue autofluorescence, but also light-generating devices such as overhead surgical lights, microscope lights and fluorescence lights) [176]. Signal processing aims to maximize the Raman component of the acquired signal while minimizing the contribution of these other processes. While many developments in hardware target this very issue [245], signal processing is still considered a key component of Raman systems [246], [247]. A complete signal processing pipeline generally includes truncation of the signal to the desire spectral range, correction for ambient light, cosmic ray removal, correction of the spectra for the system response with a standard measurement, baseline removal (mainly targeting tissue auto-fluorescence), smoothing of the spectra to remove high-frequency signal, normalization and data quality assessment [241] (Figure 1.3).

After the initial processing steps of cosmic ray removal and correction for system response, there generally remains an important signal contribution from non-Raman sources, the most important being auto-fluorescence (AF). AF is a spontaneous process resulting from the emission of light from endogenous fluorophores like elastin, tryptophan and nicotinamide adenine dinucleotide (NAD), after excitation by optical radiation [248]. As fluorophores emit at different wavelength, AF contaminates most of the spectral range. Even when mitigating the excitation of fluorophores with longer wavelengths, AF intensity can still be orders of magnitude more important than that of Raman scattering [249]. As such, automatic AF estimation and removal is critical in the analysis pipeline. It has the potential of significantly alter the shape of the final Raman spectra, to a point that some authors prefer to skip this step during their analysis [250]. Many techniques exist to mathematically estimate and remove the background in Raman spectroscopy, leveraging the smooth and predictable decay of its contribution throughout the spectral range. Polynomial fitting of the spectra has remained the most widely used technique, but heavily relies on expert knowledge to select the proper parameters and avoid over- or under-fitting the signal [241], [251]. In order to create completely automated routines, more recent algorithms have surfaced that rely on iterative fitting of the signal with sophisticated cost function ensuring a better fit while minimizing expert intervention [252]–[255]. Still, in biological experiments, the background-generating processes and fluorophores have not been clearly identified, resulting in a correction that is more based on spectral morphology than exact

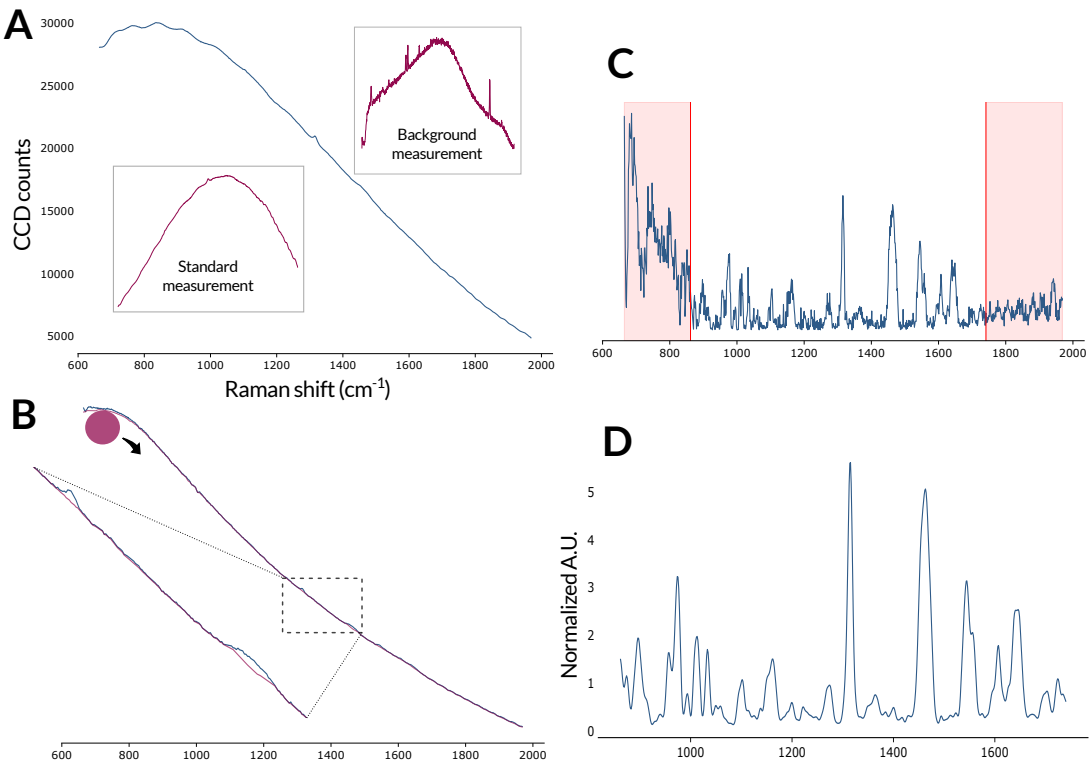

Figure 1.3 – Spectral processing of raw Raman signal in biological tissue. A.) Raw Raman measurement (blue). During the acquisition, a background measurement is also recorded with the laser turned off to correct for ambient light. After each experiment, an acquisition on a Raman Standard with known Raman response is used to correct for artefacts from the acquisition system. B.) Baseline correction. A curve fitting algorithm (pictured here: Rolling Ball algorithm) is used to estimate the shape of the baseline signal, which mainly consists in tissue auto-fluorescence. This baseline curve is then subtracted from the acquired signal. C.) Truncation to desired spectral range. Spectral regions with poor Raman information or exhibiting artefacts from the experimental design (e.g. silicate substrate) or correction algorithm are removed. D: Smoothing and Normalization. High-frequency noise is removed from the signal and the spectra are expressed in normalized units so that they can be compared across samples and experiments. A.U.: Arbitrary units.

comprehension of the underlying phenomenon [256].

1.5.2 Data analysis methods

There is no single accepted methodology for analyzing and interpreting a processed Raman spectrum. While Raman spectroscopy has historically relied on the visual assessment of the Raman spectra, the complexity of the signal acquired in living tissue has made necessary the reliance on automated algorithms [257]. We discuss three tasks that encompass most clinical application of Raman spectroscopy for neurosurgery: supervised machine learning, Raman imaging, and chemometric analysis.

1.5.2.1 Supervised machine learning

The most common application of analytical methods in neurosurgical Raman spectroscopy is to train an algorithm to recognize tissue phenotype from its Raman signature. This type of machine learning is referred to as supervised learning: a data matrix $\mathbf{X}_{n\times p}$ containing n Raman spectra represented each by p variables or features (e.g. the light intensity value for each wavenumber) is associated with a vector of labels $\boldsymbol{y}$ (e.g. the tissue diagnosis as emitted by the neuropathologist) (Figure 1.4A). The task consists in training an algorithm or function f for which $f(\mathbf{X}) = \hat{\boldsymbol{y}}$ such that the loss function $L(\boldsymbol{y}, \hat{\boldsymbol{y}})$ is minimized. The result of the loss function is called the training error. In surgical applications, however, we are truly interested in estimating the error resulting on prediction on new data not used for training: the testing error. The most popular algorithms used for this purpose are described next and in table 1.3.

Feature Engineering Machine learning algorithms rely heavily on the way they are presented the data matrix $\mathbf{X}$ [258]–[260]. Feature engineering consists in transforming the processed signal into a set of variables that will be used as representation for the learning task. Feature engineering ranges from selecting a subset of all available wavenumbers, to generating new variables and performing complex mathematical transformation of the data to unveil hidden properties not conveyed by the original spectrum. This is crucial in Raman spectroscopy because of two properties inherent to spectroscopic data: high-dimensionality and sparsity of the feature space. The concept of high dimensionality refers to the large number of available features (between 500 to 1,000 spectral bands) needed to describe a single observation. Feature sparsity means that most of this information will be unhelpful in discriminating different tissue phenotypes, both because all tissues are composed in majority of the same organic molecular compounds and because a lot of the molecular markers are redundant across the spectral range.

By far the most common feature engineering algorithm in neurosurgical Raman literature is Principal Component Analysis (PCA) [174], [194], [196], [250], [261]–[270]. PCA iteratively finds the orthogonal vectors (or Principal Components [PC]) that maximize the variance in the dataset (the eigenvectors of the covariance matrix), and then stores the projection of the data point upon each PC (Figure 1.4B). The PCs are ranked by their eigenvalues, or amount of variance explained, such that most of the variance in the dataset can be expressed in the first PCs. The other PCs can be discarded, resulting in a representation of the data with a reduced dimensionality. The number of retained PC ranged between 2–40; this number is chosen either based on pre-defined criteria such as amount of explained variance [174], [194], [264]–[267], [269], [270], or determined post-hoc, selecting the PCs that could better differentiate the different tissue types [196], [261]–[263]. The popularity of PCA in Raman spectroscopy can be attributed to its unsupervised nature: as it is agnostic to labels, it is considered unbiased [271]. It is also very effective at reducing the dimensionality of the data: most authors report that over 99% of the variance of their dataset is expressed in the firsts 2–40 PCs [174], [194], [264]–[267], [269], [270]. Moreover, the orthogonality of the extracted features can improve the efficiency of classical multivariate linear models [272].

Another common feature engineering technique involves selecting a small subset of the best features and discarding all others. These features can be identified by: 1) simultaneously assessing their individual correlation with the outcomes (called filter methods)[273]–[276], 2) iteratively evaluating changes in machine learning performances when excluding/including each features into the model (wrapper methods) [277], or 3) adding penalization terms to the optimization of the training algorithm so that some of the features' contribution are reduced to zero (embedded methods) [278]. In neurosurgical Raman literature, only the first type of feature selection has been used [279], [280]. Otherwise, some authors chose to select the features by-hand [281]–[283], or perform feature selection on previously extracted features, as part of a two-step feature engineering pipeline [261]–[263], [267], [283] (Figure 1.4B). Performance-based and optimization-embedded are more recent feature selection techniques that have yet to be adopted by Raman spectroscopists studying brain tissue. Nevertheless, they have been successfully applied in other data-driven domains, where they have proven superior to filter methods in recovering truly important features in sparse, high-dimensional dataset [284], [285]. While recent

research in proteomics and genomics focus on developing computational strategies to fully take advantage of these methods [286], [287], they are yet to be adopted by Raman spectroscopists in biomedicine.

Another feature engineering strategy involves the generation of new features, motivated by the idea that the Raman spectrum is an incomplete representation of the data for machine learning purposes. A widely used example of feature creation example to calculate the ratio between the height of two pre-defined Raman peaks, most often to summarize the lipid-to-protein content of a sample. Multiple peaks have been used and proved useful for tissue discrimination, especially to differentiate between white and grey matter—they are discussed in more details in the Chemometric analysis section. Some of these peak ratios were also used to separate malignant and normal tissue.More recent feature extraction strategies focus on the shape of the Raman signal as a marker of malignancy in brain samples[283]. In their study, Stables et al. selected eight target bands, for each of which they calculated the centroid (weighted mean of the signal in the defined region), skew (asymmetry of the intensity values) and kurtosis (prominence of certain intensity values from the rest of the bands). This way, a sequence of 10-30 contiguous variables can be represented by two or three features or parameters, resulting enhanced machine learning performances (Figure 1.4B). While this approach to feature extraction is extensively used in Raman literature [288], it is rarely use in neurosurgery-related research [271], [289]. Opponents of band fitting of biological Raman spectra argue that the selection of target bands cannot be reliable in the case of low SNR signal exhibiting a high number of potential peaks, and that our knowledge of Raman generating processes in tissue is not strong enough to limit our analysis to a few critical bands [271], [289]. As experience starts to converge towards the "true" Raman spectrum of the brain, we might see more authors incorporating band-fitting routines to the analytical pipeline, as it is an effective way to summarize the vibrational profile of a tissue in a meaningful manner, while allowing for easy statistical manipulation and even further feature engineering.

Classification After feature engineering comes the selection, training and evaluation of the machine learning algorithm. These algorithms take as input the variables selected or created during the feature engineering and map their values to the label associated with the sample (Figure 1.4D-E). The most popular of such algorithms is Linear Discriminant Analysis (LDA). LDA assumes that all observations with the same label originate from multivariate normal distributions with equal covariance and assigns new observations to the label with highest likelihood. Because it is vulnerable to highly correlated features, LDA is often preceded by PCA. However successful, LDA relies on a set of assumptions that are not respected by Raman data: multivariate normality of the distributions, independence of the predictors, homoscedasticity (homogeneity of covariance across labels) and few outliers [290]. Furthermore, because of the low SNR characteristic of biological acquisition, researchers need algorithms that are robust, i.e. are not sensitive to small changes in the data. The complexity of biological Raman data and easy access to machine learning libraries have motivated the reliance on more flexible models for this problem.

A popular example of such robust model is the Support Vector Machine (SVM) [291]. SVM finds the hyperplane that optimizes the distance between it and the closest point of each class it tries to separate. By using kernels, an SVM can adapt to a non-linear feature space with minimal computational cost. Despite its capacity to adapt to non-linear functions and relatively good performances in ex vivo studies, SVM is theoretically not the ideal solution for hierarchical data structures that is characteristic of biological Raman signal [292]. Recently, other types of models are being explored in order to stabilize the predictive performances of the machine learning, especially in anticipation of the translation to clinical practice. Decision trees are non-parametric models where each internal node represents a decision function based on an input variable. While considered a weak and highly unstable classifier, ensemble methods such as bagging and boosting which work by aggregating multiple weak classifier trained on different subset of the data can significantly improve the performances of decision trees and make them interesting candidates for real time classification [293]. Some authors have used boosted decision trees with success to classify between normal tissue and glioma, without using any prior feature engineering [133], [179]. Artificial neural networks (ANN) have receive most attention in the machine learning research over the last years due to their potentially deep structure and ability to adapt to virtually any possible function

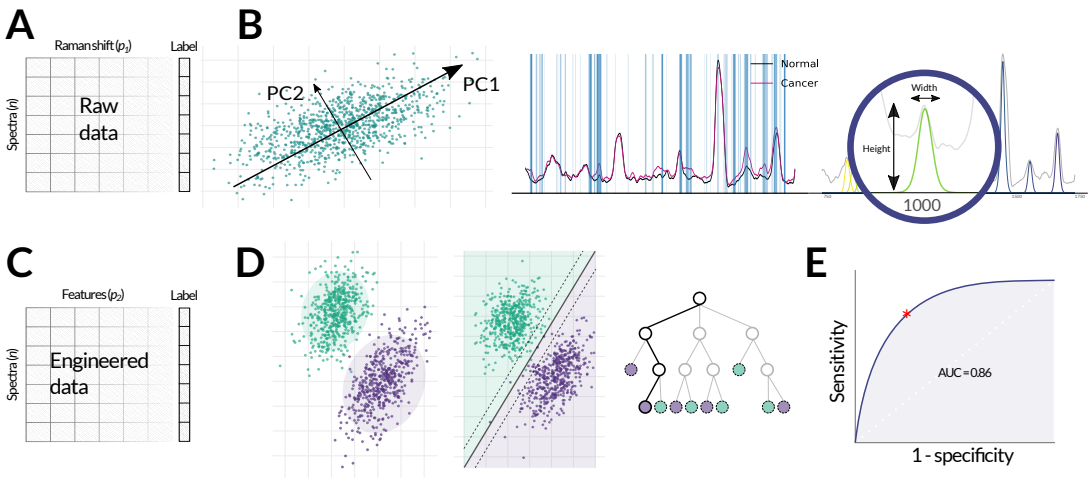

Figure 1.4 – Machine learning for Raman spectroscopy. A.) The initial data matrix is composed of n spectra and p_1 variables, where each variable represents an intensity at a particular wavelength. A standard, processed Raman spectrum can contain between 500 and 1000 variables. Each spectrum is associated with a label (e.g. *High-grade glioma* vs. *normal tissue*. B.) Feature engineering algorithms. These algorithms are designed to change the representation of the initial spectra matrix into one that will enhance performances of the machine learning predictions. From left to right: PCA, feature filtering and feature extraction (peak fitting). Each method is described in the main text. C.) The engineered data matrix. Each spectra now contain p_2 variables, which are the results of the previously applied feature engineering methods. These variables could be PC scores, intensity at specific Raman shifts, peak-fitted peak height, etc. D.) Supervised learning algorithms. Different mathematical function can be trained to separate the spectra with distinct labels based on the values of their variables. From left to right: LDA, SVM and Decision tree. E: Testing of the machine learning model. The different machine learning pipelines (including feature engineering) are trained on a subset of the data and tested on an independent subset. The prediction of the models are compared to the true labels of the testing set, and prediction performance is evaluated. A ROC curve can be drawn to estimate the performance of the prediction at varying levels of sensitivity and specificity. The best performing threshold is the point on the curve closest to the left upper corner (red star). PC: Principal Component, PCA: Principal Component Analysis, AUC: Area-under-the-curve.

[294]. In neurosurgical application, Jermyn et al. showed how that an ANN model could reduce interference with surgical ambient light, while performance of other models in such conditions was strongly affected [177]. Deep neural architectures such as Convolutional Neural Networks (CNN) have shown great promises in bio-spectroscopy, with the additional benefit of being less dependent on spectral pre-processing [295]–[301]. Data requirements to train and optimize such models are high because of the millions of parameters they contain [302]–[304]; nevertheless, open access to large Raman datasets and strategies such as transfer learning and data augmentation will make their adoption possible for biomedical application in a close future [305].

Table 1.3 – Feature engineering and supervised machine learning algorithms for classification of Raman spectroscopy in brain tissue

Task	Technique	Description	Pros	Cons
Feature Engineering	Principal component analysis	Unsupervised algorithm that extracts the projection of the data matrix onto a set of linearly uncorrelated Principal components	Agnostic to tissue classes (unbiased) Effective feature reduction Fast	Expert intervention is impossible
	Feature extraction	Generate new variables from the spectra (e.g. band-fitting) or by transformation of already available variables (e.g. peak ratios)	Increase information content of the data Account for interactions Better models molecular processes	Requires expert knowledge Time and effort-intensive Requires high data quality
	Feature selection	Identification of the variables which show highest correlation with class (filter method). Can be performed as a second feature-engineering step, after PCA or feature extraction	Simple Task-specific	Biased Prone to false positives
Supervised Learning	Linear discriminant analysis	Estimates a set of multivariate normal distributions that better explain the data and assigns new observations to the class with highest likelihood	Simple Fast Low data requirements	Assume normality of distribution Assume homoscedasticity Requires independent variables
	Support vector machine	Finds a hyperplane that maximizes the margin between the support vectors, i.e. the observations of each class closest to the hyperplane.	Adaptable to non-linear feature spaces Fast Easily implemented	Unable to model hierarchical feature spaces
	Decision trees	Non-parametric model that assigns a decision function to each variable. Decision trees can be aggregated to increase stability by averaging (Boosted trees) or training over many subsamples (Random Forests)	Intuitive Able to model hierarchical structures	Unstable by itself Aggregation is time consuming
	Artificial neural networks	Connectionist model that considers each variable as an input neuron, which are subsequently connected to a definite number of hidden layers through an activation function eventually reaching an output layer which generates the class prediction. ANN with more than one hidden layer is called a Deep Neural Network.	Adapts to any non-linear function Highly customizable High performances	High data requirements Complex Computanionnaly intensive

Descritpive comparison of different approaches to supervised machine learning applied to Raman spectroscopy in neurosurgery

1.5.2.2 Single-band to Hyperspectral Imaging

By acquiring Raman measurement at regular interval over a sample, it is possible to rasterize these acquisitions to create a Raman image, where each pixel is a Raman spectrum. Raman imaging can resolve several limitations of point-probes systems as they do not integrate over the heterogeneity of a sample and can work across scales, from microscopic imaging to "wide-field", macroscopic imaging. As a pixel can only be represented by a single value, the analytic challenge remains to reduce a Raman spectrum into a single number.

The approach to create Raman images depends on the technique used. In CARS systems, signal at a single Raman band is acquired, and no post-processing of the signal is required [200], [306]–[309]. The image contrast is therefore specific to the molecular assignment of the interrogated Raman shift—most commonly, the CH2 symmetric stretching mode of lipids around 2845 cm^{-1}. With SRS, two Raman frequencies are acquired and compared: 2845 cm^{-1} band, and the 2930 cm^{-1} protein-specific band [165], [166], [208]. Therefore, the relative concentration of proteins-to-lipids serves as contrast in the image—in other words, the amount of lipids is corrected for the protein content of each pixel.

More complex Raman data requires sophisticated tools to generate images. With Spontaneous Raman devices, a complete spectrum is acquired for each pixel. The contrast in these hyperspectral images can be tuned to varying molecular significances depending on the way the spectra are processed and analyzed. Machine learning can be harnessed to generate images from Spontaneous Raman data. Unsupervised learning is a family of machine learning algorithms that does not rely on the pre-labeling of each observation; instead, they serve to unveil hidden patterns in the data. Such an example of unsupervised learning is clustering: the dataset is divided in several groups—or clusters—where the similarities between spectra in a cluster is maximized compared to the dissimilarities with spectra from other clusters. This method has the advantage of accounting for the entire spectral information available and not just one or two definite bands. Early adopters of this technique were Koljenovic et al., who used PCA and clustering to assign each pixel to one of 70–72 distinct clusters [267]. A supervised model was then trained to map a cluster to either necrotic or vital tissue, on which the final contrast of the images was based. Other authors have used clustering, with or without prior engineering, to assign each pixel to a specific cluster and generate the contrast [266], [310], [311] (Figure 1.5A).

The downside of clustering-based imaging is that there exist no organization between the finite unordered clusters, making the interpretation of contrast challenging and somewhat arbitrary when there are more than two clusters. Other approaches were used to overcome this limitation and create images more amenable to visual interpretation. Because Spontaneous Raman signal is a linear combination of the individual Raman signals of every molecular compound in a tissue, recent research has been geared towards recovering the elements of this linear combination to quantify the relative quantity of important molecules from the tissue Raman spectra. This approach has been referred to as hyperspectral unmixing. The different methods for linear unmixing are based on three elements: the selection of the basic, reference substances or endmembers, their spectral signature and their relative abundance. In brain tissue, Vertex Component Analysis (VCA) and N-FINDR are two such algorithms. Both are unsupervised, and mostly differ in their definition of endmember spectra: in N-FINDR, reference spectra from 'pure' molecular substances are set by the user, and endmembers are set as the spectra with highest correlation to those reference substances, whereas with VCA, the endmembers spectral signatures are mathematically identified based on the variations in the dataset. Importantly, both methods assume that signal from pure substances are present in the data, and that the molecular compounds are independent [312], [313].

Applied to brain tissue, VCA and NFINDR were used to create pseudo-color images with RGB channels, each channel representing the relative abundance of one of three endmembers [250] (Figure 1.5C). The number of distinct channels used to create images varied from 3 to 9 in some studies, with higher number yielding images able to discriminate between more different molecular components [193], [194] (Figure 1.5B). This method is promis-

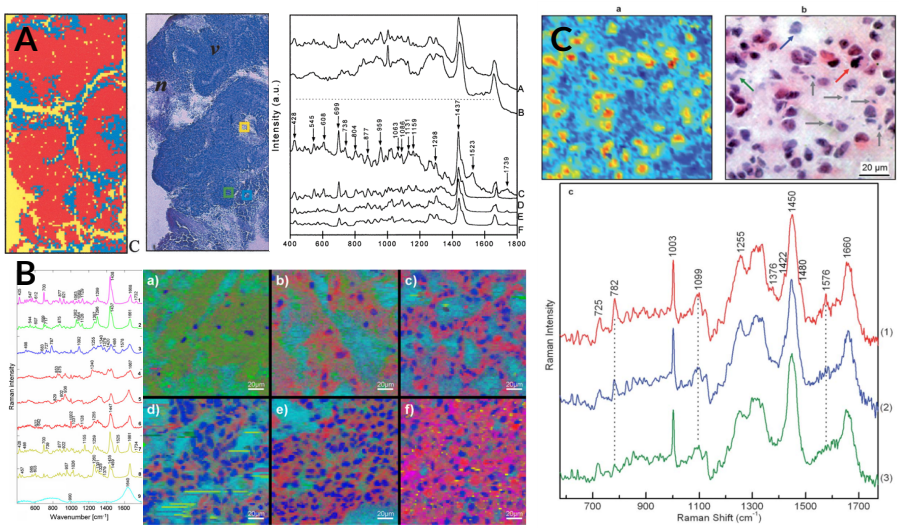

Figure 1.5 – Spectral unmixing and clustering-based approaches to Raman imaging, where every pixel consists in an entire processed Raman spectrum. A.) Machine learning-based approach. A supervised machine learning model was used to assign each spectrum acquired in glioblastoma tissue to one of two classes: vital tissue and necrotic [267]. Left: the Raman image, color-coded with the predicted class for each pixel (red: vital, blue: necrotic, yellow: background). Center: H&E image of the sample (*v*: vital,textitn: necrotic). Right: The averaged spectra of the Necrotic (A) and vital (B) samples, with the difference spectrum (C) compared to cholesterol (D), cholesterol oleate (E) and cholesterol linoleate (F). B.) Endmember-based approach. The N-FINDR unmixing algorithm was used to identify a prespecified number of endmember spectra form a dataset acquired in glioma tissue [194]. Each spectrum in the dataset is then expressed as a linear combination of these endmembers. The endmembers were assigned to cholesterol ester (1, magenta), phopsholipids (2, green), DNA (3, blue), proteins (4–6, red), beta-carotene (7, yellow), unsatturated fatty acids (8, yellow) and phophate buffer solution (9, cyan). Each pixel in the Raman image is then colored on the basis of the relative abundance of each endmember in its spectrum. C.) Endmember-based approach. VCA was used to find three endmember spectra in a dataset acquired in glioblastoma samples [250]. Each endmember was assigned to a RGB channel (spectra 1, 2, and 3). The relative abundance of each endmember in every pixel is used to color-code the Raman image (a). The H&E image (b) is provided as a comparison. VCA: Vertex Component Analysis.

ing because it can quantitatively represent signal from meaningful molecular species, bridging a gap between Raman signal and tissue metabolism and morphology in a quantifiable way. With this approach, researchers were able to generate metrics such as nucleic acid content, lipid content and lipid-to-protein ratio which correlated with malignancy in astrocytoma samples [194]. An issue with the spectral unmixing of Raman pixels is the difficulty in assessing the reliability and variance in both the endmembers definition and the relative abundance estimation. While spectral unmixing has the advantage of harnessing information from the entirety of the Raman spectral range, more recent work settled for extraction of specific, pre-defined spectral features such as band ratios and single-band intensities to represent independent molecular information [195], [314]. This simplified approach to Raman imaging still demonstrated a 90% pixel-to-pixel classification accuracy between white matter, grey matter and pathological brain tissue (glioblastoma, necrosis or infiltrating cancer) [195].

Not only these Raman images could help pathologists visualize molecular information not present in H&E stained samples, they could also be amenable to machine learning classification algorithms. This would considerably reduce time-to-diagnosis during neurosurgeries, where the aggressiveness of the resection can be dictated by a preliminary diagnosis provided by a neuropathologist from a frozen tissue sample. However, the improved diagnostic rates from Raman images is an assumption that is yet to be demonstrated. Also, the choice of colors for each channel is somewhat arbitrary, while it is known that the color shading can drastically affect images and their interpretation [315].

1.5.2.3 Chemometric analysis

Chemometric analysis refers here to the interpretation of the Raman spectra in order to quantify the biochemical content of a sample. In a static system composed of a single molecular compound acquired in perfect experimental conditions, the Raman features of the distinct vibrational modes are directly observable, and subtleties such as a slight peak shift or peak widening can be used to derive changes in the system [316]. However, Raman signal from biological tissue is much more complex and convoluted: thousands of molecular components interacting together form a heterogeneous and dynamic biochemical landscape [295], [317]. Computational strategies are therefore needed to deconstruct the Raman spectra originating from those samples.

As presented in the previous section, one approach to interpret brain Raman signal is to estimate the relative contribution of different "pure" endmembers to the total Raman signature of the tissue by linear unmixing of the spectra. Using VCA or NFINDR algorithms, authors that have used this approach concluded that cholesterol esters, nucleic acids, collagen and carotene contribution were higher in high-grade tumor while general lipid content and both lipid-to-protein and lipid-to-DNA ratios were decreased in malignant tissue [193]–[195], [314]. However, the reliability and consistency of this approach in unveiling the relative quantity of the molecular compound in the interrogated sample is has not been thoroughly validated. It does rely on two important assumption that may not hold true in biomedical applications: 1) the dataset of Raman spectra contains signal from pure molecular endmembers, and 2) the quantity of each molecular endmembers is independent of the others [312], [313].

A more widespread approach remains the comparison of specific spectral features (e.g. peak heights, band intensities, band-to-band ratios) between the averaged spectra of each tissue phenotypes (Figure 1.6A). These bands are either recovered from the difference spectra between two tissue phenotypes, or by analyzing the relative importance of each Raman bands after applying PCA.

In brain tissue, Raman signal originates predominantly from nucleic acids (782, 829 and 1339 cm^{-1}), lipids (1063, 1086, 1131, 1268, 1300, 1441, 1659, 1670 and 1739 cm^{-1}), Amide I (1659 cm^{-1}) and III (1268 and 1300 cm^{-1}), and amino acids such as tyrosine and proline (829, 852 and 877 cm^{-1}), tryptophan (877 cm^{-1}) and phenylalanine (1004 and 1032 cm^{-1}). For the high wavenumber region, the CH-stretching of lipids (2845—2885 cm^{-1}) and proteins (2930 cm^{-1}) are the predominant molecular markers. Because its high cell-density and the abundance

of myelin, lipids are human brain tissue's main constituents [318], [319]. The CH_2–CH_3 deformation at 1441 cm^{-1} often dominates the signal. The signal from amide bands is also important, but strongly overlap with lipid bands [243], [261], [265]. Markers of glioma include the phenylalanine band at 1004 cm^{-1},the nucleic acids/ CH_2–CH_3 / Amide III band at 1339 cm^{-1} and the carotenoid bands at 1159 and 1523 cm^{-1} [195], [243], [261], [265], [267], [279], [282], [310], [319]. For other bands, studies show conflicting associations. In some cases, nucleic acids signal is strongest in tumor and necrotic tissue, while other demonstrate a decrease in malignant regions. The disagreements on how Raman signal changes as a result of pathological states stem from the multiple differences in experimental design from one study to the other (e.g. which types of tissue are compared, spatial resolution of the systems, tissue processing before Raman acquisition, analytical methods used to process and compare the Raman signals), along with low sample sizes (most often less than 10 patients) [320].

As mentioned earlier, peak ratios are also considered to effectively summarize the lipid-to-protein content of a sample, with good discriminating power between white and grey matter, and normal brain and cancer. In most studies, involved bands included the 1442:1662 cm^{-1} (or 1441:1659 cm^{-1}) peaks [195], [321], [322], 1299:1439 cm^{-1} peaks [265], the 1266:1300 cm^{-1} peaks [323] and the 2930:2845 cm^{-1} peaks [136], [165]. Although simple and easily interpretable, these methods of spectral interpretation are limited by their inability to model complex interactions between the molecular species present in the living tissues.

Peak ratios can also effectively summarize the lipid-to-protein content of a sample, with good discriminating power between white and grey matter, and normal brain and cancer. In most studies, involved bands included the 1442:1662 cm^{-1} (or 1441:1659 cm^{-1}) peaks [195], [321], [322], 1299:1439 cm^{-1} peaks [265], the 1266:1300 cm^{-1} peaks [323] and the 2930:2845 cm^{-1} peaks [136], [165]. Although simple and easily interpretable, these methods of spectral interpretation are limited by their inability to model complex interactions between the molecular species present in the living tissues.

In reaction to this limitation, new approaches to interpretation of biological Raman data have emerged that embrace the complex structure of the data-generating process and integrate into their model the uncertainties around the Raman signal and sample diagnosis. In Stables et al., the authors selected spectral region with high discriminating yield between glioma and normal brain samples [283]. They extracted three markers of Raman intensity distribution in these regions: the centroid (weighted mean), skew (asymmetry), and kurtosis (central peak prominence). Therefore, instead of extracting signal intensity at a single band, they extracted spectral shape in an entire region of interest, which carries more biochemical significance and stability then signal at a single Raman shift (Figure 1.6B). Moreover, the authors incorporated the ratio between every pair of extracted features as an additional feature ensemble, expanding the idea of interactivity between spectral information to all available variables. Their results demonstrated that the 691–771 cm^{-1} spectral region associated with phospholipids and amino acids had the highest discriminatory power, followed closely by the 637–683 cm^{-1}(nucleic acids and amino acids) and 1073–1114 cm^{-1}(nucleic acids and phospholipids). However, their samples were Formalin Fixed Paraffin Processed (FFPP) and Raman signal was altered to remove the paraffin-associated bands, which could explain some discrepancies between their findings and findings from fresh or frozen tissue. Nevertheless, this work was the first to incorporate systematic interactions between spectral feature as a potential discriminator between tissue classes, a first step in bridging the gap between classical Raman analysis and more complex computational pipelines used in other data-driven technologies such a s neuroscience, genomics and proteomics. Such examples include graph-network representations as a tool to gain insight into the data's hidden structure, Bayesian statistics to model uncertainty in data acquisition and interpretation, and deep neural architecture to capture the complex hierarchy of the data-generating processes. Applied to Raman spectroscopy, these emerging techniques will likely expand the yield and depth of this technology and offer a richer information to clinicians.

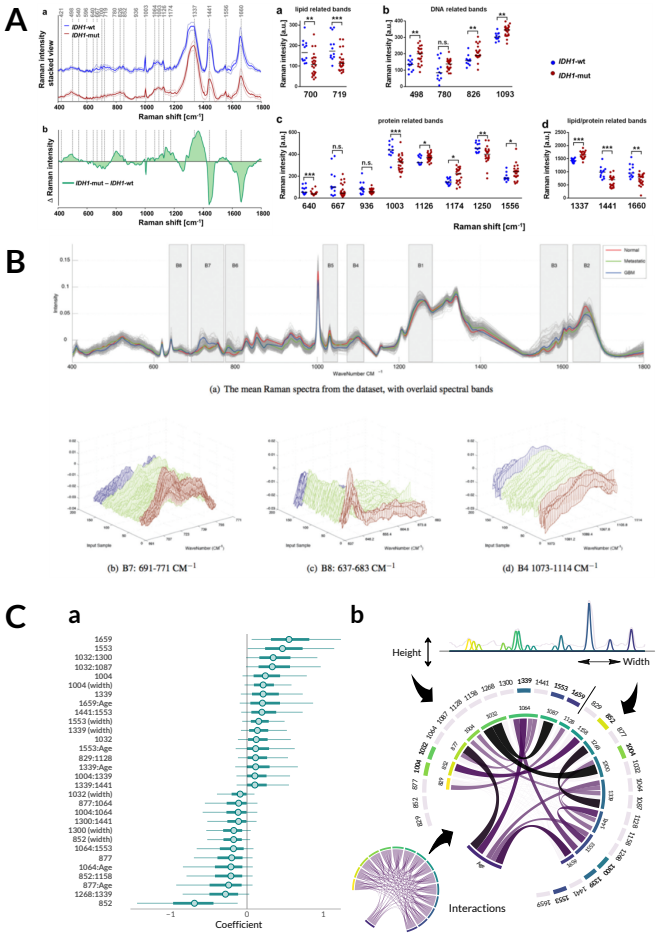

Figure 1.6 – Chemometrics analysis of Raman data. A.) Comparison of IDH mutation status in samples of human glioma [281]. Left: the difference spectrum (green) between IDH-wt (blue) and IDH-mut (red) averaged spectrum is used to identify important Raman markers. Right: univariate analysis of the distribution of Raman intensity values at different Raman shifts. B.) Spectral shape analysis of normal brain, glioma and metastatic human samples [283]. The target regions are selected (a). For each regions, parameters describing the shape of the distribution of Raman intensities inside the regions are extracted and compared between the three classes (red: normal, green: metastatic, blue: glioma). C.) Analysis of importance of spectral markers between high-density and low-density/normal brain samples from *in vivo* human brain tissue. Left: the coefficients of a multivariate linear model are plotted. Features with a positive coefficient value are more prominent in samples with high-cancer density, while negative values are associated with low or absent cancer density. Right: Visual representation of the spectral markers (peak height, peak width, peak-to-peak and peak-to-patient-age interactions).

1.6 Going beyond the current surgical workflow

1.6.1 Integrating optical information in Neuronavigation systems

In neurosurgery, optical measurement registration will be a critical aspect in the successful integration of Raman into the treatment protocol.

Neuronavigation with infrared trackers and registration to preoperative MRI is widely adopted by neuro-oncological surgeon. Registration of the Raman measurement to MRI images is an important aspect of future developments in intraoperative vibrational spectroscopy because of the possible integration of MR imaging markers (such as distance to contrast-enhancement, T2- or T1-weighted intensity, apparent diffusion coefficient) to the Raman-based markers and create a multi-modal navigating environment for the operating team, in addition to increasing the clinically-relevant information content during the labeling phase of the Raman experiments. Spectroscopic measurements are meant as an adjunct to a panoply of factors that influence the extent of resection and minimize damage to normal brain; therefore, they should seamlessly integrate with the other available modalities.

In functional neurosurgery the challenge is different, and while similar to biopsy guidance, more difficult due to the small target areas. To illustrate: as the probe is descended along a planned trajectory in the case of DBS, the position of the optical measurement must first be used to update the pre-operative imaging such as to account for any head-frame movement or brain shift[66]. Both of these steps would require electronic drive tools to perform the physical descent such as to automatically correspond probe depth with the optical measurement. While these electronic drive systems do exist for DBS surgery, manual drive screws are often used in lieu, as they are faster. Since the information would ideally be merged into the current technologies that surgeons use, partnerships with commercial providers for stereotactic planning (Medtronic, Boston Scientific, Abbot) would make the implementation in the OR much easier.

1.6.2 Neurosurgery: Outlook

At the present point in time, we are nearing a clinical revolution wherein pathology maybe no longer need to be confirmed visually by a trained clinician. We are seeing examples of this in the ocular industry where AI systems are beginning to get FDA approval to diagnose ocular pathologies[324]. While these systems still remain tools for the physician to aid in locating abnormalities, this may not be the case forever.

In the case of neuropathology, the diagnosis could soon be provided intraoperatively, greatly decreasing traditional diagnostic turn around. With this revolution, new commercial avenues will be opened up and optical modalities will compete to provide the most advantage to the surgeon. Raman's edge in this respect is the amount of information it can provide. The fingerprint type spectra, which can in its current state quantify molecular ratios and discriminate tissue types, is only beginning to be used regularly in intact brain tissue. As data is accumulated and sophosticated data science systems evolve for this application, a whole new Ramanomics field could emerge[325]. To this end, data sharing will becoming imperative. Properly labelled, raw Raman spectra databases are extremely scarce in comparison to other fields and this is something that must change if the applied data science is to advance at a similar rate as other "omic" fields.

While H&E stained slices are used as "gold-standard" for labeling of Raman data, most recent guidelines on primary brain cancer classification are based on various other tissue markers such as IDH mutation status, which has proven a unique and critical factor in establishing a progonsis orienting treatment for glioma patients. Going beyond H&E staining and understanding how Raman signal changes as a function of these new biomarkers will be an important challenge of future Raman studies that aim to translate vibrational spectroscopy as a clinically-valid decision making tool.

The display of information is also an integral discussion point. In the case of Raman spectra, the optical information is much less important to the surgeon than what the optical information means. In the case of tissue discrimination using a point probe, a simple formulated label may suffice along with a metric for certainty. In the case of histology, SRH does a great job of displaying information in a way that the pathologist is used to seeing it[171]. While the information may evolve to provide more than classical H&E staining, this step was absolutely mandatory for clinicians to agree and understand the new technology[326]. In the case of functional surgery guidance, most likely the live calculated position of the electrode overlayed on the pre-operative MRI would likely be the ultimate goal.

1.6.3 Neurology: Outlook

The information that is acquired with Raman spectroscopy is complicated and difficult to interpret in nature. Because of this, it requires both thorough fundamental and clinical research. In performing the fundamental research, we are just beginning to see the applications of Raman in neuroscience and neurology. From recent clinical work, we can start to understand the possible treatment improvements Raman can offer in neurosurgery.

From the neuroscience field, there are many exciting works showing the capability of Raman to image or sense disease biomarkers such as prion proteins, amyloid beta plaques (Alzheimer's), alpha synuclein (PD), and even in neurotransmitter detection which can be deficient in many neurological and psychiatric disorders[164], [327], [328].

In the future of Raman guidance for functional neurosurgeries, we could imagine the ability to measure the amount of a certain neurotransmitter or protein and therefor the state of the disease, to help guide treatment parameters. For instance in PD, there is a loss of dopaminergic neurons in the substantia nigra which also results in a decrease in neuromelanin[329]. If Raman is used to guide DBS surgery in the future, it could also be used to measure either dopamine or neuromelanin concentrations to give information about the type and stage of the disease[330].

Aging, more specifically brain-age, is another interesting topic for Raman spectroscopy in neurosurgery. Considerable research has gone into using MRIs to show the relation between structural changes and aging thanks to its non-invasive large-volume imaging[331], [332]. From this standpoint, Raman could be useful to complement and understand these observed trends especially in the case of region-specific lipid changes associated with brain aging[333]. Furthermore, as there is likely an age dependant change in Raman signatures, this type of data will be critical in age-matching Raman measurements to make them even more accurate for discrimination.

In a more futuristic sense, if the evergrowing field of optogenetics are ever applied to humans, this would imply the implantation of chronic fiber optics within a patient. If this was to come to fruition, the acquisition of over-time Raman measurements from within the brain is not impossible. However, this would either require considerable downsizing of equipment or an optical fiber port interface on the skin, so this remains unlikely for the near future.

Chapter 2

Intact primate brain tissue identification using a completely fibered coherent Raman spectroscopy system

Damon DePaoli[a,b], Nicolas Lapointe[c], Younes Messaddeq[b] Martin Parent[a], Daniel C. Côté[a,b]

[a]Université Laval, CERVO Brain Research Center, Neuroscience, 2325 Rue de l'Université, Quebec City, Quebec, Canada, G1V 0A6
[b] Université Laval, Center for optics, photonics and lasers (COPL), Physics Engineering, 2325 Rue de l'Université, Quebec City, Quebec, Canada, G1V 0A6

2.1 Résumé

Les sondes à fibre Raman cohérentes ne sont pas encore entrées dans la clinique malgré leur potentiel énorme en matière de détection et d'imagerie sans étiquette. Ceci est principalement dû aux systèmes laser volumineux traditionnels nécessaires à la création des impulsions lasers à haute puissance de crête nécessaires pour un Raman cohérent, ainsi qu'aux complications résultant de la propagation de ce type d'énergie à travers la silice. Spécifiquement, une sonde CARS pouvant sélectionner son volume d'intégration à haute résolution, loin de la pointe de la fibre, est particulièrement intéressant dans le cas d'une neurochirurgie d'implantation d'électrodes, où il est possible de placer des fibres optiques à bord de l'électrode chronique qui assurent un guidage optique lors de son implantation à travers la pointe semi-transparente. À cette fin clinique, nous avons créé un système CARS toutes fibres, constitué de petits lasers à fibres clés en main, accordables rapidement, capables de créer des spectres CARS à nombre d'onde élevé de l'ordre de la dizaine de millisecondes. L'utilisation des fibres de silice traditionnelles est rendue possible par l'utilisation des longues largeurs d'impulsion du laser (25 ps). La sonde elle-même a un diamètre extérieur de 250 um, ce qui lui permet de s'insérer dans des tubes métalliques disponibles sur le marché pouvant remplacer les stylets de stimulation cérébrale profonde. À l'aide

de ce système, nous avons identifié les types de tissus cérébraux dans le cerveau intact de primates et montré notre capacité à délimiter la matière blanche et grise à l'aide d'une résolution élevée. Ses avantages par rapport au Raman spontané proviennent de l'amélioration de la résolution spatiale de plusieurs ordres de grandeur, de son application clinique inhérente en imagerie 3D, ainsi que de sa capacité théorique à éliminer le signal Raman parasite des gaines de sonde, comme une électrode de stimulation cérébrale profonde. Le système devrait avoir des implications cliniques dans le guidage neurochirurgical ainsi que dans la détection des tissus malades.

2.2 Abstract

Coherent Raman fiber probes have not yet found their way into the clinic despite their immense potential for label-free sensing and imaging. This is mainly due to the traditional bulky laser systems required to create the high peak power laser pulses needed for coherent Raman, as well as the complications that arise from the propagation of this type of energy through silica. Specifically, a CARS probe that could select its integration volume at high resolution, away from the tip of the fiber, is particularly interesting in the case of electrode implantation neurosurgeries, where-in it is possible to place optical fibers on-board the chronic electrode and provide optical guidance during its implantation, through the semi-transparent tip. To this clinical end we have created an all fiber CARS system, consisting of small, rapidly-tunable, turn-key fiber-lasers, capable of creating high wavenumber CARS spectra on the order of tens-of-milliseconds. The use of traditional silica fibers is made possible by the use of the laser's long pulse-widths (25 ps). The probe itself has an outer diameter of 250 um allowing it to fit within commercially available metal tubes that can replace deep brain stimulation stylets. Using this system we identified brain tissue types in intact non-human primates brains and showed the ability to delineate white and grey matter with high resolution. Its advantages over spontaneous Raman stem from the orders of magnitude improvement in spatial resolution, its inherent translatability to 3D imaging, as well as the theoretical ability to remove parasitic Raman signal from probe encasements, such as a deep brain stimulation electrode. The system is planned to have clinical implications in neurosurgical guidance as well as diseased tissue detection.

2.3 Introduction

Coherent anti-Stokes Raman scattering (CARS) microscopy is a well established technique for studying biological systems in a label-free manner, at video-rate speeds[150], [156]. While spontaneous and coherent Raman microscopies both look at inelastic scattering from a sample, caused by inherent molecular vibrations, CARS has the advantage of a greater signal generation, intrinsic three-dimensional sectioning (due to its non-linear nature) and a blue-sifted signal, which allows easy removal of background fluorescent signals[105]. While CARS microscopy is a useful tool for probing single molecular vibrations present in a sample, the hyperspectral information routinely acquired in spontaneous Raman microscopy provides much more diagnostic information. To this end, much work has gone into further exploiting CARS to perform hyperspectral imaging. Although hyperspectral CARS imaging is slower than acquiring single bond contrast, it remains much faster than spontaneous Raman imaging. There are several strategies to perform hyperspectral CARS, namely, using broadband pulses[151], [167], spectrally focused broadband pulses[334], or by temporally encoding the signal by scanning either the pump or the stokes laser[160]. Broadband CARS (BCARS) creates an entire spectra simultaneously, but requires the use of a spectrometer to collect and spectrally decode the generated signal, decreasing its acquisition efficiency and speed in turbid media. Spectral focusing of broadband excitation pulses avoid the need for a spectrometer but rely on a mechanical delay line for vibrational tuning. Wavelength-swept systems allow the use of much more sensitive detectors and provide the ability to perform random access probing of any Raman line within the laser's tunable bandwidth, giving the potential to drastically decrease the acquisition time if the molecular vibrations of interest are known. Our group previously showed the viability of a novel laser system

using a master oscillator power amplifier pump laser synchronized with a rapidly tunable programmable laser (10 kHz wavelength step rate) to perform wavelength-swept CARS (WSCARS) imaging of biological tissues at much higher speeds than historically possible[160].

While coherent Raman (CR) such as CARS or Stimulated Raman Scattering (SRS) are the tools of choice for imaging, spontaneous Raman has dominated the domain of fiber delivered vibrational sensing, especially in the clinic. This is mainly due to the fact that coherent Raman techniques require high peak power pulses which produce non-linear effects in dispersive media, diminishing signal generation after a fiber optic. Furthermore, traditional laser systems required for CARS generating are large and designed to be placed on an optical table unmoved. Therefore, translating any of the CR techniques to a clinical fiber-based system requires careful considerations with regards to these non-linear effects, as well as the portability of the traditionally large lasers required for CR.

Many groups have provided insights into the creation of a fiber-based CARS endoscope for imaging. Légaré *et al.* provided the first work of its kind by raster-scan imaging of polystyrene beads in agarose using a 4mm focusing unit after a 1 m singlemode fiber, used for both light delivery and collection[216]. Balu *et al.* examined the non-linear effects that occur in laser delivery using singlemode silica fibers, photonic crystal fibers (PCF) and large-mode area (LMA) PCFs ($<$ 1 m fiber length). They found that the FWM in all fibers overpowered the CARS generation in the sample. Using a filter after the delivery fiber, another multimode fiber (1 m) for signal collection and a scanning microscope, they succeeded in imaging biological tissue[217]. Brustlein *et al.* showed efficient pulse delivery and coherent Raman signal collection from organic crystals using a single double-clad photonic crystal fiber in combination with a microscope after the fiber, to create an "endoscope-like" system with minimal FWM[220]. Saar *et al.* performed coherent Raman imaging using 1 m of polarization-maintaining singlemode silica fibers for pulse delivery in combination with their in-house scanning fiber endoscope (SFE) probe. However, the detection scheme in the backward direction was not ideal, using a 10 $mm \times 10$ mm photo-diode with a hole cut in the middle for probe insertion[222]. Deladurantaye *et al.* created a specially designed LMA, polarization maintaining, double clad, silica fiber with a micro-fabricated optical filter on the singlemode core of the fiber, to be used in combination with a SFE probe. Using a collimating and focusing objective after the SFE probe, they succeeded in acquiring images of polystyrene beads deposited on a mirror in the epi-direction. This paper provided valuable insight to the downfalls of micro-optical filters and double-clad fibers for single-fiber CARS generation and collection[218]. Recently, Lukic *et al.* performed fiber-based CARS imaging on human skin tissue using a 1 m, 10,000 core, coherent imaging fiber[335]. The probe design has the benefit of imaging with no moving parts; however, the acquisition time is long due to the multi-core fiber inducing substantial pulse deterioration[213]. Furthermore, the endoscope is 8 mm in diameter making it too large for any neurosurgical procedures [213]. Most recently, Lombardini *et al.* presented a multimodal non-linear endoscope using a Kagomé-lattice double-clad fiber and miniature objective and microsphere lenses [111]. This probe has the best performance to date in terms of resolution, acquisition time and signal to noise ratio (SNR), however, for use in deep brain surgery, the 4.2 mm outer diameter of the probe is still too large and the design is very complicated.

While these groups have all focused on coherent Raman imaging endoscopes, our goal is to create a smaller spectroscopic system for tissue identification and classification on-board the implantation of the chronic electrode during deep brain stimulation (DBS) neurosurgery for Parkinson's disease. Briefly, the surgery consists of a stimulating electrode being implanted with its contact terminals strategically placed deep within the brain in precise structures. The main target brain structure in DBS surgery for Parkinson's disease, the subthalamic nucleus (STN), is a cell rich region, surrounded by a thin ($<$ 1 mm) white matter fiber bundle called the Zona Incerta. The surgical accuracy of the DBS lead implantation in the dorsal region of the STN is the overall predictor of treatment outcome and therefore very high precision optical guidance would be required to improve the surgery. While we focus on STN targeted DBS, this relation between surgical outcome and surgical accuracy stands for all DBS procedures. Moreover, the need for better electrode placement is a universal desire in the neurosurgical community and electrode placement is a highly researched topic. For instance, When looking at only

unsuccessful DBS outcomes, Okun *et al.* found that of 40 patients with failed DBS treatment, 19 had misplaced leads [51]. Moreover, the repositioning of the misplaced implanted leads (some only moved on the order of 1 millimetre) rescue the treatment's efficacy with regards to the motor symptoms, quality of life, and global outcome scores [52]. Our planned technique to improve the guidance of this procedure is to replace the removable stylet which gives the electrode its rigidity during implantation, with another stylet housing fiber optics. This design limits the probe to a total outer diameter of roughly 300 um along the entire 29 cm electrode length and therefore makes imaging an unlikely solution.

Spontaneous Raman probes have been presented in the past for brain tissue identification, however, these probes were limited by their spatial resolution when trying to discriminate small brain structures [182], [336]. The need for the development for clinical CARS probes comes mainly from the substantial increase in resolution (over 2 orders of magnitude) compared with spontaneous Raman due to its non-linear signal generation. This increase in resolution not only allows for potential 3D imaging, but also for high resolution spectroscopy. As noted previously, this is imperative for DBS surgery, as high surgical precision better than 1 millimeter is critical. Furthermore, CARS has a much higher SNR in high molecular-concentration samples, such as lipid-rich myelinated axons in the brain. This advantage is amplified substantially when considering the spatial volume of acquisition of the two techniques. Fiber-based optical sectioning of spontaneous Raman is achievable, however, the signal will be extremely weak, not only due to the weaker signal generation, but also due to the required small collection-fiber core size needed for confocal detection. These facts along with the ability to generate CARS signal at a desired location away from the fiber tip makes CARS a high potential tool in DBS surgical guidance where-in optical fibers may be placed within implanted electrodes and sense through the semi-transparent plastic tips.

Our system is composed of an optimal arrangement for decreased non-linear effects and increased clinical translatability. First to reduce background four-wave mixing (FWM) within the fiber, WSCARS was chosen over BCARS for spectroscopy. By using this modality, we decrease the number of wavelengths present at any moment in the fiber, and consequently decrease the interference between them. To reduce pulse-deteriorating effects such as self-phase modulation (SPM), SRS and linear dispersion within the fiber, we used a laser system with relatively long (25 ps) pulse widths. Although this decreases our overall signal generation at the sample, it allows the use of commercially available, inexpensive silica fibers with clinically relevant fiber lengths (1 m$<$L$<$10 m). Lastly, our custom laser system is compact, turn-key and fiber terminated, dispesning from free-space optics between source and detection and making the entire arrangement completely portable and ready for the clinic.

This report shows the ability of our complete system to perform CARS spectroscopy in different brain tissue types and ultimately use that detection for high resolution white and grey matter delineation along probe trajectories in a sample of fixed primate cortex. We specifically show two probe-tip designs, one contact-based with no micro-optical components and one functionalized using a GRIN lens which adds no additional size to the probe and which produces a focal volume away from the fiber tip. The first design exhibits a very simple probe design that is not only interesting as it defies the theoretical need for high NA focusing units to generate the CARS signal, but also for clinical applications wherein a cheap disposable probe may be of interest. The second design is specifically interesting for DBS guidance wherein we aim to generate our CARS signal on the other side of a plastic electrode, a simple but imperative utility that cannot be achieved using spontaneous Raman. We hope that with future advancements of our system, this information can be used to inform the surgeon in real-time of the electrode's position in the brain during DBS neurosurgery based on the optical response along the trajectory.

2.4 Materials and Methods

2.4.1 Laser system

The laser system was a custom and compact master oscillator power amplifier (MOPA) pump laser at 792 nm synchronized with a rapidly tunable programmable laser (PL) from 1020 nm to 1044 nm (Genia Photonics, now Halifax Biomedical). These wavelength ranges were chosen to interrogate the high-wavenumber region of a Raman spectra (2800 cm^{-1} to 3050 cm^{-1}) using CARS. The two lasers have the desired pulsewidth of 25-ps and a 40MHz repetition rate. The electronics and inner workings of the laser are described in our earlier work[160]. The only differences in this newer system are the operating wavelength ranges, and the new version of the PL has a maximum 2 kHz wavelength step rate, to decrease jitter. This 2 KHz step rate corresponds to a shortest wavelength dwell time of 1 ms. Tuning of the laser could be performed in a random access manner using preset wavelengths, or in an ordered manner by choosing the desired spectral resolution. The highest spectral resolution that could be performed was using a step size of 0.2 nm.

2.4.2 Fiber optic delivery

To combine the two lasers, an in-house fiber coupler was fabricated. For pulse delivery an FC/APC terminated, 2 m, singlemode fiber was connected directly to the coupler (SM800 or 780HP, Thorlabs). Signal detection was collected and transported to the photon counter detector (H8259-02, Hamamatsu) using an adjacent 2 m multimode fiber (FG105UCA, Thorlabs). For the distal tip focusing probes, a spacer and various lengths of multimode GRIN fibers (GIF625, Thorlabs) spliced to the tip of the singlemode delivery fiber (see figure 2.1 PS)). We made many fibers with GRINs of varying focal lengths, and as expected, the closer the focus was to the fiber tip, and therefore the tighter the focal spot, the better the signal generation was. That said, even with focal points as far as 600um away from the fiber tip, GRIN terminated fibers could produce signal comparable to that created with the bare singlemode fiber. The results presented for the GRIN terminated probe has a focal distance of about 400 um. All the fibers used had an outer diameter of 125 um, giving the optical probe an outer diameter of 250 um and their graphical representation can be seen in figure 2.1. Data was acquired using a homemade system in MATLAB, which decoded the temporally encoded CARS signal from the photon counter (H8259-02, Hamamatsu) using timing outputs from the laser system and plotted the processed spectra in real-time.

Fiber length was an important constraint when designing the CARS probe due to two reasons: 1. Shorter pulsewidths and higher peak pulse powers cause faster pulse deterioration through increased FWM in the fiber, and 2. The dispersive nature of the fiber requires one to adjust the fiber lengths and delays to obtain overlapped pulses at the sample tip of the fiber and not the connector tip. Indeed, when the pulses overlap at the fiber connector side, the FWM from the fiber is very strong; however, if the pulses overlap at the sample side of the fiber, the FWM from the fiber is minimized. Due to our system's long pulse widths we were able to produce CARs spectra even after 10 m of delivery fiber, however, to adequately separate the pulse delay overlap from the fiber connector port and the fiber tip in the sample, at least 2 m of fiber was required. Shown in appendix 1, while the intensity of the FWM background from within the fiber varies greatly depending on which tip of the fiber the pulses overlap, the spectrum of the FWM background signal remains constant. The importance of the background FWM intensity as a function of delay overlap has been mentioned previously in several publications [217], [218], [337].

To decrease probe size even further and increase signal detection, we attempted to use an in-house fabricated double clad fiber. While the increased signal detection was substantial we also found a considerable increase in background which turned out to give a worse overall SNR. This was likely due to the internal reflection of the background CARS generation from within the fiber at the fiber tip.

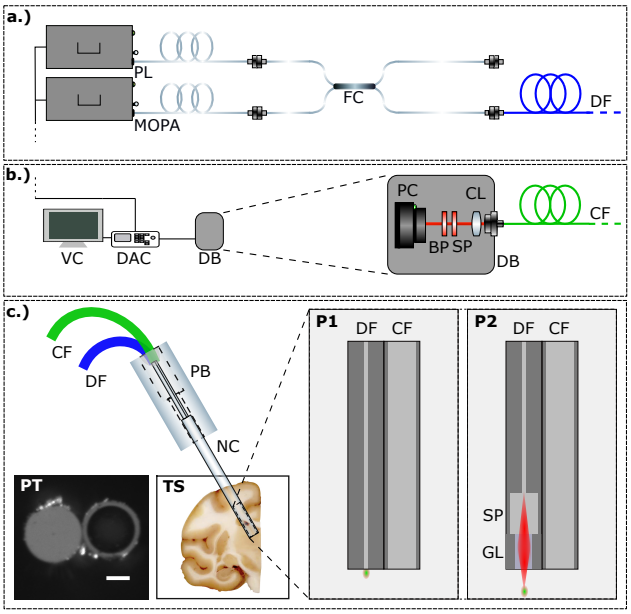

Figure 2.1 – Optical system. **a.)** Laser delivery optical layout. Abbreviations: PL = Programmable fiber laser; MOPA = Master oscillator power amplifier fiber laser; FC = In-house fiber coupler; DF = Source delivery fiber. **b.)** Signal collection and detection scheme. Abbreviations: VC = Viewing computer; DAC = data acquisition card; CF = Collection Fiber; DB = Detection box; PC = Photon counter; BP = 641/75nm bandpass filter; SP = 750nm shortpass filter; CL = Collimating lens; CF = Collection fiber. **c.)** Optical probe schematics with insets of contact-based fiber-probe tip (PT) and a tissue sample used in the study (TS). P1 inset corresponds to the contact-based probe without micro-optical components and P2 inset corresponds to the GRIN terminated distal tip focusing probe . Abbreviations: CF = Collection fiber; DF = Source delivery fiber; PB = Probe base; NC = Needle Chamber; SP = Spacer; GL = Multimode GRIN fiber lens; P1 = Bare probe without micro-optical components. P2 = Distal-tip focusing probe with micro-optical focusing components.

2.4.3 Animals

Experimental procedures were approved by the Comité de Protection des Animaux de l'Université Laval, in accordance with the Canadian Council on Animal Care's Guide to the Care and Use of Experimental Animals. Maximum efforts were made to minimize the number of animals used. As such, we used only 2 macaque brains from the brain bank we have on hand at the CERVO brain research center. At the time of death of the animals the brains were fixed by immersion in 4 % paraformaldefyde for 24 h at 4 °C and later stored in a phosphate buffer solution.

2.5 Results

2.5.1 Fiber-based CARS spectra from solutions for system characterization

To show that we were indeed capable of acquiring spectra with minimal background from the fiber, we inserted our two probes into bundle into pure solutions of DMSO, methanol and peanut oil deposited on cover slips, seen in figure 2.2 (a). The data we acquire matches well with previous reports of such solutions using SRS or CARS hyperspectral microscopy, however until now, CARS spectroscopy using a fiber optic delivery has not been presented [160], [223]. Importantly, in previous work performing CARS endoscopy, it was stated that non-resonant CARS arising from the fiber overpowered the CARS signal generated in a sample of DMSO[217]. In our experiments, this was not the case. We postulate that this dominant FWM background is due to the previous works' use of a 280 fs pulsewidth for the pump laser, which is two orders of magnitude shorter than the pulsewidths in our arrangements, and therefore is subject to a much different level non-linear effects within the fiber. It is important to note that there are no free space optics between the fiber and the sample and the signal comes only from the light that is reflected off the glass coverslip on which the solution was stored via Fresnel reflectance. For these experiments, pump and stokes laser powers were 60 mW and 20 mW respectively. The spectral resolution of the wavelength tuning was 2 cm^{-1} and therefore the total acquisition time for all the measurements was 121 ms. As we will show later, this acquisition time can be easily decreased by using a lower spectral resolution.

We confirmed our high resolution spectroscopy by stepping the probes towards a DMSO solutions but this time recording the CARS signal in both the forward direction through the glass coverslip and the backward direction using the probe to assure that our detected resolution was not affected by interface changes. For both probes, the axial and lateral resolution was under 5 um, the smallest accurate step-size of our stepping motor. The results from the backward detected signal using the GRIN terminated probe can be seen in 2.2 (b).

2.5.2 Fiber-based CARS Spectra of primate brain tissue

Pure, non-organic samples are interesting for calibrating a Raman system due to their high signal and known spectra, however, impure scattering media is often much more complicated to achieve good signal from in practice. We show here that the probe could indeed be translated to scattering, multi-molecular tissue, by acquiring spectra in fixed NHP brain tissue as seen in figure 2.3. Again, both probes provided identical results and so we only show here data in this section from the contact-based probe. The power at the tip of the probe was 80 mW total (60 mW at pump wavelength, 20 mW at stokes wavelength). Since tissue gives a much lower signal than pure solutions, and we detect only the scattered photons from the forward generated CARS, the background signal from this specific fiber (SM800, Thorlabs) now becomes apparent with a peak signal at 2950 cm^{-1}. We can conclude that it is a resonant signal coming from the fiber itself with an irrelevant molecular origin, as it appears when the delay is overlapped at the injection side of the fiber and at the sample side when no sample is present, see appendix 1 for more information. Thankfully, this signal is removable and actually can be used to help discern increase in detected signal due to classical scattering from CARS signal increase from denser molec-

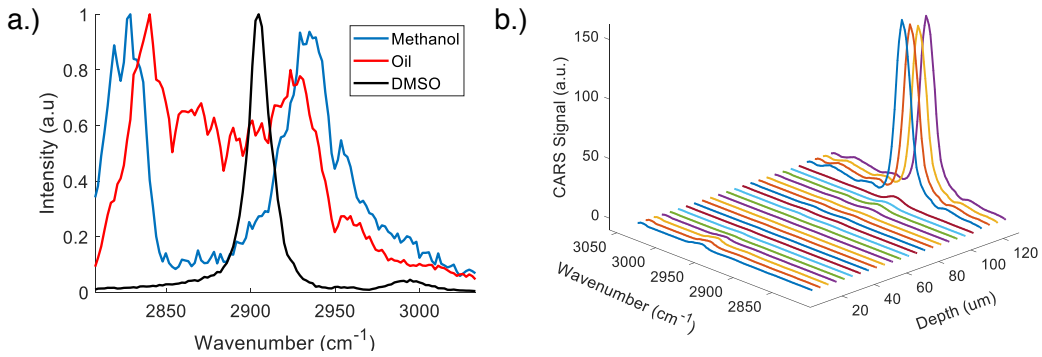

Figure 2.2 – Fiber-based CARS Spectra of pure liquids and probe resolution a) Normalized backward-detected spectra using the contact-based probe b) Resolution characterization using motorized actuator to take spectra every 5 um, stepping the GRIN terminated probe towards the DMSO solution.

ular concentrations. We present two scenarios wherein we acquire high resolution spectra in a total of 121 ms and a low resolution, random-access version that can be acquired in a total of 10 ms by limiting the number of spectral measurements. This exhibits a major strength of WS-CARS, in that random access contrasting can be achieved at very high speeds if the molecular bonds present are known. To assure the acquired spectra were not affected by the fixation solution used to preserve the tissue (4 % paraformaldehyde (PFA)) and the storage solution (0.1 Mol phosphate buffer solution) spectra were taken of each over a mirror and had no contributions in this wavelength range. That said, the application of PFA may cause a slight alteration to the Raman information from the tissue, however, our goal here was just to differentiate tissue subtypes and therefore the reported slight variations caused by PFA are acceptable [338]. The data presented has been digitally smoothed slightly using a Savistky-Golay filter. As expected, there is a general increase in CARS generated from 2830 cm^{-1} to 2950 cm^{-1} in both white and grey matter, with a clear peak at 2845 cm appearing only in white matter; this is in accordance with this peak coming from CH_2 bonds, and those bonds being much more abundant in the myelinated fibers of white matter. We are currently exploring the viability of CARS to provide a fingerprint type spectra for a given brain region and will be presented in future work.

2.5.3 Fiber-based CARS spectra acquired during descent through primate brain

As a final proof of concept for the future applications of this technology in surgical guidance, we performed a scan through the cortex of an intact primate brain. We show the measurement and discrimination can be done with a selection of only five wavelengths yielding a 5 ms acquisition time per step, showing the capability of CARS to delineate white and grey matter at high resolution, and at very high speeds. The random access capability of the system shortens the acquisition time and also reduces dramatically the amount of power dissipated in the tissue. The wavelengths chosen were strategically placed on 2845 cm^{-1} (corresponding to CH_2 backbone lipids, abundant in myelinated structures), 2880 cm^{-1} (corresponding to a variation of vibration from lipids), 2916 cm^{-1} (corresponding specifically CH_3 found more abundantly in cells due to proteins), 2950 cm^{-1} (corresponding to the resonant background coming from the fiber) and lastly 2995 cm^{-1} acting as the non-resonant contribution. It is important to mention that the we expect the signals at 2950 cm^{-1} and 2995 cm^{-1} to increase as they do along the probe descent, due to classical scattering as we approach the highly scattering white matter layer. Using this knowledge, we can use these signals as our subtractable background to improve our SNR and tissue classification. For help understanding the chosen wavelengths, refer to figure 2.3. Using these wavelength

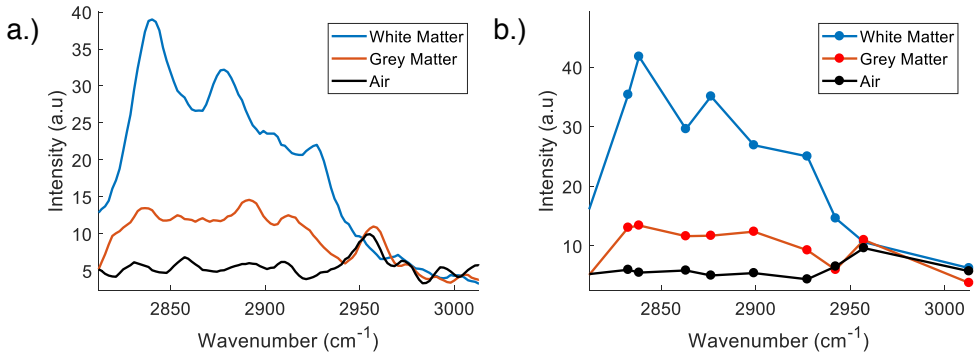

Figure 2.3 – CARS Spectra from primate brain sections. The bare probe was manually inserted into white and grey matter and measurements were taken. a.) Spectra acquired in 121 ms with 0.2 nm spectral resolution. b.) Spectra with only 10 random access wavelengths positions. Air measurements are taken with the probe just above the tissue background signal at a realistic intensity.

intensities when passing through different tissues, it becomes trivial to segment the different tissue types, as seen in figure 2.4. Specifically, in figure 2.4 (b), the heat maps labeled CH_2, and CH_3 are created through the subtraction of the 2995 cm^{-1} signal from the 2845 cm^{-1} and the sum of the 2880 cm^{-1} and 2920 cm^{-1} signals, respectively. The reflectance signal is merely the 2995 cm^{-1} itself as it is wavelength independent and is always present regardless of the medium. This reflectance signal is a useful parameter to have not only for baseline correction, but also for alluding to distant upcoming structures which can then be confirmed by a resonant CARS signal, such as the CH_2 signal as a white matter fiber bundle approaches in this example. Reflectance measurements like this have used in the past for DBS optical guidance using large probes which do not fit within the DBS electrode [81]. The white matter and grey matter segmentation performed in 2.4 (c) is done using a high threshold for 2845 cm^{-1} and a low threshold for the sum of 2880 cm^{-1} and 2920 cm^{-1}. To avoid co-registered tissues, we also restrict that if white matter is sensed, the structure is not grey matter. The "No tissue" segmentation occurs when the sum of all the lipid-originating signals is near zero. While we performed these tests with both probes, the data presented here is with the GRIN terminated probe. The probe was placed within a 26 gauge needle for rigidity, with the tip of the fiber slightly offset within tip of the needle to have the focal volume just outside the metal tube.

2.6 Discussion

Although the system is a considerable technical advancement in the field of fibered CARS spectroscopy, there are many future improvements we hope to incorporate to truly fulfill its potential. The first will be to perform the spectroscopy from within a DBS electrode. This will prove to be a difficult step, due to the tip of the DBS electrode not being perfectly transparent and therefore our signal detection will suffer both from the loss of ballistic photons and reduced collection due to interface reflections. That said, we have started to look at all the various commercially available electrodes which are FDA approved to give the system the optimal SNR. Another endeavor we are currently working on is acquiring fingerprint type spectra from specific brain regions, as has previously been done with spontaneous Raman probes, but with a much higher resolution[182]. Furthermore, CARS offers the potential to perform this fingerprint type sensing on the otherside of the electrode with, theoretically, one or two orders of magnitude faster speeds depending on the spectral resolution required, comparing

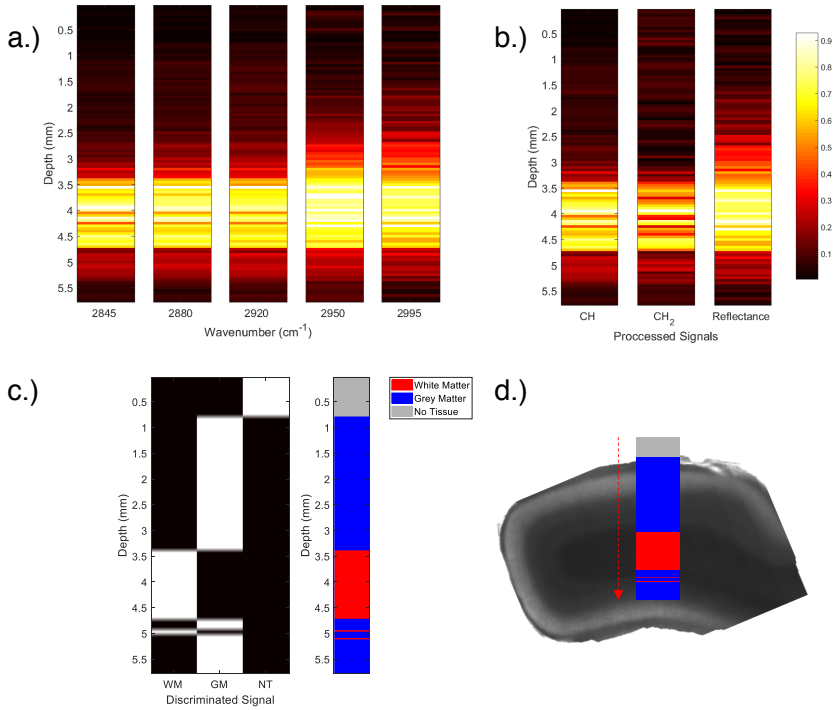

Figure 2.4 – Tissue discrimination using a selection of 5 wavelengths along a probe trajectory through fixed primate cortex. a) Heatmap of the intensity from each wavenumber logged when descending from air to grey matter to white matter. b) Heatmap of processed data showing the relative increase in overall CARS signal deriving from all CH bonds, CH_2 bonds specifically, and reflectance of fiber background. The maps in (a) and (b) are normalized from 0 to 1 in each graph for display purposes. c) Thresholded processed data to discriminate different tissue sub-types based on the 5 wavelengths acquired. WM = white matter, GM = grey matter, NT = no tissue sensed. d.) Overlay of the detected tissue subtypes on transmission image of primate cortex sample after removal from intact brain

with spontaneous Raman probes of a similar size[182]. This decrease in speed may not be so important in the operating room, however, the resulting decrease in optical power deposition in the tissue is highly desirable.

While white and grey matter can be a powerful enough tool to guide the surgery and provide locational information of the electrode within the brain [81], a fingerprint spectra would provide much more valuable information. Currently, in DBS surgery, a microelectrode recording (MER) is routinely done before electrode implantation where-in a microelectrode is descended into the brain, and then removed before implanting the chronic electrode. This is performed since MER can give a form of fingerprint-type sensing of the STN, due to its unique neuronal activity pattern, and therefore this can confirm for the surgeon their planned implantation trajectory is on target. If we can perform the same fingerprint sensing at an even higher resolution, optically, all from within the chronic electrode, we could dramatically improve the surgical outcome not only by guiding the placement of the electrode but also by removing the need for multiple foreign objects sent deep within the brain.

2.7 Conclusion

We presented here the first all-fiber based CARS spectroscopy system using simple silica fiber optics and a fast wavelength-tuning fiber-laser. With this system we have designed and created a probe with an ultra small form factor, capable of deep brain tissue sensing. We show that our laser system has the capability to be portable while also having clinically relevant fiber lengths. As a relevant proof of concept, we show, to the best of our knowledge, the first fiber-based CARS sensing of primate brain tissue. Furthermore, we show the ability of this spectroscopic technique to tell white and grey matter boundaries with very high resolution and acquisition speeds, alluding to its usefulness in DBS optical guidance.

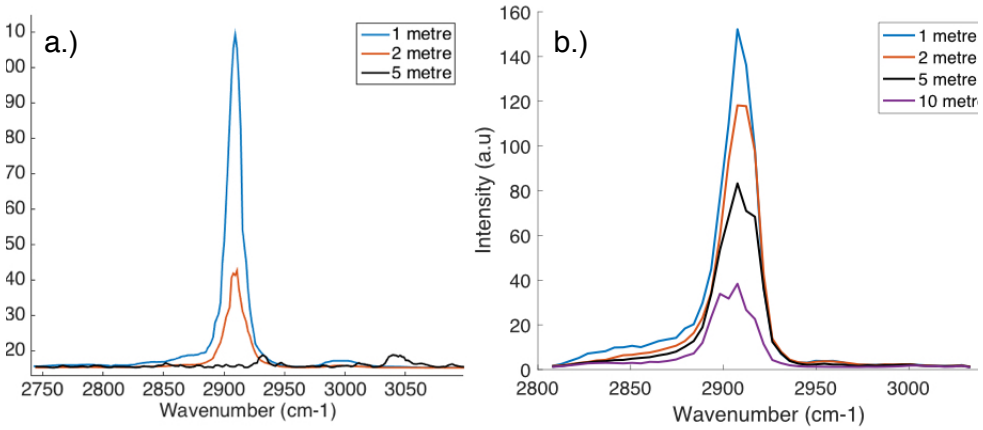

Figure 2.5 – CARS Spectrum as a function of fiber length a) OPO laser used experiments stopped at 5 metres as no signal was visible after this length. b) Genia laser system used. DMSO spectra still visible after 10 meter fiber length

Appendix 1

2.7.1 CARS spectra as a function of fiber length and laser system

High power peak pulses required for CARS signal generation deteriorate as a function of the pulse width. To show the improvement our system had over shorter pulse lasers, we aligned our labs CARS microscope lasers into the fiber probe. This laser system is composed of an optical parametric oscillator (OPO) (APE, Levante Emerald) pumped by a frequency-doubled Nd:YVO4 mode-locked laser (High Q Laser, picoTRAIN). The pump laser generates a 7 ps, 80 MHz pulse train of 532 nm and 1064 nm laser light. The OPO utilizes a temperature-tuned LBO nonlinear crystal for parametric oscillation and is pumped with 5.5W of 532 nm laser light. In our application, we used a fraction of the 1064 nm laser light in combination with a small portion the tunable wavelength range of the OPO (803 nm to 820 nm) to produce CARS spectra in the high wavenumber region (2800 cm^{-1} to 3050 cm^{-1}).

Indeed, using 7 ps pulses from the OPO laser system, we found a rapid degradation of the DMSO CARS spectra with fibers greater than 1 meter long; however, with the 25 ps pulses output from the Genia laser system, we could observe DMSO spectra with fibers lengths up to 10 m, as seen in figure 2.5. This is important when considering clinical translatability, as the possibility of longer fiber lengths are be ideal.

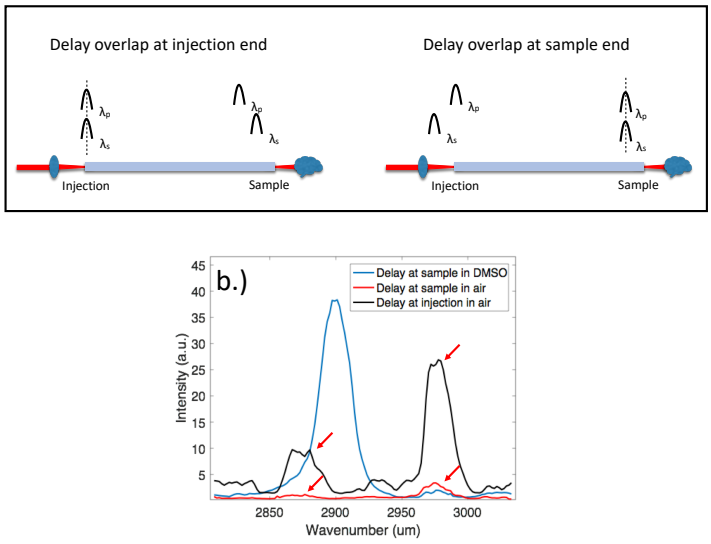

Figure 2.6 – CARS background from fiber over wavelength range. Spectra taken with detector directly in front of fiber, or through thin layer of DMSO in the case of DMSO a) Schematic to understand what is meant by pulse delay overlap. In the dispersive silica media, the two wavelengths travel at different speeds, allowing us to separate the pulses at one end of the fiber. b) Example of CARS spectra with different delay overlap positions in both air and in DMSO for comparison.

2.7.2 Background CARS generation from delivery fiber

We found that the FWM in the fiber was small in comparison to the signal generated in the sample when the delay between the two laser was zero at the sample end of the fiber. In figure 2.6 (b) we show that when the delay between the two different lasers is zero at the sample side of the fiber the background is small compared to the DMSO; however, if the delay is zero at the injection side, the intensity of the fibers' FWM background is high. When the pulses are overlapped at the injection side and the sample-side tip is in DMSO, no DMSO is detected as expected. In our work we were able to reproducibly get the same wavelength dependent background spectra from a given fiber, in this example a singlemode, polarization maintaining from Thorlabs (780HP, Thorlabs) was used.

Chapter 3

On-board optical guidance during chronic lead implantation in deep brain stimulation neurosurgery: Proof of concept in primates

Damon DePaoli[a,b], Laurent Goetz[c], Dave Gagnon[a], Gabriel Maranon[a,b], Michel Prudhomme[d], Léo Cantin[d], Martin Parent[a], Daniel C. Côté[a,b]

[a]Université Laval, CERVO Brain Research Center, Neuroscience, 2325 Rue de l'Université, Quebec City, Quebec, Canada, G1V 0A6
[b] Université Laval, Center for optics, photonics and lasers (COPL), Physics Engineering, 2325 Rue de l'Université, Quebec City, Quebec, Canada, G1V 0A6
[c]Hôpital Pitié Salpêtriére,ICM Institute for Brain and Spinal Cord, Experimental Neurosurgery, 47 Boulevard Hôpital, Paris, France, 75013
[d]Hôpital de l'Enfant-Jésus, Neurosurgery, 1401 18e Rue, Quebec City, Quebec, Canada, G1J 1Z4

3.1 Résumé

Background:
Le résultat clinique de la chirurgie de stimulation cérébrale profonde (SCP) repose largement sur la précision de l'implantation d'une électrode de stimulation chronique dans une petite région du cerveau cible. La plupart des techniques qui ont été proposées pour cibler précisément ces régions cérébrales profondes ont été conçues pour cartographier la trajectoire intracérébrale des électrodes, préalablement au placement chronique des électrodes, conduisant parfois à une erreur de positionnement de l'électrode finale.
Objective:
Cette étude visait à créer un nouvel outil de guidage peropératoire pour la neurochirurgie DBS capable d'améliorer la détection de la cible lors de l'implantation finale de l'électrode chronique.
Méthodes:

Tirant parti de la spectroscopie à réflectance diffuse, nous avons mis au point un nouvel outil chirurgical permettant de détecter le tissu cérébral proximal, à travers le bout de l'électrode chronique, au moyen d'un nouveau stylet qui offre une rigidité optimale aux dérivations DBS et abrite les fibres optiques.
Résultats:
Comme preuve de concept, nous démontrons la capacité de notre technique de guidage optique non invasive à localiser avec précision la frontière du noyau sous-thalamique lors de l'implantation d'électrodes DBS disponibles sur le marché dans un singe parkinsonien anesthésié. Des enregistrements optiques innovants combinés à une cartographie standard de microélectrodes et à un examen détaillé du cerveau post-mortem nous ont permis de confirmer la précision de la détection de cibles optiques. Nous montrons également la capacité de la technique optique à détecter, en temps réel, les vaisseaux sanguins à venir, réduisant ainsi le risque d'hémorragie lors de l'implantation chronique de la sonde.
Conclusion:
Nous présentons une nouvelle technique de guidage optique capable de détecter des régions cérébrales cibles pendant la chirurgie DBS à partir de l'électrode implantée à l'aide d'une validation du concept chez des primates non humains. La technique discrimine les tissus en temps réel, ne contribue pas au caractère invasif de la procédure en étant logée dans l'électrode et peut fournir des informations complémentaires à la cartographie des microélectrodes lors de l'implantation de l'électrode chronique. La technique peut également être un outil puissant pour fournir des informations anatomiques directes dans le cas d'implantations directes où la cartographie de microélectrodes n'est pas effectuée.

3.2 Abstract

Background:
The clinical outcome of deep brain stimulation (DBS) surgery relies heavily on the implantation accuracy of a chronic stimulating electrode in a small target brain region. Most techniques that have been proposed to precisely target these deep brain regions were designed to map intracerebral electrode trajectory, prior to the chronic electrode placement, sometimes leading to positioning error of the final electrode.
Objective:
This study was designed to create a new intraoperative guidance tool for DBS neurosurgery that can improve target detection during the final implantation of the chronic electrode.
Methods:
Taking advantage of diffuse reflectance spectroscopy, we developed a new surgical tool that senses proximal brain tissue, through the tip of the chronic electrode, by means of a novel stylet which provides rigidity to DBS leads and houses fiber optics.
Results:
As a proof of concept, we demonstrate the ability of our non-invasive optical guidance technique to precisely locate the border of the subthalamic nucleus during the implantation of commercially available DBS electrodes in anesthetized parkinsonian monkey. Innovative optical recordings combined to standard microelectrode mapping and detailed post-mortem brain examination allowed us to confirm the precision of optical target detection. We also show the optical technique's ability to detect, in real time, upcoming blood vessels, reducing the risk of hemorrhage during the chronic lead implantation.
Conclusion:
We present a new optical guidance technique that can detect target brain regions during DBS surgery from within the implanted electrode using a proof of concept in non-human primates. The technique discriminates tissue in real time, contributes no additional invasiveness to the procedure by being housed within the electrode, and can provide complementary information to microelectrode mapping, during the implantation of the chronic electrode. The technique may also be a powerful tool for providing direct anatomical information in the case direct-implantations where-in microelectrode mapping is not performed.

3.3 Introduction

Deep brain stimulation (DBS) is a neurosurgical treatment for Parkinson's disease and other disorders that can be prescribed when the clinical effectiveness of pharmacological supplementation has decreased, affecting patient quality of life.[339] During the surgery, an electrode is stereotactically implanted with the contact terminals located in a defined target brain region. Since the development made by Benabid et al. in 1987,[30] over 60,000 patients with Parkinson's disease have undergone DBS neurosurgery.[340]

The overall effectiveness of a DBS procedure relies heavily on the accuracy of the chronic electrode's placement in a target brain area. In the case of DBS used to alleviate motor symptoms of Parkinson's disease, the most common surgical target is the sensorimotor functional territory of the subthalamic nucleus (STN), followed closely by the sensorimotor area of the internal pallidum (GPi), with the optimal structure being patient specific.[341] In an analysis of DBS surgeries with unsuccessful treatment outcomes, nearly 50% of the cases were due to lead mis-placement.[51] Re-positioning of the leads in these patients, some by only 1 mm, rescued the treatment's efficacy.[52] This observation is supported by electrical field simulations, showing that an electrode shift of only 1 mm greatly effects the efficacy of stimulation.[53] Brain shifts are a major source of lead misplacement in DBS surgery and may occur at any time during the surgical procedure.[64], [65], [342] A report studying brain shift showed that on average, there is a shift of 1.8 mm between pre- and post-operative magnetic resonance images (MRI) in DBS surgery.[66] Other causes for lead misplacement can include stereotactic frame misalignment and interindividual anatomical variation with respect to brain-atlas targeting.[64] Microelectrode recording (MER) performed prior to the chronic DBS electrode placement is considered the most common technique to locate the dorsolateral region of the STN and to refine lead placement following pre-operative MRI trajectory planning.[62] The clinical advantage of using MER in DBS surgery is still an area of debate, however, taking into account the inherent increased risks of the procedure as well as the increased time spent in the surgery room.[343], [344] Furthermore, some hospitals are now emphasizing the importance of reduced surgical time and costs and consequently, a decrease in the use of MER for target-mapping has been observed in some hospitals.[63] Regardless of MER mapping, the risk for brain shift or frame misalignment during the final implantation phase of the procedure remains. Indeed, guidance during the final step of the procedure could be complementary and advantageous after MER mapping. Several groups have shown the viability of using optical measurements in lieu of MER. However, they have all been performed before the chronic electrode descent[79], [81], [82], [84], [85], [345] making their use interesting but less likely to be adopted by neurosurgeons who perform MER mapping or by neurosurgeons interested in decreasing operating time and number of probes sent into the brain. Whether or not pre-implantation trajectory refinement is performed prior to the final DBS electrode placement, the most important aspect of the surgery is to know whether: 1) the final DBS electrode has reached the target brain region and 2) how many active contacts of this electrode are precisely located in the target. Apart from intraoperative MRI, which is costly and unrealistic for many hospitals, this crucial information is currently not available during the implantation.[346] A new tool is therefore needed to sense the final position of the DBS electrode in reference to the target structure. We have designed an optical based technique that can sense anatomical information, in real-time, from within the hollow core of commercially available DBS electrodes, by replacing the traditional tungsten stylet with a fiber-optic-housing replica. Using diffuse reflectance spectroscopy (DRS), we use the entire visible and near infrared (NIR) spectrum to locate target brain structures, such as the STN, as well as blood vessels along the trajectory path of the chronic DBS electrode, during implantations in non-human primates (NHPs). We also show that we are able to sense missed trajectories and that the optical information acquired correlates with MERs. The technique is designed to supplement the information gained following MER mapping, during the insertion of the chronic electrode, however, this new approach could also be of great interest for neurosurgeons who have abandoned MER targeting altogether.

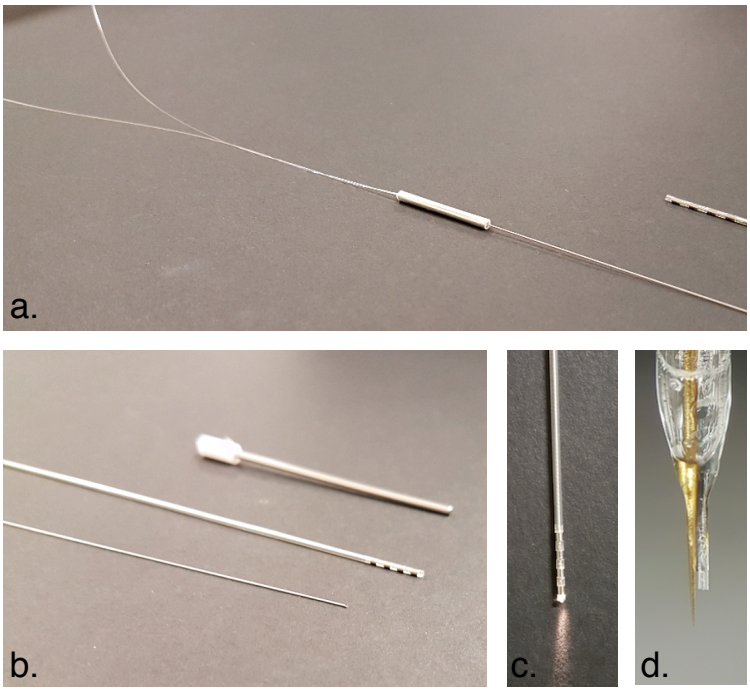

Figure 3.1 – Setup and probes. a.) Back end of optical fiber containing stylet and Medtronic 3389 DBS Lead. b.) Front end of optical fiber containing stylet, Medtronic 3389 DBS Lead and in house cannula. c.) Medtronic 3389 DBS Lead with optical fibers inserted showing light transmission through semi-transparent tip. d.) Tip of optical microelectrode probe used to measure neuronal activity and optical information simultaneously.

3.4 Methods

3.4.1 Probe design

3.4.1.1 Optical stylet design

The probe design was built under the size constraints of the inner diameter of commercially available DBS electrodes (DBS 3389 Medtronic, Minneapolis, USA). Custom stainless steel, hypodermic tubing was purchased and two 100 µm multimode fibers (FG105LCA, Thorlabs, New Jersey, USA) were inserted and glued. The optical fiber tips and tubing were then polished to assure their position was reproducible at the tip. At the other end of the tubing, a metal-machined base was glued to make the stylet robust and durable at its vulnerable end. The optical-fiber housing stylet was then placed within the DBS electrode and a custom-machined cannula was used to lock the stylet and to add rigidity to the electrode during implantation (Figure 3.1 (c)).

3.4.1.2 MER and optical probe design

A capillary tube was pulled and the tip was broken to create a hole big enough (500 µm) to place both the tip of the microelectrode as well as two polished 100 µm multimode fibers (FG105LCA, Thorlabs, New Jersey, USA) beside each other with the help of a microscope.

3.4.2 Tissue identification

3.4.2.1 Optical recording and analysis

Our tissue identification is based on sensing optical differences between white and grey matter and blood vessels using a combination of: 1. NIR reflected light intensity 2. Principal component analysis (PCA) of the entire visible spectrum and 3. Linear least-squares regression analysis of the principal components. Light was produced from a halogen white light source (SLS201L, Thorlabs, New Jersey, USA) and collected onto a spectrometer (USB2000, Ocean Optics, Largo, USA) after interaction with the sample. Hundreds of measurements were taken in fresh post-mortem NHP brain tissue, separating the data into white, grey, mixed matter and blood vessels. PCA was then performed on this data using MATLAB and the first four components that described the entire dataset were saved. Linear least-squares regression analysis (MATLAB) was then used to create reproducible contributions of each component in a given tissue type so that thresholds for each component's contribution could be used. These reproducible thresholds allowed us to discriminate a newly measured spectrum in real time (20 ms acquisition time). We coin the term "mixed tissue" due to the fact that this tissue type shows high NIR intensity while the PCA component analysis, essentially describing the color, shows that the structure is more grey than white matter normally is. Most often this subtype describes target structures such as the thalamus, STN and GPi. The data analysis procedure can be seen in figure 3.2.

3.4.3 Surgical and histological procedures

All experimental procedures were approved by the university's animal protection committee in accordance to the national Council on Animal Cares Guide and Use of Experimental Animals. Five surgeries in total were performed on adult cynomolgus monkeys (Macaca fascicularis). Two procedures were performed *in vivo* using a mix of ketamine (75 mg/kg, i.m.) and xylazine (5 mg/kg, i.m.) anesthetic to acquire better MERs during optical measurements. Three *ex vivo* procedures were performed, using whole post-mortem cynomolgus monkey heads. The *in vivo* monkeys used were parkinsonian, achieved through MPTP administration. Explicitly, these animals received MPTP (Sigma-Aldrich Canada Ltd., Oakville, Canada) via a subcutaneous osmotic mini-pump for 14 days, and the experiment was performed months after MPTP administration. The *ex-vivo* animals were healthy control cynomolgus monkeys that had been used in other research protocols wherein the head and neuroanatomy of the specimen were unaltered; the surgery was performed on these heads within 24 hrs of their sacrifice. For both the *in vivo* and *ex vivo* experiments, the heads were placed in a custom-designed stereotaxic apparatus allowing pre and per-operative x-ray imaging. After craniotamy, a radiopaque solution (Omnipaque, 2 x 0.4 mL of a 65% iohexol solution, GE Healthcare) was injected through a microsyringe into the right lateral ventricule for ventriculography. Lateral and frontal X-ray pictures of the ventricular system was then taken to precisely locate the anterior and posterior commissures as well as the midline to define the stereotactic coordinate of the STN based on a macaque stereotaxic atlas.[347], [348] The electrodes were then fixed to a 10 µm resolution micromanipulator (model 1760, Kopf Instruments) with an electrode holder (model 1770, Kopf Instruments) and optical measurements were taken in step of 100 µm until target coordinates were reached where the electrode was left in place. In the case of the MER experiment, electrophysiological measurements were also taken at the 100 µm intervals using a tungsten electrode. After experimentation, brains were chemically fixed with a solution paraformaldehyde (PFA) 4% either by transcardiac perfusion (*in vivo* experiment) or by immersion (*ex-vivo* experiments). After a 24h post-fixation period in PFA 4%, brain tissue was cut in 50 µm-thick sections with a microtome in order to perform detailed post-mortem analysis.

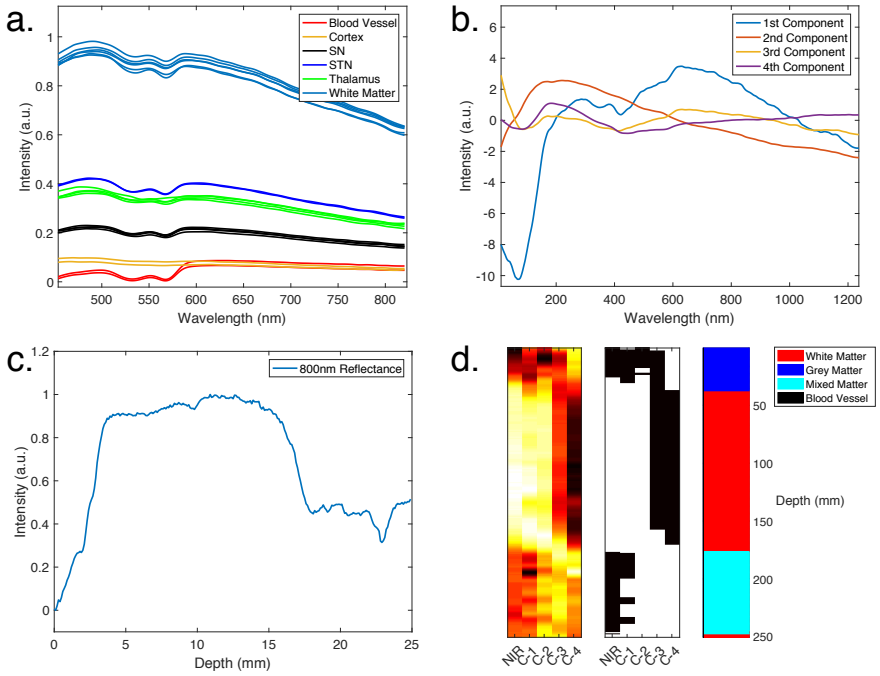

Figure 3.2 – Data Analysis a.) Example spectra measure from different sections of fresh NHP tissue. b.) Example component scores from PCA analysis over an entire trajectory during a DBS electrode implantation in NHP c.) Example of the intensity at 800nm over an entire trajectory during a DBS electrode implantation in NHP where the probe passed only through the internal capsule until the STN target structure. d.) Example of discrimination over the same trajectory using the normalized intensity at 800 nm intensity and the linear-regression-calculated contributions of each of the four preloaded PCA components describing a single spectral acquisition. The 5 variables are thresholded at their median and the algorithm chooses if a tissue is white, grey or mixed matter or a blood vessel based on the thresholded binary pattern. The color coding is designed for easy understanding of the sequence of brain structures passed along the trajectory of implantation. See the legend for which color corresponds to which tissue type.

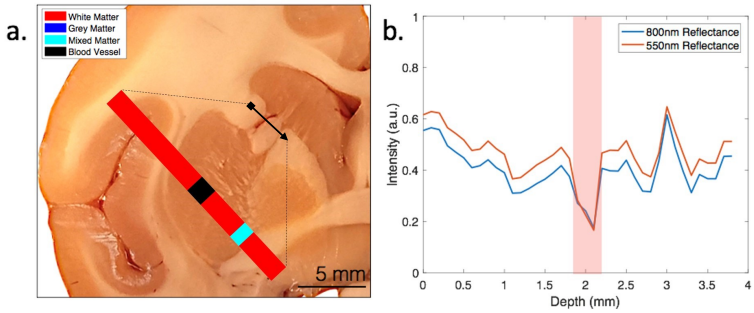

Figure 3.3 – *Ex-vivo* blood vessel detection in NHP tissue a.) Slice of brain sample and blood vessel scanned. Inset shows the automated discrimination of the blood vessel and the small grey matter area. The data started to be acquired at position "0 mm" denoted by the square end of the line and ended at "4 mm" denoted by the arrow tip. b.) Single wavelength reflectance values over the length of the scan show that they are not able to provide discrimination of the blood vessel or the grey matter region, unlike the DRS algorithm. The red rectangle overlay signifies where the blood vessel was located.

3.5 Results

3.5.1 Blood vessel detection from within chronic electrode

Since hemoglobin is the main visible wavelength chromophore in the brain, it is intuitive to think that this technique could be used for blood vessel detection. To show evidence of the ability of our probe to detect blood vessels from within the electrode, a scan was first done on a sliced portion of a fixed NHP brain showing intact blood vessels. The *ex vivo* brain section (not perfused) was stored in a phosphate buffer solution (0.01 M) and diffusive blood that had leaked from the brain into the solution evenly covered the tissue. Therefore, we still sensed normal amounts of hemoglobin at every point of our scan (as we should from the integration of absorption from small capillaries) while also showing the ability to sense larger blood vessels in the presence of this background. As shown in Figure 3.3, the 200 µm blood vessel appears in the spectral decomposition and is discernible from white, grey and mixed matter using the variable component analysis. Furthermore, the system managed to sense a small band of grey matter at the 3 mm point of the scan. It is very important to note that we are incapable of sensing the blood vessels using just a single wavelength reflectance value (Figure 3.3), furthering the case for the use of broadband spectroscopic techniques in optical DBS surgical guidance.

3.5.2 *In vivo* STN detection in macaque: comparing accuracy of MER and DRS

To compare the accuracy of DRS to sense the target region, we created a custom MER/optical probe. The probe can be seen in figure 3.1d and is explained in the methods section. With this probe, we could simultaneously record neurons along the descent, while also acquiring optical information. Our targeting of the STN was calculated using ventriculography-assisted atlas-based planning. We chose a straight-down trajectory to acquire a more diverse set of neuronal firing patterns, as the human DBS trajectory are often planned in the internal capsule, to avoid the caudate nucleus and the putamen in order to reach the STN while minimizing penetration of other neuronal cell rich structures. Due to the longer acquisition times required for MER, we used a 500 µm step size between subsequent MER acquisitions

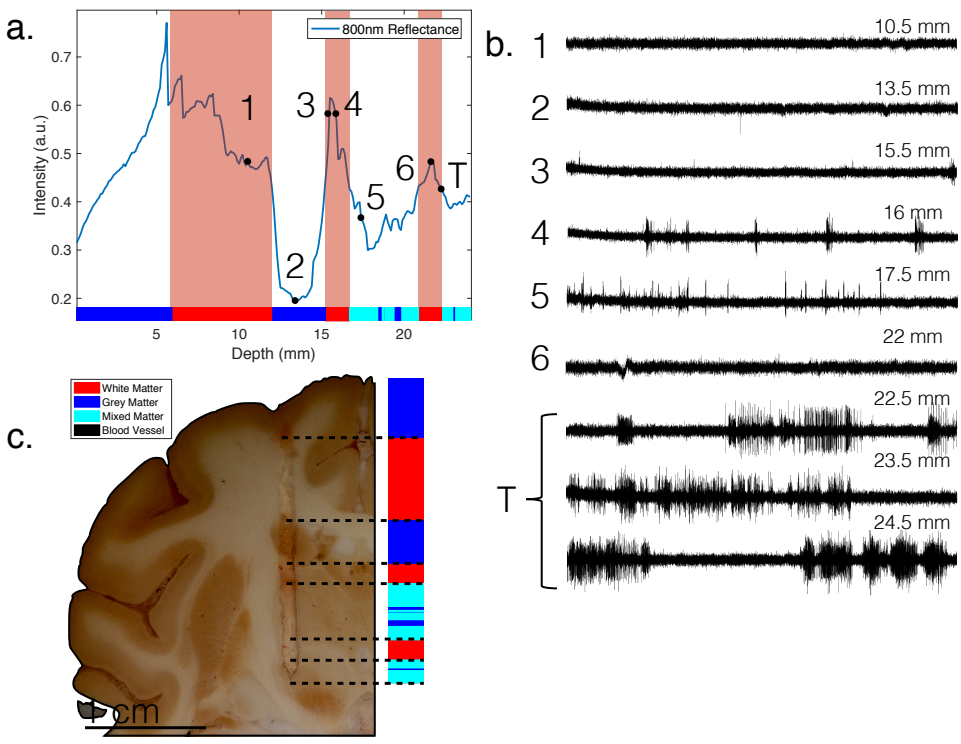

Figure 3.4 – *In Vivo* dual MER and optical probe implantation for comparing concurrent optical and electrical measurements in NHP DBS implantation. a.) Shows NIR intensity over trajectory through brain starting near the cortex/white matter boundary. Inset numbers refer to locations of concurrent neuronal recordings. Red sections signify algorithm-detected white matter. The discrimination plot is superimposed over the area where the probe was sent down during the surgery with the region numbers referring to the following: 1 – cortical white matter, 2 - caudate nucleus, 3 – medial aspect of the internal capsule/stria terminalis, 4,5 - thalamus. 6 – zona incerta, and T (for target) – STN. b.) Shows the Electrical recordings at various stages throughout the trajectory. STN activity begins at 22.5 mm, again denoted as region T for target c.) Post-mortem slice of brain fixed with the implanted probe to show true location.

In this example the optical algorithm successfully senses a thin white matter layer (lenticular fasciculus or Forel's field H2), just before the predicted anatomical location of the STN (Figure 3.4). Also seen in the figure 3.4b, as soon as this thin white matter boundary is passed, according to the optical measurements, neuronal recordings go from nearly silent in Forel's field, to an irregular burst-like firing pattern, indicative of STN neurons.[62] As expected, the optical algorithm also correctly predicts the thalamus and the STN to be mixed matter structures. To be complete, we include an X-ray calculated prediction of the electrode tip position along with the *post-mortem* tissue analysis.

3.5.3 Successful STN detection from within chronic electrode, during the final implantation

With MER confirmation of our optical method as a mean for STN target detection, we performed surgeries targeting the STN with the optical stylet probe inserted within a DBS electrode. For this specific surgery, an intact *ex vivo* NHP head was placed in the stereotactic frame and a DBS trajectory mimicking that of a human DBS electrode implantation was planned and executed. While we have performed *in vivo* experiments, we often use *ex vivo* intact heads of NHPs provided from other research projects to reduce ethical impact. We consider this acceptable since fresh (non-fixed) *ex vivo* brain anatomy and optical data do not differ from *in vivo* circumstances, as indicated by the successful analysis of optical data and algorithm performance from both the *in vivo* and the *ex vivo* measurements.

During the implantation, optical recordings were acquired every 100 μm and the measurements were displayed on the screen next to the surgeon. While this high resolution step-size is not required, the optical acquisition time is on the order of 20 ms, making it essentially instantaneous. Successful targeting was predicted using the optical readings, taken through the electrode tip, based on the detection of white, grey and mixed matter locations (Figure 3.5). Using only stereotactic planning and our optical readings, we were able to accurately predict the precise location of the STN by the detection of the last mixed matter structure optically-sensed near the calculated depth of the target. We later confirmed this prediction using *post-mortem* tissue analysis, as show in figure 3.5b. An interesting observation is the sensing of a mixed and grey matter structure, the GPe, halfway along the trajectory, labeled region (3) in figure 3.5b. In this scenario, the post-operative X-ray imaging was successful in accurately predicting the true position of the electrode.

3.5.4 Missed target detection from within chronic electrode, during implantation, with bleeding

We thought it imperative to show an example of a missed target implantation, as it is in these circumstances that the value of the technology becomes more evident. This missed trajectory was performed in an *in vivo* parkinsonian NHP, with the planned trajectory having a single mediolateral angle of insertion and targeting the STN (figure 3.6). The implantation trajectory was calculated using ventriculography-assisted atlas-based planning. However, due to anatomical variation, the targeting was still unsuccessful. This implantation was an example of how intra-operative optical information described a trajectory wherein the order and length of the sensed tissues did not match the order and length of tissues expected to be passed-through for an on-target implantation. Using this information, the implantation was interpreted correctly as a missed trajectory (confirmed by *post-mortem* tissue analysis) even though the calculation of the electrode tip location using intraoperative X-ray imaging reflected a target hit. Furthermore, prior to electrode insertion, upon cranial opening a hemorrhage occurred on the cortex causing some blood to cover the electrode tip during the implantation. The algorithm remained robust and correctly identified the different tissue types.

3.6 Discussion

We provide here a proof of concept in NHPs of a clinical tool able to discriminate brain tissue types and blood vessels during a DBS lead implantation from within the hollow core of a commercially available DBS electrode, allowing the detection of target brain regions. We achieve this by replacing the tungsten stylet with a stylet housing fiber optics allowing us to interrogate the absorption and scattering properties of a biological sample within a millimetre sized volume, proximal to the electrode tip. The device reproducibly discriminates white matter, grey matter, mixed matter and blood vessels, potentially allowing for a safer surgery while indicating the surgeon if the trajectory was on target, before post-operative imaging. While our work was done on *in vivo*

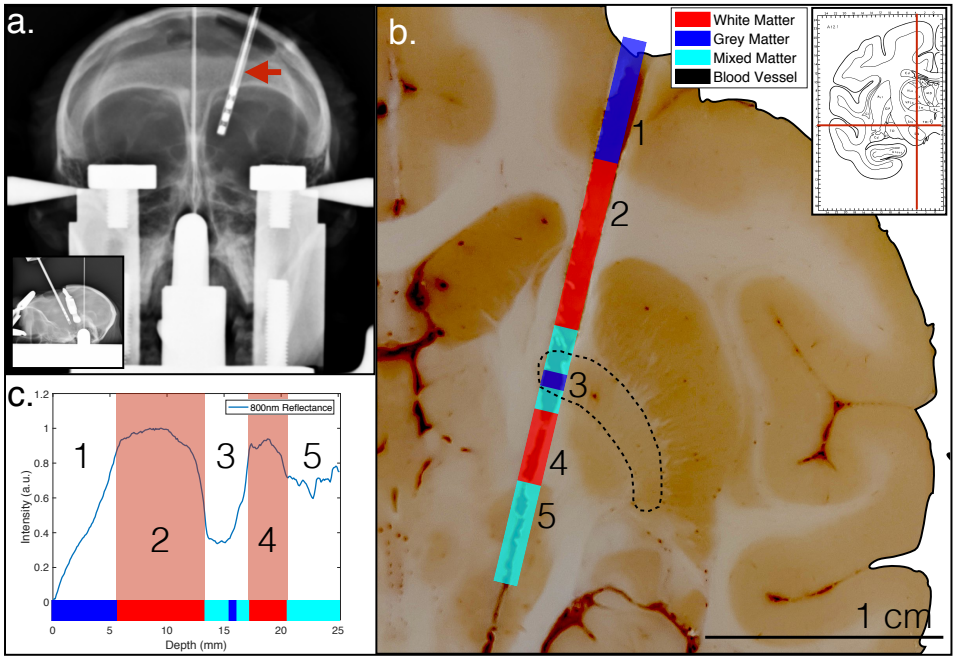

Figure 3.5 – *Ex Vivo* Stereotactic dual angle DBS lead implantation in NHP with fiber optic stylet, on target. a.) Shows the lead implant location in the left hemisphere of the NHP's brain. Inset shows a sagittal view to see dual angle trajectory b.) Shows Post-mortem brain slice of brain where implantation occurred. Inset in top right shows the calculated position on an atlas image according to the X-ray measurements made during the implantation. Discrimination plot is superimposed over the area where the probe was sent down during the surgery with the region numbers referring to the following: 1 - cortex, 2 - cortical white matter, 3 – GPe, 2, 4 - internal capsule, 5 - STN. The algorithm labelled the substantia nigra (SN) as mixed matter, but with future iterations it will include the SN as a unique tissue sub-category since it does have a unique spectral signature caused by the strong visible chromophore melanin. The GPe is detected as a mix of grey and mixed matter, which is reasonable depending on the location of the probe in the structure (ie. edge vs. central). The GPe is outlined manually since the contrast is not optimal. c.) NIR Intensity plot over trajectory starting at cortex/white matter boundary. Region numbers are located in the position along the trajectory that correspond to their respective brain regions according to the brain slice. Red sections signify algorithm-detected white matter

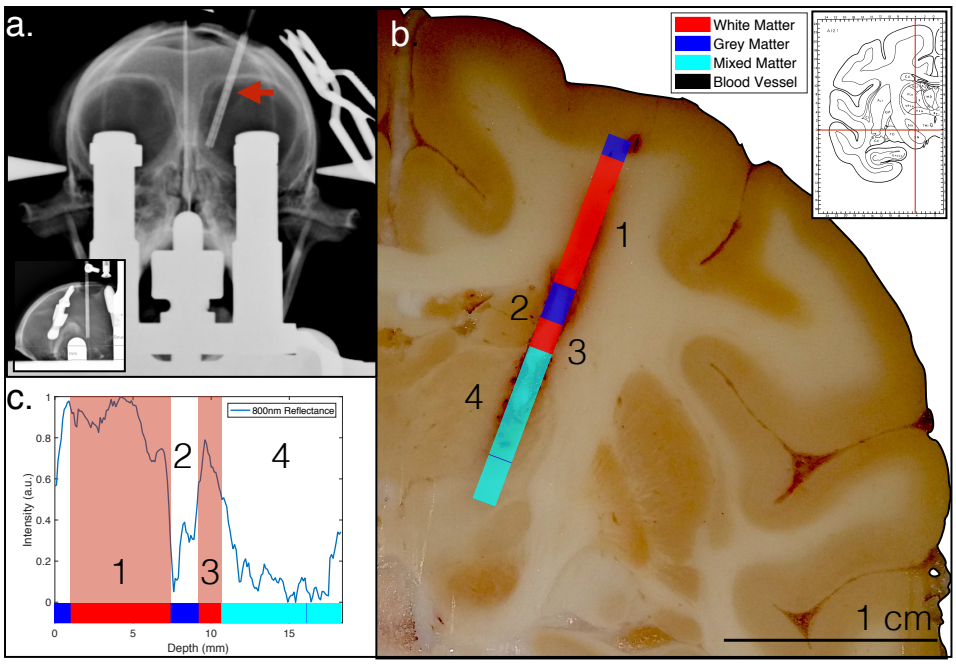

Figure 3.6 – *In Vivo* Stereotactic single angle, DBS lead implantation in NHP with fibre optic stylet, off target. a.) X-ray image showing the lead implant location in the left hemisphere of the NHP brain. b.) Shows Post-mortem brain slice of brain where implantation occurred. Inset in top right shows the calculated position designated by the cross-hairs on an atlas image according to the X-ray measurements made during the implantation. Discrimination plot is superimposed over the area where the probe was sent down during the surgery with the region numbers referring to the following: 1 - white matter, 2 - caudate nucleus, 3 - white matter, 4 – thalamus c.) NIR Intensity plot over trajectory starting at cortex/white batter boundary. Region numbers are located in the position along the trajectory that correspond to their respective brain regions according to the brain slice. Red sections signify algorithm-detected white matter

and *ex vivo* NHPs, we can assume the technique will be even more effective in humans, as the brain structures are larger and therefore easier to discriminate. To extend the utility of the device, we are investigating the ability of our optical technique to locate other DBS targets for Parkinson's disease, such as the GPi, as well as DBS targets for other neurological and psychiatric disorders [349]–[352]. Furthermore, the information we acquire can perhaps act as an "optical barcode", a term previously coined by Wardell et al.,[353] to give the surgeon an idea of where the electrode is, based on the order of tissue types that have been sensed along the electrode insertion. For instance, we found that, in general, if we did not strike the caudate nucleus or the putamen within the first couple centimetres of the descent, in other words, if there was no grey matter detected below the cerebral cortex, the trajectory was heading to the STN target. Even in hospitals that are not limited by time and that choose to perform MER mapping, optical measurements can be used subsequently during the last implantation stage of the procedure to confirm the final position of the chronic electrode and to assess any brain shift that might have occurred following the removal of the recording microelectrode. Indeed, due to the elastic nature of the brain, the small temporary hole that the microelectrode forms during its precedent decent subsequently closes and does not effect the optical measurements taken during the insertion of the chronic electrode probe. Furthermore, with future improvements and added functionality using vibrational spectroscopies such as Raman, which can acquire fingerprint type spectra of different brain regions, we hope that optical modalities could offer the same level of target specification as MERs. This could not only decrease costs of surgery and surgery time, incurred in part by the expensive equipment and trained personnel needed to interpret MER data, but also overcome the need to send multiple electrodes into the brain.

While we did not perform post-operative MRI on the primates, we opted to examine the tissue *post-mortem*. This analysis, while invasive and requiring sacrifice, is the only true method to directly view the small anatomical regions for precise analysis of probe position since post-operative MRIs rarely have the capability to directly visualize the STN, even in larger human brains.

It is worth mentioning that human and monkey brain matter are quite similar with respect to VIS-NIR absorption and scattering. To confirm this, and that the algorithm will work in humans, we have taken many DRS measurements in both fresh human samples of white and grey matter. Indeed, the main difference apart from anatomical size is the large increase in vascularization, which will need to be studied further.

3.6.1 Validation through concurrent optical and electrical recordings

A missing piece from previous literature using optical methods for brain target localization in DBS surgery was concurrent MER and optical analysis, as using multiple trajectories can induce error. Although the MER/DRS probe was not the point of our present study (since the large outer diameter of the probe precluded its placement within a DBS electrode), we believe it was an integral piece of information required to trust the optical data. While it is difficult to provide a quantifiable comparison between the two systems regarding the resolution *in vivo*, it is clear that both detection methods are accurate, or rather equivalent, at detecting the anatomical target within the 500 μm acquisition step size that was used for MER measurements, during the probe insertion.

3.6.2 Towards intraoperative optical guidance from within DBS electrode

In humans, it is not always evident if critical structures are lesioned along the electrode trajectory due to poor resolution, metal artefacts, and general error in post-operative MRIs and X-rays.[354], [355] In this regard, our optical device could shed light on some of the negative side effects caused by the lesioning of critical structures, as in the case shown in figure 3.5 where the GPe has been impaled by the electrode along its trajectory. The example of a missed target in figure 3.6 shows the optical technique could theoretically sense if the trajectory is off before the electrode even penetrates the cell-rich structures (in our case the caudate nucleus), as illustrated by the detection of grey matter in the first centimeters, markedly different from the first centimeters of measurements

of an on-target trajectory shown in figure 3.5. In modern DBS surgeries, a complete target miss is less likely and the targeting of functional territories within a target brain structure is becoming the more pressing issue. Indeed, with the current instance of our technology, we cannot acquire characteristic information of functional territories within a target brain structure. However, we believe that with future iterations of the device and optical simulations using patient-specific pre-operative MRI volumes, we could discern where precisely the electrode and its contacts are in the brain, using the sequence of distances the probe travels though alternating brain structures. This precise locational information (1 mm resolution) could be highly valuable to identify the anatomically well-defined functional territories of the STN.[356] Furthermore, we are working on a complementary optical system that uses molecular level sensing called coherent Raman spectroscopy, which should be able to classify specific brain regions at extremely high resolution (<10 μm) and perhaps even shed light on functional territories.[1]

3.6.3 Limitations of the current system

The system presented in this work is meant to display a promising idea for future surgical guidance solutions where-in biomedical optics is leveraged to create a safer procedure with no additional invasiveness. That said, there are many limitations to overcome before clinical investigation is achieved. First, while we presented the use of Medtronic electrodes in this study, we should mention that Boston Scientific electrodes were also tested with good results. The main prerequisite for this technique to be used with a given electrode is that it must have a semi-transparent tip since the optics sense in the forward direction. It is yet to be determined if the technique can be used in the newer directional electrodes from Boston Scientific.

Another concern is the workflow in the case of a missed planned trajectory using optical recordings within the chronic electrode without MER mapping. The reason being the chronic electrode would have to be removed and re-inserted, however, this is already being done with MER mapping. It is possible that this could create a problem in the subsequent insertions as the first one will have created a path-of-least-resistance. Therefore, while the optical-stylet does provide rigidity, we would still recommend a cannula be used during most of the chronic electrodes descent. In our *in vivo* experiments in NHPs, the procedure of using a cannula with the probe-housing chronic electrode 1 mm protruded most of the way to the target structure and then protruding the electrode the final centimeter is an ideal way to acquire more locational information and allow blood vessel detection along the entire descent. This technique also has circumvented any potential lead deviations. Indeed, acquiring optical information along the entire descent in this manner allows the possibility to better calculate and register the electrode position in reference to pre-operative MRI's, therefore allowing more precise localization of the electrode in reference to the target structure. Using this information alone could be enough to calculate the required corrections to re-insert the electrode if test stimulations and optical information show sub-par implantation accuracy. The same technique should be possible in humans. However, if the surgeon performs MER recording prior to chronic electrode implantation, the luxury of acquiring optical information along the entire descent may not be possible as the cannula will likely rest inserted and the optical probe will only be able to sense information for the final couple centimeters it is protruded. In this case, however, the optical probe's role will be to confirm that no shifting has occurred between removal and insertion of the two electrodes. Furthermore, the information will allow better location of the target structure in the depth direction, and can still be used in unison with the MER mapping and pre-operative MRIs for a more confident targeting.

Lastly, while sensing blood vessels is important, it is hard to say whether the technology would actually decrease hemorrhaging. We would like to think that if there was an upcoming blood vessel, the surgeon would want to know regardless of the solution. Perhaps, the surgeon would proceed to reposition the trajectory or simply opt to descend more slowly as to not rupture the blood vessel. This sort of question is currently out of the scope of our work.

3.6.4 Limitations of the current study

In the current study we have presented the first iteration of a novel optical technology that could easily be integrated into the workflow of DBS neurosurgery in order to improve target localization. Of course, the study itself does have some technical limitations at its current state. First, the use of a NHP anatomy model was used in place of humans, as a proof-of-concept was required in a living animal. The model is a relatively good one in terms of optical barcode sequences, however, there are considerable anatomical and vascular size differences. That said, these differences work in favor of the optical technique as human brain should make the resolution relatively better due to larger brain regions. Also, we have done this work in a research setting wherein we set out to show the capabilities of the optical technology in detecting on and off target trajectories. Therefore, we still must analyze the ability to provide correctional translocation information in the case of a missed target as well as investigate the overall clinical workflow of incorporating the device. Following this work, a pre-clinical study will be performed to better understand the available improvements in using the technique to provide additional information to a surgeon in the operating room.

3.7 Conclusion

We have presented a proof of concept device capable of providing optical guidance to a neurosurgeon during DBS lead implantation without incurring any additional invasiveness or surgical time to the procedure. We achieve this by replacing traditional stylets in commercially available DBS electrodes and performing DRS through their semi-transparent tips. The information provided is intuitive and allows easy interpretation without the need of highly trained personnel. We perform optical guidance using the device during DBS implantations in parkinsonian monkeys and show that the device can automatically detect white, grey and mixed matter as well as blood vessels, in real time, along the insertion of the DBS lead. The described system offers a promising avenue for improved target detection in human DBS surgery and a possible means to better understand implantation location in reference to pre-operative imaging.

Chapter 4

Convolutional Neural Networks for Spectroscopic Analysis in Retinal Oximetry

Damon DePaoli[a,b],Prudencio Tossou[c], Martin Parent[a], Dominic Sauvageau[d,e], Daniel C. Côté[a,b]

[a]Université Laval, CERVO Brain Research Center, Neuroscience, 2325 Rue de l'Université, Quebec City, Quebec, Canada, G1V 0A6
[b] Université Laval, Center for optics, photonics and lasers (COPL), Physics Engineering, 2325 Rue de l'Université, Quebec City, Quebec, Canada, G1V 0A6
[c]Université Laval, Department of software engineering and informatics, Quebec city, Québec, G1V 0A6, Canada
[d]Zilia inc., Quebec City, Québec, Canada, G1V 0A6 [e]University of Alberta, Chemical and Materials Engineering, Edmonton, Alberta, Canada, T6G 1H9

4.1 Résumé

L'oxymétrie rétinienne est une technique non invasive permettant d'étudier l'hémodynamique, le système vasculaire et la santé de l'œil. Les techniques actuelles d'oxymétrie rétinienne ont été gâchées par des mesures quantitativement incohérentes, ce qui a grandement limité leur adoption dans les environnements cliniques. Pour devenir cliniquement pertinentes, les mesures d'oxymétrie doivent devenir fiables et reproductibles pour toutes les études et tous les sites. À cette fin, nous avons développé un algorithme de réseau de neurones à convolution pour l'oxymétrie à longueurs d'onde multiples, démontrant une performance de calcul grandement améliorée par rapport aux techniques précédemment rapportées. L'algorithme ne nécessite aucun étalonnage, détecte les quatre conformations principales de l'hémoglobine sans aucune connaissance préalable de leurs spectres d'absorption caractéristiques et, du fait du calcul basé sur la convolution, il est invariable vis-à-vis du décalage spectral. Nous présentons ici les améliorations considérables apportées aux performances de l'utilisation de cet algorithme pour déduire une oxygénation efficace (SO_2), ainsi que la fonctionnalité ajoutée permettant de mesurer avec précision une oxygénation fractionnelle (SO_2^{fr}). En outre, ce rapport compare pour la première fois les performances relatives de plusieurs algorithmes d'oxymétrie à longueur d'ondes multiples précédemment rapportés, compte tenu des variations spectrales contrôlées. L'amélioration de la capacité de l'algorithme

à mesurer de manière précise et indépendante les concentrations en hémoglobine offre un potentiel élevé pour le diagnostic et la surveillance de la maladie lorsqu'elle est appliquée à la spectroscopie rétinienne.

4.2 Abstract

Retinal oximetry is a non-invasive technique to investigate the hemodynamics, vasculature and health of the eye. Current techniques for retinal oximetry have been plagued by quantitatively inconsistent measurements and this has greatly limited their adoption in clinical environments. To become clinically relevant oximetry measurements must become reliable and reproducible across studies and locations. To this end, we have developed a convolutional neural network algorithm for multi-wavelength oximetry, showing a greatly improved calculation performance in comparison to previously reported techniques. The algorithm is calibration free, performs sensing of the four main hemoglobin conformations with no prior knowledge of their characteristic absorption spectra and, due to the convolution-based calculation, is invariable to spectral shifting. We show, herein, the dramatic performance improvements in using this algorithm to deduce effective oxygenation (SO_2), as well as the added functionality to accurately measure fractional oxygenation (SO_2^{fr}). Furthermore, this report compares, for the first time, the relative performance of several previously reported multi-wavelength oximetry algorithms in the face of controlled spectral variations. The improved ability of the algorithm to accurately and independently measure hemoglobin concentrations offers a high potential tool for disease diagnosis and monitoring when applied to retinal spectroscopy.

4.3 Introduction

Retinal oximetry is a non-invasive technology drawing considerable attention in the medical field due to its ability to give unprecedented information on the vasculature health of the eye. There is considerable evidence that malfunction of the vasculature on the retina can result in, or be an indication of, serious eye diseases such as diabetic retinopathy (DR) [357]–[364], retinal vessel occlusions[365]–[369], glaucoma[368], [370]–[374], retinitis pigmentosa [375], [376], retinopathy of prematurity [377] and age related macular degeneration (AMD) [378]. Recently, retinal oximetry has even shown the possibility of non-invasively monitoring some neurodegenerative diseases[366]. This being said, the abundance of research performed using retinal oximeters has not yet translated into full deployment in clinical settings; mostly due to the semi-quantitative nature of measurements caused by the complex optical properties of the biological tissues on the retina. [379]–[383].

Retinal oximeters typically rely on either two, three or multi-wavelength analysis. Few-wavelength (<4) techniques have a long history and have been improved on greatly over the years[384]–[389], however, the general method is similar. Briefly, few-wavelength techniques require images acquired on and off isosbestic wavelengths for oxygenated and deoxygenated hemoglobin and a user-calibrated optical density ratio (ODR) method to provide oximetry measurements on large blood vessels [390]–[392]. While the technique has flourished in academia, in recent years the measurement integrity of the technique has been questioned in terms of quantitative reproducibility. Specifically, commercially available two-wavelength imaging oximeters have displayed inconsistent oxygenation measurements caused by blood vessel sizes [391], scattering and cataract variations[393], [394] and flash intensities[395]. Monte Carlo simulations on the error inherent to two-wavelength retinal oximetry has also shown the importance of proper calibration[41] as well as the possible errors cause by vessel diameter and melanin concentration in the retinal epithelium[396]. Furthermore, many disease studies draw similar conclusions, but with different quantities. For example, in the progression of diabetic retinopathy (Table 4.1), the leading cause of blindness in adults [359], [360], [362], [363], [397], [398].

With this knowledge, it is clear that systemic improvements must be made in retinal oximetery if it is to become a diagnostic device capable of being integrated into a clinical workflow. To achieve more accurate oximetry

Table 4.1 – Summary of retinal oximetry investigation of diabetic patients with or without diabetic retinopathy. The source column describes the source article and the machine used in the measurement. (Abbreviations: SO_2-A = Arterial oxygenation; SO_2-V = Venous oxygenation ; No DR = diabetic without retinopathy; NPDR = non-proliferative diabetic retinopathy; PDR = proliferative diabetes)

Source	Vasculature	Control	No DR	NPDR	PDR
Hammer *et al.* (2009)	SO_2-A	97±4	-	100±5	101±4
Imedos	SO_2-V	63±5	-	75±5	75±8
Hammer *et al.* (2012)	SO_2-A	97±6	-	97±6	-
Imedos	SO_2-V	66±5	-	68.8±7	-
Hardarson *et al.* (2012)	SO_2-A	93±4	-	-	100±5
Oxymap T1	SO_2-V	58±6	-	-	67±8
Khoobehi *et al.* (2013)	SO_2-A	92±4	96±9	102±10	104±9
Oxymap T1	SO_2-V	57±6	59±8	67±8	67±10
Jorgensen *et al.* (2014)	SO_2-A	95±1	94±2	96±1	99±2
Oxymap T1	SO_2-V	63±1	64±2	66±2	68±2
Guduru *et al.* (2016)	SO_2-A	91±4	89±8	96±14	100±7
Oxymap P2	SO_2-V	53±6	53±10	63±13	66±11

measurements and to make calibration-free systems, one solution is to include more wavelengths in the analysis to allow automatic compensation of wavelength-dependent scattering and absorption. To this end, a similar, calibration-free, solution to the ODR method used in two-wavelength oximeters was proposed by Hammer *et al.* using a 4-wavelength approach which normalizes the spectra to more than one hemoglobin isosbestic point [399]. Techniques that detect greater than 4 wavelengths routinely deploy a statistical regression method to fit the known absorption profiles of oxygenated and deoxygenated hemoglobin. Since the signal to noise ratio is proportional to the square root of the number of wavelengths considered, the more wavelengths measured, the more robust the oximetry measurement can be [400]. Furthermore, not only do these techniques allow for more robust measurements with respect to noise, they also improve the separation of hemoglobin absorption from parasitic optical attenuations such as tissue scattering, glint, and absorption from the other chromophores present in the eye. These methods, however, are not without their own flaws and, as will be seen in the present work, can be further improved upon using modern neural network approaches to achieve a precision of oximetry required for clinical use.

Firstly, as with two-wavelength techniques but to a lesser degree, multi-wavelength algorithms are sensitive to the wavelength-dependent variability from the different absorbers and scatterers in the eye. Simply-put, this is due to the optimization problem in regression analysis being a minimization of the error between the measured spectra and its respective fit using the regression components provided. This can become a problem when the best fit does not directly give the most accurate calculation of oxygenated hemoglobin, namely in the cases where the regression analysis either is missing components that are contributing to the spectral shape, or has too many components allowing untrue solving options.

Secondly, spectral mis-calibration is a problem that can appear in spectroscopy applications and often goes unnoticed. This occurs in oximetry when a measured spectra for a known chromophore and the reference spectra used to fit said chromophore is not wavelength-matched. This can play a pronounced role in oximetry techniques that use isosbestic points for calibration (2-4 wavelength techniques) as even highly-cited sources of reference absorption spectra for hemoglobin can vary; this was shown recently, in-depth, in near infrared (NIR) oximetry [401]–[404]. Adding this to possible spectrometer mis-calibration and spectral temperature variations, spectral shifting can be an important variable in measurement precision and accuracy.

Thirdly, retinal oximetry has historically focused on effective oxygen saturation (SO_2). This is by definition the ratio of hemoglobin carrying oxygen to hemoglobin capable of carrying oxygen (oxygenated hemoglobin (HbO_2) and deoxygenated hemoglobin (Hb))[405]. The mathematical representation of oxygen saturation (SO_2) can be found in equation 4.1, where C_{HbO_2} is the concentration of oxygenated hemoglobin and C_{Hb} is the concentration of deoxygenated hemoglobin. This is a useful parameter since it describes the oxygen carrying capacity, however, as it does not take into account dyshemoglobins (hemoglobin conformations which cannot carry oxygen), it does not directly measure the amount of circulating oxygen. A direct measurement of the oxygen concentration is only available in the calculation of fractional oxygen saturation (SO_2^{fr}) as it includes the most commonly present dyshemoglobins in humans: carboxyhemoglobin (COHb) and methemoglobin (MeHb), each making up roughly 1% of hemoglobin in healthy individuals[405]. SO_2^{fr} can be seen in equation 4.2, with the newly represented concentrations of COHb and MeHb, C_{COHb} and C_{MeHb}, respectively. [406]. Contrary to their traditional exclusion in retinal oximeters, knowing and accounting for these conformations is critical as their concentrations are dynamic and can be a source of considerable error, as has been shown in pulse oximetry [407]–[409]. COHb levels vary greatly between individuals, with the main factor of variation being frequency of smoking and living environment air pollution [410]–[413]. Healthy individuals that do not smoke have an average C_{COHb} of approximately 1%; however, due to environmental differences and working conditions, this can rise to as high as 3% [413]. Cigarette smokers in particular can have highly elevated COHb levels (5%-15%), depending on smoking habits and time since last smoke inhalation [410]–[412]. Furthermore, levels can reach upwards of 40% in cases of carbon monoxide poisoning [414]. MeHb is also, on average, approximately 1% in healthy individuals[406]. However, during methemoglobinemia conditions (defined as $C_{MeHb} > 2\%$) the concentration can increase to nearly 70% before death, and is more common than expected [415]. Moreover, below a fractional concentration of 15% of either dyshemoglobin, there are no observable symptoms, which further shows the need for oximetry techniques to be able to sense and account for their presence automatically.

$$SO_2 = \frac{C_{HbO_2}}{C_{Hb} + C_{HbO_2}} \tag{4.1}$$

$$SO_2^{fr} = \frac{C_{HbO_2}}{C_{Hb} + C_{HbO_2} + C_{COHb} + C_{MeHb}} \tag{4.2}$$

We present here the novel use of CNNs to overcome the aforementioned shortcomings in current retinal oximetry calculations for directly quantifying SO_2 and SO_2^{fr} concurrently in a reproducible, robust way. Convolutional neural networks (CNNs) have been finding more and more use in the biomedical field both in image recognition [416]–[421] and spectral identification [422]. For spectroscopy, CNNs have incredible advantage over statistical regression techniques, owed mainly to their ability to learn and weigh the importance of different spectral regions automatically. Furthermore, they learn this weighting of spectral characteristics with no prior knowledge of the constituent's absorption spectra. This is extremely interesting for heterogeneous tissue spectroscopy where the total attenuation is measured, as the individual attenuation coefficients for each unique structure in the optical integration volume are not always well defined, and in this case need not be. The challenge with using CNNs in retinal oximetry is to obtain large enough datasets with realistic optical variations but, most critically, with validated oxygenation measures. This difficulty results from the lack of gold-standard measurements in tissue oximetry of the eye, the prohibitive costs associated with patient measurements if there was such a technique to provide valid training targets, and the fact that current optical phantoms are too simplistic to replicate the eye appropriately.

Our solution is to train a CNN solely on a large number of simulated diffuse reflectance spectra which accurately mimic the variability in *in vivo* measurements on the optic nerve head (ONH) in humans. The CNNs were compared with several reported algorithms in an un-biased way on a wide range of test data-sets to show it's non-incremental improvements in oximetry calculation performance. This technique of training using simulated

spectra based on only a few *in vivo* measurements allows us to have an abundance of training data not traditionally available in biomedical applications. In an attempt to validate that this training technique could indeed create a CNN that had improved accuracy for *in vivo* measurements, where there are many unknowns and much optical property variation, we compared the performance of the CNN algorithms on spectra having variable contributions from chromophores not seen in the training data to regression algorithms that did not have the chromophores available for fitting in their analysis.

4.4 Methods

4.4.1 Data Creation

The method focuses on demonstrating the superiority of neural networks to extract oxygenation values from simulated data. The models used to simulate the data are based on our experience with *in vivo* measurements. Specifically, *in vivo* spectra previously acquired from the ONH of subjects using a multi-wavelength oximetry device (Zilia Inc., Quebec City, Canada) were used to model the simulated datasets based on the absorption coefficients of visible-wavelength chromophores present in the eye. An example of an experimentally measured spectra from a human ONH can be found in figure 4.1 (a). The 100 μm spot size allows us to ignore chromatic aberrations often observed in high resolution scanning systems. To model the highly scattering myelinated structure of the ONH we added a wavelength-dependent scattering component to account for optical path-length variations [423], [424], as has been done routinely in the past for retinal oximetry applications [374], [400], [425], [426]. Specifically, the normalized scattering factor proposed by Jacques *et al.* was applied with variable terms used for the reduced scattering coefficient and the scattering power[92]. We did not consider contributions coming from choroidal-vasculature cross-talk as it has been shown that minor contributions occur below 600 nm [41]. Absorption coefficients for the following chromophores were included in the data creation: HbO_2, Hb, COHb, MeHb [427] and retinal melanin[428]. A variable-magnitude constant factor (CF) was added to account for changes in light intensity. The mathematical representation of the data creation for a simulated spectra (S1) is shown in equation 4.3. A variable blood volume factor (B) was multiplied to the hemoglobin absorption component to vary the overall hemoglobin absorption. The variable combination of reflected intensity, wavelength-dependent scattering and reflections, as well as variable blood volumes can provide a reasonable simulation of different blood vessel sizes and varying amounts of specular reflection (also known as glint). The result of all these factors created extremely variable datasets, as one would expect to find in real life situations due to the vast variability in human eyes. The addition of all the fractional hemoglobins (including dyshemoglobins) in a given spectra were constraint to always equal to 100%. The known concentration for each absorber was saved in a separate file and either used for training (only in the case of CNN) or evaluation.

$$\begin{aligned} S1 = (C_1 * \mu_{a,HbO_2} + C_2 * \mu_{a,Hb} + C_3 * \mu_{a,COHb} + C_4 * \mu_{a,MeHb}) * B \\ + C_5 * \mu_{a,Retinal\ Melanin} + a * (\frac{\lambda}{500nm})^{-b} + CF \end{aligned} \tag{4.3}$$

After analyzing performances of the extraction algorithms on spectra made with the known chromophores, we created a subset of spectra (S2) having two variable yellow-lens-protein contributions added, as defined by Dillon *et al.* [429]. This addition was chosen as it is well established that there is a presence of yellowing proteins on the lens of aged and diseased individuals and therefore it is often in the optical path of the spectroscopic detection [394], [429], [430]. The absorption spectra for the yellowing proteins were purposely left out of the linear regression analyses and a CNN was trained on data without their inclusion. This constituted an integral performance comparison as there are often unknown contributions in a detected spectra in *in vivo* tissue spectroscopy. CNNs require no previous knowledge of reference spectra and therefore can learn to be completely invariant to

Table 4.2 – Variable ranges for spectral components

Variable	B	C1 (%)	C2 (%)	C3 (%)	C4 (%)	C5,C6,C7	a	b	CF
Range	[-0.1 - 0.1]	[0 - 100]	[0 - 100]	[0 - 100]	[0 - 100]	[0.01-0.05]	[0 - 3]	[0.1-3.0]	[0-1]

this addition with *in vivo* training data and so we also included another CNN, trained on data that had yellow protein contributions included, to show this effect. The first CNN without yellow proteins in the training data exemplifies how much more robust the machine-learned weighting is when presented with unknowns; the second CNN, with yellow proteins in the training data, how improved a CNN can become with *in vivo* training. The mathematical representation of the data creation for a simulated spectra (S2) is shown in equation 4.4.

$$S2 = S1 + C_7 * \mu_{a,Yellow\ Protein_1} + C_6 * \mu_{a,Yellow\ Protein_2} \tag{4.4}$$

The ranges of coefficients used in the elaboration of the spectra, defined in equations 4.3 and 4.4, are shown in table 4.2. Due to the focus on spectra originating from the ONH, the melanin contribution was assumed to be quite small and this matched the experimental reference spectra. A normalized representation of the chromophores' absorption coefficients can be found in figure 4.1 (c). For comparison, an *in vivo* spectral measurement taken on a patient's ONH with a predicted SO_2^{fr} of 68% is shown in figure 4.1 (c) along with randomly simulated spectra with SO_2^{fr} = 68% for both a typical non-smoker (COHb and MeHb $<=$ 1%) and a typical smoker with an elevated COHb concentration of 6% in figure 4.1 (b) and (d), respectively.

4.4.2 Algorithms

4.4.2.1 Convolutional Neural Networks

Opthalmology is a field that, in recent years, has seen a considerable increase in the implementation of machine learning (ML) due to impressive advancements in deep learning architectures and novel optical technologies providing more information from the retina. Recently, ML has been exploited to analyze visible images of the retina for DR diagnosis, OCT datasets to monitor retinal changes in AMD and even to automatically segment individual photoreceptors in adaptive optics ophthalmoscopy [431]–[433]. While others have focused on imaging applications, we present the use of ML to analyze 1-dimensional (1D) spectroscopic information.

Of the many state-of-the-art machine learning algorithms attempted, CNNs achieved the best performance of oximetry calculation as it is by nature optimally suited for handling spectral signals. A full description of CNNs is beyond the scope of this work (see the references [434]–[437] for a comprehensive overview), but this section will describe them briefly. CNNs can consist of several layers of operations which transform the input into a desired output, in our case, the input is a spectrum with many optical contributions and the output is the four hemoglobin quantities. While the CNN has no previous knowledge of any hemoglobin reference spectra, its training allows it to perform calibration-free calculations on their concentrations.

The training process is governed by two main operations: the convolution and the pooling. A convolution is the integral of point-wise multiplications between network parameters and an input. These parameters are random at the beginning of the optimization and become specific to the task at hand as the network is introduced to more data. These learned parameters are termed filters.

Simply put, in our case, the convolution operation can be seen as a scalar product between multiple patches of the spectra and multiple filters. Moreover, many different filters are applied to the same spectra in order to extract different types of features. The set of filters that are chosen creates what is called a kernel and all the features extracted are designated as "feature maps" (each map is associated to a filter). The intelligence of the

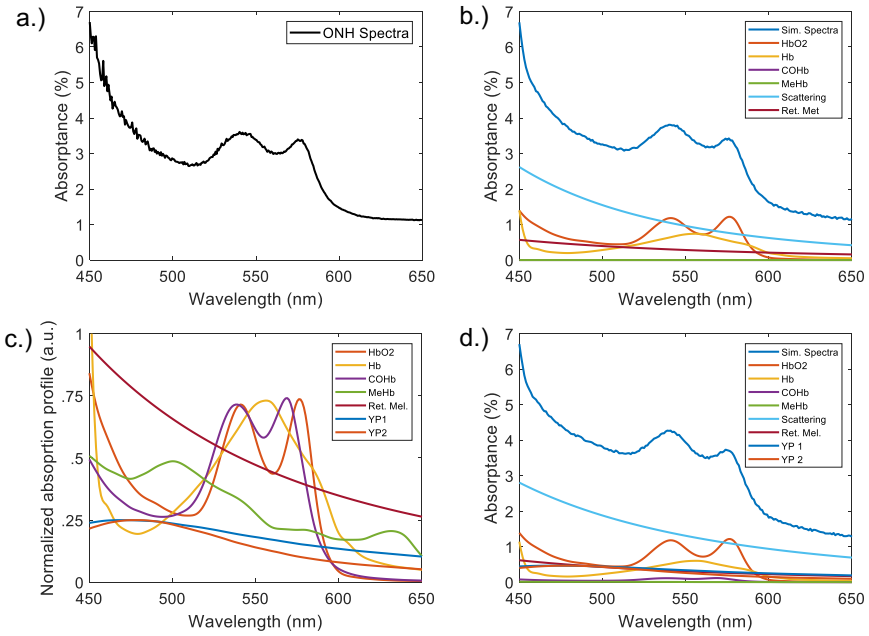

Figure 4.1 – Data creation. a.) Example spectrum taken *in vivo* on a human optic nerve head with an SO_2 of 68% b.) Randomly simulated spectrum with an SO_2 of 68%. Components are plotted to scale of their randomly generated amplitudes for this specific spectra. c.) Normalized absorption coefficient spectra used in simulated spectra creation. d.) Randomly simulated spectra with an SO_2^{fr} of 68%, COHb present at a 6% fraction and a random combination of yellow protein contributions. Components are plotted to scale of their randomly generated amplitudes for the specific spectrum. Abbreviations: ONH = Optic nerve head; Ret. Mel. = Retinal Melanin; YP1 = Yellow protein 1; YP2 = Yellow protein 2.

algorithm stems from the fact that the weights of all the filters are learned from the data itself by optimization, thus only the data dictates which features are important and should be extracted from the spectra. This is very important, for instance, if the data is noisy, the network will learn filters that are resilient to noise.

Subsequently the pooling step is applied to make the extracted features invariant to their position. Explicitly the feature maps are passed through a type of non-linear downsampling function allowing a pre-defined variable to be considered over all the features (in our case, we take the max value as our variable, therefore we perform "max-pooling.") The explanation of this step is that the exact location (wavelength) of a feature (*i.e.* the HbO_2 peak around 580 nm) is less important than its relative location to other features within a certain range, which effectively gives the algorithm its prediction invariance to spectral shifting in this range.

Using the Keras API in Python, we trained four CNN algorithms in total: 1.) a short wavelength range (500 nm - 600 nm) network trained without yellow protein absorption in the spectra (CNN-SW), 2.) a long wavelength range (450 nm - 650 nm) network trained without yellow protein absorption spectra (CNN-LW), 3.) a short wavelength range (500 nm - 600 nm) network trained with yellow protein spectra included (CNNYP-SW), 4.) a long wavelength range (450 nm - 650 nm) network trained with yellow protein spectra included (CNNYP-LW).

The adopted network has a feature extractor consisting of CNN layers and a multi-output regressor which is a fully connected layer having the four hemoglobin concentrations as outputs. The amounts of SO_2 and SO_2^{fr} were then calculated using equations (4.1) and (4.2) in a similar fashion to post-linear regression analysis. The four networks all have the same architecture, only the training data and wavelength range is varied. The feature extractors have three convolution layers having respectively 128, 128, and 64 filters. Each convolution layer has a kernel size of 25 and is followed by an exponential linear unit (ELU) activation and max pooling layer with a pooling size of 2. The output of the feature extractor is the concatenation (or flattening) of all 64 filters of the last convolution layer which was first normalized. The choice of the ELU has two desirable properties: producing a zero-centered distribution, which can make the training faster; and having one-sided saturation which leads to better convergence. For optimization, the ADAM optimizer was used, which is essentially an adaptive version of Stochastic gradient descent. Finally, the loss function for the training optimization was the summation of the mean squared errors between the predicted values and the observed values for all four of the hemoglobin concentrations.

Specifically, the network was trained using a dataset of randomly simulated spectra as described in the Data Creation section. The set contained 20,000 simulated spectra of which 75% were used to optimize the parameters of the network and the rest to validate their performance. The validation partition was used to stop the training early when the network performance on the validation dataset was optimal, rather than optimizing on and overfitting the training dataset. While the training dataset is large, it exemplifies the major advantage of training using simulated data. Once calibration data has been acquired, the pre-trained network could be retrained in an iterative fashion with a decreased demand for experimental data. For fairness in our comparison, their is no overlap between the training set and the testing sets (used for comparison between algorithms).

4.4.2.2 Comparison Algorithms

We included 6 different algorithms in our comparison of the CNNs. Two of the algorithms were previously published[399], [425] and replicated in MATLAB and the other 4 were designed in-house using MATLAB. We will go over the 6 algorithms in more detail in this section.

Two-wavelength imaging oximeters require extensive calibration using measurements on and off of an artery at an isosbestic wavelength for normalizing and a non-isosbestic wavelength for contrast. The technique is sound but incomplete spectral information often leads to variable and non-quantitative oximetry measurements. To present an alternative to these techniques using only spectral data and no imaging data, the first algorithm considered was the 4-wavelength technique by Hammer *et al.*[399]. This algorithm is similar in that the oximetry calculation is based solely on a single contrast wavelength however it uses three HbO_2/ Hb isosbestic wavelengths to remove scattering and absorption variability. In this article, we will refer to this algorithm as the Hammer algorithm (HA). The pros of this algorithm are that it is fast, calibration-free, and requires only 4 wavelengths for calculation. In short, first a measured spectrum is linearly transformed such that the slope between the isosbestic points of 522 nm and 586 nm matches the reference spectra. Subsequently the data between the isosbestic points is stretched or compressed to match the 3rd HbO_2/ Hb isosbestic wavelength at 569 nm. The oxygen saturation is then calculated using the intensity at 560 nm corresponding to one of the characteristic peaks of HbO_2. More detailed information can be found in their publication [399]. Of course, since the oxygen sensing contrast is based on a single point, this technique is susceptible to noise. Furthermore, it cannot yield measurements for SO_2^{fr} as it only considers the presence of HbO_2 and Hb.

The second algorithm was a remake of a linear regression algorithm reported by Diaconu using the lsqnonneg.m function in MATLAB. In the regression analysis it included a constant component, multiple ocular media components as defined, and Hb and HbO_2 absorption spectra [425]. Here, we will refer to the algorithm as the Diaconu algorithm (DA). This algorithm is great at *fitting* the spectra due to the many ocular media components; however, the goal in oximetry is to optimize oxygen sensing, not necessarily spectral fitting - an important distinction.

The third algorithm was a simple linear regression analysis also using lsqnonneg.m in MATLAB, but with fewer components. This regression analysis solved only using a constant factor, a fixed wavelength-dependent scattering coefficient ($a = 1$, $b = -2$, in scattering equation), retinal melanin, Hb and HbO_2 excinction spectra [92], [402], [427], [428]. This algorithm will be referred to simply as algorithm 3 (A3). A general rule for thumb in linear regression analyses are that the less components for solution, the better.

The fourth algorithm was identical to the third, with the addition of COHb and MeHb absorption spectra added to the linear regression solving components. This algorithm was, therefore, the only one that could be used to compare the performance of SO_2^{fr} calculation against the CNN. This algorithm will be referred to simply as algorithm 4 (A4)

As our work focuses on spectra in the visible wavelength region we examined two spectral windows for calculation in all of our in-house algorithms. The first, an intrinsically HbO_2/Hb peak weighted range of 500 nm - 600 nm, termed small window (SW). The second, a larger range 450 nm - 650 nm, termed large window (LW) which could have advantages for instance in CNNs where weighting is learned.

4.4.3 Statistical analysis

To compare the different algorithms, we looked at the mean absolute error (MAE) between the predicted value (p) and the known value (k) for SO_2 and SO_2^{fr}. Each test dataset included 10000 spectra and was analyzed by each algorithm. MAE was calculated using equation 4.5. In addition to MAE, which provides a measure of accuracy of calculations, we also looked at the standard deviation (STD; equation 4.6), as it provides a metric for prediction precision. The results will be presented as MAE being the highlight of the result with STD shown as the error bars.

$$\text{MAE} = \frac{\sum_{i=1}^{n} ||p_i - k_i||}{n} \tag{4.5}$$

$$\text{STD} = \sqrt{\frac{1}{N}\sum_{i=1}^{N}(x_i - \overline{x})^2} \tag{4.6}$$

4.5 Results

Base performance of SO_2 calculation

We first performed bench-marking of the different algorithms for the calculation of SO_2 in traditional conditions, without the unknown yellow protein contribution. The datasets were analyzed using each algorithm and the respective SO_2 results were compared against the known values. Four different cases were examined: 1) test spectra without any dyshemoglobins to replicate traditionally investigated scenarios, 2) test spectra having 1 % of each dyshemoglobin to replicate healthy human hemoglobin concentrations, 3) test spectra having a fixed concentration of COHB of 6 % and MeHb of 1 % to replicate a normal smoker's hemoglobin concentrations, and 4) test spectra consisting of completely random combinations of all the dyshemoglobins to measure general performance. In all cases both the small window and large window CNN had the least error in measuring SO_2 as shown in figure 4.2.

4.5.1 SO_2 calculation in the presence of unknown yellow lens proteins

In our second example we examined the robustness of the different algorithms in the presence of absorbers with unknown reference spectra. This example represents the real life scenario where some reference spectra

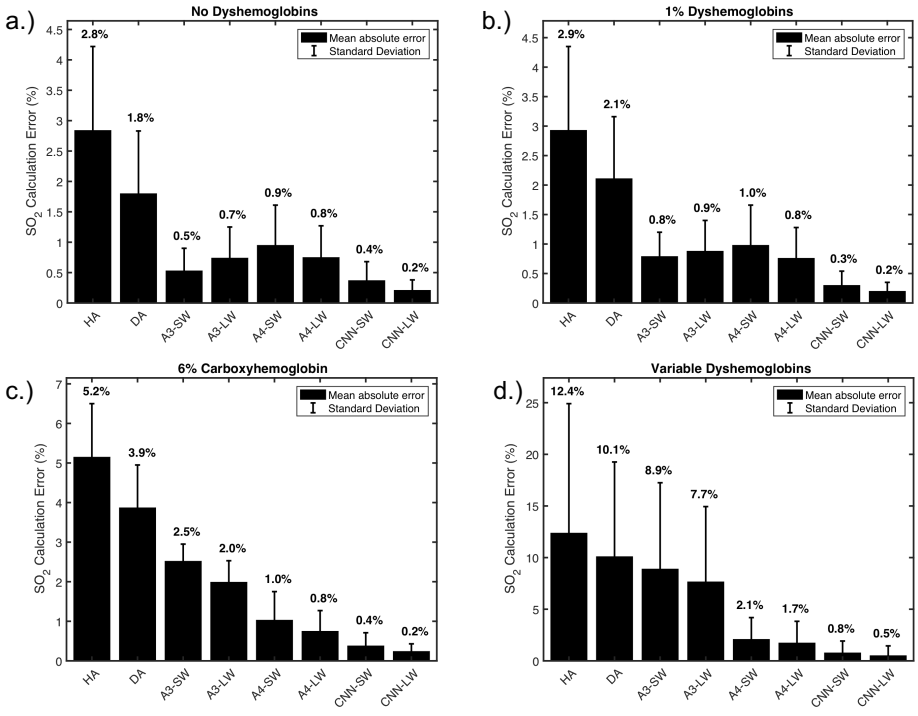

Figure 4.2 – Performance of SO_2 calculations using various oximetry algorithms. a.) Test dataset spectra without COHb or MeHb. b.) Test dataset spectra include 1 % COHb and MeHb contributions to the hemoglobin absorption component. c.) Test dataset spectra include 6 % COHb and 1 % MeHb contributions to the hemoglobin absorption component. d.) Test dataset spectra include a random contribution of each hemoglobin conformation. The printed numbers above each bar correspond to the mean absolute error value for the given algorithm.

required to perfectly fit a measured spectrum are not available or unknown. The chosen unknown absorbers in this case were two yellow proteins which are biologically relevant as they can accumulate on the lens during normal aging. For clarity, CNN-SW and CNN-LW were trained without yellow protein absorption present in the training data. We performed the same benchmarking conditions as in the previous section (no dyshemoglobins, 1 % dyshemoglobins, 6 % COHb and 1 % MeHb, and variable dyshemoglobins) and the results are shown in figure 4.3. We also added two new algorithms to the analysis at this step, CNNYP-SW and CNNYP-LW, which are simply CNNs that have been trained using the same protocol but with training data including yellow proteins contributions.

As we see CNN-SW, having never seen the yellow proteins, still provided robust analysis in all scenarios. CNN-LW loses some performance, however, it remains on-par or better than the other non-CNN algorithms. The CNNs trained with the yellow proteins, of course, showed dramatic improvements over the other algorithms.

4.5.2 Base performance of SO_2^{fr} calculation

While SO_2 can be a useful measurement, SO_2^{fr} may have more clinical relevance in the evaluation of hemodynamics. SO_2^{fr} allows the computation of the total amount of oxygen present in the blood, rather than only the

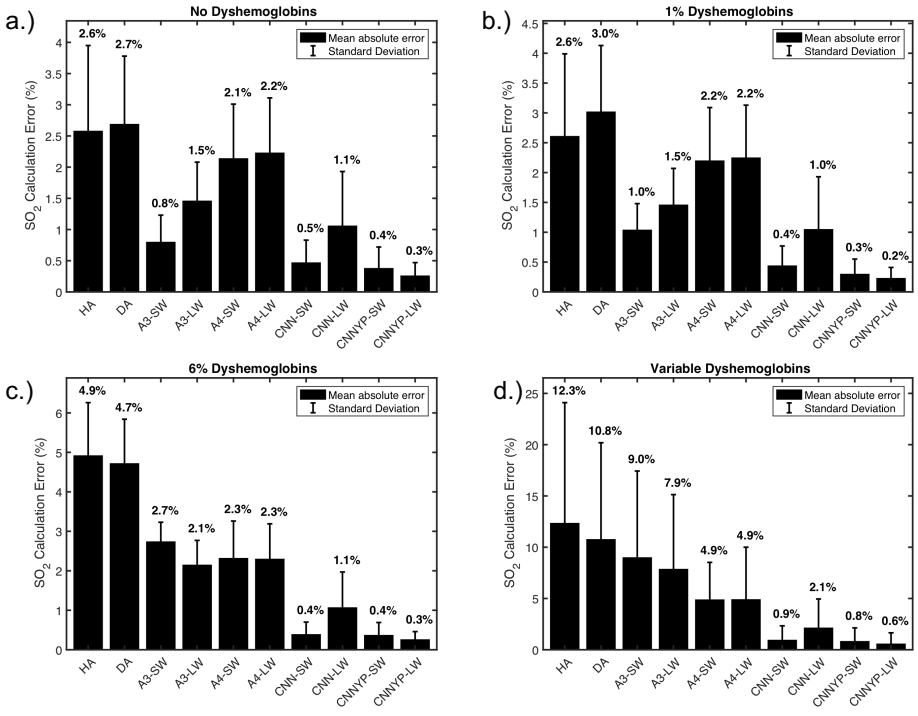

Figure 4.3 – Performance of SO_2 calculations on datasets including contributions from yellow protein components, using various oximetry algorithms. In this scenario, the linear regression analyses do not include the yellow proteins component for solving and the CNN was not trained on data having yellow proteins contributions a.) Test dataset spectra without COHb or MeHb contributions. b.) Test dataset spectra include 1 % COHb and MeHb contributions to the hemoglobin absorption component. c.) Test dataset spectra include 6 % COHb and 1 % MeHb contributions to the hemoglobin absorption component. d.) Test dataset spectra include a random contribution of each hemoglobin conformation. The printed numbers above each bar correspond to the mean absolute error value for the given algorithm.

ratio of oxygenated to oxygenatable hemoglobin. The measurement of SO_2^{fr} therefore adds a second useful variable for retinal oximetry to use towards the monitoring and diagnosis of diseases. There are two likely reasons for why SO_2^{fr} is routinely ignored in retinal oximetry: 1) 2-wavelength systems do not have the capability to sense it, and 2) the current algorithms used with multi-wavelength systems lack the high accuracy necessary for its calculation. As seen in figure 4.4, the CNN algorithms detect SO_2^{fr} with a much higher precision than the linear regression algorithms both with and without the presence of the yellow protein components. In the scenarios including yellow protein, we include the results from both CNNs to once again show the different advantages offered depending on the training.

4.5.3 Noise, spectral shifting and spectral resolution resilience

To analyze the resilience of the CNNs, we compared it against the top performing algorithms at calculating SO_2 when noise, spectral shifting and lowered resolution were applied to spectra datasets having no dyshemoglobins or yellow proteins to isolate the performance variables. We also included the HA algorithm in the noise and

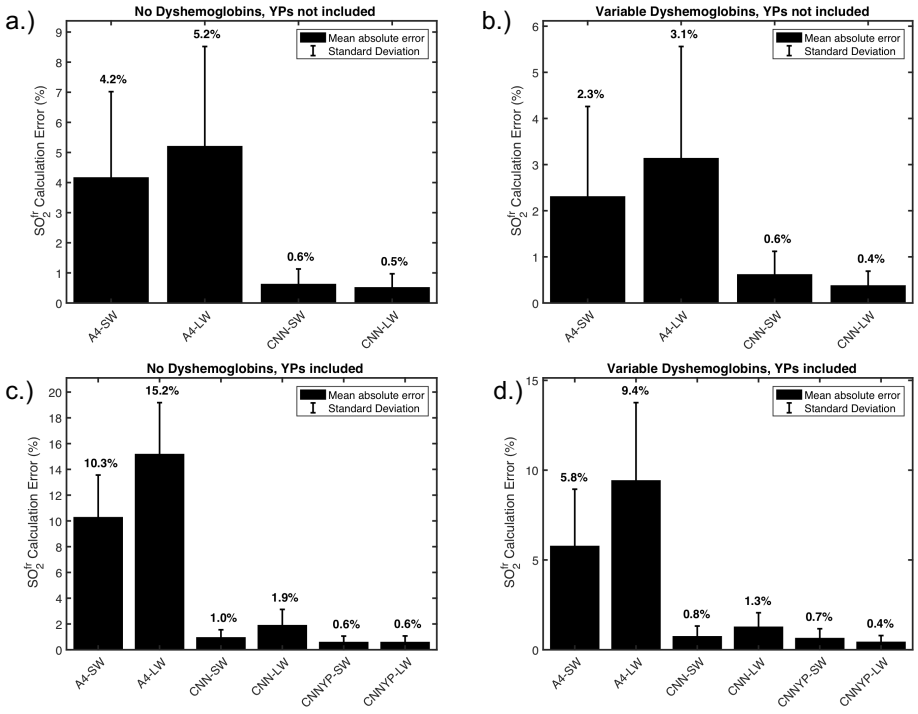

Figure 4.4 – SO_2^{fr} calculation performance on test data-sets with and without dyshemoglobins and yellow proteins. a.) Test data-set spectra do not include COHb, MeHb or yellow proteins. b.) Test data-set spectra do not include COHb or MeHb but do include a variable amount of yellow protein contributions c.) Test data-set spectra include random amounts of all hemoglobin conformations but do not include yellow protein contributions. d.) Test data-set spectra include random amounts of all hemoglobin conformations and include yellow protein contributions.

spectral shifting analyses to exemplify the improvements even the linear regression techniques bring over few-wavelength systems. In the case of noise application, 11 test datasets were created with a fixed amount of white Gaussian noise and the algorithms were run on each dataset. As can be seen in figure 4.5 a.) the CNN-LW had the best performance, however the linear regression algorithms (A3 and A4) were comparable. The poor performance of the HA algorithm in this test was to be expected due to the use of a single point intensity for oxygenation measurement after isosbestic calibration.

In the case of spectral shifting between reference spectra and measurement spectra (4.5 b.)), test data-sets were created and their corresponding wavelength was shifted from -4 nm to $+4$ nm to examine the effect of spectrometer mis-calibration, temperature changes or the use of incorrect reference spectra. The HA algorithm also performed poorly in this test as the shift ultimately leads to the use of invalid isosbestic wavelengths, greatly affecting the reliability of calculations. This is the case for any two-wavelength system, and therefore a lot of attention must be placed on the system's calibration. On the other hand, perhaps one of the most exciting advantages of using a CNN is the ability of the algorithm to be completely invariant to spectral shifting due to the convoluted nature of the calculation, as seen in figure 4.5 b.).

In the case of a decrease in spectral resolution, test data-sets with increasing distance between spectral points and

therefore decreasing resolution were created at a fixed noise factor of 3 to apply some stress to the algorithms. Interestingly, the CNN-LW performed considerably better than CNN-SW and their statistical linear regression counterparts at SO_2 calculation. The HA algorithm could not be included in this experiment as it uses four fixed wavelengths.

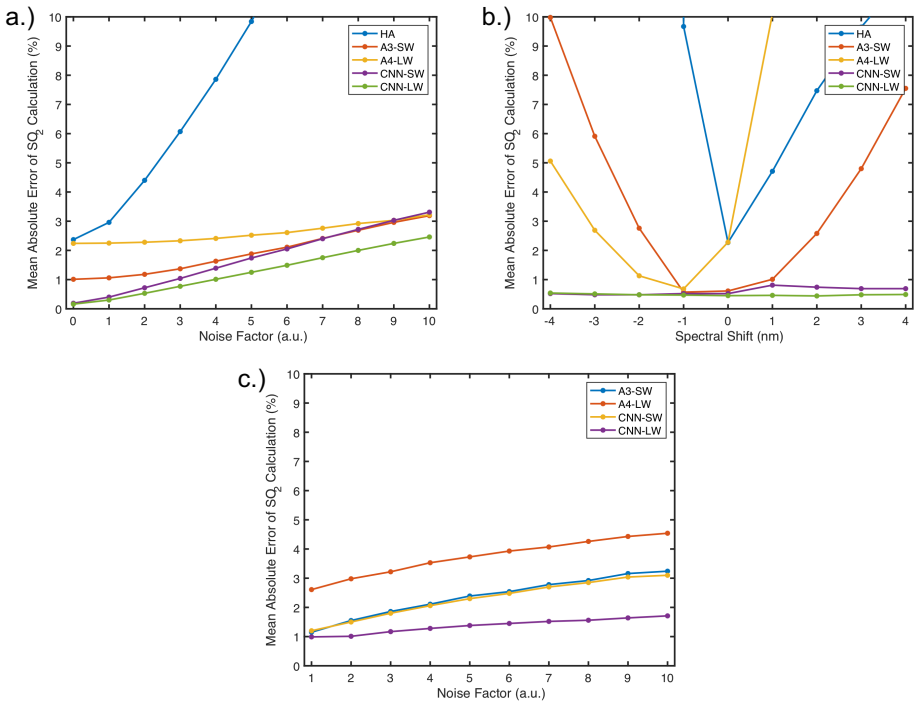

Figure 4.5 – Performance of SO_2 calculations, measured using the mean absolute error statistic, on test datasets with varying stresses. a.) Test datasets were created with varying amounts of noise applied to the spectra. b.) Test datasets were created with varying amounts of spectral shifting from reference spectra. c.) Test datasets were created with decreasing spectral resolution.

4.6 Discussion

Our results show the improvements of CNNs, trained only using simulated data, to perform high accuracy oximetry in comparison to four-wavelength, isosbestic, algorithms and many-wavelength regression analysis techniques. We validated the CNN's robustness in the face of unknown optical contributions by showing its ability to outperform regression analysis when analyzing spectra having simulated yellow protein absorption (commonly observed on an aged lens) unseen in the training data.

To further validate the CNN algorithm experimentally, we have applied the it to ONH spectra acquired *in vivo* and measured similar values to that of linear regression techniques, however, without known oxygenation quantities this remains a qualitative observation. To improve the certainty of the algorithm, the next step will involve measuring optical phantoms infused with oxygen-calibrated whole blood samples. Importantly, while we plan to confirm the CNN's efficacy on these calibrated phantoms of known oxygenation, we believe that the training of the CNN using simulated data is a strength of our approach and will not likely be replaced by only experi-

mental measurements. That said, our simulations will be refined to better resemble the experimental data if need be. Among other advantages, including experimentally-inspired simulated data allows us to: 1) greatly increase our training data and 2) teach the algorithm to ignore non-oxygen related spectral changes by adding parasitic contributions to the spectra.

While the spectra created were made to mimic those obtained from the ONH, the scaling of the approach for any retinal structure, including blood vessels, can be easily implemented. It is important to mention that traditional two-wavelength retinal oximeters can only measure oxygenation of large blood vessels due to their limited spectral information. The system we have used to base our simulations performs spectroscopy at any location on the retina (Zilia inc., Quebec City), allowing tissue oximetry of the capillary bed within the optical integration volume.

The Beer-Lambert law predicts an exponential dependence of absorbance on the photon pathlength, highly scattering media (such as the ONH, retina, blood vessels) can lead to deviations from this observation. Previously, is has been reported that ONH measurements could be better fit using a percentage-based *absorptance*, rather than taking the logarithmic form of the measurement prior to regression analysis [425]. Keeping in mind that optimizing for fit does not necessarily mean optimal oximetry calculations, this observation could be argued. However, with neural networks, the exponential form of the data does not matter, due to the fact that no knowledge on the reference absorption coefficients are needed to perform the oximetry. This represents a major advantage of CNNs in that some complicated optical properties may not need to be as thoroughly investigated if the training data is experimentally-inspired [438], [439].

The different scenarios that were tested were chosen compare the algorithms without bias, not favoring CNNs. The first scenario we examined considered spectra without any dyshemoglobins. Even if this case is not the most biologically accurate, it was important to include it as it represents the only scenario considered by most current oximetry techniques. While CNNs always performed better, the A3-SW algorithm always should and does have the best performance of the non-CNN approaches. This can be explained by the fact that: 1) it uses the fewest solving components in its regression analysis therefore forcing the use of the HbO_2 and Hb absorption coefficients to optimize the regression, and 2) the small wavelength window innately weights the characteristic peaks of HbO_2 and Hb. The second case was the most biologically relevant with the concentrations of dyshemoglobins both restrained to approximately 1% - corresponding to the estimated amounts present in healthy individuals. As expected A3 algorithms should and do lose some performance in this scenario (since they do not include dyshemoglobins in their regression analysis). In the third case, spectra represent those of a healthy individual that is also a smoker, with COHb concentrations around 6 %. A4 algorithms should and do start to outperform the other non-CNN techniques at this point due to its inclusion of all hemoglobin conformations in the regression analysis. The fourth base performance test dataset consisted of a completely random combination of all the dyshemoglobins. This case showed the robustness of the various algorithms to any possible circumstance and provided a useful random metric. Overall, the first section, which included no yellow protein contributions, provided an important base performance analysis against existing techniques, in the conditions traditionally considered. Moreover, it showed the improvements CNNs can make in oximetry analysis in the presence of dyshemoglobins, making it the first technique which can accurately analyze tissue oxygenation in individuals with elevated levels of COHb and MeHb..

The second section, including the unknown yellow protein absorbers, provided a metric to compare the different algorithms when naive to the presence of a certain optical property. Specifically, this example showed two major advantages of CNNs. First, from the CNNs that are trained with no prior knowledge of the yellow proteins (CNN-SW and CNN-LW), we see that CNN-SW in particular is much more robust to the unknown addition than the regression and isosbestic analyses. We also see here that CNN-LW becomes on par in some cases with the next-best regression algorithm (A3-SW) that is naive to yellow proteins; however, it remains more robust in the the scenarios with increased dyshemoglobins. This leads us to the conclusion that if the goal is only

to measure SO_2 than the innate weighting of small wavelength range (500nm-600nm) is still optimal, even for neural networks. A possible explanation is that when the neural network is trained over a large wavelength range and tested on data with which it is familiar (data without yellow protein absorption) it takes full advantage of the wavelengths that, relatively, do not say much about hemoglobin oxygenation (outside of 500-600nm). Therefore, when a spectra has a new component (yellow protein) that is highly absorbing below 510 nm, it does not realize as readily that this is not caused by hemoglobin absorption changes. Whereas in the short wavelength range, the weights are better assigned. We also show that the improvements in using the longer wavelength range returns when the network is trained with yellow protein contributions present, allowing it to learn how to properly weight this region.

Second, from the CNNs trained on data having seen the yellow proteins (CNNYP-SW and CNNYP-LW) we better understand the importance of the fact that CNNs do not require prior knowledge of the constituents absorption spectra. This means that as long as the training data for the CNN is experimentally acquired and calibrated, it can learn to ignore non-important contributions during its optimizations, without dissecting and analyzing the each layer of the heterogenous tissue. CNNYP-SW and CNNYP-LW, we can therefore think of as the resulting accuracy we may attain if we train our network using spectra measured from calibration phantoms and *in vivo* measurements. Likewise, with the same train of thought, we could imagine including all the absorption coefficients from known (and relevant) biological chromophores found in human ocular tissue in the training data, serving only to teach the neural network what is not an important wavelength region for oximetry calculations.

The third section analyzing SO_2^{fr} shows that CNNs can overcome the shortcomings of classical regression algorithms in measuring dyshemoglobins by providing a drastic (relative order of magnitude) improvement in measurement accuracy. These resulting improvements can be important not only for oximetry resilience but also for diagnosing dyshemoglobin-affiliated conditions, *i.e.* carbon monoxide poisoning and methemoglobinemia. Interestingly, the algorithms perform better when calculating SO_2^{fr} on the datasets with variable amounts of each hemoglobin conformation than in the cases with no dyshemoglobins present at all (figure 4.4 b.) vs 4.4 a.) for cases without yellow proteins contributions, and figure 4.4 d.) vs 4.4 a.) for cases with unknown yellow proteins contributions). This phenomenon is likely due to overestimation of the dyshemoglobins when they are present at low concentration. This is likely why most linear regression analyses choose to ignore the presence of dyshemoglobin altogether, since they are most often at low concentrations.

Overall, the examples show the strength of performance, robustness and versatility of the CNN approach to provide a new framework for the analysis of hemoglobin conformations and perhaps other biomarkers. While previous techniques vary in performance based on the scenario, the CNNs remain optimal, throughout all the sections. This is an important point, as in a device it is not desirable, nor often possible, to choose a specific algorithm to use based on the patient (ie. cataracts, smoker, methemoglobinemia). With the abundance of publications on retinal oximetry in recent years and its potential to be integrated in diagnostic efforts, we believe that switching to a more quantitative and universal system that can provide information about all hemoglobin conformations will greatly benefit oximetry analysis and applications.

4.7 Conclusion

We have presented theoretical evidence that neural networks have great potential in retinal oximetry for the quantitative assessment of both SO_2 and SO_2^{fr}. Specifically, we show that the neural networks we have designed have the lowest error in the estimation of SO_2 and that they can improve SO_2^{fr} prediction by roughly an order of magnitude, relative to the other oximetry algorithms considered. The additional information provided by the CNN in the form of accurate and concurrent SO_2^{fr} measurements could have profound effects on increasing the reliability and diagnostic applications of measuring retinal oxygenation. Furthermore, the deduction of

individual dyshemoglobin concentrations may add new variables towards novel diagnostic measurements.

Chapter 5

Anisotropic light scattering from myelinated axons in the spinal cord

Damon DePaoli[a,b*], Alicja Gasecka[a,b*], Mohamed Bahdine[a,b], Jean Michael Deschenes[a,b], Laurent Goetz[a], Jimena Perez-Sanchez[a], Robert P. Bonin[c], Yves De Koninck[a,b], Martin Parent[a], Daniel C. Côté[a,b]

* Authors contributed equally to this work

[a]CERVO Brain Research Center, 2601 Chemin de la Canardière, Quebec City, Quebec, Canada, G1J 2G3

[b]Center for optics, photonics and lasers, 2325 Rue de l'Université, Quebec City, Quebec, Canada, G1V 0A6

[c]University of Toronto, Leslie Dan Faculty of Pharmacy, 144 College St., Toronto, Ontario, Canada, M5S 3M2

5.1 Résumé

L'optogénétique est devenue un outil essentiel pour étudier et disséquer les circuits neuronaux du cerveau à l'aide d'un contrôle optique. Récemment, il a également commencé à être utilisé dans les enquêtes sur la moelle épinière et le système nerveux périphérique. Toutefois, les informations sur les propriétés optiques de ces régions sont rares. De plus, il existe un manque de données sur la dépendance de la propagation de la lumière en ce qui concerne l'organisation et l'orientation des tissus neuraux. Ces informations sont importantes pour des simulations efficaces et une planification optogénétique, en particulier dans la moelle épinière, où les axones myélinisés sont très organisés. À cette fin, nous rapportons des mesures expérimentales du coefficient de diffusion, validées avec trois méthodes différentes dans les directions longitudinale et radiale de la moelle épinière de nombreux mammifères. Dans notre analyse, nous trouvons qu'il existe effectivement une dépendance directionnelle de la propagation des photons lors de l'interaction avec des axones myélinisés organisés. Plus précisément, la lumière se propageant perpendiculairement aux axones myélinisés dans la substance blanche de la moelle épinière a produit un coefficient de diffusion réduit mesuré ($\mu_s^{'}$) of 3.52 ± 0.1 mm^{-1}, alors que la lumière qui se propageait le long des axones myélinisés dans la substance blanche produisait un $\mu_s^{'}$ of 1.57 ± 0.03 mm^{-1}, parmi les différentes espèces considérées. Cette diminution de 50 % du pouvoir diffusant le long des axones myélinisés est observée avec trois stratégies de mesure différentes (intégration des sphères, transmittance observée et méthode du punch-through). En outre, cette dépendance directionnelle du pouvoir diffusant et de l'atténuation globale de la lumière ne s'est pas produite dans les régions de la substance grise où l'organisation de la myéline est presque aléatoire. Les informations acquises feront partie intégrante de la préparation des futures simulations de transport de la lumière et de la planification optogénétique globale à la fois de la moelle épinière et du cerveau.

5.2 Abstract

Optogenetics has become an integral tool for studying and dissecting the neural circuitries of the brain using optical control. Recently, it has also begun to be used in the investigation of the spinal cord and peripheral nervous system, however, information on these regions' optical properties is sparse. Moreover, there is a lack of data on the dependence of light propagation with respect to neural tissue organization and orientation. This information is important for effective simulations and optogenetic planning, particularly in the spinal cord where the myelinated axons are highly organized. To this end, we report experimental measurements for the scattering coefficient, validated with three different methods in both the longitudinal and radial direction of multiple mammalian spinal cords. In our analysis, we find that there is indeed a directional dependence of photon propagation when interacting with organized myelinated axons. Specifically, light propagating perpendicular to myelinated axons in the white matter of the spinal cord produced a measured reduced scattering coefficient ($\mu_s^{'}$) of 3.52 ± 0.1 mm^{-1}, while light that was propagated along the myelinated axons in the white matter produced a measured $\mu_s^{'}$ of 1.57 ± 0.03 mm^{-1}, across the various species considered. This 50% decrease in scattering power along the myelinated axons is observed with three different measurement strategies (integrating spheres, observed transmittance and punch-through method). Furthermore, this directional dependence in scattering power and overall light attenuation did not occur in the grey matter regions where the myelin organization is nearly random. The acquired information will be integral in preparing future light-transport simulations and in overall optogenetic planning in both the spinal cord and the brain.

5.3 Introduction

Optogenetics, the use of light and genetic engineering to probe and manipulate cell activity, is an important emerging technology that is instrumental in decoding the functional organization of brain tissue. More recently, the technique has also shown promise in the study of the spinal cord and peripheral nervous system [89], [440], [441]. In the context of motor guidance, optogenetic tools have been used to establish the role played by individual neural populations in motor navigation and have shown potential for restoring function after spinal cord injury or motor neuron disease [442]–[445]. In the study of sensory and pain processing, experiments involving targeted optical stimulation have greatly expanded our knowledge about the connectivity and function of peripheral and spinal sensory neurons [148], [446]–[449]. In the future, *in vivo* control of somatosensory circuits will continue to enable researchers to study behavioural consequences of stimulation of specific classes of neurons under both normal and pathological conditions without confounding effects of genetic ablation or pharmacological intervention [450], [451].

A question that will continue to affect interpretation of optogenetic experiments is whether a lack of physiological response to the light stimuli comes from abnormalities in neural circuit activity or failure of the stimulation itself. Optogenetic control of nerve cell activity relies on the expression of light-sensitive proteins called opsins which generate depolarizing or hyperpolarizing currents when exposed to light [452]. Cell-selective and temporally precise control over action potential generation in neural circuits, however, requires a specific knowledge and consideration of the tissue optical properties and illumination profiles.

Understanding and overcoming obstacles related to targeted illumination is therefore an essential step in designing effective *in vivo* experiments. A critical difference between the optogenetic stimulation in the brain and in the spinal cord lies in the light delivery system. In the brain, light can be delivered to any cortical or subcortical regions through a fiber-optic tip, often extended deep into tissue with minimal reported changes in animal behaviour [453]–[455]. This approach is unlikely to be successful in the spinal cord or periphery because an implanted optical fiber would severely damage the white matter tracts, which have minimal redundancy and carry high information density. Furthermore, the spinal cord is a much smaller and more mobile structure in comparison to the brain making the targeting even more of a challenge. Light delivery systems are thus super-

ficial, wrapping around a nerve, or fixed immediately dorsal to the spinal cord [446], [456]. As a consequence, the light source is placed relatively far from the target activation region and light must pass through the myelinated dorsal white matter of the spinal cord before reaching the opsin-expressing gray matter. Evaluating light propagation patterns is therefore critical for efficient optogenetic modulation.

While anisotropic light propagation has been observed in many biological tissues, an important piece of information that is currently missing is the directional dependence of light scatter in the highly organized spinal cord [457], [458]. Indeed, in the brain it has been shown that nerve fiber orientation can induce a dramatic difference in effective attenuation depending on the angle of incident light with regards to the white matter tracts [459]. Given this, and due to the fact that the spinal cord contains very highly organized white matter tracts extending the length of the vertebrae, a more in depth characterization of this directional effect was required.

To this end we characterized the reduced scattering coefficient (μ_s') in both the radial and longitudinal direction of the myelinated fibers in perfused macaque spinal cord, as well fixed and fresh human spinal cord. We use integrating sphere measurements and validate with microscope images and the "punch-through" method[460]. We incorporate these data into a modified open-source 3-D Monte Carlo program (mxcxyz) to allow the use of multi-dimensional scattering coefficients. Although diffusion theory may not fully apply in these highly organized structures, we show that the light distribution that results has an ellipticity of 20%.

5.4 Results

We show herein that light propagation patterns in the spinal cord depend both on local tissue scattering properties as well as the regional tissue organization. With the goal of creating a more accurate simulation of light propagation at the output of an optical fiber positioned on the spinal cord we: (i) conducted scattering and absorption measurements in both the longitudinal and radial direction of cervical-level spinal cord and (ii) measured the effective attenuation coefficient in both the longitudinal and radial direction.

5.4.1 Scattering coefficient depends on white matter tract orientation

Spinal cord grey matter consists mainly of neuron and glial cell bodies along with non-uniform combinations of myelinated and non-myelinated nerve fibers. On the other hand, spinal cord white matter is built up almost entirely of highly organized myelinated nerve fibers. While the anisotrpoic nature of neural tissue is often ignored, it is generally accepted that overall, the myelinated axons in white matter lead to increased scattering in comparison to grey matter [92], [95], [461]–[463]. We show here that this is not always true, and that the direction of light propagation with respect to white matter fiber tracts plays a profound role in the observed scattering effects.

Specifically interesting, the white matter in the spinal cord has lower scattering in the longitudinal direction (along axons) and higher scattering in the radial direction (perpendicular to axons) compared to the grey matter present on the same slices. The results of these integrating sphere measurements are tabulated in figure 5.1. The difference in scattering power between the longitudinal and radial white matter was profound, with a 50% decrease measured in the longitudinal direction in all the tissues considered. The measurements in grey matter, however, produced similar results in both directions, suggesting that this effect arises due to the organized myelinated structures in white matter. While we measured μ_s' in each Cartesian direction (x,y and z), we reduce the terms to radial and longitudinal due to the symmetry of the organized myelin structures resulting in equal μ_{s_x}' and μ_{s_z}'. Moreover, our results in radial white matter are very much in agreement with previous measurements of μ_s' using a fiber optic probe [464].

We further validated the light transmission of two 1 mm fixed macaque tissue samples in both directions using

a transmission microscope (figure 5.1a and 5.1b). Indeed, we see the white matter regions have a directional dependence with respect to transmission which is in good agreement with the inverse of scattering relationship (white matter transmits more than grey matter in the longitudinal direction and less than grey matter in the radial direction). We also include images we have taken using coherent anti-Stoke Raman Scattering (CARS) in primate spinal cord, in the various directions, showing the organization of the spinal cord segments at sub-cellular scale for reference (figure 5.1c and 5.1d). In all the experiments, the measured absorption coefficient in all tissue regions and sections were below 0.1 mm^{-1}.

As an additional and final validation that the reduced scattering coefficient is anisotropic in the white matter of the spinal cord, we performed the punch-through [460] method. We experimentally estimate the relative values of μ_{eff} in perfused mouse and macaque spinal cord white and grey matter sections, also in the longitudinal and radial directions. Due to the limited thickness of mouse spinal cord, it is not possible to obtain tissue samples for which the diffusion approximation is valid and $\mu_{\text{eff}} = \sqrt{\mu_a(\mu_a + \mu_s(1-g)}$. Nevertheless, the initial exponential decrease is related to μ_{eff}. As seen in table 5.2, we found the light traveling along the white matter tract axis is also roughly 50% less attenuated than light traveling perpendicular to the white matter tract. We again observed the lack of a directional preference in the the grey matter structures, due once again to the lack of organized myelin.

Table 5.1 – Measured values of $\mu_s^{'}$ in in longitudinal and radial directions at 633 nm

Species	Tissue Type	$\mu_{s_{Long}}^{'}$ (1/mm)	$\mu_{s_{Rad}}^{'}$ (1/mm)
Human (fresh)	White Matter	1.56 ± 0.2	3.51 ± 0.3
	Grey Matter	2.61 ± 0.2	2.69 ± 0.3
Human (fixed)	White Matter	1.59 ± 0.1	3.46 ± 0.3
	Grey Matter	2.24 ± 0.2	2.57 ± 0.2
Macaque (fixed)	White Matter	1.58 ± 0.2	3.59 ± 0.3
	Grey Matter	2.67 ± 0.2	2.90 ± 0.2

Table 5.2 – Measured values for μ_{eff} in longitudinal and radial directions at 594 nm

Species	Tissue Type	$\mu_{eff_{Long}}$ (1/mm)	$\mu_{eff_{Rad}}$ (1/mm)
Macaque (fixed)	White Matter	1.90 ± 0.2	3.83 ± 0.45
	Grey Matter	2.65 ± 0.6	3.02 ± 0.32
Mouse (fixed)	White Matter	1.87 ± 0.22	3.48 ± 0.46
	Grey Matter	2.46 ± 0.16	2.36 ± 0.32

5.5 Discussion

5.5.1 Simulating 3-D Optogenetic activation volumes using multi-directional scattering coefficients

Using the different experimental evidences, we have shown that the scattering coefficient along the myelin fibres is approximately half the value obtained across the myelin fibres. Here we investigate the impact on the

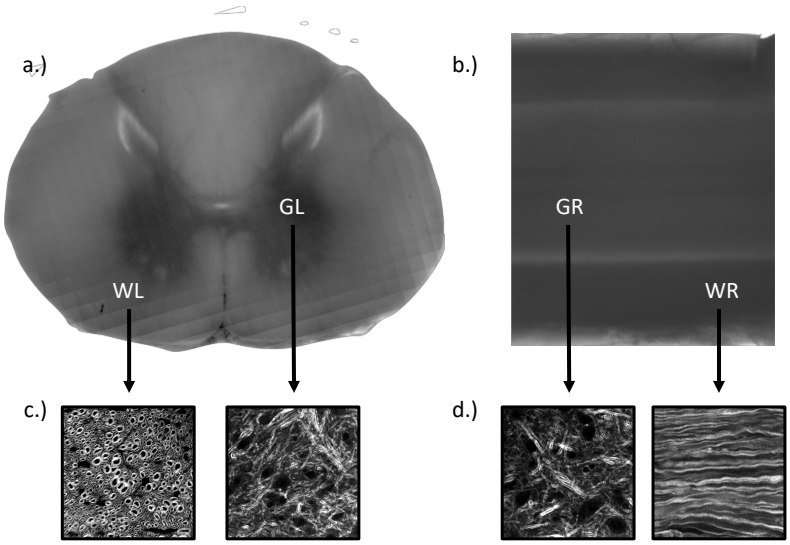

Figure 5.1 – Transmission images of 1 mm spinal cord sections a.) Transmission microscope image of 1 mm slice of macaque spinal cord in the longitudinal direction. Higher transmission in white matter when imaging in this direction. b.) Transmission microscope image of 1 mm slice of macaque spinal cord in the radial direction. Higher transmission in grey matter when imaging in this direction. c.) Backward-detected CARS images of white and grey matter in the longitudinal direction showing sub-cellular myelin composition. d.) Backward-detected CARS images of white and grey matter in the radial direction showing sub-cellular myelin composition. Abbreviations: WL = White matter in longitudinal direction; GL = Grey matter in longitudinal direction; WR = White matter in radial direction; GR = Grey matter in radial direction

light distribution in tissue by performing simplified light propagation simulations in spinal cord tissue volumes, showing the repercussions of directional light scattering on the optogenetic activation volume using an adjacent optical fiber illumination source. To do this we have edited an existing open-source 3-D Monte Carlo package[465] to accept multi-directional scattering coefficients (see Methods section for more information). It is understood that it would require a complete treatment modelling the cylindrical structures of the white matter to obtain accurate values. However, the focus is to obtain an estimate of the volume of tissue illuminated and the impact of an anisotropic scattering coefficient on that volume. The results of these simulations with 10 mW laser power at 473 nm (channel rhodopsin excitation), in the various species' spinal cords can be seen in figure 5.2. The spinal cords are to scale in this simulation and we can see here the obvious difficulties and importance of accurate planning in translating optogenetics to larger animals. For the case of the mouse simulation, $\mu_s^{'}$ values from the macaque spinal cord were used, as small size made it too difficult to separately measure $\mu_s^{'}$ in the white and grey matter regions. We believe this to be a satisfactory assumption based on the similarity in measured μ_{eff} in the macaque and mouse spinal cord. To elaborate on the implications of illumination volume in the mouse spinal cord, 10 mW is enough optical energy to activate channel rhodopsin (activation energy: 1 mW/mm^2)[466], [467] in every laminae down to the upper edges of the laminae 7. This corresponds to about 1.2 mm of tissue being

activated in the dorsal to ventral direction, when the the fiber output is perpendicular to the myelin sheaths. In the longitudinal direction, however, channel rhodopsin can be activated up to 1.6 mm away from the fiber tip, in both directions. A cervical vertebrae length in mice is about 800 um, meaning that effective simulations which take into account anisotropic scattering are important for optogenetic planning, especially if only specific vertebrae are to be optogenetically investigated[468]. In the macaque and human, this illumination scheme does not penetrate deep enough to activate even the first laminae. While increasing input power is an option, more elaborate fiber optic placement will become a critical factor in planning the optogenetic experiments in larger animals, and the observations provided herein will be useful for this.

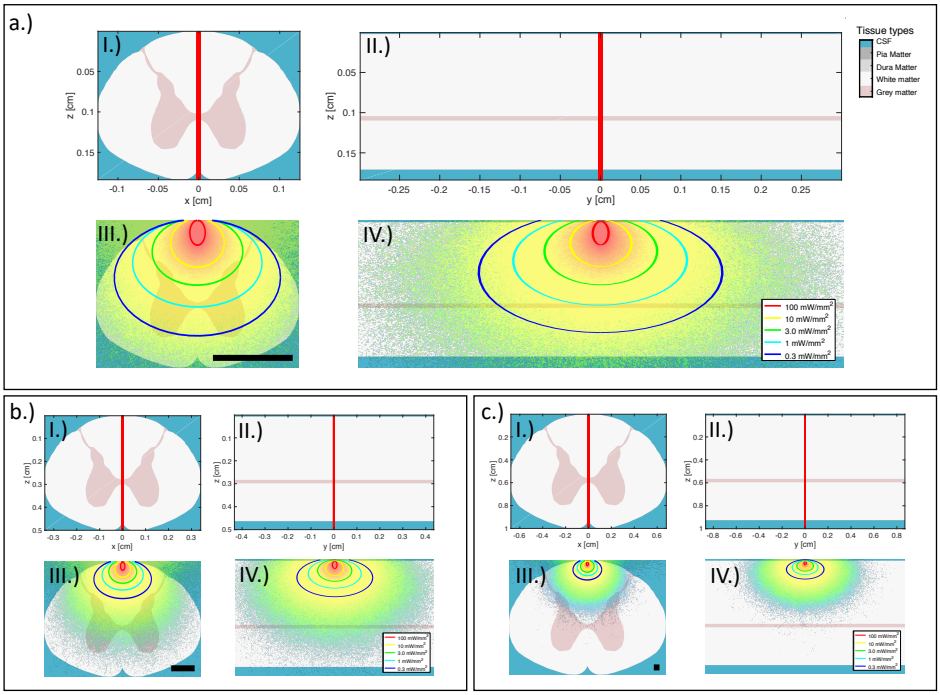

Figure 5.2 – Monte Carlo simulation of fluence rate in different mammalian spinal cords using mcxyz. a) Light deposition in mouse spinal cord. Also included here is the color-coded tissue type for each of the simulations. b) Light deposition in macaque spinal cord. c) Light deposition in human spinal cord. I.) Tissue-type defined volume with photon trajectory in longitudinal plane. II.) Tissue-type defined volume with photon trajectory in radial plane. III.) Results of simulation in longitudinal plane with activation circles for optogenetic planning. IV.) Results of simulation in radial plane with activation circles for optogenetic planning. Input power is 10 mW in all simulations. Scale bars in III.) are 1 mm.

5.5.2 The myelinated axons may act as naturally occurring optical waveguides

Perhaps the most interesting theory for the observed anisotropy was proposed by Kumar et al., who put forth the idea of myelin sheaths acting as natural optical waveguides [121]. While their hypothesis was only investigated theoretically, we believe this to be a plausible answer. As an initial experimental test, we imaged a 500 μm and 1 mm thick longitudinal spinal cord section in a transmission arrangement to see if the myelin sheaths were indeed visible and more bright than the axon core. At this thickness, without any waveguiding effects the sheaths should not be visible due to multiple scattering events. However, we did indeed observe myelin rings appearing

brighter than the axon cores in the transmission orientation. These results, while not conclusive, suggest a clear need for further investigation of the waveguide hypothesis (See Appendix 1 for more information).

5.5.3 Tissue fixation caused negligible effects in data analysis

In our work we used perfused, PFA fixed tissue to explicitly remove any blood absorption that could be present in the measurements. This allowed us to directly compare the effective attenuation and the scattering power of the tissue in the different directions. While fixing tissue has been reported to change the optical properties of the sample, at 633 nm, the effects are minimal[469]. We strengthen this claim by comparing our fresh and fixed tissue measurements in the human tissue, showing that fixation does not significantly alter the light scattering properties of spinal cord tissue at this wavelength.

5.5.4 Spinal cord measurements along with DTI tractography of the brain could make present myelin information translatable

Due to the symmetry of the myelin sheath and the spinal cord organization, we use the terminology radial and longitudinal rather than Cartesian units for μ_s' in x,y,z. We believe that this representation is more translational for expanding the technique to the brain along with diffuse tensor imaging (DTI) of white matter tractography [470].

Some work has been done in measuring the optical properties of brain tissue in all 3 dimensions in rat using discrete raster-scanned slices with a similar integrating sphere arrangement used here [471]. This could offer an interesting opportunity to compare a full 3-dimensional Monte Carlo simulation using these measured values for μ_s' in x,y,z with a 2-dimensional symmetry-inspired μ_s' simulation in just the radial and longitudinal directions using non-invasive DTI, in the future goal of patient specific simulations. This ability could improve both optogenetic experiments and clinical technologies such as tissue oximeters.

5.6 Conclusion

We present here experimental evidence of a directional dependence of light propagation in the white matter of the spinal cord. We also show that this effect is not species dependent and that the reduced scattering coefficient is approximately 50% smaller along the myelin fibres compared to perpendicular to these fibres. This results in a light distribution that extends 20% further along the fibres, when the input beam is perpendicular to them. Using the information we present, we believe that improved Monte Carlo simulations for both stimulating and sensing endeavors can be achieved. This will be especially important for optogenetic planning wherein the experiment requires a specific laminae to be reached, or where the light must remain local to a specific spinal region (ie. cervical region). While the work we present here is in the spinal cord, due to the symmetry of myelin, the information can also be used to improve optical simulations in the brain, using information from routine DTI tractography.

5.7 Methods

5.7.1 Scattering and absorption coefficient calculation

The scattering and absorption coefficients were acquired using double-integrating-sphere setups which measure the total diffuse reflection and transmission of a laser beam traveling through the tissue sample located between the two spheres. These measurements were performed on fixed macaque and human spinal cord tissue as well

as fresh human tissue. This technique is routine and is explained in detail elsewhere [472]. All tissue samples were cut in 1 mm intervals in both the longitudinal direction (along length of the spinal cord) and in the radial direction (along width of spinal cord) and measured along the two directions using the integrating sphere arrangement. With the measures of the integrating spheres, the inverse adding doubling (IAD) algorithm was performed to estimate the optical properties of the tissue under investigation. Also a routine technique, the procedure and theory of the calculation can be read elsewhere [473]. Attention was given to assure the the tissue sections were indeed homogeneous in the areas of measurements, as is a requirement for IAD. The laser wavelength used for these measurements was 633 nm and the beam spot was about 1 mm. The laser wavelength was specifically chosen to diminish absorption effects caused by hemoglobin as to target the directional dependence of scattering.

We acknowledge that the dataset size is small for the human tissue, however, it is rare to acquire measurements on fresh human spinal cord and therefore we included the results. We also thought that this data was important to reduce speculation over the effect of tissue fixation at this wavelength (633 nm). The wavelength 633 nm was chosen explicitly to decrease the contributions of any leftover hemoglobin absorption. In the analysis of myelin birefringence, it was also shown that in this wavelength range, formalin fixation does not cause changes to the birefringent nature of the myelinated axon [474].

5.7.2 Attenuation coefficient estimation

Light transmission measurements were conducted with mouse and macaque spinal cord slices using a fiber punch-through method[460]. 594nm (MBL-FN, Changchun New Industries Optoelectronics Technology, China) laser light was delivered to a 105 μm diameter optical fiber (FG105UCA, Thorlabs). The fiber tip was then lowered into the tissue in 5 μm steps and the light intensity was collected on the underside of the slice by a low numerical aperture objective (10X, 0.25NA) and recorded by two CMOS cameras (2 X DMK23UP031, Imaging Source), seen in figure 5.3 (a). Optical transmittance, the amount of light transmitted through a slice, decays exponentially with the tissue thickness and thereby its evolution can be parametrized by fitting the observed intensity profiles with a single exponential function, as seen in figure 5.3(b).

5.7.2.1 Data analysis

Optical transmittance, the amount of light transmitted through a slice, was calculated as a ratio of the total integrated intensity (summed over all pixels in the image) at a given depth over the optical fiber intensity with no tissue present. Transmission of light through the tissue was then plotted as a function of the tissue thickness and parametrized by fitting the observed intensity profiles with a single exponential function. In the diffusion regime the light can be modelled by the modified Beer-Lambert Law[460]:

$$\frac{I(z)}{I_0} = T(z) = \exp(-\mu_{eff} z)\,, \tag{5.1}$$

with $I(z)$ being the total intensity detected by camera, z being the tissue thickness, and I_0 being the intensity at the fiber tip. $T(z)$ is the optical transmittance which follows an exponential decay against the tissue thickness. Here we do not reach the diffusion regime in our experiment because the spinal cord is simply too small (therefore $\mu_{\text{eff}} \neq \sqrt{3\mu_a\left[\mu_a + \mu_s(1-g)\right]}$). Nevertheless, the exponential coefficient is obtained as a relative value of μ_{eff}

5.7.3 3D Monte Carlo Simulations with multi-directional scattering coefficients

We achieve the simulations using an altered 3-dimensional Monte Carlo program (mcxyz) provided open-source by Jacques, used previously in the brain [465], [471]. This program is a verified variation of the 2-D Monte Carlo program created for multi-layered tissue (MCML), used routinely for biological applications [475]. Using

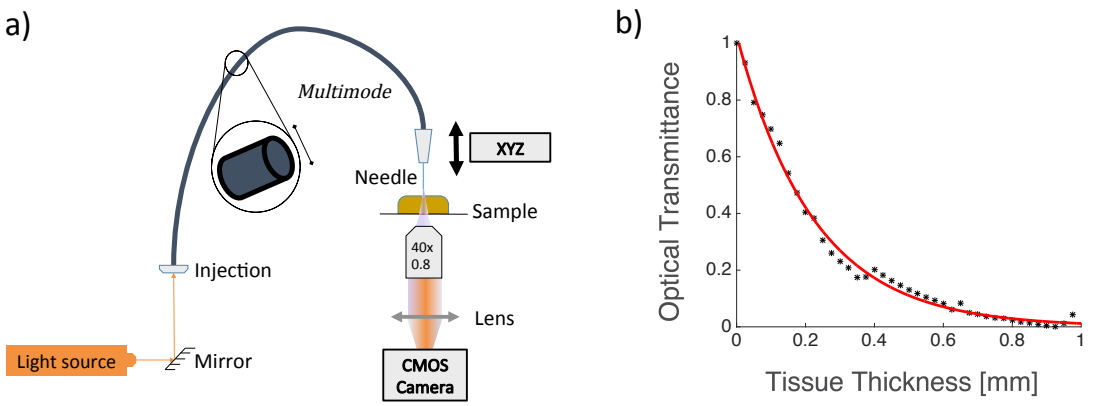

Figure 5.3 – Punch-through method experimental setup. (a) Spinal cord slices were illuminated by 594 nm laser beam coupled to a multimode optical fiber. The fiber was lowered into the tissue and the light transmitted through a slide was collected on the underside by a low numerical aperture objective (10X, 0.25NA) and recorded by two cameras. (b) model of the lumbar spinal cord anatomy, with white matter located at the periphery and surrounded by gray matter which shape and size varies according to the lumbar spinal cord level. (c) Optical transmittance as a function of tissue thickness. Experimental measurements (black), exponential fit (red line).

a simple segmentation program, we converted our spinal cord models from an image stack to a tissue-type-defined 3-D volume for the simulation.

An immense advantage of the mcxyz program is the inclusion of Jacques's method for creating generic tissues, allowing a highly malleable simulation based on few input parameters [92]. First and foremost, it allows the ability to use a scattering coefficient acquired at any visible or NIR wavelength (in our case 633 nm) and to then perform the simulation at another wavelength. This allows us to simulate the light propagation at traditional optogenetic activation wavelengths. Secondly, while the measurements are made in fixed, bloodless tissue, we are able to simply add an estimated blood concentration to each tissue type separately, for the inclusion of hemoglobin absorption as has been done in the brain [476]. Lastly, the program allows to input the light source properties such as: angle of incidence, incident laser wavelength, beam divergence and beam starting position. We display herein the case of a 105 um multimode optical fiber with a numerical aperture (N.A.) of 0.22 situated against and perpendicular to the white matter tracts in the center of the spinal cord (figure 5.2). The laser wavelength used in this simulation was 473 nm (to make the simulation relevant to those using channel rhodopsin) and a blood volume of 2.8% oxygen saturation: 62%) was deployed, as was described for brain tissue in other work [92], [476].

To accommodate our findings of a directional scattering dependence, we included a small alteration in the Monte Carlo action of the mcxyz program where rather than having a sole scattering coefficient for each pixel in the volume, there exists one for each 3-D direction. During the process of the photon step, where the scattering coefficient is considered, the three pixel-corresponding scattering coefficients are linearly combined using the unit vector of the photon's current propagating direction, and from there the program resumes normally. The modified version has been validated to give identical results to the original mcxyz code when all three directional scattering coefficients are equal.

5.7.4 Sample preparation

All animal tissues were obtained according to protocols that had been approved by the Institutional Animal Care and Use Committee (Comité de Protection des Animaux de l'Université Laval), and all procedures involving animals and their care were made in accordance with the Canadian Council on Animal Care's Guide to the Care and Use of Experimental Animals. Human post-mortem brain tissues were obtained from the human brain bank of the Centre de Recherche de l'Institut Universitaire en Santé Mentale de Québec (CERVO), which required informed consent before donation of tissues. The CERVO's Ethics Committee approved the brain collection, storage and handling procedures, which were described in detail elsewhere [477].

5.7.4.1 Mice and monkey

3 mice and 3 macaque specimens were anesthetized with urethane (2 g/kg) and perfused intracardially with 4% paraformaldehyde (PFA) in 0.1 M phosphate buffer; spinal cords were postfixed overnight in the same solution at 4C. The tissue was then stored in a 0.1M phosphate buffer solution (PBS). The slices were embeded in agarose and cut in parasagittal and transversal planes at varying thicknesses. Before measurements, the tissue was always thoroughly rinsed in a water bath for 2 hours.

5.7.4.2 Human

Two cervical sections of the same human spinal cord were extracted upon the arrival of newly post-mortem tissue at the brain bank. The first section was fixed in a 4% PFA bath, while the other was immediately used for optical analysis. To slice the sections they were embedded in agarose, and cut in parasagittal and transversal planes at 1 mm thicknesses.

Appendix 1

5.7.5 Myelin may act as an optical waveguide

Recently, it has been theorized that myelin sheaths may act as natural optical waveguides [121]. To experimentally investigate this we imaged thick sections of longitudinal spinal cord where the myelin sheaths are highly organized at high magnification, in a transmission arrangement. While we have not exhausted the possibilities of other optical effects, it looks as though the myelin is indeed transmitting more light in the sheath, as opposed to the axon - which matches the theoretical investigation (see figure 5.4). We tried two different thicknesses and two different sources and the pattern of brighter myelin sheaths remained in all cases.

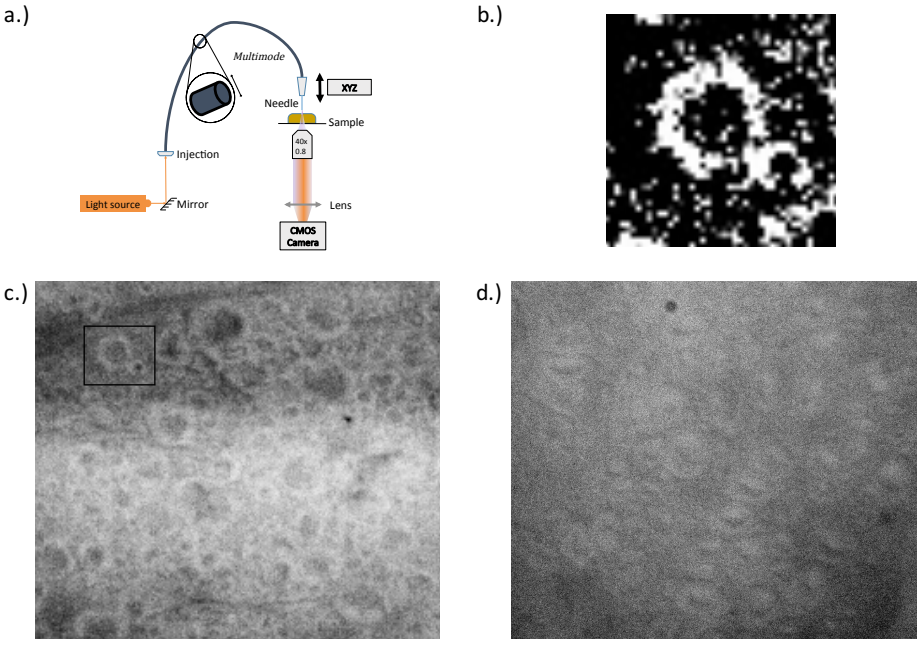

Figure 5.4 – Possible transmission of light through myelin sheaths in thick longitudinal slices of spinal cord. a.) Optical arrangement for the imaging experiment. Light was collected on the underside of the slice by a 40x objective and recorded by a CMOS cameras (DMK 23UP031, Imaging Source). b.) Magnified and contrasted image of bright myelin sheath and dark axon center from (c.)). c.) 500 um longitudinal slice illuminated using a 594 nm fiber laser source (MBL-FN, Changchun New Industries Optoelectronics Technology, China.). Inset square shows location of zoomed image in b.). d.) 1 mm longitudinal slice illuminated with a fibered white lamp source (SLS201L, Thorlabs, New Jersey, USA).

Conclusion

The overall goal of this thesis project was to create an optical guidance system to improve deep brain stimulation neurosurgery for PD treatment. To this end, 3 already published articles in peer-reviewed journals along with 1 article in review and another in preparation are presented. While the articles do not present a complete clinical system, the depth of original content within this thesis does show considerable progress towards the end goal. In this section we will briefly summarize the importance of each chapter, describe their limitations and offer suggestions for future improvements. While the Chapter order is advantageous for reading the entire document, here I will describe the project in a different sequence to better illustrate the state of the project.

To begin, the overall conclusion at the current stage of the project is that optical information can be acquired onboard the DBS electrode and that this information can confirm on and off target trajectories during its implantation. We have showed this using DRS in *in vivo* primate brain which is neuroanatomically similar to the larger human counterpart. The details of this engineering feat are shown in Chapter 3. The novelty of the system presented originated from: 1) the use of small OD probes which could fit within the DBS electrode, thereby adding no additional invasiveness to the procedure, 2) the use of visible and NIR spectral information to spectrally discriminate 4 different tissue types (white matter, grey matter, mixed matter, and blood vessels) and 4) the use of a 2-bit optical barcode along the trajectory provided by the spectral discrimination able to allude to on- and off-target implantations. The implication of this device is reasonably profound as it is the first time that optics have been introduced during the implantation stage of the DBS procedure. The introduction of the device could ultimately improve patient treatment outcome by providing confirmatory or negatory feedback to the surgeon during the descent of the critical electrode, prior to closing the cranium. Furthermore, adding guidance at this stage could decrease haemorrhaging both by detecting blood vessels in front of the chronic electrode, as well as, by reducing the number of electrodes sent into the brain if it is found that MER can be replaced by optical information. This is still far from reality, but may be possible with Raman systems that provide enough molecular information for brain region classification.

While the DRS system is an encouraging step forward towards an optically-guided DBS procedure, there do exist several limitations to be overcome before it can be adopted in the clinic. First, we have presented and used data from only two commercially available DBS electrodes (Medtronic 3389 and Boston Scientific Vercise) as they have a semi-transparent tip and an inner-diameter hollow core of roughly the same size ($\tilde{4}$00 m). While these electrodes are two of the most commonly used, there are many new commercially available leads which may require our device to be adapted. Second, while we can estimate on- and off-target trajectories, much more work must go into predicting the phsyical location of the electrode using the acquired optical barcode. This will require patient-specific photon-propagation simulations to better predict the barcodes that may be measured during the probe insertion. Third, while the stylet we have designed which houses the fiber optics is comparable in rigidity to the commercial counterpart, it is not identical. Research will be required to quantify the difference in the likelihood of lead deviation during lead-descent, prior to incorporating it into a commercial device. Fourth, while we have been successful in discriminating blood vessels in front of the electrode, a more robust analysis on the detectable size of possible oncoming blood vessels will be required to characterize the system. Fifth, and

most importantly, a quantifiable benefit to the patient must be shown using the optical guidance system, as this is the ultimate goal of the device.

To improve the performance of this system, a more transparent electrode would be highly favourable, as to decrease the non-useful reflections coming from within the electrode. Moreover, more sophisticated probe tips should be investigated. A possible tip may have side facing fibers or a combination of side-facing and forward facing fibers, all with the intention of minimizing specular reflections from the electrode surface and maximizing diffuse reflections from the tissue. Finally, the inclusion of other modalities which can increase the discriminatory information should be pursued, as we have begun to do using CARS.

In Chapter 2, I present progress towards such a multi-modal device, showing high-resolution white and grey matter discrimination using fiber-based CARS spectroscopy. CARS and Raman counterparts have the great potential to provide enough molecular information on the tissue to enable brain region classification (ie. STN, GPi, SN). Moreover, CARS uniquely provides micron-level resolution allowing brain region classification immediately upon the probe entering specifica nuclei, without cross-talk from surrounding structures (similar to MER). This work was a major step forward in terms of clinical translational for CARS spectroscopy as an all-fibered system was used, enable by portable fibered lasers, allowing the entire setup to be transported into operating rooms. Furthermore, this was the first time that CARS spectra had been acquired in the backwards direction, using an an all silica-fiber conduit with no bulky optics after the fiber. The use of silica fibers is interesting since they are inexpensive and fairly robust in comparison to specialty fiber counterparts (ie. hollow core fibers), and this further proclaims the system's translatable value. Finally, the custom laser systems allows for random-access probing, which allows the user to define which wavelengths, and therefore chemical bonds, to probe. This feature can greatly decrease acquisition time, as we show visibly discernible CARS spectra of white and grey matter on the order of 10 ms, and simple tissue discrimination on the order of 5 ms. The number of vibrational bonds which must be probed is more or less proportional to the number of tissue types which are to be discriminated, with a minimum of 2 wavelengths used (1 used for normalizing for tissue optical properties). That said, thresholds of even a single vibrational bond may be used to differentiate tissue subtypes, as the signal is proportional to the quantity of the oscillators present (squared dependance).

The CARS system hold considerable potential for future optical guidance, not only in neurosurgery, but in many biomedical applications. That said, there exist major limitations, which are to be expected with a novel research device. The most limiting factor is the current irradiance level required to produce a reasonable spectra in tissue. Due to the non-linear nature of CARS, small focal volumes must be used to create the signal, thus increasing the irradiance substantially in comparison to linear Raman modalities which probe large volumes. This can be decreased in future work by decreasing the repetition rate and peak pulse-width, while remaining below ionization limits. Furthermore, the main interest in CARS is imaging, due to its intrinsic optical sectioning. A system which could rotate or vibrate the optical fiber could disperse the illumination over larger areas or enable imaging similar to that done in OCT and SFE.

At this point, the most important improvement required for this system is an increase in SNR to better differentiate tissue regions. To achieve this, the laser must be optimized to generate more CARS signal, while keeping the average power constant (as mentioned above). Furthermore, the optical probe can be improved by using better geometries for signal collection and by including a thin film filter on the delivery fiber to remove signal generation from within the fiber. Also, while the laser system in use is state-of-the-art, there is still room for improvement. An optimal system for clinical CARS would operate in the NIR region to offset ambient lighting and the CARS signal (pump & stokes = 1000 - 1500nm), have a relatively low repetition rate near 1 MHz and use pulsewidths of about 10 ps to increase peak power, and operate at about 15 mW total average power to reduce linear heathing. Other tactics to increase the SNR may include better electronic filtering in the data acquisition segment. Furthermore, ideally the CARS probe could be housed within the DBS electrode. For this to occur, a transparent electrode tip will be required to allow for the efficient focusing of ballistic photons on the other side

of the electrode. Finally, incorporation of the system into an imaging apparatus would be very exciting to gauge its ability to perform hyperspectral imaging during neurosurgery.

Using the expertise gained during this doctoral program, a review on using Raman spectroscopy in neurosurgery is in preparation and was included in Chapter 1, as an introductory section to spontaneous and coherent Raman techniques. While this review is not yet submitted, it is a thorough summary of efforts to bring Raman based technologies to the OR. It manages to discuss many of the important hardware and software considerations required to bring a translational Raman device to fruition for neurosurgery, providing a roadmap for future adopters. Critically, the review touches on the importance of registering optical information within the surgical suite routinely used by the neurosurgeon. This aspect of the design process will be substantial and imperative for the clinical adoption of DRS and CARS in the clinic.

During my degree, I was fortunate enough to explore tissue spectroscopy outside of the confinements of a single project. Due to this freedom, our team made other discoveries and developed novel tools not immediately pertinent to DBS neurosurgery. Both works presented herein, however, will have translatable applications for this thesis goal by ultimately improving the clinical implementation of a future system.

In Chapter 4, I present a data analysis technique to analyze DRS spectra using convolutional neural networks, which can provide accurate tissue-oxygenation measurements. While the work was based on spectra acquired on the optic nerve head, the techniques are translatable and useful for DRS-based optical guidance, where tissue oxygenation can serve as an interesting biomarker for both optical guidance and disease state. Overall, the article presented a useful application of machine learning for spectroscopic analysis which is now implemented in a commercial device. Furthermore, a central aspect of this work was the idea of using simulated data to train the neural network. While this is routine in machine learning for image analysis, it is novel for the application of spectra and can serve as a framework for future spectral analysis projects. Furthermore, while the algorithm is designed to quantify hemoglobin concentrations, it can also be repurposed for accurate measurements of other chromophores, such as neuromelanin - an important chromophore in PD. Overall, the data analysis aspect of the surgical guidance system will be an interesting topic to expand on once measurements in human tissue are acquired, and, the techniques in this Chapter can facilitate that.

The second translatable discovery was presented in Chapter 5, showing empirical measurements of anisotropic scattering in organized myelin using the spinal cord as the substrate. While anisotropic scattering has been postulated in the past, empirical, macro-scale measurements in a well organized structure was lacking. We filled this gap and presented the importance of the observation with respect to optical simulations in optogenetic experiment planning. Especially interesting for this thesis, however, is the Monte Carlo package that was presented to take into account multi-directional scattering coefficients. Combining this package with patient-specific pre-operative diffuse tensor imaging (DTI) of white matter tractography could allow for more precise optical simulations by taking into account mylein orientation and therefore could improve optical guidance. Developing a Monte Carlo package which can perform patient-specific simulations of spectroscopy at different probe depths represents another major project required for a complete optical guidance system.

Looking ahead to the future of this technology, there is exciting potential in the utility of optical guidance technology to help study PD and the mechanism of DBS. While not possible yet, we can imagine a CARS imaging endoscope capable of directly imaging the electrodes location within the brain and registering that information onto the pre- and post- operative MRIs. This type of optical confirmation would provide unequivocal information as to the location of each contact terminal within the brain and this could help to demystify questions pertaining to: the optimal target location within the STN, the direction of the axons in this location, the distance from other structures which may or may not cause adverse side effects, etc. With the field now moving towards understanding the DBS mechanism and building functional connectomes of the human brain, optical confirmation of electrode location, along with the tunable stimulation parameters on DBS leads, will provide a valuable

tool in studying both PD and the human brain in its entirety.

In summary, to re-iterate, the goal of this thesis project was first and foremost to create an optical guidance system for DBS neurosurgery for improved treatment of PD. Importantly, the word system, by definition, is a group of things working together as parts of an overarching mechanism. While my project was to create an optical guidance system, what I have accomplished should rather be seen as a part. Indeed, the work presented was foundational in allowing us to acquire and analyze the potential of spectroscopic information to effectively guide DBS. Now, to complete this system, many other parts will be needed, all of which representing exciting projects for future graduate students.

Bibliography

[1] D. T. DePaoli, N. Lapointe, Y. Messaddeq, M. Parent, and D. C. Côté, "Intact primate brain tissue identification using a completely fibered coherent Raman spectroscopy system", *Neurophotonics*, vol. 5, no. 03, p. 1, 2018, ISSN: 2329-423X. DOI: 10.1117/1.NPh.5.3.035005. [Online]. Available: https://www.spiedigitallibrary.org/journals/neurophotonics/volume-5/issue-03/035005/Intact-primate-brain-tissue-identification-using-a-completely-fibered-coherent/10.1117/1.NPh.5.3.035005.full.

[2] D. DePaoli, L. Goetz, D. Gagnon, G. Maranon, M. Prud'homme, L. Cantin, M. Parent, and D. C. Côté, "Intraoperative fiber optic guidance during chronic electrode implantation in deep brain stimulation neurosurgery: proof of concept in primates", *Journal of Neurosurgery*, pp. 1–10, 2019, ISSN: 0022-3085. DOI: 10.3171/2019.1.jns182600. [Online]. Available: https://thejns.org/view/journals/j-neurosurg/aop/article-10.3171-2019.1.JNS182600.xml.

[3] D. T. DePaoli, P. Tossou, M. Parent, D. Sauvageau, and D. C. Côté, "Convolutional Neural Networks for Spectroscopic Analysis in Retinal Oximetry", *Scientific Reports*, vol. 9, no. 1, p. 11 387, 2019, ISSN: 2045-2322. DOI: 10.1038/s41598-019-47621-7. [Online]. Available: http://www.nature.com/articles/s41598-019-47621-7.

[4] W. Poewe, K. Seppi, C. M. Tanner, G. M. Halliday, J Patrik Brundin, E. Volkmann, A.-E. Schrag, and A. E. Lang, "Parkinson disease", *Nature Reviews Disease Primers*, vol. 3, no. 1, 2017, ISSN: 22124152. DOI: 10.1016/B978-0-444-63916-5.00011-2.

[5] E. Ray Dorsey, A. Elbaz, E. Nichols, F. Abd-Allah, A. Abdelalim, J. C. Adsuar, M. G. Ansha, C. Brayne, J. Y. J. Choi, D. Collado-Mateo, N. Dahodwala, H. P. Do, D. Edessa, M. Endres, S. M. Fereshtehnejad, K. J. Foreman, F. G. Gankpe, R. Gupta, G. J. Hankey, S. I. Hay, M. I. Hegazy, D. T. Hibstu, A. Kasaeian, Y. Khader, I. Khalil, Y. H. Khang, Y. J. Kim, Y. Kokubo, G. Logroscino, J. Massano, N. M. Ibrahim, M. A. Mohammed, A. Mohammadi, M. Moradi-Lakeh, M. Naghavi, B. T. Nguyen, Y. L. Nirayo, F. A. Ogbo, M. O. Owolabi, D. M. Pereira, M. J. Postma, M. Qorbani, M. A. Rahman, K. T. Roba, H. Safari, S. Safiri, M. Satpathy, M. Sawhney, A. Shafieesabet, M. S. Shiferaw, M. Smith, C. E. Szoeke, R. Tabarés-Seisdedos, N. T. Truong, K. N. Ukwaja, N. Venke-

tasubramanian, S. Villafaina, K. G. Weldegwergs, R. Westerman, T. Wijeratne, A. S. Winkler, B. T. Xuan, N. Yonemoto, V. L. Feigin, T. Vos, and C. J. Murray, "Global, regional, and national burden of Parkinson's disease, 1990–2016: a systematic analysis for the Global Burden of Disease Study 2016", *The Lancet Neurology*, vol. 17, no. 11, pp. 939–953, 2018, ISSN: 14744465. DOI: 10.1016/S1474-4422(18)30295-3.

[6] V. Bellou, L. Belbasis, I. Tzoulaki, E. Evangelou, and J. P. Ioannidis, "Environmental risk factors and Parkinson's disease: An umbrella review of meta-analyses", *Parkinsonism and Related Disorders*, vol. 23, no. 2015, pp. 1–9, 2016, ISSN: 18735126. DOI: 10.1016/j.parkreldis.2015.12.008. [Online]. Available: http://dx.doi.org/10.1016/j.parkreldis.2015.12.008.

[7] C. W. Olanow and M. B. Stern, "The scientific and clinical basis for the treatment of Parkinson disease (2009)", *Neurology*, vol. 72, 2009.

[8] D. W. Dickson, "Neuropathology of Parkinson's disease", *Parkinsonism and Related Disorders*, vol. 46, s30–s33, 2018, ISSN: 1353-8020. DOI: 10.1201/b12948. [Online]. Available: https://doi.org/10.1016/j.parkreldis.2017.07.033.

[9] A. H. Schapira, K. R. Chaudhuri, and P. Jenner, *Non-motor features of Parkinson disease*, 2017. DOI: 10.1038/nrn.2017.62. [Online]. Available: http://dx.doi.org/10.1038/nrn.2017.62.

[10] B. A. Faucheux, A.-M. Bonnet, Y. Agid, and E. C. Hirsch, "Blood vessels change in the mesencephalon of patients with Parkinson ' s disease Platelet glycoprotein IIIa polymorphism , aspirin , and", *The Lancet*, vol. 353, pp. 981–982, 1999.

[11] B. Thanvi, N. Lo, and T. Robinson, "Vascular parkinsonism - An important cause of parkinsonism in older people", *Age and Ageing*, vol. 34, no. 2, pp. 114–119, 2005, ISSN: 00020729. DOI: 10.1093/ageing/afi025.

[12] J Guan, P Yang, C Turner, N. Lfb, M Dragunow, and W. Hj, "Vascular Degeneration in Parkinson ' s Disease -", *Alzheimer's & Parkinson's Disease: Open Access*, vol. 2, pp. 1–5, 2016.

[13] J. Jankovic, "Parkinson's disease: clinical features and diagnosis", *Journal Neurology, Neurosurgery & Psychiatry*, vol. 79, pp. 368–376, 2008, ISSN: 17589061. DOI: 10.1136/jnnp.2007.131045.

[14] A Berardelli, G. K. Wenning, A Antonini, D Berg, B. R. Bloem, V Bonifati, D Brooks, D. J. Burn, C. Colosimo, A. Fanciulli, J. Ferreira, T. Gasser, F. Grandas, P. Kanovsky, V. Kostic, J. Kulisevsky, W. Oertel, W. Poewe, J. P. Reese, M. Relja, E. Ruzicka, A. Schrag, K. Seppi, P. Taba, and M. Vidailhet, "EFNS/MDS-ES recommendations for the diagnosis of Parkinson's disease", *European Journal of Neurology*, vol. 20, no. 1, pp. 16–34, 2013, ISSN: 13515101. DOI: 10.1111/ene.12022.

[15] A. Samii, J. G. Nutt, and B. R. Ransom, "Parkinson's disease", *The Lancet*, vol. 363, pp. 1783–1793, 2004.

[16] C. Marras and A. Lang, "Parkinson's disease subtypes: Lost in translation?", *Journal of Neurology, Neurosurgery and Psychiatry*, vol. 84, no. 4, pp. 409–415, 2013, ISSN: 1468330X. DOI: 10.1136/jnnp-2012-303455.

[17] A. Schrag, M. Jahanshahi, and N. Quinn, "What contributes to quality of life in patients with Parkinson's disease?", *Journal of Neurology Neurosurgery and Psychiatry*, vol. 69, no. 3, pp. 308–312, 2000, ISSN: 00223050. DOI: 10.1136/jnnp.69.3.308.

[18] K. Simonyan, "Recent advances in understanding the role of the basal ganglia", *F1000Research*, vol. 8, no. 0, pp. 1–9, 2019, ISSN: 1759796X. DOI: 10.12688/f1000research.16524.1.

[19] A. Nambu, H. Tokuno, and M. Takada, "Functional significance of the cortico-subthalamo-pallidal 'hyperdirect' pathway", *Neuroscience Research*, vol. 43, no. 2, pp. 111–117, 2002, ISSN: 01680102. DOI: 10.1016/S0168-0102(02)00027-5.

[20] A. E. Lang and A. M. Lozano, "Parkinson's Disease", *The New England Journal of Medicine*, no. 18, p. 1130, 1998, ISSN: 2376-8118. DOI: 10.1001/jama.1883.02390180014002.

[21] A. Barbeau, "L-Dopa Therapy in Parkinson's Disease: A Critical Review of Nine Years' Experience", *Science & Research*, vol. 101, p. 791, 1969.

[22] P. A. LeWitt and S. Fahn, "Levodopa therapy for Parkinson disease: Table", *Neurology*, vol. 86, no. 14 Supplement 1, S3–S12, 2016, ISSN: 0028-3878. DOI: 10.1212/wnl.0000000000002509.

[23] B. S. Connolly and A. E. Lang, *Pharmacological treatment of Parkinson disease: A review*, 2014. DOI: 10.1001/jama.2014.3654.

[24] M. I. Hariz, "From functional neurosurgery to "interventional" neurology: Survey of publications on thalamotomy, pallidotomy, and deep brain stimulation for Parkinson's disease from 1966 to 2001", *Movement Disorders*, vol. 18, no. 8, pp. 845–852, 2003, ISSN: 08853185. DOI: 10.1002/mds.10470.

[25] M. Hariz, "My 25 stimulating years with DBS in Parkinson's disease", *Journal of Parkinson's Disease*, vol. 7, S33–S41, 2017, ISSN: 1877718X. DOI: 10.3233/JPD-179007.

[26] R. A. Esselink, R. M. De Bie, R. J. De Haan, M. W. Lenders, P. C. Nijssen, M. J. Staal, H. M. Smeding, P. R. Schuurman, D. A. Bosch, and J. D. Speelman, "Unilateral pallidotomy versus bilateral subthalamic nucleus stimulation in PD: A randomized trial", *Neurology*, vol. 62, no. 2, pp. 201–207, 2004, ISSN: 00283878. DOI: 10.1212/01.WNL.0000103235.12621.C3.

[27] S. Janezic, S. Threlfell, P. D. Dodson, M. J. Dowie, T. N. Taylor, D. Potgieter, L. Parkkinen, S. L. Senior, S. Anwar, B. Ryan, T. Deltheil, P. Kosillo, M. Cioroch, K. Wagner, O. Ansorge, D. M. Bannerman, J. P. Bolam, P. J. Magill, S. J. Cragg, and R. Wade-Martins, "Deficits in dopaminergic transmission precede neuron loss and dysfunction in a new Parkinson model", *Proceedings of the National Academy of Sciences*, vol. 110, no. 42, E4016–E4025, 2013, ISSN: 0027-8424. DOI: 10.1073/pnas.1309143110.

[28] A. A. Dijkstra, P. Voorn, H. W. Berendse, H. J. Groenewegen, A. J. M. Rozemuller, and W. D. J. van de Berg, "Stage-dependent nigral neuronal loss in incidental Lewy body and parkinson's disease", *Movement Disorders*, vol. 29, no. 10, pp. 1244–1251, 2014, ISSN: 15318257. DOI: 10.1002/mds.25952.

[29] D. Iacono, M. Geraci-Erck, M. L. Rabin, C. H. Adler, G. Serrano, T. G. Beach, and R. Kurlan, "Parkinson disease and incidental Lewy body disease", *Neurology*, vol. 85, no. 19, pp. 1670–1679, 2015, ISSN: 0028-3878. DOI: 10.1212/wnl.0000000000002102.

[30] A. L. Benabid, P. Pollak, A. Louveau, S. Henry, and J. de Rougemont, "Combined (Thalamotomy and Stimulation) Stereotactic Surgery of the VIM Thalamic Nucleus for Bilateral Parkinson Disease", *Stereotactic and Functional Neurosurgery*, vol. 50, no. 1-6, pp. 344–346, 1987, ISSN: 1011-6125. [Online]. Available: http://www.karger.com/DOI/10.1159/000100803.

[31] H. Bergman, T. Wichmann, and M. R. DeLong, *Reversal of Experimental Parkinsonism By Lesions of the STN*, 1990.

[32] P Limousin, P Pollack, A Benazzouz, D Hoffman, J. EBas, E Brouselle, J. Perret, and B. AL., "Effect on parkinsonian signs and subthalamic nucleus stimulation symptoms of bilateral", *Lancet*, vol. 345, no. 1, pp. 91–95, 2005.

[33] C. S. Lozano, M. Ranjan, A. Boutet, D. S. Xu, W. Kucharczyk, A. Fasano, and A. M. Lozano, "Imaging alone versus microelectrode recording–guided targeting of the STN in patients with Parkinson's disease", vol. 130, no. June, pp. 1847–1852, 2019. DOI: 10.3171/2018.2.JNS172186..

[34] A. M. Lozano and R. E. Gross, "Introduction to Deep Brain Stimulation", *Neurosurgical Focus*, vol. 42, no. videosuppl2, Intro, 2017. DOI: 10.3171/2017.2.focusvid.intro.

[35] K. Ashkan, P. Rogers, H. Bergman, and I. Ughratdar, *Insights into the mechanisms of deep brain stimulation*, 2017. DOI: 10.1038/nrneurol.2017.105.

[36] M. Jakobs, A. Fomenko, A. M. Lozano, and K. L. Kiening, "Cellular, molecular, and clinical mechanisms of action of deep brain stimulation—a systematic review on established indications and outlook on future developments", *EMBO Molecular Medicine*, vol. 11, no. 4, e9575, 2019, ISSN: 1757-4676. DOI: 10.15252/emmm.201809575.

[37] G. Suarez-cedeno, J. Suescun, and M. C. Schiess, "Earlier Intervention with Deep Brain Stimulation for Parkinson ' s Disease", *Parkinson's Disease*, vol. 2017, 2017, ISSN: 20420080. DOI: https://doi.org/10.1155/2017/9358153.

[38] B. Rosin, M. Slovik, R. Mitelman, M. Rivlin-Etzion, S. N. Haber, Z. Israel, E. Vaadia, and H. Bergman, "Closed-loop deep brain stimulation is superior in ameliorating parkinsonism", *Neuron*, vol. 72, no. 2, pp. 370–384, 2011, ISSN: 08966273. DOI: 10.1016/j.neuron.2011.08.023. [Online]. Available: http://dx.doi.org/10.1016/j.neuron.2011.08.023.

[39] A. Gunduz, K. D. Foote, and M. S. Okun, "Reengineering deep brain stimulation for movement disorders: Emerging technologies", *Current Opinion in Biomedical Engineering*, vol. 4, pp. 97–105, 2017, ISSN: 24684511. DOI: 10.1016/j.cobme.2017.09.001. [Online]. Available: https://doi.org/10.1016/j.cobme.2017.09.001.

[40] E. Calabrese, "Diffusion Tractography in Deep Brain Stimulation Surgery: A Review", *Frontiers in Neuroanatomy*, vol. 10, no. May, pp. 1–11, 2016. DOI: 10.3389/fnana.2016.00045.

[41] D. A. Rodriguez, T. J. Pfefer, Q. Wang, P. F. Lopez, and J. C. Ramella-Roman, "A Monte Carlo analysis of error associated with twowavelength algorithms for retinal oximetry", *Investigative Ophthalmology and Visual Science*, vol. 57, no. 14, pp. 6474–6481, 2016, ISSN: 15525783. DOI: 10.1167/iovs.16-20138.

[42] W. I. Essayed, F. Zhang, P. Unadkat, G. R. Cosgrove, A. J. Golby, and L. J. O'Donnell, *White matter tractography for neurosurgical planning: A topography-based review of the current state of the art*, 2017. DOI: 10.1016/j.nicl.2017.06.011. [Online]. Available: http://dx.doi.org/10.1016/j.nicl.2017.06.011.

[43] L. Goetz, M. Bhattacharjee, M. U. Ferraye, V. Fraix, C. Maineri, D. Nosko, A. J. Fenoy, B. Piallat, N. Torres, A. Krainik, E. Seigneuret, O. David, M. Parent, A. Parent, P. Pollak, A. L. Benabid, B. Debu, and S. Chabardès, "Deep Brain Stimulation of the Pedunculopontine Nucleus Area in Parkinson Disease: MRI-Based Anatomoclinical Correlations and Optimal Target", *Clinical Neurosurgery*, vol. 84, no. 2, pp. 506–518, 2019, ISSN: 0148396X. DOI: 10.1093/neuros/nyy151.

[44] C. Hamani, A. M. Lozano, P. A. Mazzone, E. Moro, W. Hutchison, P. A. Silburn, L. Zrinzo, M. Alam, L. Goetz, E. Pereira, A. Rughani, W. Thevathasan, T. Aziz, B. R. Bloem, P. Brown, S. Chabardes, T. Coyne, K. Foote, E. Garcia-Rill, E. C. Hirsch, M. S. Okun, and J. K. Krauss, "Pedunculopontine nucleus region deep brain stimulation in Parkinson disease: Surgical techniques, side effects, and postoperative imaging", *Stereotactic and Functional Neurosurgery*, vol. 94, no. 5, pp. 307–319, 2016, ISSN: 14230372. DOI: 10.1159/000449011.

[45] K. A. Follett, F. M. Weaver, M. Stern, K. Hur, C. L. Harris, P. Luo, W. J. Marks, J. Rothlind, O. Sagher, C. Moy, R. Pahwa, K. Burchiel, P. Hogarth, E. C. Lai, J. E. Duda, K. Holloway, A. Samii, S. Horn, J. M. Bronstein, G. Stoner, P. A. Starr, R. Simpson, G. Baltuch, A. De Salles, G. D. Huang, and D. J. Reda, "Pallidal versus Subthalamic Deep-Brain Stimulation for Parkinson's Disease", *New England Journal of Medicine*, vol. 362, no. 22, pp. 2077–2091, 2010, PMID: 20519680. DOI: 10.1056/NEJMoa0907083. eprint: https://doi.org/10.1056/NEJMoa0907083. [Online]. Available: https://doi.org/10.1056/NEJMoa0907083.

[46] V. J. Odekerken, J. A. Boel, B. A. Schmand, R. J. De Haan, M. Figee, P. Van Den Munckhof, P. R. Schuurman, and R. M. De Bie, "GPi vs STN deep brain stimulation for Parkinson disease: Three-year follow-up", *Neurology*, vol. 86, no. 8, R. M. A. de Bie, L Bour, M. F. Contarino, R. J. de Haan, M Iwan, M. S. J. Mink, P van den Munckhof, V. J. J. Odekerken, M Postma, B. A. Schmand, M. N. Scholten, P. R. Schuurman, T van Laar, J. M. C. van Dijk, C. F. E. Hoffmann, A Mosch, G. N. Beute, P. C. G. Nijssen, T van Asseldonk, M. Lenders, and J. P. P. van Vugt, Eds., pp. 755–761, 2016, ISSN: 1526632X. DOI: 10.1212/WNL.0000000000002401. [Online]. Available: https://n.neurology.org/content/86/8/755.

[47] N. R. Williams, K. D. Foote, and M. S. Okun, "Subthalamic Nucleus Versus Globus Pallidus Internus Deep Brain Stimulation: Translating the Rematch Into Clinical Practice", *Movement Disorders Clinical Practice*, vol. 1, no. 1, pp. 24–35, 2014, ISSN: 23301619. DOI: 10.1002/mdc3.12004.

[48] Medtronic. (2019). Medtronic surgical planning user-interface, [Online]. Available: https://www.medtronic.com/ca-en/healthcare-professionals/products/neurological/surgical-navigation-systems/stealthstation/cranial-neurosurgery-navigation.html (visited on 08/10/2019).

[49] Medscape. (2017). Deep Brain Stimulation for Parkinson Disease, [Online]. Available: https://www.medtronic.com/ca-en/healthcare-professionals/products/neurological/surgical-navigation-systems/stealthstation/cranial-neurosurgery-navigation.html (visited on 08/10/2019).

[50] S Wong, G. H. Baltuch, J. L. Jaggi, and S. F. Danish, "Functional localization and visualization of the subthalamic nucleus from microelectrode recordings acquired during DBS surgery with unsupervised machine learning.", *Journal of neural engineering*, vol. 6, no. 2, p. 026 006, 2009, ISSN: 17412552. DOI: 10.1088/1741-2560/6/2/026006.

[51] M. S. Okun, M. Tagliati, M. Pourfar, H. H. Fernandez, R. L. Rodriguez, R. L. Alterman, and K. D. Foote, "Management of Referred Deep Brain Stimulation Failures", *Archives of Neurology*, vol. 62, no. 8, p. 1250, 2005, ISSN: 0003-9942. DOI: 10.1001/archneur.62.8.noc40425. [Online]. Available: http://archneur.jamanetwork.com/article.aspx?doi=10.1001/archneur.62.8.noc40425.

[52] T. M. Ellis, K. D. Foote, H. H. Fernandez, A. Sudhyadhom, R. L. Rodriguez, P. Zeilman, C. E. Jacobson IV, and M. S. Okun, "Reoperation for suboptimal outcomes after deep brain stimulation surgery", *Neurosurgery*, vol. 63, no. 4, pp. 754–760, 2008, ISSN: 0148396X. DOI: 10.1227/01.NEU.0000325492.58799.35.

[53] C. C. McIntyre, S. Mori, D. L. Sherman, N. V. Thakor, and J. L. Vitek, "Electric field and stimulating influence generated by deep brain stimulation of the subthalamic nucleus", *Clinical Neurophysiology*, vol. 115, no. 3, pp. 589–595, 2004, ISSN: 1388-2457. DOI: http://dx.doi.org/10.1016/j.clinph.2003.10.033. [Online]. Available: http://www.sciencedirect.com/science/article/pii/S1388245703004048.

[54] A. Nowacki, T. A.-k. Nguyen, G. Tinkhauser, K. Petermann, I. Debove, R. Wiest, and C. Pollo, "Accuracy of different three-dimensional subcortical human brain atlases for DBS –lead localisation", *NeuroImage: Clinical*, vol. 20, no. May, pp. 868–874, 2018, ISSN: 22131582. DOI: 10.1016/j.nicl.2018.09.030. [Online]. Available: https://doi.org/10.1016/j.nicl.2018.09.030.

[55] J. Engelhardt, D. Guehl, N. Damon-Perrière, O. Branchard, P. Burbaud, and E. Cuny, "Localization of deep brain stimulation electrode by image registration is software dependent: A comparative study between four widely used software programs", *Stereotactic and Functional Neurosurgery*, vol. 96, no. 6, pp. 364–369, 2019, ISSN: 14230372. DOI: 10.1159/000494982.

[56] Y. M. Andrade-Souza, J. M. Schwalb, C. Hamani, H. Eltahawy, T. Hoque, J. Saint-Cyr, and A. M. Lozano, "Comparison of three methods of targeting the subthalamic nucleus for chronic stimulation in Parkinson's disease", *Neurosurgery*, vol. 56, no. 4 SUPPL. Pp. 360–368, 2005, ISSN: 0148396X. DOI: 10.1227/01.NEU.0000156547.24603.EE.

[57] R. B. Kochanski and S. Sani, "Awake versus Asleep Deep Brain Stimulation Surgery : Technical Considerations and Critical Review of the Literature", *brain sciences*, vol. 8, no. 17, 2018, ISSN: 20763425. DOI: 10.3390/brainsci8010017.

[58] P. S. Lee, G. M. Weiner, D. Corson, J. Kappel, Y. F. Chang, V. R. Suski, S. B. Berman, H. Homayoun, A. D. Van Laar, D. J. Crammond, and R. M. Richardson, "Outcomes of interventional-MRI versus microelectrode recording-guided subthalamic deep brain stimulation", *Frontiers in Neurology*, vol. 9, no. APR, pp. 1–8, 2018, ISSN: 16642295. DOI: 10.3389/fneur.2018.00241.

[59] W. Hamel, J. A. Köppen, F. Alesch, A. Antonini, J. A. Barcia, H. Bergman, S. Chabardes, M. F. Contarino, P. Cornu, W. Demmel, G. Deuschl, A. Fasano, A. A. Kühn, P. Limousin, C. C. McIntyre, H. M. Mehdorn, M. Pilleri, P. Pollak, M. C. Rodríguez-Oroz, J. Rumià, M. Samuel, L. Timmermann, F. Valldeoriola, J. Vesper, V. Visser-Vandewalle, J. Volkmann, and A. M. Lozano, "Targeting of the Subthalamic Nucleus for Deep Brain

Stimulation: A Survey Among Parkinson Disease Specialists", *World Neurosurgery*, vol. 99, pp. 41–46, 2017, ISSN: 18788769. DOI: 10.1016/j.wneu.2016.11.012.

[60] A. Amon and F. Alesch, *Systems for deep brain stimulation: review of technical features*, 2017. DOI: 10.1007/s00702-017-1751-6.

[61] S. T. Tsai, T. Y. Chen, S. H. Lin, and S. Y. Chen, "Five-year clinical outcomes of local versus general anesthesia deep brain stimulation for Parkinson's disease", *Parkinson's Disease*, vol. 2019, 2019, ISSN: 20420080. DOI: 10.1155/2019/5676345.

[62] R. E. Gross, P. Krack, M. C. Rodriguez-Oroz, A. R. Rezai, and A. L. Benabid, "Electrophysiological mapping for the implantation of deep brain stimulators for Parkinson's disease and tremor", *Movement Disorders*, vol. 21, no. SUPPL. 14, 2006, ISSN: 08853185. DOI: 10.1002/mds.20960.

[63] S. Mcclelland, "A cost analysis of intraoperative microelectrode recording during subthalamic stimulation for Parkinson's disease", vol. 26, no. 8, pp. 1422–1427, 2011. DOI: 10.1002/mds.23787.

[64] P. A. Starr, "Placement of Deep Brain Stimulators into the Subthalamic Nucleus or Globus pallidus internus: Technical Approach", *Stereotactic and Functional Neurosurgery*, vol. 79, no. 3-4, pp. 118–145, 2002, ISSN: 1011-6125. [Online]. Available: http://www.karger.com/DOI/10.1159/000070828.

[65] P. A. Starr, C. W. Christine, P. V. Theodosopoulos, N. Lindsey, D. Byrd, A. Mosley, and W. J. Marks, "Implantation of deep brain stimulators into subthalmic nucleus: technical approach and magnetic imaging "verified electrode locations", *Journal of Neurosurgery*, vol. 97, no. 2, pp. 370–387, 2002. DOI: 10.3171/jns.2002.97.2.0370.

[66] M. F. Khan, K Mewes, R. E. Gross, and O Škrinjar, "Assessment of Brain Shift Related to Deep Brain Stimulation Surgery", *Stereotactic and Functional Neurosurgery*, vol. 86, no. 1, pp. 44–53, 2008, ISSN: 1011-6125. [Online]. Available: https://www.karger.com/DOI/10.1159/000108588.

[67] C. A. Giller and P. Jenkins, "Some technical nuances for deep brain stimulator implantation", *Interdisciplinary Neurosurgery: Advanced Techniques and Case Management*, vol. 2, no. 1, pp. 29–39, 2015, ISSN: 22147519. DOI: 10.1016/j.inat.2014.11.001. [Online]. Available: http://dx.doi.org/10.1016/j.inat.2014.11.001.

[68] M. A. Brodsky, S. Anderson, C. Murchison, M. Seier, J. Wilhelm, A. Vederman, and K. J. Burchiel, "Clinical outcomes of asleep vs awake deep brain stimulation for Parkinson disease", *Neurology*, vol. 89, no. 19, pp. 1944–1950, 2017, ISSN: 1526632X. DOI: 10.1212/WNL.0000000000004630.

[69] T. Nakajima, L. Zrinzo, T. Foltynie, I. A. Olmos, C. Taylor, M. I. Hariz, and P. Limousin, "MRI-guided subthalamic nucleus deep brain stimulation without microelectrode recording: Can we dispense with surgery under local anaesthesia?", *Stereotactic and Functional Neurosurgery*, vol. 89, no. 5, pp. 318–325, 2011, ISSN: 10116125. DOI: 10.1159/000330379.

[70] Z. Li, J. G. Zhang, Y. Ye, and X. Li, *Review on Factors Affecting Targeting Accuracy of Deep Brain Stimulation Electrode Implantation between 2001 and 2015*, 2017. DOI: 10.1159/000449206.

[71] M. Tonge, L. Ackermans, E. Kocabicak, V. Van Kranen-Mastenbroek, M. Kuijf, M. Oosterloo, P. Kubben, and Y. Temel, "A detailed analysis of intracerebral hemorrhages in DBS surgeries", *Clinical Neurology and Neurosurgery*, vol. 139, pp. 183–187, 2015, ISSN: 18726968. DOI: 10.1016/j.clineuro.2015.10.017. [Online]. Available: http://dx.doi.org/10.1016/j.clineuro.2015.10.017.

[72] M. Johns, C. A. Giller, and H. Liu, "Computational and In Vivo Investigation of Optical Reflectance from Human Brain to Assist Neurosurgery", *Journal of Biomedical Optics*, vol. 3, no. 4, p. 437, 1998, ISSN: 10833668. DOI: 10.1117/1.429894.

[73] M. Johns, C. A. Giller, and H. Liu, "In Vivo Optical Reflectance Measurement of Human Brain Tissue with Calculation of Absorption and Scattering Coefficients", in *Biomedical Diagnostic, Guidance, and Surgical-Assist Systems*, 1999. DOI: 10.1117/12.351519.

[74] H. Liu, M. Johns, and C. Giller, "Modified diffusion models for steady-state broadband reflectance with a needle-like optic probe", in *Proceedings of SPIE - The International Society for Optical Engineering*, vol. 4250, 2001, pp. 76–81. DOI: 10.1117/12.434472.

[75] M. Johns, C. A. Giller, and H. Liu, "Calculation of Hemoglobin Saturation from In Vivo Human Brain Tissues Using a Modified Diffusion Theory Model", *Biomedical Diagnostic, Guidance, and Surgical-Assist Systems III*, vol. 4254, no. Section 5, pp. 194–203, 2003. DOI: 10.1117/12.427934. [Online]. Available: http://dx.doi.org/10.1117/12.427934.

[76] M. Johns, C. Giller, D. German, and H. Liu, "Determination of reduced scattering coefficient of biological tissue from a needle-like probe.", *Optics express*, vol. 13, no. 13, pp. 4828–4842, 2005, ISSN: 1094-4087. DOI: 10.1364/OPEX.13.004828.

[77] Z. Qian, S. Victor, Y. Gu, C. Giller, and H. Liu, "Look-Ahead Distance of a fiber probe used to assist neurosurgery: Phantom and Monte Carlo study.", *Optics express*, vol. 11, no. 16, pp. 1844–55, 2003, ISSN: 1094-4087. [Online]. Available: http://www.ncbi.nlm.nih.gov/pubmed/19466067.

[78] A. N. Bahadur, C. A. Giller, D. Kashyap, and H. Liu, "Determination of optical probe interrogation field of near-infrared reflectance: phantom and Monte Carlo study", *Applied Optics*, vol. 46, no. 23, p. 5552, 2007, ISSN: 0003-6935. DOI: 10.1364/ao.46.005552. [Online]. Available: http://ao.osa.org/abstract.cfm?URI=ao-46-23-5552.

[79] C. A. Giller, H Liu, P Gurnani, S Victor, U Yazdani, and D. C. German, "Validation of a near-infrared probe for detection of thin intracranial white matter structures", *Journal of Neurosurgery*, vol. 98, no. 6, pp. 1299–1306, 2003, ISSN: 0022-3085. DOI: 10.3171/jns.2003.98.6.1299. [Online]. Available: http://www.scopus.com/inward/record.url?eid=2-s2.0-0037512469{\&}partnerID=40{\&}md5=479e173971adeef22245202c97911a8c.

[80] C. A. Giller, M. Johns, and H. Liu, "Use of an intracranial near-infrared probe for localization during stereotactic surgery for movement disorders", *Journal of Neurosurgery*, vol. 93, no. 3, pp. 498–505, 2009, ISSN: 0022-3085. DOI: 10.3171/jns.2000.93.3.0498. [Online]. Available: http://www.ncbi.nlm.nih.gov/pubmed/10969953.

[81] C. a. Giller, H. Liu, D. C. German, D. Kashyap, and R. B. Dewey, "A stereotactic near-infrared probe for localization during functional neurosurgical procedures: further experience.", *Journal of neurosurgery*, vol. 110, no. 2, pp. 263–273, 2009, ISSN: 0022-3085. DOI: 10.3171/2008.8.JNS08728.

[82] J. D. Johansson, P. Blomstedt, N. Haj-Hosseini, A. T. Bergenheim, O. Eriksson, and K. Wårdell, "Combined diffuse light reflectance and electrical impedance measurements as a navigation aid in deep brain surgery", *Stereotactic and Functional Neurosurgery*, vol. 87, no. 2, pp. 105–113, 2009, ISSN: 10116125. DOI: 10.1159/000202977.

[83] K. Wårdell, P. Blomstedt, J. Richter, J. Antonsson, O. Eriksson, P. Zsigmond, A. T. Bergenheim, and M. I. Hariz, "Intracerebral microvascular measurements during deep brain stimulation implantation using laser doppler perfusion monitoring", *Stereotactic and Functional Neurosurgery*, vol. 85, no. 6, pp. 279–286, 2007, ISSN: 10116125. DOI: 10.1159/000107360.

[84] J. Antonsson, O. Eriksson, P. Blomstedt, A. T. Bergenheim, M. I. Hariz, J. Richter, P. Zsigmond, and K. Wårdell, "Diffuse reflectance spectroscopy measurements for tissue-type discrimination during deep brain stimulation", *Journal of Neural Engineering*, vol. 5, no. 2, pp. 185–190, 2008, ISSN: 17412560. DOI: 10.1088/1741-2560/5/2/009.

[85] K. Wårdell, P. Zsigmond, J. Richter, and S. Hemm, "Relationship between laser doppler signals and anatomy during deep brain stimulation electrode implantation toward the ventral intermediate nucleus and subthalamic nucleus", *Neurosurgery*, vol. 72, no. June, pp. 127–140, 2013, ISSN: 0148396X. DOI: 10.1227/NEU.0b013e31827e5821.

[86] J. D. Johansson and K. Wårdell, "Intracerebral quantitative chromophore estimation from reflectance spectra captured during deep brain stimulation implantation", *Journal of Biophotonics*, vol. 6, no. 5, pp. 435–445, 2013, ISSN: 1864063X. DOI: 10.1002/jbio.201200055.

[87] P. Rejmstad, P. Zsigmond, and K. Wårdell, "Oxygen saturation estimation in brain tissue using diffuse reflectance spectroscopy along stereotactic trajectories", *Optics Express*, vol. 25, no. 7, p. 8192, 2017. DOI: 10.1364/oe.25.008192. [Online]. Available: http://www.opticsexpress.org/abstract.cfm?URI=oe-25-7-8192.

[88] P. Rejmstad, J. D. Johansson, N. Haj-Hosseini, and K. Wårdell, "A method for monitoring of oxygen saturation changes in brain tissue using diffuse reflectance spectroscopy", *Journal of Biophotonics*, vol. 10, no. 3, pp. 446–455, 2017, ISSN: 18640648. DOI: 10.1002/jbio.201500334.

[89] W. Wang, M. Short, I. T. Tai, and H. Zeng, "Disposable sheath that facilitates endoscopic Raman spectroscopy", *Journal of Biomedical Optics*, vol. 21, no. 2, p. 025 001, 2016, ISSN: 1083-3668. DOI: 10.1117/1.jbo.21.2.025001.

[90] P. Zsigmond, S. Hemm-Ode, and K. Wårdell, "Optical Measurements during Deep Brain Stimulation Lead Implantation: Safety Aspects", *Stereotactic and Functional Neurosurgery*, vol. 95, no. 6, pp. 392–399, 2018, ISSN: 14230372. DOI: 10.1159/000484944.

[91] S. H. Yun and S. J. J. Kwok, "Light in diagnosis, therapy and surgery", *Nature Biomedical Engineering*, vol. 1, no. 1, p. 0008, 2017, ISSN: 2157-846X. DOI: 10.1038/s41551-016-0008. arXiv: 15334406. [Online]. Available: http://www.nature.com/articles/s41551-016-0008.

[92] S. L. Jacques, "Optical properties of biological tissues: a review", *Physics in Medicine and Biology*, vol. 58, no. 11, R37, 2013. [Online]. Available: http://stacks.iop.org/0031-9155/58/i=11/a=R37.

[93] S. J. Madsen and B. C. Wilson, "Optical Properties of Brain Tissue BT - Optical Methods and Instrumentation in Brain Imaging and Therapy", in, S. J. Madsen, Ed., New York, NY: Springer New York, 2013, pp. 1–22, ISBN: 978-1-4614-4978-2. DOI: 10.1007/978-1-4614-4978-2_1. [Online]. Available: https://doi.org/10.1007/978-1-4614-4978-2{_}1.

[94] W. F. Cheong, S. A. Prahl, and A. J. Welch, "A Review of the Optical Properties of Biological Tissues", *IEEE Journal of Quantum Electronics*, vol. 26, no. 12, pp. 2166–2185, 1990, ISSN: 15581713. DOI: 10.1109/3.64354.

[95] F Bevilacqua, D Piguet, P Marquet, J. D. Gross, B. J. Tromberg, and C Depeursinge, "In vivo local determination of tissue optical properties: applications to human brain.", *Applied optics*, vol. 38, no. 22, pp. 4939–4950, 1999, ISSN: 0003-6935. DOI: 10.1117/12.301063.

[96] A. Sassaroli and S. Fantini, *Comment on the modified Beer-Lambert law for scattering media*, 2004. DOI: 10.1088/0031-9155/49/14/N07.

[97] L. Kocsis, P. Herman, and A. Eke, "The modified Beer-Lambert law revisited", *Physics in Medicine and Biology*, vol. 51, no. 5, 2006, ISSN: 00319155. DOI: 10.1088/0031-9155/51/5/N02.

[98] D. A. Boas, T. Gaudette, G. Strangman, X. Cheng, J. J. Marota, and J. B. Mandeville, "The accuracy of near infrared spectroscopy and imaging during focal changes in cerebral hemodynamics", *NeuroImage*, vol. 13, no. 1, pp. 76–90, 2001, ISSN: 10538119. DOI: 10.1006/nimg.2000.0674.

[99] M. Jermyn, J. Mercier, K. Aubertin, J. Desroches, K. Urmey, J. Karamchandiani, E. Marple, M. C. Guiot, F. Leblond, and K. Petrecca, "Highly accurate detection of cancer in situ with intraoperative, label-free, multimodal optical spectroscopy", *Cancer Research*, vol. 77, no. 14, pp. 3942–3950, 2017, ISSN: 15387445. DOI: 10.1158/0008-5472.CAN-17-0668.

[100] A. Goyette, J. Pichette, M.-A. Tremblay, A. Laurence, M. Jermyn, K. Mok, K. D. Paulsen, D. W. Roberts, K. Petrecca, B. C. Wilson, and F. Leblond, "Sub-diffuse interstitial optical tomography to improve the safety of brain needle biopsies: a proof-of-concept study", *Optics Letters*, vol. 40, no. 2, pp. 170–173, 2015, ISSN: 0146-9592. DOI: 10.1364/OL.40.000170.

[101] J. Pichette, A. Goyette, F. Picot, M.-A. Tremblay, G. Soulez, B. C. Wilson, and F. Leblond, "Sensitivity analysis aimed at blood vessels detection using interstitial optical tomography during brain needle biopsy procedures", *Biomedical Optics Express*, vol. 6, no. 11, p. 4238, 2015, ISSN: 2156-7085. DOI: 10.1364/boe.6.004238.

[102] J. Pichette, A. Laurence, L. Angulo, F. Lesage, A. Bouthillier, D. K. Nguyen, and F. Leblond, "Intraoperative video-rate hemodynamic response assessment in human cortex using snapshot hyperspectral optical imaging", *Neurophotonics*, vol. 3, no. 4, p. 045 003, 2016, ISSN: 2329-423X. DOI: 10.1117/1.nph.3.4.045003.

[103] R. McCreery, *Raman Spectroscopy for Chemical Analysis*, ser. Chemical Analysis: A Series of Monographs on Analytical Chemistry and Its Applications. Wiley, 2005, ISBN: 978-0-471-23187-5. [Online]. Available: https://books.google.ca/books?id=qY4MI0Zln1YC.

[104] M. G. Shim, L.-M. Wong Kee Song, N. E. Marcon, and B. C. Wilson, "In vivo Near-infrared Raman Spectroscopy: Demonstration of Feasibility During Clinical Gastrointestinal Endoscopy ¶", *Photochemistry and Photobiology*, vol. 72, no. 1, pp. 146–150, 2000. DOI: 10.1562/0031-8655(2000)0720146IVNIRS2.0.CO2. eprint: https://onlinelibrary.wiley.com/doi/pdf/10.1562/0031-8655%282000%290720146IVNIRS2.0.CO2. [Online]. Available: https://onlinelibrary.wiley.com/doi/abs/10.1562/0031-8655%282000%290720146IVNIRS2.0.CO2.

[105] C. L. Evans and X. S. Xie, "Coherent Anti-Stokes Raman Scattering Microscopy: Chemical Imaging for Biology and Medicine", *Annual Review of Analytical Chemistry*, vol. 1, no. 1, pp. 883–909, 2008, ISSN: 1936-1327. DOI: 10.1146/annurev.anchem.1.031207.112754. [Online]. Available: http://www.annualreviews.org/doi/abs/10.1146/annurev.anchem.1.031207.112754.

[106] C. W. Freudiger, W. Min, B. G. Saar, S. Lu, G. R. Holtom, C. He, J. C. Tsai, J. X. Kang, and X. S. Xie, "Label-free biomedical imaging with high sensitivity by stimulated Raman scattering microscopy.", *Science*, vol. 322, no. 5909, pp. 1857–61, 2008, ISSN: 1095-9203. DOI: 10.1126/science.1165758. [Online]. Available: http://ieeexplore.ieee.org/xpls/abs{_}all.jsp?arnumber=6151800http://www.ncbi.nlm.nih.gov/pubmed/19095943{\%}0Ahttp://www.pubmedcentral.nih.gov/articlerender.fcgi?artid=PMC3576036.

[107] J. X. Cheng and X. S. Xie, "Vibrational spectroscopic imaging of living systems: An emerging platform for biology and medicine", *Science*, vol. 350, no. 6264, 2015, ISSN: 10959203. DOI: 10.1126/science.aaa8870.

[108] D. W. Shipp, F. Sinjab, and I. Notingher, "Raman spectroscopy: techniques and applications in the life sciences", *Advances in Optics and Photonics*, vol. 9, no. 2, p. 315, 2017. DOI: 10.1364/aop.9.000315.

[109] U. Utzinger and R. R. Richards-Kortum, "Fiber optic probes for biomedical optical spectroscopy", *Journal of Biomedical Optics*, vol. 8, no. 1, p. 121, 2003, ISSN: 10833668. DOI: 10.1117/1.1528207.

[110] M. Jermyn, K. Mok, J. Mercier, J. Desroches, J. Pichette, K. Saint-Arnaud, L. Bernstein, M. C. Guiot, K. Petrecca, and F. Leblond, "Intraoperative brain cancer detection with Raman spectroscopy in humans", *Science Translational Medicine*, vol. 7, no. 274, 2015, ISSN: 19466242. DOI: 10.1126/scitranslmed.aaa2384.

[111] A. Lombardini, V. Mytskaniuk, S. Sivankutty, E. R. Andresen, X. Chen, J. Wenger, M. Fabert, N. Joly, F. Louradour, A. Kudlinski, and H. Rigneault, "High-resolution multimodal flexible coherent Raman endoscope article", *Light: Science and Applications*, vol. 7, no. 1, 2018, ISSN: 20477538. DOI: 10.1038/s41377-018-0003-3. [Online]. Available: http://dx.doi.org/10.1038/s41377-018-0003-3.

[112] Kokyo. (2019). SI type multimode optical fiber, [Online]. Available: https://en.symphotony.com/fiber-lasers/propagation-property/singlemode-multimode-fibers/si-multimode-mmf/20/ (visited on 08/10/2019).

[113] B. C. Wilson and G Adam, "A Monte Carlo model for the absorption and flux distributions of light in tissue", *Medical Physics*, vol. 10, no. 6, pp. 824–830, 1983. DOI: 10.1118/1.595361. [Online]. Available: https://aapm.onlinelibrary.wiley.com/doi/abs/10.1118/1.595361.

[114] L. Wang, S. L. Jacques, and L. Zheng, "MCML-Monte Carlo modeling of light transport in multi-layered tissues", *Computer Methods and Programs in Biomedicine*, vol. 47, no. 2, pp. 131–146, 1995, ISSN: 01692607. DOI: 10.1016/0169-2607(95)01640-F.

[115] T. Vo-Dinh, "Biomedical Photonics Handbook", 2003.

[116] N. Ren, J. Liang, X. Qu, J. Li, B. Lu, and J. Tian, "GPU-based Monte Carlo simulation for light propagation in complex heterogeneous tissues", *Optics Express*, vol. 18, no. 7, pp. 6811–6823, 2010. DOI: 10.1364/OE.18.006811. [Online]. Available: http://www.opticsexpress.org/abstract.cfm?URI=oe-18-7-6811.

[117] D. A. Boas, J. P. Culver, J. J. Stott, and A. K. Dunn, "Three dimensional Monte Carlo code for photon migration through complex heterogeneous media including the adult human head", *Optics Express*, vol. 10, no. 3, pp. 159–170, 2002. DOI: 10.1364/OE.10.000159. [Online]. Available: http://www.opticsexpress.org/abstract.cfm?URI=oe-10-3-159.

[118] S. L. Jacques and M. Carlo, "Photoacoustics Coupling 3D Monte Carlo light transport in optically heterogeneous tissues to photoacoustic signal generation", *Biochemical Pharmacology*, vol. 2, no. 4, pp. 137–142, 2014, ISSN: 2213-5979. DOI: 10.1016/j.pacs.2014.09.001. [Online]. Available: http://dx.doi.org/10.1016/j.pacs.2014.09.001.

[119] Q. Fang, "Mesh-based Monte Carlo method using fast ray-tracing in Plücker coordinates", *Biomedical Optics Express*, vol. 1, no. 1, pp. 165–175, 2010. DOI: 10.1364/BOE.1.000165. [Online]. Available: http://www.osapublishing.org/boe/abstract.cfm?URI=boe-1-1-165.

[120] H. Wang, C. Magnain, S. Sakadžić, B. Fischl, and D. A. Boas, "Characterizing the optical properties of human brain tissue with high numerical aperture optical coherence tomography", *Biomedical Optics Express*, vol. 8, no. 12, p. 5617, 2017, ISSN: 2156-7085. DOI: 10.1364/boe.8.005617.

[121] S. Kumar, K. Boone, J. Tuszynski, P. E. Barclay, and C. Simon, "Possible existence of optical communication channels in the brain", no. October, pp. 36–38, 2016. DOI: 10.1038/srep36508. arXiv: 1607.02969. [Online]. Available: http://arxiv.org/abs/1607.02969.

[122] A. Zangari, D. Micheli, R. Galeazzi, and A. Tozzi, "Node of Ranvier as an Array of Bio-Nanoantennas for Infrared Communication in Nerve Tissue", *Scientific Reports*, no. December 2017, pp. 1–19, 2018, ISSN: 2045-2322. DOI: 10.1038/s41598-017-18866-x. [Online]. Available: http://dx.doi.org/10.1038/s41598-017-18866-x.

[123] N. P. Kutuzov, A. R. Brazhe, V. L. Lyaskovskiy, and G. V. Maksimov, "Laser beam coupling into nerve fiber myelin allows one to assess its structural membrane properties", *Journal of Biomedical Optics*, vol. 20, no. 5, p. 050 501, 2015, ISSN: 1083-3668. DOI: 10.1117/1.jbo.20.5.050501.

[124] W. Stummer, S. Stocker, S. Wagner, H. Stepp, C. Fritsch, C. Goetz, A. E. Goetz, R. Kiefmann, and H. J. Reulen, "Intraoperative detection of malignant gliomas by 5-aminolevulinic acid- induced porphyrin fluorescence", *Neurosurgery*, vol. 42, no. 3, pp. 518–526, 1998, ISSN: 0148396X. DOI: 10.1097/00006123-199803000-00017.

[125] W. Stummer, U. Pichlmeier, T. Meinel, O. D. Wiestler, F. Zanella, and H. J. Reulen, "Fluorescence-guided surgery with 5-aminolevulinic acid for resection of malignant glioma: a randomised controlled multicentre phase III trial", *Lancet Oncology*, vol. 7, no. 5, pp. 392–401, 2006, ISSN: 14702045. DOI: 10.1016/S1470-2045(06)70665-9.

[126] P. A. Valdés, F. Leblond, V. L. Jacobs, B. C. Wilson, K. D. Paulsen, and D. W. Roberts, "Quantitative, spectrally-resolved intraoperative fluorescence imaging", *Scientific Reports*, vol. 2, 2012, ISSN: 20452322. DOI: 10.1038/srep00798.

[127] P. A. Valdes, V. L. Jacobs, B. C. Wilson, F. Leblond, D. W. Roberts, and K. D. Paulsen, "System and methods for wide-field quantitative fluorescence imaging during neurosurgery", *Optics Letters*, vol. 38, no. 15, p. 2786, 2013, ISSN: 0146-9592. DOI: 10.1364/ol.38.002786.

[128] L. Marcu, J. A. Jo, P. V. Butte, W. H. Yong, B. K. Pikul, K. L. Black, and R. C. Thompson, "Fluorescence Lifetime Spectroscopy of Glioblastoma Multiforme", *Photochemistry and Photobiology*, vol. 80, no. 1, p. 98, 2004, ISSN: 0031-8655. DOI: 10.1562/2003-12-09-ra-023.1.

[129] P. V. Butte, A. N. Mamelak, M. Nuno, S. I. Bannykh, K. L. Black, and L. Marcu, "Fluorescence lifetime spectroscopy for guided therapy of brain tumors", *NeuroImage*, vol. 54, no. SUPPL. 1, S125–S135, 2011, ISSN: 10538119. DOI: 10.1016/j.neuroimage.2010.11.001. [Online]. Available: http://dx.doi.org/10.1016/j.neuroimage.2010.11.001.

[130] S. R. Kantelhardt, D. Kalasauskas, K. König, E. Kim, M. Weinigel, A. Uchugonova, and A. Giese, "In vivo multiphoton tomography and fluorescence lifetime imaging of human brain tumor tissue", *Journal of Neuro-Oncology*, vol. 127, no. 3, pp. 473–482, 2016, ISSN: 15737373. DOI: 10.1007/s11060-016-2062-8.

[131] C. Kut, J. Xi, E. R. McVeigh, X. Li, K. L. Chaichana, S. M. Raza, X. Ye, A. Quiñones-Hinojosa, and F. J. Rodriguez, "Detection of human brain cancer infiltration ex vivo and in vivo using quantitative optical coherence tomography", *Science Translational Medicine*, vol. 7, no. 292, 2015, ISSN: 1946-6242. DOI: 10.1126/scitranslmed.3010611.

[132] H. Fabelo, S. Ortega, R. Lazcano, D. Madroñal, G. M. Callicó, E. Juárez, R. Salvador, D. Bulters, H. Bulstrode, A. Szolna, J. F. Piñeiro, C. Sosa, A. J. O'Shanahan, S. Bisshopp, M. Hernández, J. Morera, D. Ravi, B. R. Kiran, A. Vega, A. Báez-Quevedo, G. Z. Yang, B. Stanciulescu, and R. Sarmiento, "An intraoperative visualization system using hyperspectral imaging to aid in brain tumor delineation", *Sensors (Switzerland)*, vol. 18, no. 2, 2018, ISSN: 14248220. DOI: 10.3390/s18020430.

[133] M. Jermyn, K. Mok, J. Mercier, J. Desroches, J. Pichette, K. Saint-Arnaud, L. Bernstein, M.-C. Guiot, K. Petrecca, and F. Leblond, "Intraoperative brain cancer detection with Raman spectroscopy in humans", *Science Translational Medicine*, vol. 7, no. 274, 274ra19–274ra19, Feb. 11, 2015, ISSN: 1946-6234, 1946-6242. DOI: 10.1126/scitranslmed.aaa2384. [Online]. Available: http://stm.sciencemag.org/lookup/doi/10.1126/scitranslmed.aaa2384 (visited on 10/03/2018).

[134] K. Wårdell, "Optical Monitoring Techniques for Navigation during Stereotactic Neurosurgery", *Sensors and Materials*, vol. 28, no. 10, p. 1105, 2016, ISSN: 0914-4935. DOI: 10.18494/sam.2016.1327.

[135] H. Ramakonar, B. C. Quirk, R. W. Kirk, J. Li, A. Jacques, C. R. P. Lind, and R. A. McLaughlin, "Intraoperative detection of blood vessels with an imaging needle during neurosurgery in humans", *Science Advances*, vol. 4, no. 12, eaav4992, 2018. DOI: 10.1126/sciadv.aav4992.

[136] J. Desroches, M. Jermyn, M. Pinto, F. Picot, M.-A. Tremblay, S. Obaid, E. Marple, K. Urmey, D. Trudel, G. Soulez, M.-C. Guiot, B. C. Wilson, K. Petrecca, and F. Leblond, "A new method using Raman spectroscopy for in vivo targeted brain cancer tissue biopsy", *Scientific Reports*, vol. 8, no. 1, Dec. 2018, ISSN: 2045-2322. DOI: 10.1038/s41598-018-20233-3. [Online]. Available: http://www.nature.com/articles/s41598-018-20233-3 (visited on 10/15/2018).

[137] J. Desroches, É. Lemoine, M. Pinto, E. Marple, K. Urmey, R. Diaz, M. C. Guiot, B. C. Wilson, K. Petrecca, and F. Leblond, *Development and first in-human use of a Raman spectroscopy guidance system integrated with a brain biopsy needle*, 2019. DOI: 10.1002/jbio.201800396.

[138] K. M. Brindle, J. L. Izquierdo-García, D. Y. Lewis, R. J. Mair, and A. J. Wright, "Brain Tumor Imaging", *Journal of Clinical Oncology*, vol. 35, no. 21, pp. 2432–2438, Jun. 22, 2017, ISSN: 0732-183X. DOI: 10.1200/JCO.2017.72.7636. [Online]. Available: https://ascopubs.org/doi/10.1200/JCO.2017.72.7636 (visited on 08/11/2019).

[139] W. Stummer, T. Meinel, C. Ewelt, P. Martus, O. Jakobs, J. Felsberg, and G. Reifenberger, "Prospective Cohort Study of Radiotherapy with Concomitant and Adjuvant Temozolomide Chemotherapy for Glioblastoma Patients with No or Minimal Residual Enhancing Tumor Load after Surgery", *Journal of Neuro-Oncology*, vol. 108, no. 1,

pp. 89–97, May 1, 2012, ISSN: 1573-7373. DOI: 10.1007/s11060-012-0798-3. [Online]. Available: https://doi.org/10.1007/s11060-012-0798-3.

[140] K. L. Chaichana, I. Jusue-Torres, R. Navarro-Ramirez, S. M. Raza, M. Pascual-Gallego, A. Ibrahim, M. Hernandez-Hermann, L. Gomez, X. Ye, J. D. Weingart, A. Olivi, J. Blakeley, G. L. Gallia, M. Lim, H. Brem, and A. Quinones-Hinojosa, "Establishing Percent Resection and Residual Volume Thresholds Affecting Survival and Recurrence for Patients with Newly Diagnosed Intracranial Glioblastoma", *Neuro-Oncology*, vol. 16, no. 1, pp. 113–122, Nov. 26, 2013, ISSN: 1522-8517. DOI: 10.1093/neuonc/not137. [Online]. Available: https://doi.org/10.1093/neuonc/not137 (visited on 08/11/2019).

[141] K. Petrecca, M.-C. Guiot, V. Panet-Raymond, and L. Souhami, "Failure pattern following complete resection plus radiotherapy and temozolomide is at the resection margin in patients with glioblastoma", *Journal of Neuro-Oncology*, vol. 111, no. 1, pp. 19–23, Jan. 2013, ISSN: 0167-594X, 1573-7373. DOI: 10.1007/s11060-012-0983-4. [Online]. Available: http://link.springer.com/10.1007/s11060-012-0983-4 (visited on 02/25/2019).

[142] A. Noorbakhsh, J. A. Tang, L. P. Marcus, B. McCutcheon, D. D. Gonda, C. S. Schallhorn, M. A. Talamini, D. C. Chang, B. S. Carter, and C. C. Chen, "Gross-total resection outcomes in an elderly population with glioblastoma: a SEER-based analysis", *Journal of Neurosurgery*, vol. 120, no. 1, pp. 31–39, Jan. 2014, ISSN: 1933-0693. DOI: 10.3171/2013.9.JNS13877. pmid: 24205904.

[143] M. J. van den Bent, M. Smits, J. M. Kros, and S. M. Chang, "Diffuse Infiltrating Oligodendroglioma and Astrocytoma", *Journal of Clinical Oncology*, vol. 35, no. 21, pp. 2394–2401, Jun. 22, 2017, ISSN: 0732-183X. DOI: 10.1200/JCO.2017.72.6737. [Online]. Available: https://doi.org/10.1200/JCO.2017.72.6737 (visited on 08/11/2019).

[144] T. K. Owonikoko, J. Arbiser, A. Zelnak, H.-K. G. Shu, H. Shim, A. M. Robin, S. N. Kalkanis, T. G. Whitsett, B. Salhia, N. L. Tran, T. Ryken, M. K. Moore, K. M. Egan, and J. J. Olson, "Current Approaches to the Treatment of Metastatic Brain Tumours", *Nature Reviews Clinical Oncology*, vol. 11, p. 203, Feb. 25, 2014. [Online]. Available: https://doi.org/10.1038/nrclinonc.2014.25.

[145] S. Lapointe, A. Perry, and N. A. Butowski, "Primary brain tumours in adults", *The Lancet*, vol. 392, no. 10145, pp. 432–446, Aug. 2018, ISSN: 01406736. DOI: 10.1016/S0140-6736(18)30990-5. [Online]. Available: https://linkinghub.elsevier.com/retrieve/pii/S0140673618309905 (visited on 03/12/2019).

[146] A. Alfonso-García, R. Mittal, E. S. Lee, and E. O. Potma, "Biological imaging with coherent Raman scattering microscopy: a tutorial.", *Journal of biomedical optics*, vol. 19, no. 7, p. 71 407, 2014, ISSN: 1560-2281. DOI: 10.1117/1.JBO.19.7.071407. [Online]. Available: http://www.pubmedcentral.nih.gov/articlerender.fcgi?artid=4019423{\&}tool=pmcentrez{\&}rendertype=abstract.

[147] W. Min, C. W. Freudiger, S. Lu, and X. S. Xie, "Coherent Nonlinear Optical Imaging: Beyond Fluorescence Microscopy", *Annual Review of Physical Chemistry*, vol. 62, no. 1, pp. 507–530, 2011, ISSN: 0066-426X. DOI: 10.1146/annurev.physchem.012809.103512.

[148] D. Zhang, P. Wang, M. N. Slipchenko, and J. X. Cheng, "Fast vibrational imaging of single cells and tissues by stimulated raman scattering microscopy", *Accounts of Chemical Research*, vol. 47, no. 8, pp. 2282–2290, 2014, ISSN: 15204898. DOI: 10.1021/ar400331q.

[149] R. S. Das and Y. K. Agrawal, "Raman Spectroscopy: Recent Advancements, Techniques and Applications", *Vibrational Spectroscopy*, vol. 57, no. 2, pp. 163–176, Nov. 1, 2011, ISSN: 0924-2031. DOI: 10.1016/j.vibspec.2011.08.003. [Online]. Available: http://www.sciencedirect.com/science/article/pii/S0924203111001111 (visited on 08/11/2019).

[150] A Zumbusch, G. R. Holtom, and X. S. Xie, "Three-dimensional vibrational imaging by coherent anti-Stokes Raman scattering", *Physical Review Letters*, vol. 82, no. 20, pp. 4142–4145, 1999, ISSN: 0031-9007. DOI: 10.1103/PhysRevLett.82.4142. [Online]. Available: isi:000080319900055.

[151] J. X. Cheng, Y. K. Jia, G. Zheng, and X. S. Xie, "Laser-scanning coherent anti-Stokes Raman scattering microscopy and applications to cell biology", *Biophysical Journal*, vol. 83, no. 1, pp. 502–509, 2002, ISSN: 00063495. DOI: 10.1016/S0006-3495(02)75186-2. [Online]. Available: http://dx.doi.org/10.1016/S0006-3495(02)75186-2.

[152] E. O. Potma, W. P. de Boeij, P. J. M. van Haastert, and D. A. Wiersma, "Real-time visualization of intracellular hydrodynamics in single living cells", *Proceedings of the National Academy of Sciences*, vol. 98, no. 4, pp. 1577–1582, 2001, ISSN: 0027-8424. DOI: 10.1073/pnas.98.4.1577.

[153] X. Nan, J.-X. Cheng, and X. S. Xie, "Vibrational imaging of lipid droplets in live fibroblast cells with coherent anti-Stokes Raman scattering microscopy", *Journal of Lipid Research*, vol. 44, no. 11, pp. 2202–2208, 2003, ISSN: 0022-2275. DOI: 10.1194/jlr.d300022-jlr200.

[154] E. O. Potma and X. S. Xie, "Detection of single lipid bilayers with coherent anti-Stokes Raman scattering (CARS) microscopy", *Journal of Raman Spectroscopy*, vol. 34, no. 9, pp. 642–650, 2003, ISSN: 03770486. DOI: 10.1002/jrs.1045.

[155] H. Wang, Y. Fu, P. Zickmund, R. Shi, and J.-X. Cheng, "Coherent anti-stokes Raman scattering imaging of axonal myelin in live spinal tissues.", *Biophysical journal*, vol. 89, no. 1, pp. 581–91, 2005, ISSN: 0006-3495. DOI: 10.1529/biophysj.105.061911. [Online]. Available: http://www.ncbi.nlm.nih.gov/pubmed/15834003{\%}0Ahttp://www.pubmedcentral.nih.gov/articlerender.fcgi?artid=PMC1366558.

[156] C. L. Evans, E. O. Potma, M. Puoris'haag, D. Côté, C. P. Lin, and X. S. Xie, "Chemical imaging of tissue in vivo with video-rate coherent anti-Stokes Raman scattering microscopy.", *Proceedings of the National Academy of Sciences of the United States of America*, vol. 102, no. 46, pp. 16 807–16 812, 2005, ISSN: 0027-8424. DOI: 10.1073/pnas.0508282102.

[157] T. B. Huff and J.-X Cheng, "In vivo coherent anti-Stokes Raman scattering imaging of sciatic nerve tissue", *Journal of Microscopy*, vol. 225, no. 2, pp. 175–182, 2007, ISSN: 1365-2818. DOI: 10.1111/j.1365-2818.2007.01729.x.

[158] Y. Fu, T. B. Huff, H.-W. Wang, J.-X. Cheng, and H. Wang, "Ex vivo and in vivo imaging of myelin fibers in mouse brain by coherent anti-Stokes Raman scattering microscopy", *Optics Express*, vol. 16, no. 24, p. 19 396, 2008. DOI: 10.1364/oe.16.019396.

[159] E. Bélanger, S. Bégin, S. Laffray, Y. De Koninck, R. Vallée, and D. Côté, "Quantitative myelin imaging with coherent anti-Stokes Raman scattering microscopy: alleviating the excitation polarization dependence with circularly polarized laser beams", *Optics Express*, vol. 17, no. 21, p. 18 419, 2009. DOI: 10.1364/oe.17.018419.

[160] S. Bégin, B. Burgoyne, V. Mercier, A. Villeneuve, R. Vallée, and D. Côté, "Coherent anti-Stokes Raman scattering hyperspectral tissue imaging with a wavelength-swept system", *Biomedical Optics Express*, vol. 2, no. 5, p. 1296, 2011, ISSN: 2156-7085. DOI: 10.1364/BOE.2.001296. [Online]. Available: https://www.osapublishing.org/boe/abstract.cfm?uri=boe-2-5-1296.

[161] E. Bélanger, J. Crépeau, S. Laffray, R. Vallée, Y. De Koninck, and D. Côté, "Live animal myelin histomorphometry of the spinal cord with video-rate multimodal nonlinear microendoscopy", *Journal of Biomedical Optics*, vol. 17, no. 2, p. 021 107, 2012, ISSN: 10833668. DOI: 10.1117/1.jbo.17.2.021107.

[162] R. Turcotte, D. J. Rutledge, E. Bélanger, D. Dill, W. B. Macklin, and D. C. Côté, "Intravital assessment of myelin molecular order with polarimetric multiphoton microscopy", *Scientific Reports*, vol. 6, pp. 1–8, 2016, ISSN: 20452322. DOI: 10.1038/srep31685. [Online]. Available: http://dx.doi.org/10.1038/srep31685.

[163] L. Wei, Y. Shen, F. Xu, F. Hu, J. K. Harrington, K. L. Targoff, and W. Min, "Imaging Complex Protein Metabolism in Live Organisms by Stimulated Raman Scattering Microscopy with Isotope Labeling", *ACS Chemical Biology*, vol. 10, no. 3, pp. 901–908, 2015, ISSN: 1554-8929. DOI: 10.1021/cb500787b. [Online]. Available: https://doi.org/10.1021/cb500787b.

[164] D. Fu, W. Yang, and X. S. Xie, "Label-free imaging of neurotransmitter acetylcholine at neuromuscular junctions with stimulated Raman scattering", *Journal of the American Chemical Society*, vol. 139, no. 2, pp. 583–586, 2017, ISSN: 15205126. DOI: 10.1021/jacs.6b10727.

[165] M. Ji, D. A. Orringer, C. W. Freudiger, S. Ramkissoon, X. Liu, D. Lau, A. J. Golby, I. Norton, M. Hayashi, N. Y. R. Agar, G. S. Young, C. Spino, S. Santagata, S. Camelo-Piragua, K. L. Ligon, O. Sagher, and X. S. Xie, "Rapid, Label-Free Detection of Brain Tumors with Stimulated Raman Scattering Microscopy", *Science Translational Medicine*, vol. 5, no. 201, 201ra119–201ra119, Sep. 4, 2013, ISSN: 1946-6234, 1946-6242. DOI: 10.1126/scitranslmed.3005954. [Online]. Available: http://stm.sciencemag.org/cgi/doi/10.1126/scitranslmed.3005954 (visited on 10/15/2018).

[166] "Detection of Human Brain Tumor Infiltration with Quantitative Stimulated Raman Scattering Microscopy.", *Science translational medicine*, vol. 7, no. 309, 309ra163, 2015, ISSN: 1946-6242. DOI: 10.1126/scitranslmed.aab0195.

[167] C. H. Camp, Y. J. Lee, J. M. Heddleston, C. M. Hartshorn, A. R. Walker, J. N. Rich, J. D. Lathia, and M. T. Cicerone, "High-speed coherent Raman fingerprint imaging of biological tissues", *Nature Photonics*, vol. 8, no. 8, pp. 627–634, 2014, ISSN: 17494893. DOI: 10.1038/nphoton.2014.145. arXiv: arXiv:1402.3211v2.

[168] D. Fu, G. Holtom, C. Freudiger, X. Zhang, and X. S. Xie, "Hyperspectral imaging with stimulated raman scattering by chirped femtosecond lasers", *Journal of Physical Chemistry B*, vol. 117, no. 16, pp. 4634–4640, 2013, ISSN: 15205207. DOI: 10.1021/jp308938t.

[169] J. G. Porquez, R. A. Cole, J. T. Tabarangao, and A. D. Slepkov, "Spectrally-broad coherent anti-Stokes Raman scattering hyper-microscopy utilizing a Stokes supercontinuum pumped at 800 nm", *Biomedical Optics Express*, vol. 7, no. 10, p. 4335, 2016, ISSN: 2156-7085. DOI: 10.1364/boe.7.004335.

[170] T. Ideguchi, S. Holzner, B. Bernhardt, G. Guelachvili, N. Picqué, and T. W. Hänsch, "Coherent Raman spectro-imaging with laser frequency combs", *Nature*, vol. 502, no. 7471, pp. 355–358, 2013, ISSN: 00280836. DOI: 10.1038/nature12607.

[171] D. A. Orringer, B. Pandian, Y. S. Niknafs, T. C. Hollon, J. Boyle, S. Lewis, M. Garrard, S. L. Hervey-Jumper, H. J. Garton, C. O. Maher, J. A. Heth, O. Sagher, D. A. Wilkinson, M. Snuderl, S. Venneti, S. H. Ramkissoon, K. A. McFadden, A. Fisher-Hubbard, A. P. Lieberman, T. D. Johnson, X. S. Xie, J. K. Trautman, C. W. Freudiger, and S. Camelo-Piragua, "Rapid intraoperative histology of unprocessed surgical specimens via fibre-laser-based stimulated Raman scattering microscopy", *Nature Biomedical Engineering*, vol. 1, no. 2, 2017, ISSN: 2157846X. DOI: 10.1038/s41551-016-0027.

[172] L. F. Santos, R. Wolthuis, S. Koljenović, R. M. Almeida, and G. J. Puppels, "Fiber-Optic Probes for in Vivo Raman Spectroscopy in the High-Wavenumber Region", *Analytical Chemistry*, vol. 77, no. 20, pp. 6747–6752, Oct. 2005, ISSN: 0003-2700, 1520-6882. DOI: 10.1021/ac0505730. [Online]. Available: http://pubs.acs.org/doi/abs/10.1021/ac0505730 (visited on 10/04/2018).

[173] S. Koljenović, T. C. Bakker Schut, R Wolthuis, B. de Jong, L. Santos, P. J. Caspers, J. M. Kros, and G. J. Puppels, "Tissue characterization using high wave number Raman spectroscopy", *Journal of Biomedical Optics*, vol. 10, no. 3, p. 031 116, 2005, ISSN: 10833668. DOI: 10.1117/1.1922307.

[174] S. Koljenović, T. C. Bakker Schut, R. Wolthuis, A. J. P. E. Vincent, G. Hendriks-Hagevi, L. Santos, J. M. Kros, and G. J. Puppels, "Raman Spectroscopic Characterization of Porcine Brain Tissue Using a Single Fiber-Optic Probe", *Analytical Chemistry*, vol. 79, no. 2, pp. 557–564, Jan. 2007, ISSN: 0003-2700, 1520-6882. DOI: 10.1021/ac0616512. [Online]. Available: http://pubs.acs.org/doi/abs/10.1021/ac0616512 (visited on 10/03/2018).

[175] A. Beljebbar, S. Dukic, N. Amharref, and M. Manfait, "Ex vivo and in vivo diagnosis of C6 glioblastoma development by Raman spectroscopy coupled to a microprobe", *Analytical and Bioanalytical Chemistry*, vol. 398, no. 1, pp. 477–487, 2010, ISSN: 16182642. DOI: 10.1007/s00216-010-3910-6.

[176] J. Desroches, M. Jermyn, K. Mok, C. Lemieux-Leduc, J. Mercier, K. St-Arnaud, K. Urmey, M.-C. Guiot, E. Marple, K. Petrecca, and F. Leblond, "Characterization of a Raman spectroscopy probe system for intraoperative brain tissue classification", *Biomedical Optics Express*, vol. 6, no. 7, p. 2380, Jul. 1, 2015, ISSN: 2156-7085, 2156-7085. DOI: 10.1364/BOE.6.002380. [Online]. Available: https://www.osapublishing.org/abstract.cfm?URI=boe-6-7-2380 (visited on 10/03/2018).

[177] M. Jermyn, J. Desroches, J. Mercier, M.-A. Tremblay, K. St-Arnaud, M.-C. Guiot, K. Petrecca, and F. Leblond, "Neural networks improve brain cancer detection with Raman spectroscopy in the presence of operating room light artifacts", *Journal of Biomedical Optics*, vol. 21, no. 9, p. 094 002, Sep. 8, 2016, ISSN: 1083-3668. DOI: 10.1117/1.JBO.21.9.094002. [Online]. Available: http://biomedicaloptics.spiedigitallibrary.org/article.aspx?doi=10.1117/1.JBO.21.9.094002 (visited on 10/03/2018).

[178] M. Jermyn, J. Desroches, J. Mercier, K. St-Arnaud, M.-C. Guiot, F. Leblond, and K. Petrecca, "Raman spectroscopy detects distant invasive brain cancer cells centimeters beyond MRI capability in humans", *Biomedical Optics Express*, vol. 7, no. 12, p. 5129, 2016, ISSN: 2156-7085. DOI: 10.1364/BOE.7.005129. [Online]. Available: https://www.osapublishing.org/abstract.cfm?URI=boe-7-12-5129.

[179] M. Jermyn, J. Mercier, K. Aubertin, J. Desroches, K. Urmey, J. Karamchandiani, E. Marple, M.-C. Guiot, F. Leblond, and K. Petrecca, "Highly Accurate Detection of Cancer *In Situ* with Intraoperative, Label-Free, Multimodal Optical Spectroscopy", *Cancer Research*, vol. 77, no. 14, pp. 3942–3950, Jul. 15, 2017, ISSN: 0008-5472, 1538-7445. DOI: 10.1158/0008-5472.CAN-17-0668. [Online]. Available: http://cancerres.aacrjournals.org/lookup/doi/10.1158/0008-5472.CAN-17-0668 (visited on 10/03/2018).

[180] O. A. C. Stevens, J. Hutchings, W. Gray, R. L. Vincent, and J. C. Day, "Miniature standoff Raman probe for neurosurgical applications", *Journal of Biomedical Optics*, vol. 21, no. 8, p. 087 002, 2016, ISSN: 1083-3668. DOI: 10.1117/1.jbo.21.8.087002.

[181] J. Desroches, M. Jermyn, M. Pinto, F. Picot, M. A. Tremblay, S. Obaid, E. Marple, K. Urmey, D. Trudel, G. Soulez, M. C. Guiot, B. C. Wilson, K. Petrecca, and F. Leblond, "A new method using Raman spectroscopy for in vivo targeted brain cancer tissue biopsy", *Scientific Reports*, vol. 8, no. 1, pp. 1–10, 2018, ISSN: 20452322. DOI: 10.1038/s41598-018-20233-3.

[182] S. Koljenović, T. C. Schut, R Wolthuis, A. J. Vincent, G. Hendriks-Hagevi, L. Santos, J. M. Kros, and G. J. Puppels, "Raman spectroscopic characterization of porcine brain tissue using a single fiber-optic probe", *Analytical Chemistry*, vol. 79, no. 2, pp. 557–564, 2007, ISSN: 00032700. DOI: 10.1021/ac0616512.

[183] M. Agenant, M. Grimbergen, R. Draga, E. Marple, R. Bosch, and C. van Swol, "Clinical superficial Raman probe aimed for epithelial tumor detection: Phantom model results", *Biomedical Optics Express*, vol. 5, no. 4, p. 1203, 2014, ISSN: 2156-7085. DOI: 10.1364/boe.5.001203.

[184] B. Burgoyne, N. Godbout, and S. Lacroix, "Nonlinear pulse propagation in optical fibers using second order moments", vol. 15, no. 16, pp. 10 075–10 090, 2007.

[185] M. T. Cicerone and C. H. Camp, "Potential Roles for Spectroscopic Coherent Raman Imaging for Histopathology and Biomedicine", in *Neurophotonics and Biomedical Spectroscopy*, Elsevier Ltd, 2019, pp. 547–570, ISBN: 9780323480673. DOI: 10.1016/b978-0-323-48067-3.00021-4. [Online]. Available: http://dx.doi.org/10.1016/B978-0-323-48067-3.00021-4.

[186] Y. Fu, H. Wang, R. Shi, and J.-x. Cheng, "Characterization of photodamage in coherent anti-Stokes Raman scattering microscopy", *Optics Express*, vol. 14, no. 9, p. 3942, 2006. DOI: 10.1364/oe.14.003942.

[187] A. Hopt and E. Neher, "Highly Nonlinear Photodamage in Two-Photon Fluorescence Microscopy", *Biophysical Journal*, vol. 80, no. April, pp. 1–8, 2001. [Online]. Available: papers3://publication/uuid/117F0D01-1F10-494A-BC54-4FE0D1BA64A2.

[188] T. Gottschall, T. Meyer, M. Baumgartl, C. Jauregui, M. Schmitt, J. Popp, J. Limpert, and A. Tünnermann, "Fiber-based light sources for biomedical applications of coherent anti-Stokes Raman scattering microscopy", *Laser and Photonics Reviews*, vol. 9, no. 5, pp. 435–451, 2015, ISSN: 18638899. DOI: 10.1002/lpor.201500023.

[189] K. Charan, B. Li, M. Wang, C. P. Lin, and C. Xu, "Fiber-based tunable repetition rate source for deep tissue two-photon fluorescence microscopy", *Biomedical Optics Express*, vol. 9, no. 5, p. 2304, 2018, ISSN: 2156-7085. DOI: 10.1364/boe.9.002304.

[190] Z. Li, W. Minzhu, Z. Jian, and Z. Ju, "Application of Infrared Spectroscopy in Biomedical Polymer Materials", in *Macro To Nano Spectroscopy*, 2012. DOI: 10.5772/48060.

[191] N. Haj-Hosseini, J. C. O. Richter, P. Milos, M. Hallbeck, and K. Wårdell, "5-ALA fluorescence and laser Doppler flowmetry for guidance in a stereotactic brain tumor biopsy", *Biomedical Optics Express*, vol. 9, no. 5, p. 2284, 2018, ISSN: 2156-7085. DOI: 10.1364/boe.9.002284.

[192] F. Picot, S. Lessard, M.-a. Tremblay, F. Picot, A. Goyette, S. Obaid, J. Desroches, S. Lessard, and M.-a. Tremblay, "Interstitial imaging with multiple diffusive reflectance spectroscopy projections for in vivo blood vessels detection during brain needle biopsy procedures spectroscopy projections for in vivo blood vessels", vol. 6, no. 2, 2019. DOI: 10.1117/1.NPh.6.2.025003.

[193] N. Bergner, C. Krafft, K. D. Geiger, M. Kirsch, G. Schackert, and J. Popp, "Unsupervised Unmixing of Raman Microspectroscopic Images for Morphochemical Analysis of Non-Dried Brain Tumor Specimens.", *Analytical and bioanalytical chemistry*, vol. 403, no. 3, pp. 719–25, 2012, Bergner, Norbert. Institute of Photonic Technology, Albert Einstein Strase 9, 07745, Jena, Germany., ISSN: 1618-2650. DOI: 10.1007/s00216-012-5858-1.

[194] N. Bergner, A. Medyukhina, K. D. Geiger, M. Kirsch, G. Schackert, C. Krafft, and J. Popp, "Hyperspectral Unmixing of Raman Micro-Images for Assessment of Morphological and Chemical Parameters in Non-Dried Brain Tumor Specimens.", *Analytical and bioanalytical chemistry*, vol. 405, no. 27, pp. 8719–28, 2013, Bergner, Norbert. Institute of Photonic Technology, Albert Einstein Strase 9, 07745, Jena, Germany., ISSN: 1618-2650. DOI: 10.1007/s00216-013-7257-7.

[195] R. Kast, G. Auner, S. Yurgelevic, B. Broadbent, A. Raghunathan, L. M. Poisson, T. Mikkelsen, M. L. Rosenblum, and S. N. Kalkanis, "Identification of regions of normal grey matter and white matter from pathologic glioblastoma and necrosis in frozen sections using Raman imaging", *Journal of Neuro-Oncology*, vol. 125, no. 2, pp. 287–295, Nov. 2015, ISSN: 0167-594X, 1573-7373. DOI: 10.1007/s11060-015-1929-4. [Online]. Available: http://link.springer.com/10.1007/s11060-015-1929-4 (visited on 10/15/2018).

[196] "The Biochemical, Nanomechanical and Chemometric Signatures of Brain Cancer.", *Spectrochimica acta. Part A, Molecular and biomolecular spectroscopy*, vol. 188, pp. 8–19, cuo, 9602533 2018, ISSN: 1873-3557. DOI: 10.1016/j.saa.2017.06.037.

[197] C. L. Evans, X. Xu, S. Kesari, X. S. Xie, S. T. C. Wong, and G. S. Young, "Chemically-selective imaging of brain structures with CARS microscopy.", *Optics express*, vol. 15, no. 19, pp. 12 076–12 087, 2007, ISSN: 1094-4087. DOI: 10.1364/OE.15.012076.

[198] "Label-Free Delineation of Brain Tumors by Coherent Anti-Stokes Raman Scattering Microscopy in an Orthotopic Mouse Model and Human Glioblastoma.", *PloS one*, vol. 9, no. 9, e107115, 2014, ISSN: 1932-6203. DOI: 10.1371/journal.pone.0107115.

[199] B. F. M. Romeike, T. Meyer, R. Reichart, R. Kalff, I. Petersen, B. Dietzek, and J. Popp, "Coherent anti-Stokes Raman scattering and two photon excited fluorescence for neurosurgery", *Clinical Neurology and Neurosurgery*, vol. 131, pp. 42–46, 2015, ISSN: 18726968. DOI: 10.1016/j.clineuro.2015.01.022. [Online]. Available: http://dx.doi.org/10.1016/j.clineuro.2015.01.022.

[200] R. Galli, O. Uckermann, A. Temme, E. Leipnitz, M. Meinhardt, E. Koch, G. Schackert, G. Steiner, and M. Kirsch, "Assessing the Efficacy of Coherent Anti-Stokes Raman Scattering Microscopy for the Detection of Infiltrating Glioblastoma in Fresh Brain Samples", *Journal of Biophotonics*, vol. 10, no. 3, pp. 404–414, 2017, ISSN: 1864063X. DOI: 10.1002/jbio.201500323.

[201] R. Galli, O. Uckermann, T. Sehm, E. Leipnitz, C. Hartmann, F. Sahm, E. Koch, G. Schackert, G. Steiner, and M. Kirsch, "Identification of distinctive features in human intracranial tumors by label-free nonlinear multimodal microscopy", *Journal of Biophotonics*, no. June, e201800465, 2019, ISSN: 1864-063X. DOI: 10.1002/jbio.201800465.

[202] A. H. Fischer, K. A. Jacobson, J. Rose, and R. Zeller, "Hematoxylin and eosin staining of tissueand cell sections", *Cold Spring Harbor Protocols*, vol. 3, no. 5, pp. 4986–4988, 2008, ISSN: 15596095. DOI: 10.1101/pdb.prot4986.

[203] C. W. Freudiger, R. Pfannl, D. A. Orringer, B. G. Saar, M. Ji, Q. Zeng, L. Ottoboni, W. Ying, C. Waeber, J. R. Sims, P. L. De Jager, O. Sagher, M. A. Philbert, X. Xu, S. Kesari, X. S. Xie, and G. S. Young, "Multicolored stain-free histopathology with coherent Raman imaging", *Laboratory Investigation*, vol. 92, no. 10, pp. 1492–1502, 2012, ISSN: 00236837. DOI: 10.1038/labinvest.2012.109. arXiv: NIHMS150003. [Online]. Available: http://dx.doi.org/10.1038/labinvest.2012.109.

[204] B. G. Saar, C. W. Freudiger, J. Reichman, C. M. Stanley, G. R. Holtom, and X. S. Xie, "Video-rate molecular imaging in vivo with stimulated Raman scattering", *Science*, vol. 330, no. 6009, pp. 1368–1370, 2010, ISSN: 00368075. DOI: 10.1126/science.1197236.

[205] F. K. Lu, D. Calligaris, O. I. Olubiyi, I. Norton, W. Yang, S. Santagata, X. S. Xie, A. J. Golby, and N. Y. Agar, "Label-free neurosurgical pathology with stimulated Raman imaging", *Cancer Research*, vol. 76, no. 12, pp. 3451–3462, 2016, ISSN: 15387445. DOI: 10.1158/0008-5472.CAN-16-0270.

[206] F.-K. Lu, S. Santagata, X. S. Xie, A. J. Golby, and N. Y. R. Agar, *Label-Free Neurosurgical Pathology with Stimulated Raman Imaging: A Dataset*, version V1, 2016. DOI: 10.7910/DVN/EZW4EK. [Online]. Available: https://doi.org/10.7910/DVN/EZW4EK.

[207] C. W. Freudiger, W. Yang, G. R. Holtom, N. Peyghambarian, X. S. Xie, and K. Q. Kieu, "Stimulated Raman scattering microscopy with a robust fibre laser source", *Nature Photonics*, vol. 8, no. 2, pp. 153–159, 2014, ISSN: 17494885. DOI: 10.1038/nphoton.2013.360. [Online]. Available: http://dx.doi.org/10.1038/nphoton.2013.360.

[208] T. C. Hollon, S. Lewis, B. Pandian, Y. S. Niknafs, M. R. Garrard, H. Garton, C. O. Maher, K. McFadden, M. Snuderl, A. P. Lieberman, K. Muraszko, S. Camelo-Piragua, and D. A. Orringer, "Rapid intraoperative diagnosis of pediatric brain tumors using stimulated raman histology", *Cancer Research*, vol. 78, no. 1, pp. 278–289, 2018, ISSN: 15387445. DOI: 10.1158/0008-5472.CAN-17-1974.

[209] K. Bae, W. Zheng, K. Lin, S. W. Lim, Y. K. Chong, and C. Tang, "Epi-Detected Hyperspectral Stimulated Raman Scattering Microscopy for Label-Free Molecular Subtyping of Glioblastomas", *Analytical Chemistry*, vol. 90, pp. 10 249–10 255, 2018, ISSN: 0003-2700. DOI: 10.1021/acs.analchem.8b01677.

[210] R. Galli, O. Uckermann, E. F. Andresen, K. D. Geiger, E. Koch, G. Schackert, G. Steiner, and M. Kirsch, "Intrinsic indicator of photodamage during label-free multiphoton microscopy of cells and tissues", *PLoS ONE*, vol. 9, no. 10, pp. 19–23, 2014, ISSN: 19326203. DOI: 10.1371/journal.pone.0110295.

[211] C. S. Liao, P. Wang, C. Y. Huang, P. Lin, G. Eakins, R. T. Bentley, R. Liang, and J. X. Cheng, "In Vivo and in Situ Spectroscopic Imaging by a Handheld Stimulated Raman Scattering Microscope", *ACS Photonics*, vol. 5, no. 3, pp. 947–954, 2018, ISSN: 23304022. DOI: 10.1021/acsphotonics.7b01214.

[212] K. St-Arnaud, K. Aubertin, M. Strupler, W. J. Madore, A. A. Grosset, K. Petrecca, D. Trudel, and F. Leblond, "Development and characterization of a handheld hyperspectral Raman imaging probe system for molecular characterization of tissue on mesoscopic scales", *Medical Physics*, vol. 45, no. 1, pp. 328–339, 2018, ISSN: 00942405. DOI: 10.1002/mp.12657.

[213] A. Lukic, S. Dochow, H. Bae, G. Matz, I. Latka, B. Messerschmidt, M. Schmitt, and J. Popp, "Endoscopic fiber probe for nonlinear spectroscopic imaging", *Optica*, vol. 4, no. 5, p. 496, 2017. DOI: 10.1364/optica.4.000496.

[214] P. Zirak, G. Matz, B. Messerschmidt, T. Meyer, M. Schmitt, J. Popp, O. Uckermann, R. Galli, M. Kirsch, M. J. Winterhalder, and A. Zumbusch, "Invited Article: A rigid coherent anti-Stokes Raman scattering endoscope with high resolution and a large field of view", *APL Photonics*, vol. 3, no. 9, 2018, ISSN: 23780967. DOI: 10.1063/1.5027182.

[215] K. St-Arnaud, K. Aubertin, M. Strupler, M. Jermyn, K. Petrecca, D. Trudel, and F. Leblond, "Wide-field spontaneous Raman spectroscopy imaging system for biological tissue interrogation", *Optics Letters*, vol. 41, no. 20, p. 4692, 2016, ISSN: 0146-9592. DOI: 10.1364/ol.41.004692.

[216] F. Légaré, C. L. Evans, F. Ganikhanov, and X. S. Xie, "Towards CARS Endoscopy", *Opt. Express*, vol. 14, no. 10, pp. 4427–4432, 2006. DOI: 10.1364/OE.14.004427. [Online]. Available: http://www.opticsexpress.org/abstract.cfm?URI=oe-14-10-4427.

[217] M. Balu, G. Liu, Z. Chen, B. J. Tromberg, and E. O. Potma, "Fiber delivered probe for efficient CARS imaging of tissues.", *Optics express*, vol. 18, no. 3, pp. 2380–2388, 2010, ISSN: 1094-4087. DOI: 10.1364/OE.18.002380. arXiv: NIHMS150003.

[218] P. Deladurantaye, A. Paquet, C. Paré, H. Zheng, M. Doucet, D. Gay, M. Poirier, J.-F. Cormier, O. Mermut, B. C. Wilson, and E. J. Seibel, "Advances in engineering of high contrast CARS imaging endoscopes", *Optics Express*, vol. 22, no. 21, p. 25 053, 2014, ISSN: 1094-4087. DOI: 10.1364/oe.22.025053. [Online]. Available: http://www.ncbi.nlm.nih.gov/pubmed/25401538.

[219] H Wang, T. B. Huff, and J. X. Cheng, "Coherent anti-Stokes Raman scattering imaging with a laser source delivered by a photonic crystal fiber", *Opt Lett*, vol. 31, no. 10, pp. 1417–1419, 2006. [Online]. Available: http://www.ncbi.nlm.nih.gov/entrez/query.fcgi?cmd=Retrieve{\&}db=PubMed{\&}dopt=Citation{\&}list{_}uids=16642124.

[220] S. Brustlein, P. Berto, R. Hostein, P. Ferrand, C. Billaudeau, D. Marguet, A. Muir, J. Knight, and H. Rigneault, "Double-clad hollow core photonic crystal fiber for coherent Raman endoscope.", *Optics express*, vol. 19, no. 13, pp. 12 562–12 568, 2011, ISSN: 1094-4087. DOI: 10.1364/OE.19.012562.

[221] A. Lombardini, E. R. Andresen, A. Kudlinski, I. Rimke, and H. Rigneault, "Origin and suppression of parasitic signals in Kagomé lattice hollow core fibers used for SRS microscopy and endoscopy", *Optics Letters*, vol. 42, no. 9, p. 1824, 2017, ISSN: 0146-9592. DOI: 10.1364/ol.42.001824.

[222] B. G. Saar, R. S. Johnston, C. W. Freudiger, X. S. Xie, and E. J. Seibel, "Coherent Raman scanning fiber endoscopy.", *Optics letters*, vol. 36, no. 13, pp. 2396–2398, 2011, ISSN: 0146-9592. DOI: 10.1364/OL.36.002396.

[223] C.-S. Liao, K.-C. Huang, W. Hong, A. J. Chen, C. Karanja, P. Wang, G. Eakins, and J.-X. Cheng, "Stimulated Raman spectroscopic imaging by microsecond delay-line tuning", *Optica*, vol. 3, no. 12, p. 1377, 2016, ISSN: 2334-2536. DOI: 10.1364/OPTICA.3.001377. [Online]. Available: https://www.osapublishing.org/abstract.cfm?URI=optica-3-12-1377.

[224] T. Gottschall, T. Meyer, M. Schmitt, J. Popp, J. Limpert, and A. Tünnermann, "Advances in laser concepts for multiplex, coherent Raman scattering micro-spectroscopy and imaging", *TrAC - Trends in Analytical Chemistry*, vol. 102, pp. 103–109, 2018, ISSN: 18793142. DOI: 10.1016/j.trac.2018.01.010. [Online]. Available: https://doi.org/10.1016/j.trac.2018.01.010.

[225] C. C. McIntyre, S. Mori, D. L. Sherman, N. V. Thakor, and J. L. Vitek, "Electric field and stimulating influence generated by deep brain stimulation of the subthalamic nucleus", *Clinical Neurophysiology*, vol. 115, no. 3, pp. 589–595, 2004, ISSN: 1388-2457. DOI: http://dx.doi.org/10.1016/j.clinph.2003.10.033. [Online]. Available: http://www.sciencedirect.com/science/article/pii/S1388245703004048.

[226] Laser Institute of America, *ANSI Z136.1-2014*. 2014, vol. 90, ISBN: 9781940168012. DOI: 10.5594/j01369.

[227] ICNIRP, "Icnirp guidelines on limits of exposure to laser radiation of wavelengths between 180 nm and 1,000 μm", *Health Physics*, vol. 105, no. 3, pp. 271–295, 2013, ISSN: 00179078. DOI: 10.1097/HP.0b013e3182983fd4.

[228] M. Nourhashemi, M. Mahmoudzadeh, and F. Wallois, "Thermal impact of near-infrared laser in advanced noninvasive optical brain imaging", *Neurophotonics*, vol. 3, no. 1, p. 015 001, 2016, ISSN: 2329-423X. DOI: 10.1117/1.NPh.3.1.015001. [Online]. Available: http://neurophotonics.spiedigitallibrary.org/article.aspx?doi=10.1117/1.NPh.3.1.015001.

[229] H. Wang, B. Wang, K. P. Normoyle, K. Jackson, K. Spitler, M. Sharrock, C. M. Miller, C. Best, D. Llano, and R. Du, "Brain temperature and its fundamental properties: A review for clinical neuroscientists", *Frontiers in Neuroscience*, vol. 8, no. SEP, pp. 1–17, 2014, ISSN: 1662453X. DOI: 10.3389/fnins.2014.00307.

[230] E. A. Kiyatkin, P. L. Brown, and R. A. Wise, "Brain temperature fluctuation: A reflection of functional neural activation", *European Journal of Neuroscience*, vol. 16, no. 1, pp. 164–168, 2002, ISSN: 0953816X. DOI: 10.1046/j.1460-9568.2002.02066.x.

[231] S. Thomsen, "Pathologic Analysis of Photothermal and Photomechanical Effects of Laser–Tissue Interactions", *Photochemistry and Photobiology*, vol. 53, no. 6, pp. 825–835, 1991, ISSN: 17511097. DOI: 10.1111/j.1751-1097.1991.tb09897.x.

[232] I. N. Christie, J. A. Wells, P. Southern, N. Marina, S. Kasparov, A. V. Gourine, and M. F. Lythgoe, "FMRI response to blue light delivery in the naïve brain: Implications for combined optogenetic fMRI studies", *NeuroImage*, vol. 66, pp. 634–641, 2013, ISSN: 10538119. DOI: 10.1016/j.neuroimage.2012.10.074. [Online]. Available: http://dx.doi.org/10.1016/j.neuroimage.2012.10.074.

[233] J. M. Stujenske, T. Spellman, and J. A. Gordon, "Modeling the Spatiotemporal Dynamics of Light and Heat Propagation for InVivo Optogenetics", *Cell Reports*, vol. 12, no. 3, pp. 525–534, 2015, ISSN: 22111247. DOI: 10.1016/j.celrep.2015.06.036. arXiv: 15334406. [Online]. Available: http://dx.doi.org/10.1016/j.celrep.2015.06.036.

[234] Y. Shin, M. Yoo, H.-S. Kim, S.-K. Nam, H.-I. Kim, S.-K. Lee, S. Kim, and H.-S. Kwon, "Characterization of fiber-optic light delivery and light-induced temperature changes in a rodent brain for precise optogenetic neuromodulation", *Biomedical Optics Express*, vol. 7, no. 11, p. 4450, 2016, ISSN: 2156-7085. DOI: 10.1364/BOE.7.004450. [Online]. Available: https://www.osapublishing.org/abstract.cfm?URI=boe-7-11-4450.

[235] S. Senova, I. Scisniak, C.-c. Chiang, I. Doignon, and S. Palfi, "Experimental assessment of the safety and potential efficacy of high irradiance photostimulation of brain tissues", *Nature Publishing Group*, no. March, pp. 1–12, 2017. DOI: 10.1038/srep43997. [Online]. Available: http://dx.doi.org/10.1038/srep43997.

[236] B. Gysbrechts, L. Wang, N. N. D. Trong, H. Cabral, Z. Navratilova, F. Battaglia, W. Saeys, and C. Bartic, "Light distribution and thermal effects in the rat brain under optogenetic stimulation", *Journal of Biophotonics*, vol. 9, no. 6, pp. 576–585, 2016, ISSN: 18640648. DOI: 10.1002/jbio.201500106.

[237] H. J. Koester, D. Baur, R. Uhl, and S. W. Hell, "Ca2+ fluorescence imaging with pico- and femtosecond two-photon excitation: Signal and photodamage", *Biophysical Journal*, vol. 77, no. 4, pp. 2226–2236, 1999, ISSN: 00063495. DOI: 10.1016/S0006-3495(99)77063-3. [Online]. Available: http://dx.doi.org/10.1016/S0006-3495(99)77063-3.

[238] A. Vogel, J. Noack, G. Hüttman, and G. Paltauf, "Mechanisms of femtosecond laser nanosurgery of cells and tissues", *Applied Physics B: Lasers and Optics*, vol. 81, no. 8, pp. 1015–1047, 2005, ISSN: 09462171. DOI: 10.1007/s00340-005-2036-6.

[239] K. Podgorski and G. Ranganathan, "Brain heating induced by near-infrared lasers during multiphoton microscopy", *Journal of Neurophysiology*, vol. 116, no. 3, pp. 1012–1023, 2016, ISSN: 0022-3077. DOI: 10.1152/jn.00275.2016.

[240] B. G. Saar, C. W. Freudiger, X. Xu, A. Huttner, S. Kesari, G. Young, and X. S. Xie, "Coherent raman tissue imaging in the brain", *Cold Spring Harbor Protocols*, vol. 2014, no. 5, pp. 472–482, 2014, ISSN: 15596095. DOI: 10.1101/pdb.top081695.

[241] H. J. Butler, L. Ashton, B. Bird, G. Cinque, K. Curtis, J. Dorney, K. Esmonde-White, N. J. Fullwood, B. Gardner, P. L. Martin-Hirsch, M. J. Walsh, M. R. McAinsh, N. Stone, and F. L. Martin, "Using Raman spectroscopy to characterize biological materials", *Nature Protocols*, vol. 11, no. 4, pp. 664–687, Mar. 10, 2016, ISSN: 1754-2189, 1750-2799. DOI: 10.1038/nprot.2016.036. [Online]. Available: http://www.nature.com/doifinder/10.1038/nprot.2016.036 (visited on 10/18/2018).

[242] M. Brusatori, G. Auner, T. Noh, L. Scarpace, B. Broadbent, and S. N. Kalkanis, "Intraoperative Raman Spectroscopy", *Neurosurgery Clinics of North America*, vol. 28, no. 4, pp. 633–652, Oct. 2017, ISSN: 10423680. DOI: 10.1016/j.nec.2017.05.014. [Online]. Available: https://linkinghub.elsevier.com/retrieve/pii/S1042368017300724 (visited on 09/30/2018).

[243] C. Beleites, K. Geiger, M. Kirsch, S. B. Sobottka, G. Schackert, and R. Salzer, "Raman Spectroscopic Grading of Astrocytoma Tissues: Using Soft Reference Information.", *Analytical and bioanalytical chemistry*, vol. 400, no. 9, pp. 2801–16, 2011, ISSN: 1618-2650. DOI: 10.1007/s00216-011-4985-4.

[244] A. C. S. Talari, Z. Movasaghi, S. Rehman, and I. ur Rehman, "Raman Spectroscopy of Biological Tissues", *Applied Spectroscopy Reviews*, vol. 50, no. 1, pp. 46–111, Jan. 2, 2015, ISSN: 0570-4928, 1520-569X. DOI: 10.1080/05704928.2014.923902. [Online]. Available: http://www.tandfonline.com/doi/abs/10.1080/05704928.2014.923902 (visited on 09/26/2018).

[245] B. Chase, "A New Generation of Raman Instrumentation", *Applied Spectroscopy*, vol. 48, no. 7, 14A–19A, Jul. 1, 1994. [Online]. Available: https://www.osapublishing.org/as/abstract.cfm?uri=as-48-7-14A (visited on 06/19/2019).

[246] N. K. Afseth, V. H. Segtnan, and J. P. Wold, "Raman Spectra of Biological Samples: A Study of Preprocessing Methods", *Applied Spectroscopy*, vol. 60, no. 12, pp. 1358–1367, Dec. 1, 2006, ISSN: 0003-7028. DOI: 10.1366/000370206779321454. [Online]. Available: https://doi.org/10.1366/000370206779321454 (visited on 06/19/2019).

[247] Z Dehghani-Bidgoli, M. H. Miran Baygi, E Kabir, and R Malekfar, "Developing an Instrument-Independent Algorithm for Raman Spectroscopy: A Case of Cancer Detection.", *Technology in cancer research & treatment*, vol. 13, no. 2, pp. 119–27, 2014, Dehghani-Bidgoli, Z. Department of Electrical and Computer Engineering, Tarbiat Modares University, Tehran, I. R. Iran. miranbmh@modares.ac.ir., ISSN: 1533-0338. DOI: 10.7785/tcrt.2012.500373.

[248] A. C. Croce and G Bottiroli, "Autofluorescence spectroscopy and imaging: a tool for biomedical research and diagnosis", *European Journal of Histochemistry*, p. 18, 2014.

[249] S. Yang, B. Li, M. N. Slipchenko, A. Akkus, N. G. Singer, and O. Akkus, "Laser Wavelength Dependence of Background Fluorescence in Raman Spectroscopic Analysis of Synovial Fluid from Symptomatic Joints", p. 16, 2014.

[250] C. Krafft, B. Belay, N. Bergner, B. F. M. Romeike, R. Reichart, R. Kalff, and J. Popp, "Advances in Optical Biopsy–Correlation of Malignancy and Cell Density of Primary Brain Tumors Using Raman Microspectroscopic Imaging.", *The Analyst*, vol. 137, no. 23, pp. 5533–7, 2012, Krafft, Christoph. Institute of Photonic Technology, Albert-Einstein-Str 9, 07745 Jena, Germany. christoph.krafft@ipht-jena.de, ISSN: 1364-5528. DOI: 10.1039/c2an36083g.

[251] H. J. Byrne, P. Knief, M. E. Keating, and F. Bonnier, "Spectral pre and post processing for infrared and Raman spectroscopy of biological tissues and cells", *Chemical Society Reviews*, vol. 45, no. 7, pp. 1865–1878, Mar. 29, 2016, ISSN: 1460-4744. DOI: 10.1039/C5CS00440C. [Online]. Available: https://pubs.rsc.org/en/content/articlelanding/2016/cs/c5cs00440c (visited on 08/10/2019).

[252] J. Zhao, H. Lui, D. I. McLean, and H. Zeng, "Automated Autofluorescence Background Subtraction Algorithm for Biomedical Raman Spectroscopy", *Applied Spectroscopy*, vol. 61, no. 11, pp. 1225–1232, Nov. 2007, ISSN: 0003-7028, 1943-3530. DOI: 10.1366/000370207782597003. [Online]. Available: http://journals.sagepub.com/doi/10.1366/000370207782597003 (visited on 10/15/2018).

[253] S. He, W. Zhang, L. Liu, Y. Huang, J. He, W. Xie, P. Wu, and C. Du, "Baseline correction for Raman spectra using an improved asymmetric least squares method", *Analytical Methods*, p. 6, 2014.

[254] S. Guo, T. Bocklitz, and J. Popp, "Optimization of Raman-spectrum baseline correction in biological application", *The Analyst*, vol. 141, no. 8, pp. 2396–2404, 2016, ISSN: 0003-2654, 1364-5528. DOI: 10.1039/C6AN00041J. [Online]. Available: http://xlink.rsc.org/?DOI=C6AN00041J (visited on 10/18/2018).

[255] Y. Cai, C. Yang, D. Xu, and W. Gui, "Baseline correction for Raman spectra using penalized spline smoothing based on vector transformation", *Analytical Methods*, vol. 10, no. 28, pp. 3525–3533, Jul. 19, 2018, ISSN: 1759-9679. DOI: 10.1039/C8AY00914G. [Online]. Available: https://pubs.rsc.org/en/content/articlelanding/2018/ay/c8ay00914g (visited on 08/10/2019).

[256] *Biomedical Applications of Synchrotron Infrared Microspectroscopy*. Dec. 15, 2010, ISBN: 978-0-85404-154-1. DOI: 10.1039/9781849731997. [Online]. Available: https://pubs.rsc.org/en/content/ebook/978-0-85404-154-1 (visited on 08/10/2019).

[257] M. J. Pelletier, "Quantitative Analysis Using Raman Spectrometry", *Applied Spectroscopy*, vol. 57, no. 1, 20A–42A, Jan. 1, 2003. [Online]. Available: https://www.osapublishing.org/as/abstract.cfm?uri=as-57-1-20A (visited on 06/19/2019).

[258] I. Guyon and A. Elisseeff, "An Introduction to Variable and Feature Selection", *Journal of Machine Learning Research*, p. 26, 2003.

[259] Y. Bengio, A. Courville, and P. Vincent, "Representation Learning: A Review and New Perspectives", *IEEE Transactions on Pattern Analysis and Machine Intelligence*, vol. 35, no. 8, pp. 1798–1828, Aug. 2013, ISSN: 0162-8828, 2160-9292. DOI: 10.1109/TPAMI.2013.50. [Online]. Available: http://ieeexplore.ieee.org/document/6472238/ (visited on 02/25/2019).

[260] Z. He and W. Yu, "Stable Feature Selection for Biomarker Discovery", *Computational Biology and Chemistry*, vol. 34, no. 4, pp. 215–225, Aug. 1, 2010, ISSN: 1476-9271. DOI: 10.1016/j.compbiolchem.2010.07.002. [Online]. Available: http://www.sciencedirect.com/science/article/pii/S1476927110000502.

[261] R. P. Aguiar, L. Silveira, E. T. Falcão, M. T. T. Pacheco, R. A. Zângaro, and C. A. Pasqualucci, "Discriminating Neoplastic and Normal Brain Tissues *in Vitro* Through Raman Spectroscopy: A Principal Components Analysis Classification Model", *Photomedicine and Laser Surgery*, vol. 31, no. 12, pp. 595–604, Dec. 2013, ISSN: 1549-5418, 1557-8550. DOI: 10.1089/pho.2012.3460. [Online]. Available: https://www.liebertpub.com/doi/10.1089/pho.2012.3460 (visited on 10/15/2018).

[262] E. Ostertag, M. Stefanakis, K. Rebner, and R. W. Kessler, "Elastic and Inelastic Light Scattering Spectroscopy and Its Possible Use for Label-Free Brain Tumor Typing.", *Analytical and bioanalytical chemistry*, vol. 409, no. 28, pp. 6613–6623, 2017, ISSN: 1618-2650. DOI: 10.1007/s00216-017-0614-1.

[263] K. Tanahashi, A. Natsume, F. Ohka, H. Momota, A. Kato, K. Motomura, N. Watabe, S. Muraishi, H. Nakahara, Y. Saito, I. Takeuchi, and T. Wakabayashi, "Unique Spectral Markers Discern Recurrent Glioblastoma Cells from Heterogeneous Parent Population.", *Scientific reports*, vol. 6, no. 101563288, p. 26 538, 2016, ISSN: 2045-2322. DOI: 10.1038/srep26538.

[264] Y. Zhou, C.-H. Liu, Y. Sun, Y. Pu, S. Boydston-White, Y. Liu, and R. R. Alfano, "Human Brain Cancer Studied by Resonance Raman Spectroscopy.", *Journal of biomedical optics*, vol. 17, no. 11, p. 116 021, 2012, Zhou, Yan. The Air Force General Hospital, PLA, No. 30 Fuchenglu, Haidian District, Beijing 100142, China., ISSN: 1560-2281. DOI: 10.1117/1.JBO.17.11.116021.

[265] A. Beljebbar, S. Dukic, N. Amharref, and M. Manfait, "Ex Vivo and in Vivo Diagnosis of C6 Glioblastoma Development by Raman Spectroscopy Coupled to a Microprobe.", *Analytical and bioanalytical chemistry*, vol. 398, no. 1, pp. 477–87, 2010, Beljebbar, Abdelilah. Unite MeDIAN, UMR CNRS 6237-MEDyC, Universite de Reims Champagne-Ardenne, IFR 53, UFR de Pharmacie, 51 rue Cognacq-Jay, 51096 Reims Cedex, France. abdelilah.beljebbar@univ-reims.fr, ISSN: 1618-2650. DOI: 10.1007/s00216-010-3910-6.

[266] N. Amharref, A. Beljebbar, S. Dukic, L. Venteo, L. Schneider, M. Pluot, and M. Manfait, "Discriminating Healthy from Tumor and Necrosis Tissue in Rat Brain Tissue Samples by Raman Spectral Imaging.", *Biochimica et biophysica acta*, vol. 1768, no. 10, pp. 2605–15, 2007, Amharref, Nadia. Unite MeDIAN, CNRS-UMR 6142, UFR de Pharmacie, IFR 53, Universite de Reims Champagne-Ardenne, 51 rue Cognacq-Jay, 51096 Reims Cedex, France., ISSN: 0006-3002.

[267] S. Koljenovic, L.-P. Choo-Smith, T. C. Bakker Schut, J. M. Kros, H. J. van den Berge, and G. J. Puppels, "Discriminating Vital Tumor from Necrotic Tissue in Human Glioblastoma Tissue Samples by Raman Spectroscopy.", *Laboratory investigation; a journal of technical methods and pathology*, vol. 82, no. 10, pp. 1265–77, 2002, Koljenovic, Senada.

Department of General Surgery 10M, Erasmus University Rotterdam and University Hospital Rotterdam Dijkzigt, Rotterdam, The Netherlands., ISSN: 0023-6837.

[268] L. M. Fullwood, G. Clemens, D. Griffiths, K. Ashton, T. P. Dawson, R. W. Lea, C. Davis, F. Bonnier, H. J. Byrne, and M. J. Baker, "Investigating the Use of Raman and Immersion Raman Spectroscopy for Spectral Histopathology of Metastatic Brain Cancer and Primary Sites of Origin", *Analytical Methods*, vol. 6, no. 12, pp. 3948–3961, 2014, ISSN: 17599660. DOI: 10.1039/c3ay42190b.

[269] N. Bergner, T. Bocklitz, B. Romeike, R. Reichart, R. Kalff, C. Krafft, and J. Popp, "Identification of Primary Tumors of Brain Metastases by Raman Imaging and Support Vector Machines", *Chemometrics and Intelligent Laboratory Systems*, Chemometr. Intell. Lab. Syst. (Netherlands), vol. 117, pp. 224–32, Aug. 1, 2012, ISSN: 0169-7439. DOI: 10.1016/j.chemolab.2012.02.008.

[270] K. Gajjar, L. D. Heppenstall, W. Pang, K. M. Ashton, J. Trevisan, I. I. Patel, V. Llabjani, H. F. Stringfellow, P. L. Martin-Hirsch, T. Dawson, and F. L. Martin, "Diagnostic segregation of human brain tumours using Fourier-transform infrared and/or Raman spectroscopy coupled with discriminant analysis", *Anal. Methods*, vol. 5, no. 1, pp. 89–102, 2013, ISSN: 1759-9660, 1759-9679. DOI: 10.1039/C2AY25544H. [Online]. Available: http://xlink.rsc.org/?DOI=C2AY25544H (visited on 12/12/2018).

[271] J. Trevisan, P. P. Angelov, P. L. Carmichael, A. D. Scott, and F. L. Martin, "Extracting biological information with computational analysis of Fourier-transform infrared (FTIR) biospectroscopy datasets: current practices to future perspectives", *The Analyst*, vol. 137, no. 14, p. 3202, 2012, ISSN: 0003-2654, 1364-5528. DOI: 10.1039/c2an16300d. [Online]. Available: http://xlink.rsc.org/?DOI=c2an16300d (visited on 02/24/2019).

[272] S. Wold, A. Ruhe, H. Wold, and I. Dunn W., "The Collinearity Problem in Linear Regression. The Partial Least Squares (PLS) Approach to Generalized Inverses", *SIAM Journal on Scientific and Statistical Computing*, vol. 5, no. 3, pp. 735–743, Sep. 1, 1984, ISSN: 0196-5204. DOI: 10.1137/0905052. [Online]. Available: https://epubs.siam.org/doi/10.1137/0905052 (visited on 06/20/2019).

[273] M. Robnik-Šikonja and I. Kononenko, "Theoretical and Empirical Analysis of ReliefF and RReliefF", *Machine Learning*, vol. 53, no. 1, pp. 23–69, Oct. 1, 2003, ISSN: 1573-0565. DOI: 10.1023/A:1025667309714. [Online]. Available: https://doi.org/10.1023/A:1025667309714 (visited on 06/23/2019).

[274] L. Yu and H. Liu, "Feature Selection for High-Dimensional Data: A Fast Correlation-Based Filter Solution", *Proceedings, Twentieth International Conference on Machine Learning*, p. 8, 2003.

[275] N. Hoque, D. Bhattacharyya, and J. Kalita, "MIFS-ND: A Mutual Information-Based Feature Selection Method", *Expert Systems with Applications*, vol. 41, no. 14, pp. 6371–6385, Oct. 15, 2014, ISSN: 0957-4174. DOI: 10.1016/j.eswa.2014.04.019. [Online]. Available: http://www.sciencedirect.com/science/article/pii/S0957417414002164.

[276] M. Radovic, M. Ghalwash, N. Filipovic, and Z. Obradovic, "Minimum Redundancy Maximum Relevance Feature Selection Approach for Temporal Gene Expression Data", *BMC Bioinformatics*, vol. 18, no. 1, p. 9, Jan. 3, 2017, ISSN: 1471-2105. DOI: 10.1186/s12859-016-1423-9. [Online]. Available: https://doi.org/10.1186/s12859-016-1423-9.

[277] R. Kohavi and G. H. John, "Wrappers for Feature Subset Selection", *Relevance*, vol. 97, no. 1, pp. 273–324, Dec. 1, 1997, ISSN: 0004-3702. DOI: 10.1016/S0004-3702(97)00043-X. [Online]. Available: http://www.sciencedirect.com/science/article/pii/S000437029700043X.

[278] R. Tibshirani, "Regression Shrinkage and Selection via the Lasso", *Journal of the Royal Statistical Society. Series B (Methodological)*, vol. 58, no. 1, pp. 267–288, 1996, ISSN: 00359246. JSTOR: 2346178.

[279] "Assessment of Tumor Cells in a Mouse Model of Diffuse Infiltrative Glioma by Raman Spectroscopy.", *BioMed research international*, vol. 2014, no. 101600173, p. 860 241, 2014, ISSN: 2314-6141. DOI: 10.1155/2014/860241.

[280] A. W. Auner, R. E. Kast, R. Rabah, J. M. Poulik, and M. D. Klein, "Conclusions and Data Analysis: A 6-Year Study of Raman Spectroscopy of Solid Tumors at a Major Pediatric Institute.", *Pediatric surgery international*, vol. 29, no. 2, pp. 129–40, 2013, Auner, Alexander W. Department of Physics and Astronomy, University of Michigan-Dearborn, Dearborn, MI, USA. aauner@umd.umich.edu, ISSN: 1437-9813. DOI: 10.1007/s00383-012-3211-6.

[281] O. Uckermann, W. Yao, T. A. Juratli, R. Galli, E. Leipnitz, M. Meinhardt, E. Koch, G. Schackert, G. Steiner, and M. Kirsch, "IDH1 mutation in human glioma induces chemical alterations that are amenable to optical Raman spectroscopy", *Journal of Neuro-Oncology*, vol. 139, no. 2, pp. 261–268, Sep. 1, 2018, ISSN: 1573-7373. DOI: 10.1007/s11060-018-2883-8. [Online]. Available: https://doi.org/10.1007/s11060-018-2883-8 (visited on 09/25/2018).

[282] S. N. Kalkanis, R. E. Kast, M. L. Rosenblum, T. Mikkelsen, S. M. Yurgelevic, K. M. Nelson, A. Raghunathan, L. M. Poisson, and G. W. Auner, "Raman spectroscopy to distinguish grey matter, necrosis, and glioblastoma multiforme in frozen tissue sections", *Journal of Neuro-Oncology*, vol. 116, no. 3, pp. 477–485, Feb. 2014, ISSN: 0167-594X, 1573-7373. DOI: 10.1007/s11060-013-1326-9. [Online]. Available: http://link.springer.com/10.1007/s11060-013-1326-9 (visited on 10/15/2018).

[283] R. Stables, G. Clemens, H. J. Butler, K. M. Ashton, A. Brodbelt, T. P. Dawson, L. M. Fullwood, M. D. Jenkinson, and M. J. Baker, "Feature Driven Classification of Raman Spectra for Real-Time Spectral Brain Tumour Diagnosis Using Sound.", *The Analyst*, vol. 142, no. 1, pp. 98–109, 2016, ISSN: 1364-5528.

[284] A. Jović, K. Brkić, and N. Bogunović, "A Review of Feature Selection Methods with Applications", in *2015 38th International Convention on Information and Communication Technology, Electronics and Microelectronics (MIPRO)*, May 25, 2015–May 29, 2015, pp. 1200–1205. DOI: 10.1109/MIPRO.2015.7160458.

[285] Y. Saeys, I. Inza, and P. Larrañaga, "A Review of Feature Selection Techniques in Bioinformatics", *Bioinformatics*, vol. 23, no. 19, pp. 2507–2517, Aug. 24, 2007, ISSN: 1367-4803. DOI: 10.1093/bioinformatics/btm344. [Online]. Available: https://doi.org/10.1093/bioinformatics/btm344 (visited on 06/26/2019).

[286] N. Dridi, A. Giremus, J.-F. Giovannelli, C. Truntzer, M. Hadzagic, J.-P. Charrier, L. Gerfault, P. Ducoroy, B. Lacroix, P. Grangeat, and P. Roy, "Bayesian inference for biomarker discovery in proteomics: an analytic solution", *EURASIP journal on bioinformatics & systems biology*, vol. 2017, no. 1, pp. 9–9, Jul. 14, 2017, ISSN: 1687-4145. DOI: 10.1186/s13637-017-0062-4. PMID: 28710702. [Online]. Available: https://www.ncbi.nlm.nih.gov/pubmed/28710702.

[287] Z. M. Hira and D. F. Gillies, "A Review of Feature Selection and Feature Extraction Methods Applied on Microarray Data", *Advances in Bioinformatics*, vol. 2015, pp. 1–13, 2015, ISSN: 1687-8027, 1687-8035. DOI: 10.1155/2015/198363. [Online]. Available: http://www.hindawi.com/journals/abi/2015/198363/ (visited on 02/25/2019).

[288] X. Yuan and R. A. Mayanovic, "An Empirical Study on Raman Peak Fitting and Its Application to Raman Quantitative Research", *Applied Spectroscopy*, vol. 71, no. 10, pp. 2325–2338, Oct. 2017, ISSN: 0003-7028, 1943-3530. DOI: 10.1177/0003702817721527. [Online]. Available: http://journals.sagepub.com/doi/10.1177/0003702817721527 (visited on 10/18/2018).

[289] R. Gautam, S. Vanga, F. Ariese, and S. Umapathy, "Review of multidimensional data processing approaches for Raman and infrared spectroscopy", *EPJ Techniques and Instrumentation*, vol. 2, no. 1, Dec. 2015, ISSN: 2195-7045. DOI: 10.1140/epjti/s40485-015-0018-6. [Online]. Available: http://www.epjtechniquesandinstrumentation.com/content/2/1/8 (visited on 10/18/2018).

[290] T. Hastie, R. Tibshirani, and J. Friedman, *The Elements of Statistical Learning: Data Mining, Inference, and Prediction*, ser. Springer Series in Statistics. Springer, 2009, ISBN: 978-0-387-84884-6. [Online]. Available: https://books.google.ca/books?id=eBSgoAEACAAJ.

[291] C. Cortes and V. Vapnik, "Support-Vector Networks", *Machine Learning*, vol. 20, no. 3, pp. 273–297, Sep. 1, 1995, ISSN: 1573-0565. DOI: 10.1007/BF00994018. [Online]. Available: https://doi.org/10.1007/BF00994018.

[292] Leon Bottou, Olivier Chapelle, Dennis DeCoste, and Jason Weston, "Scaling Learning Algorithms toward AI", in *Large-Scale Kernel Machines*, MITP, 2007, p. 1, ISBN: 978-0-262-25579-0. [Online]. Available: http://ieeexplore.ieee.org/document/6279976.

[293] X. Chen, M. Wang, and H. Zhang, "The use of classification trees for bioinformatics", *Wiley interdisciplinary reviews. Data mining and knowledge discovery*, vol. 1, no. 1, pp. 55–63, 2011, ISSN: 1942-4787. DOI: 10.1002/widm.14. PMID: 22523608. [Online]. Available: https://www.ncbi.nlm.nih.gov/pubmed/22523608.

[294] Y. LeCun, Y. Bengio, and G. Hinton, "Deep Learning", *Nature*, vol. 521, p. 436, May 27, 2015. [Online]. Available: https://doi.org/10.1038/nature14539.

[295] T. Bocklitz, M. Putsche, and A. Niendorf, "A comprehensive study of classification methods for medical diagnosis", *J. Raman Spectrosc.*, p. 8, 2009.

[296] X. Fan, W. Ming, H. Zeng, Z. Zhang, and H. Lu, "Deep Learning-Based Component Identification for the Raman Spectra of Mixtures", *Analyst*, vol. 144, no. 5, pp. 1789–1798, 2019, ISSN: 0003-2654. DOI: 10.1039/C8AN02212G. [Online]. Available: http://dx.doi.org/10.1039/C8AN02212G.

[297] J. Liu, M. Osadchy, L. Ashton, M. Foster, C. J. Solomon, and S. J. Gibson, "Deep Convolutional Neural Networks for Raman Spectrum Recognition: A Unified Solution", *Analyst*, vol. 142, no. 21, pp. 4067–4074, 2017, ISSN: 0003-2654. DOI: 10.1039/C7AN01371J. [Online]. Available: http://dx.doi.org/10.1039/C7AN01371J.

[298] S. Malek, F. Melgani, and Y. Bazi, "One-Dimensional Convolutional Neural Networks for Spectroscopic Signal Regression", *Journal of Chemometrics*, vol. 32, no. 5, e2977, May 1, 2018, ISSN: 0886-9383. DOI: 10.1002/cem.2977. [Online]. Available: https://doi.org/10.1002/cem.2977 (visited on 06/26/2019).

[299] S. L. Neal, "Multivariate Analysis of Mixed Lipid Aggregate Phase Transitions Monitored Using Raman Spectroscopy", *Applied Spectroscopy*, vol. 72, no. 1, pp. 102–113, Sep. 15, 2017, ISSN: 0003-7028. DOI: 10.1177/0003702817729347. [Online]. Available: https://doi.org/10.1177/0003702817729347 (visited on 06/26/2019).

[300] C. Cui and T. Fearn, "Modern Practical Convolutional Neural Networks for Multivariate Regression: Applications to NIR Calibration", *Chemometrics and Intelligent Laboratory Systems*, vol. 182, pp. 9–20, Nov. 15, 2018, ISSN: 0169-7439. DOI: 10.1016/j.chemolab.2018.07.008. [Online]. Available: http://www.sciencedirect.com/science/article/pii/S0169743918301382.

[301] J. Acquarelli, T. van Laarhoven, J. Gerretzen, T. N. Tran, L. M. Buydens, and E. Marchiori, "Convolutional Neural Networks for Vibrational Spectroscopic Data Analysis", *Analytica Chimica Acta*, vol. 954, pp. 22–31, Feb. 15, 2017, ISSN: 0003-2670. DOI: 10.1016/j.aca.2016.12.010. [Online]. Available: http://www.sciencedirect.com/science/article/pii/S0003267016314842.

[302] S. Liu and W. Deng, "Very Deep Convolutional Neural Network Based Image Classification Using Small Training Sample Size", in *2015 3rd IAPR Asian Conference on Pattern Recognition (ACPR)*, 2015, pp. 730–734, ISBN: 2327-0985. DOI: 10.1109/ACPR.2015.7486599.

[303] K. He, X. Zhang, S. Ren, and J. Sun, "Deep Residual Learning for Image Recognition", in *2016 IEEE Conference on Computer Vision and Pattern Recognition (CVPR)*, Jun. 2016, pp. 770–778. DOI: 10.1109/CVPR.2016.90.

[304] C. Szegedy, Wei Liu, Yangqing Jia, P. Sermanet, S. Reed, D. Anguelov, D. Erhan, V. Vanhoucke, and A. Rabinovich, "Going Deeper with Convolutions", in *2015 IEEE Conference on Computer Vision and Pattern Recognition (CVPR)*, Jun. 7, 2015–Jun. 12, 2015, pp. 1–9, ISBN: 1063-6919. DOI: 10.1109/CVPR.2015.7298594.

[305] J. Gu, Z. Wang, J. Kuen, L. Ma, A. Shahroudy, B. Shuai, T. Liu, X. Wang, G. Wang, J. Cai, and T. Chen, "Recent Advances in Convolutional Neural Networks", *Pattern Recognition*, vol. 77, pp. 354–377, May 1, 2018, ISSN: 0031-3203. DOI: 10.1016/j.patcog.2017.10.013. [Online]. Available: http://www.sciencedirect.com/science/article/pii/S0031320317304120.

[306] C. L. Evans, X. Xu, S. Kesari, X. S. Xie, S. T. C. Wong, and G. S. Young, "Chemically-selective imaging of brain structures with CARS microscopy", *Optics Express*, vol. 15, no. 19, pp. 12 076–12 087, Sep. 17, 2007, ISSN: 1094-4087. DOI: 10.1364/OE.15.012076. [Online]. Available: https://www.osapublishing.org/oe/abstract.cfm?uri=oe-15-19-12076 (visited on 07/22/2019).

[307] Y. Fu, T. B. Huff, H.-W. Wang, H. Wang, and J.-X. Cheng, "Ex Vivo and in Vivo Imaging of Myelin Fibers in Mouse Brain by Coherent Anti-Stokes Raman Scattering Microscopy.", *Optics express*, vol. 16, no. 24, pp. 19 396–409, 2008, Fu, Yan. Weldon School of Biomedical Engineering, Purdue University, West Lafayette, IN 47907, USA., ISSN: 1094-4087.

[308] T. Meyer, N. Bergner, C. Bielecki, C. Krafft, D. Akimov, B. F. M. Romeike, R. Reichart, R. Kalff, B. Dietzek, and J. Popp, "Nonlinear Microscopy, Infrared, and Raman Microspectroscopy for Brain Tumor Analysis.", *Journal of biomedical optics*, vol. 16, no. 2, p. 021 113, 2011, Meyer, Tobias. Institute of Photonic Technology e.V., Albert-Einstein-Strasse 9, 07745 Jena, Germany., ISSN: 1560-2281. DOI: 10.1117/1.3533268.

[309] T. Meyer, N. Bergner, A. Medyukhina, B. Dietzek, C. Krafft, B. F. M. Romeike, R. Reichart, R. Kalff, and J. Popp, "Interpreting CARS Images of Tissue within the C-H-Stretching Region.", *Journal of biophotonics*, vol. 5, no. 10, pp. 729–33, 2012, Meyer, Tobias. Institute of Photonic Technology e.V., Albert-Einstein-Strase 9, 07745 Jena, Germany., ISSN: 1864-0648. DOI: 10.1002/jbio.201200104.

[310] C. Krafft, S. B. Sobottka, G. Schackert, and R. Salzer, "Near infrared Raman spectroscopic mapping of native brain tissue and intracranial tumors", *The Analyst*, vol. 130, no. 7, p. 1070, 2005, ISSN: 0003-2654, 1364-5528. DOI: 10.1039/b419232j. [Online]. Available: http://xlink.rsc.org/?DOI=b419232j (visited on 10/04/2018).

[311] M. Kirsch, G. Schackert, R. Salzer, and C. Krafft, "Raman spectroscopic imaging for in vivo detection of cerebral brain metastases", *Analytical and Bioanalytical Chemistry*, vol. 398, no. 4, pp. 1707–1713, Oct. 2010, ISSN: 1618-2642, 1618-2650. DOI: 10.1007/s00216-010-4116-7. [Online]. Available: http://link.springer.com/10.1007/s00216-010-4116-7 (visited on 10/01/2018).

[312] J. M. P. Nascimento and J. M. B. Dias, "Vertex component analysis: a fast algorithm to unmix hyperspectral data", *IEEE TRANSACTIONS ON GEOSCIENCE AND REMOTE SENSING*, vol. 43, no. 4, p. 13, 2005.

[313] M. E. Winter, "N-FINDR: An Algorithm for Fast Autonomous Spectral End-Member Determination in Hyperspectral Data", in *Imaging Spectrometry V*, vol. 3753, International Society for Optics and Photonics, Oct. 27, 1999, pp. 266–275. DOI: 10.1117/12.366289. [Online]. Available: https://www.spiedigitallibrary.org/conference-proceedings-of-spie/3753/0000/N-FINDR--an-algorithm-for-fast-autonomous-spectral-end/10.1117/12.366289.short (visited on 07/27/2019).

[314] R. E. Kast, G. W. Auner, M. L. Rosenblum, T. Mikkelsen, S. M. Yurgelevic, A. Raghunathan, L. M. Poisson, and S. N. Kalkanis, "Raman Molecular Imaging of Brain Frozen Tissue Sections.", *Journal of neuro-oncology*, vol. 120, no. 1, pp. 55–62, 2014, Kast, Rachel E. Electrical and Computer Engineering, Wayne State University, Detroit, MI, 48202, USA., ISSN: 1573-7373. DOI: 10.1007/s11060-014-1536-9.

[315] L. Ashton, K. A. Hollywood, and R. Goodacre, "Making colourful sense of Raman images of single cells", p. 7, 2015.

[316] P. Larkin, "Chapter 7 - General Outline and Strategies for IR and Raman Spectral Interpretation", in *Infrared and Raman Spectroscopy*, P. Larkin, Ed., Oxford: Elsevier, Jan. 1, 2011, pp. 117–133, ISBN: 978-0-12-386984-5. DOI: 10.1016/B978-0-12-386984-5.10007-2. [Online]. Available: http://www.sciencedirect.com/science/article/pii/B9780123869845100072.

[317] Z. Movasaghi, S. Rehman, and I. U. Rehman, "Raman Spectroscopy of Biological Tissues", *Applied Spectroscopy Reviews*, vol. 42, no. 5, pp. 493–541, Sep. 1, 2007, ISSN: 0570-4928. DOI: 10.1080/05704920701551530. [Online]. Available: https://doi.org/10.1080/05704920701551530.

[318] C. Krafft, S. B. Sobottka, G. Schackert, and R. Salzer, "Near infrared Raman spectroscopic mapping of native brain tissue and intracranial tumors", *The Analyst*, vol. 130, no. 7, p. 1070, 2005, ISSN: 0003-2654, 1364-5528. DOI: 10.1039/b419232j. [Online]. Available: http://xlink.rsc.org/?DOI=b419232j (visited on 10/04/2018).

[319] M. Köhler, S. Machill, R. Salzer, and C. Krafft, "Characterization of lipid extracts from brain tissue and tumors using Raman spectroscopy and mass spectrometry", *Analytical and Bioanalytical Chemistry*, vol. 393, no. 5, pp. 1513–1520, Mar. 2009, ISSN: 1618-2642, 1618-2650. DOI: 10.1007/s00216-008-2592-9. [Online]. Available: http://link.springer.com/10.1007/s00216-008-2592-9 (visited on 10/01/2018).

[320] J. Zhang, Y. Fan, M. He, X. Ma, Y. Song, M. Liu, and J. Xu, "Accuracy of Raman spectroscopy in differentiating brain tumor from normal brain tissue", *Oncotarget*, vol. 8, no. 22, May 30, 2017, ISSN: 1949-2553. DOI: 10.18632/oncotarget.15975. [Online]. Available: http://www.oncotarget.com/fulltext/15975 (visited on 10/15/2018).

[321] A. Mizuno, T. Hayashi, K. Tashibu, S. Maraishi, K. Kawauchi, and Y. Ozaki, "Near-Infrared FT-Raman Spectra of the Rat Brain Tissues", *Neuroscience Letters*, vol. 141, no. 1, pp. 47–52, Jul. 6, 1992, ISSN: 0304-3940. DOI: 10.1016/0304-3940(92)90331-Z. [Online]. Available: http://www.sciencedirect.com/science/article/pii/030439409290331Z (visited on 06/17/2019).

[322] A. Mizuno, H. Kitajima, K. Kawauchi, S. Muraishi, and Y. Ozaki, "Near-Infrared Fourier Transform Raman Spectroscopic Study of Human Brain Tissues and Tumours", *Journal of Raman Spectroscopy*, J. Raman Spectrosc. (UK), vol. 25, no. 1, pp. 25–9, Jan. 1994, ISSN: 0377-0486. DOI: 10.1002/jrs.1250250105.

[323] C. W. Ong, Z. X. Shen, Y. He, T. Lee, and S. H. Tang, "Raman microspectroscopy of the brain tissues in the substantia nigra and MPTP-induced Parkinson's disease", *Journal of Raman Spectroscopy*, vol. 30, no. 2, pp. 91–96, 1999, ISSN: 1097-4555. DOI: 10.1002/(SICI)1097-4555(199902)30:2<91::AID-JRS351>3.0.CO;2-H. [Online]. Available: https://onlinelibrary.wiley.com/doi/abs/10.1002/%28SICI%291097-4555%28199902%2930%3A2%3C91%3A%3AAID-JRS351%3E3.0.CO%3B2-H (visited on 06/17/2019).

[324] U. Food and D. Administration. (2018). FDA permits marketing of artificial intelligence-based device to detect certain diabetes-related eye problems, [Online]. Available: https://www.fda.gov/news-events/press-announcements/fda-permits-marketing-artificial-intelligence-based-device-detect-certain-diabetes-related-eye (visited on 06/31/2019).

[325] A. N. Kuzmin, A. Pliss, and P. N. Prasad, "Ramanomics: New omics disciplines using micro raman spectrometry with biomolecular component analysis for molecular profiling of biological structures", *Biosensors*, vol. 7, no. 4, 2017, ISSN: 20796374. DOI: 10.3390/bios7040052.

[326] C. A. Figueiredo and J. T. Rutka, "Diagnostic imaging: Intraoperative virtual histology", *Nature Biomedical Engineering*, vol. 1, no. 2, pp. 1–2, 2017, ISSN: 2157846X. DOI: 10.1038/s41551-017-0033. [Online]. Available: http://dx.doi.org/10.1038/s41551-017-0033.

[327] R. Michael, A. Lenferink, G. F. Vrensen, E. Gelpi, R. I. Barraquer, and C. Otto, "Hyperspectral Raman imaging of neuritic plaques and neurofibrillary tangles in brain tissue from Alzheimer's disease patients", *Scientific Reports*, vol. 7, no. 1, pp. 1–11, 2017, ISSN: 20452322. DOI: 10.1038/s41598-017-16002-3. [Online]. Available: http://dx.doi.org/10.1038/s41598-017-16002-3.

[328] G. Devitt, K. Howard, A. Mudher, and S. Mahajan, "Raman Spectroscopy: An Emerging Tool in Neurodegenerative Disease Research and Diagnosis", *ACS Chemical Neuroscience*, vol. 9, no. 3, pp. 404–420, 2018, ISSN: 19487193. DOI: 10.1021/acschemneuro.7b00413.

[329] L. Zecca, R. Fariello, P. Riederer, D. Sulzer, A. Gatti, and D. Tampellini, "The absolute concentration of nigral neuromelanin, assayed by a new sensitive method, increases throughout the life and is dramatically decreased in Parkinson's disease", *FEBS Letters*, vol. 510, no. 3, pp. 216–220, 2002, ISSN: 00145793. DOI: 10.1016/S0014-5793(01)03269-0.

[330] M. G. Bridelli, D. Tampellini, and L. Zecca, "The structure of neuromelanin and its iron binding site studied by infrared spectroscopy", *FEBS Letters*, vol. 457, no. 1, pp. 18–22, 1999, ISSN: 00145793. DOI: 10.1016/S0014-5793(99)01001-7.

[331] K. Franke, G. Ziegler, S. Klöppel, and C. Gaser, "Estimating the age of healthy subjects from T1-weighted MRI scans using kernel methods: Exploring the influence of various parameters", *NeuroImage*, vol. 50, no. 3, pp. 883–892, 2010, ISSN: 10538119. DOI: 10.1016/j.neuroimage.2010.01.005. [Online]. Available: http://dx.doi.org/10.1016/j.neuroimage.2010.01.005.

[332] I. Beheshti, N. Maikusa, and H. Matsuda, "The association between "Brain-Age Score" (BAS) and traditional neuropsychological screening tools in Alzheimer's disease", *Brain and Behavior*, vol. 8, no. 8, pp. 1–14, 2018, ISSN: 21623279. DOI: 10.1002/brb3.1020.

[333] S. Filo, O. Shtangel, N. Salamon, A. Kol, B. Weisinger, S. Shifman, and A. A. Mezer, "Disentangling molecular alterations from water-content changes in the aging human brain using quantitative MRI", *Nature Communications*, vol. 10, no. 1, p. 3403, 2019,

ISSN: 2041-1723. DOI: 10.1038/s41467-019-11319-1. [Online]. Available: http://www.nature.com/articles/s41467-019-11319-1.

[334] W. Langbein, I. Rocha-Mendoza, and P. Borri, "Single source coherent anti-Stokes Raman microspectroscopy using spectral focusing", *Applied Physics Letters*, vol. 95, no. 8, p. 81 109, 2009. DOI: 10.1063/1.3216073. [Online]. Available: http://dx.doi.org/10.1063/1.3216073.

[335] A. Lukić, S. Dochow, O. Chernavskaia, I. Latka, C. Matthäus, A. Schwuchow, M. Schmitt, and J. Popp, "Fiber probe for nonlinear imaging applications", *Journal of Biophotonics*, vol. 9, no. 1-2, pp. 138–143, 2016, ISSN: 18640648. DOI: 10.1002/jbio.201500010.

[336] F Santos, R. Wolthuis, S Koljenovic, R. M. Almeida, and G. J. Puppels, "Fiber-Optic Probes for in Vivo Raman Spectroscopy in the High-Wavenumber Region", vol. 77, no. 20, pp. 6747–6752, 2005. DOI: 10.1021/ac0505730.

[337] C. S. Jun, B. Y. Kim, J. H. Park, J. Y. Lee, E. S. Lee, and D.-I. Yeom, "Investigation of a four-wave mixing signal generated in fiber-delivered CARS microscopy.", *Applied optics*, vol. 49, no. 20, pp. 3916–3921, 2010, ISSN: 0003-6935. DOI: 10.1364/AO.49.003916.

[338] R. Galli, O. Uckermann, E. Koch, G. Schackert, M. Kirsch, and G. Steiner, "Effects of tissue fixation on coherent anti-Stokes Raman scattering images of brain", *Journal of Biomedical Optics*, vol. 19, no. 7, p. 071 402, 2013, ISSN: 1083-3668. DOI: 10.1117/1.JBO.19.7.071402. [Online]. Available: http://biomedicaloptics.spiedigitallibrary.org/article.aspx?doi=10.1117/1.JBO.19.7.071402.

[339] J. M. Beitz, "Parkinson's disease: a review", *Frontiers in Bioscience*, pp. 65–74, 2014.

[340] F. A. Ponce and A. M. Lozano, "Chapter 16 - Deep brain stimulation: state of the art and novel stimulation targets", in *Recent Advances in Parkinsons Disease: Translational and Clinical Research*, ser. Progress in Brain Research, vol. 184, Elsevier, 2010, pp. 311 –324. DOI: http://dx.doi.org/10.1016/S0079-6123(10)84016-6. [Online]. Available: http://www.sciencedirect.com/science/article/pii/S0079612310840166.

[341] V. J. Odekerken, T. van Laar, M. J. Staal, A. Mosch, C. F. Hoffmann, P. C. Nijssen, G. N. Beute, J. P. van Vugt, M. W. Lenders, M. F. Contarino, M. S. Mink, L. J. Bour, P. van den Munckhof, B. A. Schmand, R. J. de Haan, P. R. Schuurman, and R. M. de Bie, "Subthalamic nucleus versus globus pallidus bilateral deep brain stimulation for advanced Parkinson's disease (NSTAPS study): A randomised controlled trial", *The Lancet Neurology*, vol. 12, no. 1, pp. 37–44, 2013, ISSN: 14744422. DOI: 10.1016/S1474-4422(12)70264-8.

[342] M. I. Hariz, "Complications of deep brain stimulation surgery", *Movement Disorders*, vol. 17, no. S3, S162–S166, 2002, ISSN: 1531-8257. DOI: 10.1002/mds.10159. [Online]. Available: http://dx.doi.org/10.1002/mds.10159.

[343] J. L. Vitek, R. A. E. Bakay, T. Hashimoto, Y. Kaneoke, K. Mewes, J. Y. Zhang, D. Rye, P. Starr, M. Baron, R. Turner, and M. R. Delong, "Microelectrode-guided pallidotomy: technical approach and its application in medically intractable Parkinson's disease", *Journal of Neurosurgery*, vol. 88, no. 6, pp. 1027–1043, 1998, PMID: 9609298. DOI: 10.3171/jns.1998.88.6.1027. eprint: https://doi.org/10.3171/jns.1998.88.6.1027. [Online]. Available: https://doi.org/10.3171/jns.1998.88.6.1027.

[344] H. E. Ward, N. Hwynn, and M. S. Okun, "Update on deep brain stimulation for neuropsychiatric disorders", *Neurobiology of Disease*, vol. 38, no. 3, pp. 346–353, 2010, ISSN: 09699961. DOI: 10.1016/j.nbd.2010.01.011. [Online]. Available: http://dx.doi.org/10.1016/j.nbd.2010.01.011.

[345] C. a. Giller, M Johns, and H Liu, "Use of an intracranial near-infrared probe for localization during stereotactic surgery for movement disorders.", *Journal of neurosurgery*, vol. 93, no. 3, pp. 498–505, 2000, ISSN: 0022-3085. DOI: 10.3171/jns.2000.93.3.0498. [Online]. Available: http://www.ncbi.nlm.nih.gov/pubmed/10969953.

[346] Z. Cui, L. Pan, H. Song, X. Xu, B. Xu, X. Yu, and Z. Ling, "Intraoperative MRI for optimizing electrode placement for deep brain stimulation of the subthalamic nucleus in Parkinson disease", *Journal of Neurosurgery*, vol. 124, no. 1, pp. 62–69, 2016, PMID: 26274983. DOI: 10.3171/2015.1.JNS141534. eprint: https://doi.org/10.3171/2015.1.JNS141534. [Online]. Available: https://doi.org/10.3171/2015.1.JNS141534.

[347] G Percheron, "Ventricular landmarks for thalamic stereotaxy in Macaca.", *Journal of medical primatology*, vol. 4, no. 4, pp. 217–244, 1975.

[348] J. Szabo and W. M. Cowan, "A stereotaxic atlas of the brain of the cynomolgus monkey (Macaca fascicularis)", *The Journal of Comparative Neurology*, vol. 222, no. 2, pp. 265–300, 1984, ISSN: 1096-9861. DOI: 10.1002/cne.902220208. [Online]. Available: http://dx.doi.org/10.1002/cne.902220208.

[349] A. M. Kanner, "Deep brain stimulation for intractable epilepsy: which target and for which seizures?", *Clinical Science*, vol. 4, no. 6, pp. 231–2, 2004, ISSN: 1535-7597. DOI: 10.1111/j.1535-7597.2004.46006.x. [Online]. Available: http://www.pubmedcentral.nih.gov/articlerender.fcgi?artid=1176383{\&}tool=pmcentrez{\&}rendertype=abstract.

[350] S. Kohl, D. M. Schönherr, J. Luigjes, D. Denys, U. J. Mueller, D. Lenartz, V. Visser-Vandewalle, and J. Kuhn, "Deep brain stimulation for treatment-refractory obsessive compulsive disorder: a systematic review", *BMC Psychiatry*, vol. 14, no. 1, p. 214,

2014, ISSN: 1471-244X. DOI: 10.1186/s12888-014-0214-y. [Online]. Available: http://dx.doi.org/10.1186/s12888-014-0214-y.

[351] H. S. Mayberg, A. M. Lozano, V. Voon, H. E. McNeely, D. Seminowicz, C. Hamani, J. M. Schwalb, and S. H. Kennedy, "Deep Brain Stimulation for Treatment-Resistant Depression", *Neuron*, vol. 45, no. 5, pp. 651–660, XXXX, ISSN: 0896-6273. DOI: 10.1016/j.neuron.2005.02.014. [Online]. Available: http://dx.doi.org/10.1016/j.neuron.2005.02.014.

[352] C. B. Mikell, G. M. McKhann, S. Segal, R. A. McGovern, M. B. Wallenstein, and H. Moore, "The Hippocampus and Nucleus Accumbens as Potential Therapeutic Targets for Neurosurgical Intervention in Schizophrenia", *Stereotactic and Functional Neurosurgery*, vol. 87, no. 4, pp. 256–265, 2009, ISSN: 1011-6125. [Online]. Available: http://www.karger.com/DOI/10.1159/000225979.

[353] S. Hemm and K. Wårdell, "Stereotactic implantation of deep brain stimulation electrodes: A review of technical systems, methods and emerging tools", *Medical and Biological Engineering and Computing*, vol. 48, no. 7, pp. 611–624, 2010, ISSN: 01400118. DOI: 10.1007/s11517-010-0633-y.

[354] S. Hemm, J. Coste, J. Gabrillargues, L. Ouchchane, L. Sarry, F. Caire, F. Vassal, C. Nuti, P. Derost, F. Durif, and J. J. Lemaire, "Contact position analysis of deep brain stimulation electrodes on post-operative CT images", *Acta Neurochirurgica*, vol. 151, no. 7, pp. 823–829, 2009, ISSN: 00016268. DOI: 10.1007/s00701-009-0393-3.

[355] M. O. Pinsker, J. Herzog, D. Falk, J. Volkmann, G. Deuschl, and M. Mehdorn, "Accuracy and distortion of deep brain stimulation electrodes on postoperative MRI and CT", *Zentralblatt fur Neurochirurgie*, vol. 69, no. 3, pp. 144–147, 2008, ISSN: 00444251. DOI: 10.1055/s-2008-1077075.

[356] A. Parent and L. Hazrati, "Functional anatomy of the basal ganglia. II. The place of subthalamic nucleus and external pallidum in basal ganglia circuitry", *Brain Research Reviews*, vol. 20, pp. 128–154, 1995, ISSN: 0022510X. DOI: 10.1016/0022-510X(93)90325-S.

[357] J. S. Tiedeman, S. E. Kirk, S. Srinivas, and J. M. Beach, "Retinal oxygen consumption during hyperglycemia in patients with diabetes without retinopathy", *Ophthalmology*, vol. 105, no. 1, pp. 31–36, 1998, ISSN: 01616420. DOI: 10.1016/S0161-6420(98)71029-1.

[358] K. Fondi, P. A. Wozniak, K. Howorka, A. M. Bata, G. C. Aschinger, A. Popa-Cherecheanu, K. J. Witkowska, A. Hommer, D. Schmidl, R. M. Werkmeister, G. Garhöfer, and L. Schmetterer, "Retinal oxygen extraction in individuals with type 1 diabetes with no or mild diabetic retinopathy", *Diabetologia*, vol. 60, no. 8, pp. 1534–1540, 2017, ISSN: 14320428. DOI: 10.1007/s00125-017-4309-0.

[359] C. M. Jorgensen, S. H. Hardarson, and T. Bek, "The oxygen saturation in retinal vessels from diabetic patients depends on the severity and type of vision-threatening retinopathy", *Acta Ophthalmologica*, vol. 92, no. 1, pp. 34–39, 2014, ISSN: 1755375X. DOI: 10.1111/aos.12283.

[360] M. Hammer, W. Vilser, T. Riemer, A. Mandecka, D. Schweitzer, U. Kühn, J. Dawczynski, F. Liemt, and J. Strobel, "Diabetic patients with retinopathy show increased retinal venous oxygen saturation", *Graefe's Archive for Clinical and Experimental Ophthalmology*, vol. 247, no. 8, pp. 1025–1030, 2009, ISSN: 0721832X. DOI: 10.1007/s00417-009-1078-6.

[361] F. Tayyari, L.-A. Khuu, J. G. Flanagan, S. Singer, M. H. Brent, and C. Hudson, "Retinal Blood Flow and Retinal Blood Oxygen Saturation in Mild to Moderate Diabetic Retinopathy", *Investigative Opthalmology & Visual Science*, vol. 56, no. 11, p. 6796, 2015, ISSN: 1552-5783. DOI: 10.1167/iovs.15-17481. [Online]. Available: http://iovs.arvojournals.org/article.aspx?doi=10.1167/iovs.15-17481.

[362] A. Guduru, T. G. Martz, A. Waters, A. V. Kshirsagar, and S. Garg, "Oxygen saturation of retinal vessels in all stages of diabetic retinopathy and correlation to ultra-wide field fluorescein angiography", *Investigative Ophthalmology and Visual Science*, vol. 57, no. 13, pp. 5278–5284, 2016, ISSN: 15525783. DOI: 10.1167/iovs.16-20190.

[363] S. H. Hardarson and E. Stefánsson, "Retinal oxygen saturation is altered in diabetic retinopathy", *British Journal of Ophthalmology*, vol. 96, no. 4, pp. 560–563, 2012, ISSN: 0007-1161. DOI: 10.1136/bjophthalmol-2011-300640. [Online]. Available: http://bjo.bmj.com/lookup/doi/10.1136/bjophthalmol-2011-300640.

[364] F. Semeraro, A. Cancarini, R. Dell'Omo, S. Rezzola, M. R. Romano, and C. Costagliola, "Diabetic retinopathy: Vascular and inflammatory disease", *Journal of Diabetes Research*, vol. 2015, 2015, ISSN: 23146753. DOI: 10.1155/2015/582060.

[365] T. H. Williamson, J. Grewal, B. Gupta, B. Mokete, M. Lim, and C. H. Fry, "Measurement of PO2 during vitrectomy for central retinal vein occlusion, a pilot study", *Graefe's Archive for Clinical and Experimental Ophthalmology*, vol. 247, no. 8, pp. 1019–1023, 2009, ISSN: 0721832X. DOI: 10.1007/s00417-009-1072-z.

[366] E. Stefánsson, O. B. Olafsdottir, A. B. Einarsdottir, T. S. Eliasdottir, T. Eysteinsson, W. Vehmeijer, E. Vandewalle, T. Bek, and S. H. Hardarson, "Retinal Oximetry Discovers Novel Biomarkers in Retinal and Brain Diseases", *Investigative ophthalmology & visual science*, vol. 58, no. 6, BIO227–BIO233, 2017, ISSN: 15525783. DOI: 10.1167/iovs.17-21776.

[367] S. Traustason, M. la Cour, and M. Larsen, "Retinal vascular oximetry during ranibizumab treatment of central retinal vein occlusion", *British Journal of Ophthalmology*, vol. 98, no. 9, pp. 1208–1211, 2014, ISSN: 0007-1161. DOI: 10.1136/bjophthalmol-2013-

304580. [Online]. Available: http://bjo.bmj.com/lookup/doi/10.1136/bjophthalmol-2013-304580.

[368] S. H. Hardarson, "Retinal oximetry", *Acta Ophthalmologica*, pp. 1–47, 2013, ISSN: 1755375X. DOI: 10.1111/aos.12086.

[369] T. S. Eliasdottir, D. Bragason, S. H. Hardarson, G. Kristjansdottir, and E. Stefánsson, "Venous oxygen saturation is reduced and variable in central retinal vein occlusion", *Graefe's Archive for Clinical and Experimental Ophthalmology*, vol. 253, no. 10, pp. 1653–1661, 2015, ISSN: 1435702X. DOI: 10.1007/s00417-014-2849-2.

[370] O. B. Olafsdottir, E. Vandewalle, L. Abegão Pinto, A. Geirsdottir, E. De Clerck, P. Stalmans, M. S. Gottfredsdottir, J. V. Kristjansdottir, J. Van Calster, T. Zeyen, E. Stefánsson, and I. Stalmans, "Retinal oxygen metabolism in healthy subjects and glaucoma patients", *British Journal of Ophthalmology*, vol. 98, no. 3, pp. 329–333, 2014, ISSN: 0007-1161. DOI: 10.1136/bjophthalmol-2013-303162. [Online]. Available: http://bjo.bmj.com/lookup/doi/10.1136/bjophthalmol-2013-303162.

[371] L. A. Tobe, A. Harris, A. Schroeder, A. Gerber, S. Holland, A. Amireskandari, N. J. Kim, and B. Siesky, "Retinal oxygen saturation and metabolism: How does it pertain to glaucoma? An update on the application of retinal oximetry in glaucoma", *European Journal of Ophthalmology*, vol. 23, no. 4, pp. 465–472, 2013, ISSN: 11206721. DOI: 10.5301/ejo.5000289.

[372] E. Vandewalle, L. A. Pinto, O. B. Olafsdottir, E. De Clerck, P. Stalmans, J. Van Calster, T. Zeyen, E. Stefánsson, and I. Stalmans, "Oximetry in glaucoma: Correlation of metabolic change with structural and functional damage", *Acta Ophthalmologica*, vol. 92, no. 2, pp. 105–110, 2014, ISSN: 1755375X. DOI: 10.1111/aos.12011.

[373] D. J. Mordant, I Al-Abboud, G Muyo, A Gorman, A. R. Harvey, and A. I. McNaught, "Oxygen saturation measurements of the retinal vasculature in treated asymmetrical primary open-angle glaucoma using hyperspectral imaging", *Eye*, vol. 28, no. 10, pp. 1190–1200, 2014, ISSN: 0950-222X. DOI: 10.1038/eye.2014.169. [Online]. Available: http://www.nature.com/doifinder/10.1038/eye.2014.169.

[374] M. Desjardins, J. P. Sylvestre, R. Jafari, S. Kulasekara, K. Rose, R. Trussart, J. D. Arbour, C. Hudson, and F. Lesage, "Preliminary investigation of multispectral retinal tissue oximetry mapping using a hyperspectral retinal camera", *Experimental Eye Research*, vol. 146, pp. 330–340, 2016, ISSN: 10960007. DOI: 10.1016/j.exer.2016.04.001.

[375] S. Kayser, P. Vargas, D. Mendelsohn, J. Han, H. Bi, A. Benavente, and A. K. Bittner, "Reduced Central Retinal Artery Blood Flow Is Related to Impaired Central Visual Function in Retinitis Pigmentosa Patients", *Current Eye Research*, vol. 42, no. 11, pp. 1503–1510, 2017, ISSN: 0271-3683. DOI: 10.1080/02713683.2017.1338350. [Online]. Available: https://www.tandfonline.com/doi/full/10.1080/02713683.2017.1338350.

[376] Y. Zhang, J. M. Harrison, O. S. E. Nateras, S. Chalfin, and T. Q. Duong, "Decreased retinal-choroidal blood flow in retinitis pigmentosa as measured by MRI", *Documenta Ophthalmologica*, vol. 126, no. 3, pp. 187–197, 2013, ISSN: 00124486. DOI: 10.1007/s10633-013-9374-1.

[377] W. B. Vehmeijer, V. Magnusdottir, T. S. Eliasdottir, S. H. Hardarson, N. E. Schalij-Delfos, and E. Stefánsson, "Retinal oximetry with scanning laser ophthalmoscope in infants", *PLoS ONE*, vol. 11, no. 2, pp. 1–11, 2016, ISSN: 19326203. DOI: 10.1371/journal.pone.0148077.

[378] A. Geirsdottir, S. H. Hardarson, O. B. Olafsdottir, and E. Stefánsson, "Retinal oxygen metabolism in exudative age-related macular degeneration", *Acta Ophthalmologica*, vol. 92, no. 1, pp. 27–33, 2014, ISSN: 1755375X. DOI: 10.1111/aos.12294.

[379] F. C. Delori and K. P. Pflibsen, "Spectral reflectance of the human ocular fundus", *Applied Optics*, vol. 28, no. 6, p. 1061, 1989, ISSN: 0003-6935. DOI: 10.1364/AO.28.001061. [Online]. Available: https://www.osapublishing.org/abstract.cfm?URI=ao-28-6-1061.

[380] M. Hammer, A Roggan, and G Muller, "Optical properties of ocular fundus tissues-an in vitro study using the double-integrating-sphere technique and inverse Monte Carlo simulation using the double-integrating-sphere technique and inverse", *Phys. Med. Biol.*, vol. 40, pp. 963–978, 1995.

[381] M. H. Smith, K. R. Denninghoff, A. Lompado, and L. W. Hillman, "Effect of multiple light paths on retinal vessel oximetry", *Applied Optics*, vol. 39, no. 7, p. 1183, 2000, ISSN: 0003-6935. DOI: 10.1364/AO.39.001183. [Online]. Available: https://www.osapublishing.org/abstract.cfm?URI=ao-39-7-1183.

[382] M. Hammer, S. Leistritz, L. Leistritz, and D. Schweitzer, "Light paths in retinal vessel oxymetry", *IEEE Transactions on Biomedical Engineering*, vol. 48, no. 5, pp. 592–598, 2001, ISSN: 00189294. DOI: 10.1109/10.918598.

[383] P. I. Rodmell, J. A. Crowe, A. Gorman, A. R. Harvey, G. Muyo, D. J. Mordant, A. I. McNaught, and S. P. Morgan, "Light path-length distributions within the retina", *Journal of Biomedical Optics*, vol. 19, no. 3, p. 036 008, 2014, ISSN: 1083-3668. DOI: 10.1117/1.JBO.19.3.036008. [Online]. Available: http://biomedicaloptics.spiedigitallibrary.org/article.aspx?doi=10.1117/1.JBO.19.3.036008.

[384] J. B. Hickam, R. Frayser, and J. C. Ross, "A study of retinal venous blood oxygen saturation in human subjects by photographic means.", *Circulation*, vol. 27, no. March, pp. 375–385, 1963, ISSN: 00097322. DOI: 10.1161/01.CIR.27.3.375.

[385] F. C. Delori, "Noninvasive technique for oximetry of blood in retinal vessels", *Applied Optics*, vol. 27, no. 6, pp. 1113–1125, 1988.

[386] A. Harris, R. Dinn, L. Kagemann, and E. Rechtman, *A Review of Methods for Human Retinal Oximetry*.

[387] D Schweitzer, M Hammer, J Kraft, E Thamm, E Königsdörffer, and J Strobel, "In vivo measurement of the oxygen saturation of retinal vessels in healthy volunteers.", *IEEE transactions on bio-medical engineering*, vol. 46, no. 12, pp. 1454–1465, 1999, ISSN: 0018-9294. DOI: 10.1109/10.804573.

[388] M. H. Smith, "Optimum wavelength combinations for retinal vessel oximetry.", *Applied optics*, vol. 38, no. 1, pp. 258–267, 1999, ISSN: 0003-6935. DOI: 10.1364/AO.38.000258. [Online]. Available: papers2://publication/uuid/426A564A-059D-4AFE-82C9-1BDB54F0FB63.

[389] J. Beach, "Pathway to retinal oximetry.", *Transl Vis Sci Technol*, vol. 3, no. 5, Article 2, 2014, ISSN: 2164-2591. DOI: 10.1167/tvst.3.5.2. [Online]. Available: http://www.pubmedcentral.nih.gov/articlerender.fcgi?artid=4164112{\&}tool=pmcentrez{\&}rendertype=abstract.

[390] J. M. Beach, K. J. Schwenzer, S Srinivas, D Kim, and J. S. Tiedeman, "Oximetry of retinal vessels by dual-wavelength imaging: calibration and influence of pigmentation", *Journal of Applied Physiology*, pp. 748–758, 1999.

[391] M. Hammer and D. Schweitzer, "Retinal vessel oximetry-calibration , compensation for vessel diameter and fundus pigmentation , and reproducibility", *Journal of biomedical optics*, vol. 13, no. October 2008, pp. 1–7, 2008. DOI: 10.1117/1.2976032.

[392] S. H. Hardarson, A. Harris, R. A. Karlsson, G. H. Halldorsson, L. Kagemann, E. Rechtman, G. M. Zoega, T. Eysteinsson, J. A. Benediktsson, A. Thorsteinsson, P. K. Jensen, J. Beach, and E. Stefánsson, "Automatic retinal oximetry", *Investigative Ophthalmology and Visual Science*, vol. 47, no. 11, pp. 5011–5016, 2006, ISSN: 01460404. DOI: 10.1167/iovs.06-0039.

[393] S. R. Patel, J. G. Flanagan, A. M. Shahidi, J. P. Sylvestre, and C. Hudson, "A prototype hyperspectral system with a tunable laser source for retinal vessel imaging", *Investigative Ophthalmology and Visual Science*, vol. 54, no. 8, pp. 5163–5168, 2013, ISSN: 01460404. DOI: 10.1167/iovs.13-12124.

[394] R. Heitmar and A. Attardo, "The influence of simulated cataract on retinal vessel oximetry measurements", *Acta Ophthalmologica*, vol. 94, no. 1, pp. 48–55, 2016, ISSN: 17553768. DOI: 10.1111/aos.12826.

[395] R. Heitmar and R. P. Cubbidge, "The impact of flash intensity on retinal vessel oxygen saturation measurements using dual wavelength oximetry", *Investigative Ophthalmology and Visual Science*, vol. 54, no. 4, pp. 2807–2811, 2013, ISSN: 01460404. DOI: 10.1167/iovs.12-10493.

[396] W. Liu, S. Jiao, and H. F. Zhang, "Accuracy of retinal oximetry: a Monte Carlo investigation", *Journal of Biomedical Optics*, vol. 18, no. 6, p. 066 003, 2013, ISSN: 1083-3668. DOI: 10.1117/1.JBO.18.6.066003. [Online]. Available: http://biomedicaloptics.spiedigitallibrary.org/article.aspx?doi=10.1117/1.JBO.18.6.066003.

[397] M. Hammer, T. Heller, S. Jentsch, J. Dawczynski, D. Schweitzer, S. Peters, K. U. Schmidtke, and U. A. Muller, "Retinal vessel oxygen saturation under flicker light stimulation in patients with nonproliferative diabetic retinopathy", *Investigative Ophthalmology and Visual Science*, vol. 53, no. 7, pp. 4063–4068, 2012, ISSN: 01460404. DOI: 10.1167/iovs.12-9659.

[398] B. Khoobehi, A. Eaton, H. Wafapoor, P. Fournier, K. Firn, M. Peters, E. Rodebeck, and B. Templet, "Determination of oxygen saturation of the optic nerve head and overlying artery and vein using a snapshot multi-spectral imaging system", *Investigative ophthalmology & visual science*, vol. 8229, pp. 822 906–822906–19, 2012, ISSN: 16057422. DOI: 10.1117/12.910030. [Online]. Available: http://proceedings.spiedigitallibrary.org/proceeding.aspx?articleid=1276672.

[399] M. Hammer, D. Schweitzer, M. Hammer, E. Thamm, and D. Schweitzer, "A simple algorithm for in vivo ocular fundus oximetry compensating for non-haemoglobin absorption and scattering", *Phys. Med. Biol.*, vol. 47, N233–N238, 2002.

[400] D. Schweitzer, L. Leistritz, M. Hammer, M. Scibor, U. Bartsch, and J. Strobel, "Calibration-free measurement of the oxygen saturation in human retinal vessels", *SPIE proceedings*, vol. 2393, pp. 210–218, 1995. [Online]. Available: http://link.aip.org/link/?PSI/2393/210/1.

[401] E. J. Van Kampen and W. G. Zijlstra, "Spectrophotometry of hemoglobin and hemoglobin derivatives", *Advances in Clinical Chemistry*, vol. 23, no. C, pp. 199–257, 1983, ISSN: 00652423. DOI: 10.1016/S0065-2423(08)60401-1.

[402] S. Prahl. (1999). Optical Absorption of Hemoglobin, [Online]. Available: http://omlc.ogi.edu/spectra/hemoglobin/ (visited on 12/15/1999).

[403] Y. Zhao, L. Qiu, Y. Sun, C. Huang, and T. Li, "Optimal hemoglobin extinction coefficient data set for near-infrared spectroscopy", *Biomedical Optics Express*, vol. 8, no. 11, p. 5151, 2017, ISSN: 2156-7085. DOI: 10.1364/BOE.8.005151. [Online]. Available: https://www.osapublishing.org/abstract.cfm?URI=boe-8-11-5151.

[404] N. Bosschaart, G. J. Edelman, M. C. Aalders, T. G. Van Leeuwen, and D. J. Faber, "A literature review and novel theoretical approach on the optical properties of whole blood", *Lasers in Medical Science*, vol. 29, no. 2, pp. 453–479, 2014, ISSN: 1435604X. DOI: 10.1007/s10103-013-1446-7.

[405] K. J. Reynold, E Palayiwa, J. Moyle, K. Sykes, and C. E. W. Hahn, "The Effect of Dyshemoglobins on Pulse Oximetry: Part I, Theoretical Approach and Part II: Experimental Results Using an In Vitro Test System", *Journal of Clinical Monitoring*, vol. 9, no. 2, pp. 81–90, 1993.

[406] S. Curry, "Methemoglobinemia", *Annals of Emergency Medicine*, vol. 11, no. 4, pp. 214–221, 1982, ISSN: 01960644. DOI: 10.1016/S0196-0644(82)80502-7.

[407] S. J. Barker and K. K. Tremper, "The effect of carbon monoxide inhalation on pulse oximetry and transcutaneous P02", *Anesthesiology*, vol. 66, pp. 677–679, 1987.

[408] S. J. Barker, K. K. Tremper, and J. Hyatt, "Effects of Methemoglobinemia on Pulse Oximetry and Mixed Venous Oximetry", *Anesthesiology*, vol. 70, pp. 112–117, 1989.

[409] S. J. Barker, J. Curry, D. Redford, and S. Morgan, "Measurement of Carboxyhemoglobin and Methemoglobin by Pulse Oximetry", *Anesthesiology*, vol. 105, no. 5, pp. 892–897, 2006, ISSN: 0003-3022. DOI: 10.1097/00000542-200611000-00008. [Online]. Available: http://content.wkhealth.com/linkback/openurl?sid=WKPTLP:landingpage{\&}an=00000542-200611000-00008.

[410] R. Zander, "Concentrations of Carboxyhemoglobin in the Blood of Smokers and Non-Smokers", in *The ocygen status of Arterial Blood*, Karger. Basel, 1991, pp. 184–189.

[411] C. M. Castleden and P. V. Cole, "Carboxyhaemoglobin levels of smokers and non-smokers working in the City of London.", *British journal of industrial medicine*, vol. 32, no. 2, pp. 115–8, 1975, ISSN: 0007-1072. DOI: 10.1136/oem.32.2.115. [Online]. Available: http://www.ncbi.nlm.nih.gov/pubmed/1131338{\%}5Cnhttp://www.pubmedcentral.nih.gov/articlerender.fcgi?artid=PMC1008037.

[412] W. S. Aronow and S. N. Rokaw, "Carboxyhemoglobin Caused by Smoking Nonnicotine Cigarettes Effects in Angina Pectoris", *Circulation*, vol. 44, no. 5, pp. 782–788, 1971, ISSN: 00097322. [Online]. Available: http://circ.ahajournals.org/content/44/5/782.short{\%}5Cnhttp://circ.ahajournals.org/content/44/5/782.full.pdf.

[413] R. D. Stewart, E. D. Baretta, L. R. Platte, E. B. Stewart, J. H. Kalbfleisch, B Van Yserloo, and A. A. Rimm, "Carboxyhemoglobin levels in American blood donors.", *Jama*, vol. 229, no. 9, pp. 1187–95, 1974, ISSN: 0098-7484. DOI: 10.1001/jama.1974.03230470029019. [Online]. Available: http://www.ncbi.nlm.nih.gov/pubmed/4407933.

[414] N. B. Hampson and N. M. Hauff, "Carboxyhemoglobin levels in carbon monoxide poisoning: do they correlate with the clinical picture?", *The American journal of emergency medicine*, vol. 26, no. 6, pp. 665–9, 2008, ISSN: 1532-8171. DOI: 10.1016/j.ajem.2007.10.005. [Online]. Available: http://www.ncbi.nlm.nih.gov/pubmed/18606318.

[415] R. Ash-Bernal, R. Wise, and S. M. Wright, "Acquired methemoglobinemia: a retrospective series of 138 cases at 2 teaching hospitals.", *Medicine*, vol. 83, no. 5, pp. 265–73, 2004, ISSN: 0025-7974. DOI: 10.1016/j.annemergmed.2005.09.014. [Online]. Available: http://www.ncbi.nlm.nih.gov/pubmed/15342970.

[416] Y. Bar, I. Diamant, L. Wolf, S. Lieberman, E. Konen, and H. Greenspan, "Chest pathology detection using deep learning with non-medical training", in *Biomedical Imaging (ISBI), 2015 IEEE 12th International Symposium on*, IEEE, 2015, pp. 294–297.

[417] H.-C. Shin, H. R. Roth, M. Gao, L. Lu, Z. Xu, I. Nogues, J. Yao, D. Mollura, and R. M. Summers, "Deep convolutional neural networks for computer-aided detection: CNN architectures, dataset characteristics and transfer learning", *IEEE transactions on medical imaging*, vol. 35, no. 5, pp. 1285–1298, 2016.

[418] C. D. Malon and E. Cosatto, "Classification of mitotic figures with convolutional neural networks and seeded blob features", *Journal of pathology informatics*, vol. 4, 2013.

[419] J Dheeba, N. A. Singh, and S. T. Selvi, "Computer-aided detection of breast cancer on mammograms: A swarm intelligence optimized wavelet neural network approach", *Journal of biomedical informatics*, vol. 49, pp. 45–52, 2014.

[420] P. Moeskops, M. A. Viergever, A. M. Mendrik, L. S. de Vries, M. J. Benders, and I. Išgum, "Automatic segmentation of MR brain images with a convolutional neural network", *IEEE transactions on medical imaging*, vol. 35, no. 5, pp. 1252–1261, 2016.

[421] A. Cruz-Roa, A. Basavanhally, F. González, H. Gilmore, M. Feldman, S. Ganesan, N. Shih, J. Tomaszewski, and A. Madabhushi, "Automatic detection of invasive ductal carcinoma in whole slide images with convolutional neural networks", in *Medical Imaging 2014: Digital Pathology*, International Society for Optics and Photonics, vol. 9041, 2014, p. 904 103.

[422] M. Jermyn, J. Desroches, K. Aubertin, K. St-Arnaud, W. J. Madore, E. De Montigny, M. C. Guiot, D. Trudel, B. C. Wilson, K. Petrecca, and F. Leblond, "A review of Raman spectroscopy advances with an emphasis on clinical translation challenges in oncology", *Physics in Medicine and Biology*, vol. 61, no. 23, R370–R400, 2016, ISSN: 13616560. DOI: 10.1088/0031-9155/61/23/R370.

[423] D. T. Delpy, M Cope, P van der Zee, S Arridge, S Wray, and J Wyatt, "Estimation of optical pathlegth through tissue from direct time of flight measurement", *Phys. Med. Biol.*, vol. 33 %6, no. 12, 1433–1442 %&, 1988.

[424] M. Kohl, U. Lindauer, G. Royl, M. Kühl, L. Gold, A. Villringer, and U. Dirnagl, "Physical model for the spectroscopic analysis of cortical intrinsic optical signals", *Physics in Medicine and Biology*, vol. 45, no. 12, pp. 3749–3764, 2000, ISSN: 0031-9155. DOI: 10.1088/0031-9155/45/12/317. [Online]. Available: http://stacks.iop.org/0031-9155/45/i=12/a=317?key=crossref.57b04528fca6a69d2e1fed56afed4765.

[425] V. Diaconu, "Multichannel spectroreflectometry : a noninvasive method for assessment of on-line hemoglobin derivatives", *Applied optics*, vol. 48, no. 10, 2009.

[426] V. Vucea, P.-j. Bernard, P. Sauvageau, and V. Diaconu, "Blood oxygenation measurements by multichannel reflectometry on the venous and arterial structures of the retina", *Applied Optics*, vol. 50, no. 26, pp. 5185–5191, 2011.

[427] O. Siggaard-Andersen, B. Nørgaard-Pedersen, and J. Rem, "Hemoglobin pigments. spectrophotometric determination of oxy-, carboxy-, met-, and sulfhemoglobin in capillary blood", *Clinica Chimica Acta*, vol. 42, no. 1, pp. 85–100, 1972, ISSN: 00098981. DOI: 10.1016/0009-8981(72)90380-4.

[428] S. L. Jacques, R. D. Glickman, and J. A. Schwartz, "Internal absorption coefficient and threshold for pulsed laser disruption", *Proceedings of SPIE*, vol. 2681, no. May 1996, pp. 468–477, 1996. DOI: http://dx.doi.org/10.1117/12.239608.

[429] J. Dillon and J Atherton, "INTACT HUMAN LENS", *Photochemistry and Photobiology*, vol. 51, no. 4, pp. 465–468, 1989.

[430] E. R. Gaillard, L. Zheng, J. C. Merriam, and J. Dillon, "Age-Related Changes in the Absorption Characteristics of the Primate Lens", *Investigative Ophthalmology & Visual Science*, vol. 41, no. 6, pp. 1454–1459, 2000.

[431] V. Gulshan, L. Peng, M. Coram, M. C. Stumpe, D. Wu, A. Narayanaswamy, S. Venugopalan, K. Widner, T. Madams, J. Cuadros, R. Kim, R. Raman, P. C. Nelson, J. L. Mega, and D. R. Webster, "Development and validation of a deep learning algorithm for detection of diabetic retinopathy in retinal fundus photographs", *JAMA - Journal of the American Medical Association*, vol. 316, no. 22, pp. 2402–2410, 2016, ISSN: 15383598. DOI: 10.1001/jama.2016.17216. arXiv: 1803.04337.

[432] L. Fang, D. Cunefare, C. Wang, R. H. Guymer, S. Li, and S. Farsiu, "Automatic segmentation of nine retinal layer boundaries in OCT images of non-exudative AMD patients using deep learning and graph search", *Biomedical Optics Express*, vol. 8, no. 5, p. 2732, 2017, ISSN: 2156-7085. DOI: 10.1364/BOE.8.002732. [Online]. Available: https://www.osapublishing.org/abstract.cfm?URI=boe-8-5-2732.

[433] D. Cunefare, L. Fang, R. F. Cooper, A. Dubra, J. Carroll, and S. Farsiu, "Open source software for automatic detection of cone photoreceptors in adaptive optics ophthalmoscopy using convolutional neural networks", *Scientific Reports*, vol. 7, no. 1, pp. 1–11, 2017, ISSN: 20452322. DOI: 10.1038/s41598-017-07103-0. [Online]. Available: http://dx.doi.org/10.1038/s41598-017-07103-0.

[434] A. Krizhevsky, I. Sutskever, and G. E. Hinton, "Imagenet classification with deep convolutional neural networks", in *Advances in neural information processing systems*, 2012, pp. 1097–1105.

[435] S. Lawrence, C. L. Giles, A. C. Tsoi, and A. D. Back, "Face recognition: A convolutional neural-network approach", *IEEE transactions on neural networks*, vol. 8, no. 1, pp. 98–113, 1997.

[436] P. Y. Simard, D. Steinkraus, J. C. Platt, *et al.*, "Best practices for convolutional neural networks applied to visual document analysis.", in *ICDAR*, vol. 3, 2003, pp. 958–962.

[437] N. Kalchbrenner, E. Grefenstette, and P. Blunsom, "A convolutional neural network for modelling sentences", *arXiv preprint arXiv:1404.2188*, 2014.

[438] T. J. F. Patterson, B. C. Wilson, and M S, "The use of a neural network to determine tissue optical properties from spatially resolved diffuse reflectance measurements", *Physics in Medicine and Biology*, vol. 37, no. 12, p. 2281, 1992, ISSN: 0031-9155. [Online]. Available: http://stacks.iop.org/0031-9155/37/i=12/a=009.

[439] A. Kienle, L. Lilge, M. S. Patterson, R. Hibst, R. Steiner, and B. C. Wilson, "Spatially resolved absolute diffuse reflectance measurements for noninvasive determination of the optical scattering and absorption coefficients of biological tissue", *Applied Optics*, vol. 35, no. 13, p. 2304, 1996, ISSN: 0003-6935. DOI: 10.1364/AO.35.002304. [Online]. Available: https://www.osapublishing.org/abstract.cfm?URI=ao-35-13-2304.

[440] K. Birmingham, V. Gradinaru, P. Anikeeva, W. M. Grill, V. Pikov, B. McLaughlin, P. Pasricha, D. Weber, K. Ludwig, and K. Famm, "Bioelectronic medicines: A research roadmap", *Nature Reviews Drug Discovery*, vol. 13, no. 6, pp. 399–400, 2014, ISSN: 14741784. DOI: 10.1038/nrd4351. [Online]. Available: http://dx.doi.org/10.1038/nrd4351.

[441] K. L. Montgomery, S. M. Iyer, A. J. Christensen, K. Deisseroth, and S. L. Delp, "Beyond the brain: Optogenetic control in the spinal cord and peripheral nervous system", *Science Translational Medicine*, vol. 8, no. 337, 2016, ISSN: 19466242. DOI: 10.1126/scitranslmed.aad7577.

[442] K. J. Dougherty, L. Zagoraiou, D. Satoh, I. Rozani, S. Doobar, S. Arber, T. M. Jessell, and O. Kiehn, "Locomotor Rhythm Generation Linked to the Output of Spinal Shox2 Excitatory Interneurons", *Neuron*, vol. 80, no. 4, pp. 920–933, 2013, ISSN: 08966273. DOI: 10.1016/j.neuron.2013.08.015. [Online]. Available: http://dx.doi.org/10.1016/j.neuron.2013.08.015.

[443] T. Kamiyama, H. Kameda, N. Murabe, S. Fukuda, N. Yoshioka, H. Mizukami, K. Ozawa, and M. Sakurai, "Corticospinal Tract Development and Spinal Cord Innervation Differ between Cervical and Lumbar Targets", *Journal of Neuroscience*, vol. 35, no. 3, pp. 1181–1191, 2015, ISSN: 0270-6474. DOI: 10.1523/JNEUROSCI.2842-13.2015. [Online]. Available: http://www.jneurosci.org/cgi/doi/10.1523/JNEUROSCI.2842-13.2015.

[444] V. Caggiano, M. Sur, and E. Bizzi, "Rostro-caudal inhibition of hindlimb movements in the spinal cord of mice", *PLoS ONE*, vol. 9, no. 6, 2014, ISSN: 19326203. DOI: 10.1371/journal.pone.0100865.

[445] W. J. Alilain, D Ph, X. Li, K. P. Horn, R. Dhingra, E Dick, S. Herlitze, and J. Silver, "Light Induced Rescue of Breathing After Spinal Cord Injury", *Journal of Neuroscience*, vol. 28, no. 46, pp. 11 862–11 870, 2009, ISSN: 0270-6474. DOI: 10.1523/JNEUROSCI.3378-08.2008.Light.

[446] R. P. Bonin, F. Wang, M. Desrochers-Couture, A. Ga¸secka, M. E. Boulanger, D. C. Côté, and Y. De Koninck, "Epidural optogenetics for controlled analgesia", *Molecular Pain*, vol. 12, pp. 1–11, 2016, ISSN: 17448069. DOI: 10.1177/1744806916629051.

[447] E. Foster, H. Wildner, L. Tudeau, S. Haueter, W. T. Ralvenius, M. Jegen, H. Johannssen, L. Hösli, K. Haenraets, A. Ghanem, K. K. Conzelmann, M. Bösl, and H. U. Zeilhofer, "Targeted ablation, silencing, and activation establish glycinergic dorsal horn neurons as key components of a spinal gate for pain and itch", *Neuron*, vol. 85, no. 6, pp. 1289–1304, 2015, ISSN: 10974199. DOI: 10.1016/j.neuron.2015.02.028.

[448] H. Wang and M. J. Zylka, "Mrgprd-Expressing Polymodal Nociceptive Neurons Innervate Most Known Classes of Substantia Gelatinosa Neurons", *Journal of Neuroscience*, vol. 29, no. 42, pp. 13 202–13 209, 2009, ISSN: 0270-6474. DOI: 10.1523/JNEUROSCI.3248-09.2009. arXiv: NIHMS150003. [Online]. Available: http://www.jneurosci.org/cgi/doi/10.1523/JNEUROSCI.3248-09.2009.

[449] K. Yang, R. Ma, Q. Wang, P. Jiang, and Y.-Q. Li, "Optoactivation of parvalbumin neurons in the spinal dorsal horn evokes GABA release that is regulated by presynaptic GABAB receptors", *Neuroscience Letters*, vol. 594, pp. 55 –59, 2015, ISSN: 0304-3940. DOI: https://doi.org/10.1016/j.neulet.2015.03.050. [Online]. Available: http://www.sciencedirect.com/science/article/pii/S0304394015002438.

[450] M. W. Mathis, A. Mathis, and N. Uchida, "Somatosensory Cortex Plays an Essential Role in Forelimb Motor Adaptation in Mice", *Neuron*, vol. 93, no. 6, 1493–1503.e6, 2017, ISSN: 10974199. DOI: 10.1016/j.neuron.2017.02.049. [Online]. Available: http://dx.doi.org/10.1016/j.neuron.2017.02.049.

[451] B. A. Copits, M. Y. Pullen, and R. W. Gereau, "Spotlight on pain: Optogenetic approaches for interrogating somatosensory circuits", *Pain*, vol. 157, no. 11, pp. 2424–2433, 2016, ISSN: 18726623. DOI: 10.1097/j.pain.0000000000000620.

[452] K. Deisseroth, "Optogenetics", *Nature Methods*, vol. 8, no. 1, pp. 26–29, 2011, ISSN: 15487091. DOI: 10.1038/nmeth.f.324.

[453] M. R. Warden, J. A. Cardin, and K. Deisseroth, "Optical Neural Interfaces", *Annual Review of Biomedical Engineering*, vol. 16, no. 1, pp. 103–129, 2014, ISSN: 1523-9829. DOI: 10.1146/annurev-bioeng-071813-104733. [Online]. Available: http://www.annualreviews.org/doi/10.1146/annurev-bioeng-071813-104733.

[454] R. Pashaie, P. Anikeeva, J. H. Lee, R. Prakash, O. Yizhar, M. Prigge, D. Chander, T. J. Richner, and J. Williams, "Optogenetic brain interfaces", *IEEE Reviews in Biomedical Engineering*, vol. 7, pp. 3–30, 2014, ISSN: 19411189. DOI: 10.1109/RBME.2013.2294796.

[455] A. M. Aravanis, L. P. Wang, F. Zhang, L. A. Meltzer, M. Z. Mogri, M. B. Schneider, and K. Deisseroth, "An optical neural interface: in vivo control of rodent motor cortex with integrated fiberoptic and optogenetic technology.", *Journal of neural engineering*, vol. 4, no. 3, 2007, ISSN: 17412560. DOI: 10.1088/1741-2560/4/3/S02.

[456] C. Towne, K. L. Montgomery, S. M. Iyer, K. Deisseroth, and S. L. Delp, "Optogenetic Control of Targeted Peripheral Axons in Freely Moving Animals", *PLoS ONE*, vol. 8, no. 8, 2013, ISSN: 19326203. DOI: 10.1371/journal.pone.0072691. arXiv: NIHMS150003.

[457] A. Kienle, F. K. Forster, and R. Hibst, "Anisotropy of light propagation in biological tissue", *Optics Letters*, vol. 29, no. 22, p. 2617, 2004, ISSN: 0146-9592. DOI: 10.1364/OL.29.002617. [Online]. Available: https://www.osapublishing.org/abstract.cfm?URI=ol-29-22-2617.

[458] S. Nickell, M. Hermann, M. Essenpreis, T. J. Farrell, U. Kramer, and M. S. Patterson, "Anisotropy of light propagation in human skin", *Physics in Medicine & Biology*, vol. 45, no. 10, 2000.

[459] K. Hebeda, T. Menovsky, J. Beek, J. Wolbers, and M. van Gemert, "Light Propagation in the Brain Depends on Nerve Fiber Orientation", vol. 35, no. 4, pp. 0–6, 2018.

[460] S. I. Al-Juboori, A. Dondzillo, E. A. Stubblefield, G. Felsen, T. C. Lei, and A. Klug, "Light Scattering Properties Vary across Different Regions of the Adult Mouse Brain", *PLoS ONE*, vol. 8, no. 7, pp. 1–9, 2013, ISSN: 19326203. DOI: 10.1371/journal.pone.0067626.

[461] P. van der Zee, M. Essenpreis, and D. T. Delpy, "Optical properties of brain tissue", no. September 1993, pp. 454–465, 1993. DOI: 10.1117/12.154665. [Online]. Available: http://proceedings.spiedigitallibrary.org/proceeding.aspx?articleid=1007752.

[462] A. Taddeucci, F. Martelli, M. Barilli, M. Ferrari, G. Zaccanti, and D. Fisica, "Optical Properties of Brain Tissue", vol. 1, no. 1, pp. 117–123, 2018.

[463] A. Yaroslavsky, P. C. Schulze, I. V. Yaroslavsky, R Schober, F Ulrich, and H.-J. Schwarzmaier, "Optical properties of selected native and coagulated human brain tissues in vitro in the visible and near infrared spectral range", *Physics In Medicine And Biology*, vol. 47, pp. 2059–2073, 2002. [Online]. Available: http://iopscience.iop.org/0031-9155/47/12/305.

[464] H. Radhakrishnan, A. Senapati, D. Kashyap, Y. B. Peng, and H. Liu, "Light scattering from rat nervous system measured intraoperatively by near-infrared reflectance spectroscopy", *Journal of Biomedical Optics*, vol. 10, no. 5, pp. 1–8, 2005, ISSN: 10833668. DOI: 10.1117/1.2098487.

[465] S. L. Jacques, *3D Monte Carlo simulation of heterogeneous tissues*, https://omlc.org/software/mc/mcxyz/, 2013.

[466] W.-c. Lin, D. I. Sandberg, S. Bhatia, M. Johnson, S. Oh, and J. Ragheb, "Diffuse reflectance spectroscopy for in vivo pediatric brain tumor detection", *Journal of Biomedical Optics*, vol. 15, no. 6, p. 061 709, 2010, ISSN: 10833668. DOI: 10.1117/1.3505012.

[467] K. Deisseroth and P. Hegemann, "The form and function of channelrhodopsin", *Science*, vol. 357, no. 6356, 2017, ISSN: 10959203. DOI: 10.1126/science.aan5544. [Online]. Available: https://www.ncbi.nlm.nih.gov/pmc/articles/PMC5723383/pdf/nihms923716.pdf.

[468] M. Harrison, A. O'Brien, L. Adams, G. Cowin, M. J. Ruitenberg, G. Sengul, and C. Watson, "Vertebral landmarks for the identification of spinal cord segments in the mouse", *NeuroImage*, vol. 68, pp. 22–29, 2013, ISSN: 10538119. DOI: 10.1016/j.neuroimage.2012.11.048. [Online]. Available: http://dx.doi.org/10.1016/j.neuroimage.2012.11.048.

[469] S. Anand, R. Cicchi, F. Martelli, F. Giordano, A. M. Buccoliero, R. Guerrini, and F. S. Pavone, "Effects of formalin fixation on tissue optical properties of in-vitro brain samples", vol. 9321, 2015, 93210Z, ISBN: 9781628414110. DOI: 10.1117/12.2076961. [Online]. Available: http://proceedings.spiedigitallibrary.org/proceeding.aspx?doi=10.1117/12.2076961.

[470] M. Lazar, D. M. Weinstein, J. S. Tsuruda, K. M. Hasan, K. Arfanakis, M. E. Meyerand, B. Badie, H. A. Rowley, V. Haughton, A. Field, and A. L. Alexander, "White matter tractography using diffusion tensor deflection", *Human Brain Mapping*, vol. 18, no. 4, pp. 306–321, 2003, ISSN: 10659471. DOI: 10.1002/hbm.10102.

[471] M. Azimipour, R. Baumgartner, Y. Liu, S. L. Jacques, K. Eliceiri, and R. Pashaie, "Extraction of optical properties and prediction of light distribution in rat brain tissue", *Journal of Biomedical Optics*, vol. 19, no. 7, p. 075 001, 2014, ISSN: 1083-3668. DOI: 10.1117/1.JBO.19.7.075001. [Online]. Available: http://biomedicaloptics.spiedigitallibrary.org/article.aspx?doi=10.1117/1.JBO.19.7.075001.

[472] J. W. Pickering, S. A. Prahl, N. V. Wieringen, J. F. Beek, H. J. C. M. Sterenborg, and M. J. C. V. Gemert, "Double-integrating-sphere system for measuring the optical properties of tissue", vol. 32, no. 4, 1993.

[473] S. A. Prahl, M. J. C. van Gemert, and A. J. Welch, "Determining the optical properties of turbid media by using the adding–doubling method", *Applied Optics*, vol. 32, no. 4, p. 559, 1993, ISSN: 0003-6935. DOI: 10.1364/AO.32.000559. [Online]. Available: https://www.osapublishing.org/abstract.cfm?URI=ao-32-4-559.

[474] B. de Campos Vidal, M. L. S. Mello, A. C. Caseiro-Filho, and C. Godo, "Anisotropic properties of the myelin sheath", *Acta Histochemica*, vol. 66, no. 1, pp. 32–39, 1980, ISSN: 00651281. DOI: 10.1016/S0065-1281(80)80079-1.

[475] L. Wang, L., Jacques, S. L., & Zheng, "MCML - Monte Carlo modeling of light transport in multi-layered tissues", *Computer methods and programs in biomedicine*, vol. 47, no. 2, pp. 131–146, 1995, ISSN: 01692607. DOI: 10.1007/978-1-4757-6092-7_4. [Online]. Available: http://www.ncbi.nlm.nih.gov/pubmed/7587160.

[476] Y. Liu, S. L. Jacques, M. Azimipour, J. D. Rogers, R. Pashaie, and K. W. Eliceiri, "OptogenSIM: a 3D Monte Carlo simulation platform for light delivery design in optogenetics", *Biomedical Optics Express*, vol. 6, no. 12, p. 4859, 2015, ISSN: 2156-7085. DOI: 10.1364/BOE.6.004859. [Online]. Available: https://www.osapublishing.org/abstract.cfm?URI=boe-6-12-4859.

[477] P. Huot, M. Lévesque, and A. Parent, "The fate of striatal dopaminergic neurons in Parkinson's disease and Huntington's chorea", *Brain*, vol. 130, no. 1, pp. 222–232, 2007, ISSN: 14602156. DOI: 10.1093/brain/awl332.